Investigation of mid-infrared supercontinuum generation in soft-glass fibers from a Q-switched mode-locked 2 mm fiber laser

Christian Kneis

To cite this version:

Christian Kneis. Investigation of mid-infrared supercontinuum generation in soft-glass fibers from a Q-switched mode-locked 2 mm fiber laser. Other. Université de Bordeaux, 2016. English. NNT : 2016BORD0135 . tel-01398415

HAL Id: tel-01398415
https://theses.hal.science/tel-01398415

Submitted on 9 Jan 2017

THÈSE PRÉSENTÉE
POUR OBTENIR LE GRADE DE

DOCTEUR DE
L'UNIVERSITÉ DE BORDEAUX

SCIENCES PHYSIQUES ET DE L'INGENIEUR

LASERS, MATIÈRE, NANOSCIENCES

Christian KNEIS

INVESTIGATION OF MID-INFRARED SUPERCONTINUUM GENERATION IN SOFT-GLASS FIBERS FROM A Q-SWITCHED MODE-LOCKED 2 μm FIBER LASER

Sous la direction de: Inka MANEK-HÖNNINGER

Soutenue le 20 septembre 2016

Membres du jury:

M. BALCOU, Philippe	Professeur	*CELIA*	Président
Mme KIELECK, Christelle	Docteur	*ISL*	Examinatrice
M. EICHHORN, Marc	Docteur, HDR	*ISL*	Examinateur
Mme MANEK-HÖNNINGER, Inka	Docteur, HDR	*CELIA*	Examinatrice
M. FANJOUX, Gil	Professeur	*FEMTO-ST*	Rapporteur
M. JOLY, Nicolas	Professeur	*MPL*	Rapporteur
M. VERHAEGHE, Kévin	Ingénieur	*DGA*	invité

Titre: Etude de génération de supercontinuum dans des verres spéciaux dans le domaine du moyen infrarouge à la base d'un laser à fibre à 2 μm en régime simultanément déclenché et à verrouillage de modes (QML)

Résumé: Cette thèse est dédiée à l'étude de la génération de supercontinuum (SCG) de forte puissance moyenne dans le domaine spectral entre 2 μm et 5,5 μm. Un laser à fibre dopée thulium (Tm^{3+}) opérant dans un régime simultanément déclenché et à verrouillage de modes (QML) a été développé. En régime continu ce laser a délivré 70 W et en régime QML, 26 W moyens ont été obtenus pour des taux de répétition en QS de 180 kHz ou plus. L'énergie la plus élevée contenue dans une enveloppe QS a été évaluée à 166 μJ avec 66 μJ contenue dans la sous-impulsion à verrouillage de mode la plus énergétique. L'émission du laser à fibre correspondait toujours à un facteur de qualité M^2 excellent, entre 1,1 et 1,2. La SCG couvrant la plage spectrale de 2 μm à 5,5 μm a été réalisée en implémentant différentes fibres en cascade. Des supercontinua jusqu'à environ 4 μm ont été générés dans des fibres en fluorure puis pour la plage spectrale complémentaire entre 4 μm et 5,5 μm, des fibres en chalcogénure ont été utilisées.

La puissance moyenne maximale de 7,8 W a été démontrée pour un supercontinuum dans une fibre en ZBLAN. Le spectre s'étend jusqu'à 4,2 μm. Au total, 69%/43%/30%/16,5% de la puissance totale ont été mesurés au-delà de 2,15 μm/2,65 μm/3,1 μm/3,5 μm respectivement. La fibre en InF_3 a permis d'atteindre une puissance moyenne de 0,8 W et le supercontinuum s'étend jusqu'à 2,95 μm.

Pour les essais d'élargissement spectral complémentaire, trois fibres en chalcogénure ont été utilisées. L'élargissement spectral a été démontré pour toutes les fibres en chalcogénure. Jusqu'à 20 mW de puissance ont été obtenus avec une fibre As_2Se_3. Le spectre a été étendu jusqu'à 4,9 μm.

Mots clés: Supercontinuum, fibres non-linéaires, lasers à fibre pulsés dans le moyen infrarouge

---

Title: Investigation of mid-infrared supercontinuum generation in soft-glass fibers from a Q-switched mode-locked 2 μm fiber laser

Abstract: This thesis reports about the investigation of high power supercontinuum (SC) generation between 2 μm and 5.5 μm. A Q-switched mode-locked (QML) thulium (Tm^{3+})-doped fiber laser has been developpped to pump different nonlinear fibers. The fiber laser provided in continuous wave regime an output power of 70 W. In QML operation, 26 W have been obtained with Q-switched repetition rates of 180 kHz or higher. The highest energy of the QS envelopes has been 166 μJ with 66 μJ contained in the most-energetic ML pulses, which have been surrounded by Gaussian-like pedestals with temporal widths around 2.5 ns. On top of these pedestals, very short temporal peaks with pulse durations around 15 ps appeared. The highest achieved peak power of a pedestal has been 25 kW. The beam parameter product M^2 of the fiber laser has been measured in different operational regimes and resulted always in an excellent value around 1.2.

The highest SC output power level from a ZBLAN fiber has been 7.8 W. In total, 69%/43%/ 30%/16.5% of the transmitted SC output radiation could be converted beyond the wavelength of 2.15 μm/2.65 μm/3.1 μm/3.5 μm, respectively, with the broadest output spectrum from the ZBLAN fiber exceeding 4.2 μm. The InF_3 fiber provided a total output power of 0.8 W with an output spectrum up to 2.95 μm.

Successful broadening of the wavelength-limited SC output from the ZBLAN fibers has been achieved with all three investigated chalcogenide fibers with as much as 20 mW of output power by using an arsenic selenide fiber. The output spectrum exceeded 4.9 μm.

Keywords: Supercontinuum, nonlinear fibers, pulsed mid-infrared fiber lasers

---

Unité de recherche

CELIA (Centre Lasers Intenses et Applications)
UMR5107 CNRS - Université de Bordeaux - CEA
43 Rue Pierre Noailles Bât C6
33400 TALENCE

Acknowledgments

First and foremost I have to express my deepest gratitude to my main supervisors at the French-German Research Institute of Saint-Louis (ISL), Dr. Christelle Kieleck and Dr. rer. nat. habil. Marc Eichhorn, for giving me the opportunity to conduct such an exciting research activity for my dissertation. Both gave me besides the invaluable physical and experimental aid, also the encouraging support and motivation to finish this thesis. I rarely had the possibility to meet researchers with such an attitude and willingness to push forward a certain research domain.

I would also like to express my sincere gratitude to my supervisor at the University of Bordeaux, Dr. Inka Manek-Hönninger. The uncountable hours on the phone for discussing physical details together with her patience for thoughtfully guiding me through this thesis have been essential. Even over the distance between the ISL and the University of Bordeaux, I never felt lack of interest from her side, moreover, I could not think about a better supervision.

I want also to thank Prof. Gil Fanjoux, Prof. Nicolas Joly and Kévin Verhaeghe for having accepted to review this manuscript. Furthermore, I want to thank Prof. Philippe Balcou for leading my defense as president.

I have to express my gratitude to the *Direction générale de l'armement* for partially funding this thesis, in particular to Anthony Cannas for the fruitful discussions. In this context I want also to thank the directors of the ISL, who accepted me as a Ph.D. student at their institute.

During the thesis, I could benefit from collaborations to researchers from many other institutes, where I want to highlight Laurent Brilland from the company *SelenOptics*, Johann Troles from the *University of Rennes*, Marcel Poulain and Franck Joulain from the company *Le Verre Fluoré* and Brandon Shaw, Rafael Gattass and Jas Sanghera from *U.S. Naval Research Laboratory* for fruitful discussions and material.

I also have to thank many colleagues from the group *Directed Photonics and Applications* at ISL. In particular, Dr. Stefano Bigotta, Dr. Martin Schellhorn, Dr. Łukasz Gałecki and Dr. Anne Dhollande for their enthusiastic support in explaining me many details in experimental laser physics to elaborate advice on my research. Furthermore, I want to express my thanks to Marc Christen and Jean-Luc Muller for the realization of many mechanical parts necessary for my laboratory setup. I also want to acknowledge Brenda Donelan, Thierry Ibach, Dr. Fabrice Lacroix, Dr. Olivier Muller and Dr. Karsten Diener for fruitful discussions and the support when things did not work properly. It was a real pleasure to work in such a friendly group.

By the end, I also have to highlight the aid of my family, who supported me in all my pursuits. Without your education and assistance over the last decades, I would not have been where I am now. And last but not least I want to acknowledge my girlfriend Nina for the countless support and the encouragement during the last years. When I was feeling down it was you cheering me up and giving me the important motivation to continue.

Contents

List of Symbols and Abbreviations

Symbols

Symbol	**Unit**	**Description**
a	[m]	Core radius of a fiber
A		Longitudinal shape of an optical pulse
A_0	[m^2]	Sellmeier coefficient
A_{21}	[s^{-1}]	Rate for spontaneous emission
A_{core}	[m^2]	Core area of an optical fiber
A_{iclad}	[m^2]	Cladding area of an optical fiber
A_j	[m^2]	Sellmeier coefficient
b		Normalized propagation constant
B	[T]	Magnetic induction
B_j	[m^2]	Sellmeier coefficient
C		Constant of a photonic crystal fiber
d	[m]	Diameter of an air channel in a photonic crystal fiber
D	[C m^{-2}]	Electric displacement
D	[ps(nm km)$^{-1}$]	Dispersion parameter
D		Ratio of power in the fiber core to the total injected pump power
D_g	[s^2]	Gain dispersion
D_m	[ps(nm km)$^{-1}$]	Dispersion parameter of an optical material
D_w	[ps(nm km)$^{-1}$]	Dispersion parameter of a waveguide
E	[V m^{-1}]	Electric field
E_0	[V m^{-1}]	Amplitude of an electrical field
E_{ML}	[J]	Pulse energy of a mode-locked pulse
$E_{p,sol}$	[J]	Pulse energy of a soliton
E_{QS}	[J]	Pulse energy of a Q-switched pulse
$E_{QS,th}$	[J]	Q-Switched pulse energy at the threshold for supercontinuum generation
F	[J m^{-2}]	Fluence
FOM	[μm kW^{-1}]	Figure of merit of a nonlinear fiber
F_{th}	[J m^{-2}]	Fluence at the threshold for supercontinuum generation
g	[m^{-1}]	Gain coefficient of a laser medium
g_{BS}	[m W^{-1}]	Gain coefficient for Brillouin scattering
g_{RS}	[m W^{-1}]	Gain coefficient for Raman scattering
G		Gain factor of a laser medium

Symbol	**Unit**	**Description**
G_i		Initial gain factor before the Q-switched pulse builds up
G_{th}		Gain factor at the threshold for lasing operation
H	[A m^{-1}]	Magnetic field strength
I	[W m^{-2}]	Intensity
$\hat{I}$	[W m^{-2}]	Peak intensity
I_c	[W m^{-2}]	Intensity of a co-propagating signal
I_{Gauss}	[W m^{-2}]	Gaussian intensity profile
I_i	[W m^{-2}]	Intensity of the intracavity radiation
I_p	[W m^{-2}]	Intensity of the pump radiation
$I_{p,sat}$	[W m^{-2}]	Saturation intensity at the pump wavelength of a laser medium
$I_{p,th}$	[W m^{-2}]	Pump intensity causing saturation
I_s	[W m^{-2}]	Intensity of the signal
j	[A m^{-2}]	Electric current density
k_0	[m^{-1}]	Wavenumber
K_{Osc}		Time-bandwidth parameter of the oscilloscope
$K_{PD\#2}$		Time-bandwidth parameter of the photo diode#2
l		Order of Laguerre-Gaussian modes
l	[m]	Length of the fiber
l_{cav}	[m]	Optical length of the laser resonator
l_{eff}	[m]	Effective length of the fiber
L		Losses of the laser resonator
m		Order of Hermite-Gaussian modes
M	[A m^{-1}]	Magnetization
M		Number of transverse modes in a fiber
MFA	[m^2]	Mode field area of a propagating mode
MFD	[m]	Mode field diameter of a propagating mode
M_s	[s^{-2}]	Modulation strength of the modulator for mode-locking
n		Order of Hermite-Gaussian modes
n		Refractive index
n_2	[m$^2W^{-1}$]	nonlinear-index coefficient
n_{core}		Refractive index of the core of a fiber
n_{eff}		Effective refractive index of the core and the inner cladding of a fiber
n_g		Group refractive index
n_{iclad}		Refractive index of the inner cladding of a fiber
$n_{iclad,eff}$		Effective refractive index of the inner cladding of a photonic crystal fiber
n_{mat}		Refractive index of an optical material
n_{oclad}		Refractive index of the outer cladding of a fiber
N_1	[m^{-3}]	Population density of the lower laser level
$N_{1,f}$	[m^{-3}]	Residual population density of the lower laser level
$N_{1,i}$	[m^{-3}]	Initial population density of the lower laser level
$N_{1,th}$	[m^{-3}]	Population density of the lower laser level at the lasing threshold
N_2	[m^{-3}]	Population density of the upper laser level

Symbol	**Unit**	**Description**
$N_{2,th}$	[m^{-3}]	Population density of the upper laser level at the lasing threshold
$N_{2,i}$	[m^{-3}]	Initial population density of the upper laser level
$N_{2,f}$	[m^{-3}]	Residual population density of the upper laser level
N_4	[m^{-3}]	Population density of the upper pump level
N_{sol}		Number of solitons
N_{tot}	[m^{-3}]	Total population density of a doped laser material
NA		Numerical aperture
p		Order of Laguerre-Gaussian modes
$\hat{P}$	[W]	Peak power of an optical pulse
P	[C m^{-2}]	Polarization
P_0	[W]	Total power of a mode
P_{ASE}	[W]	Pump power at the ASE-related threshold
$P_{BS,th}$	[W]	Threshold power for Brillouin scattering
P_l	[W]	Launched pump power
P_l	[C m^{-2}]	Linear polarization
P_{nl}	[C m^{-2}]	Nonlinear polarization
P_{out}	[W]	Output power of a fiber laser
P_p	[W]	Pump power of a fiber laser
$P_{p,th}$	[W]	Pump power at the lasing threshold
$P_{RS,th}$	[W]	Threshold power for Raman scattering
P_{th}	[W]	Pump power at the threshold for supercontinuum generation
r		Q-switch factor
R	[m]	Bend radius
R_{HR}		Reflectivity of the high reflective mirror
R_{OC}		Reflectivity of the output coupler
s		Degeneracy factor
$t_{p,meas}$	[s]	Measured pulse duration
$t_{p,ML}$	[s]	Mode-locked pulse duration
$t_{p,ML,min}$	[s]	Minimal achievable mode-locked pulse duration
$t_{p,QS}$	[s]	Q-switched pulse duration
$t_{p,sol}$	[s]	Pulse duration of a soliton
$t_{p,sys}$	[s]	Time constant of the measurement system
T_b	[s]	Build-up time of the Q-switched pulse
T_p	[s]	Pumping time during Q-switching
v_g	[m s^{-1}]	Group velocity of the envelope of an optical pulse
V		Normalized frequency
W_{12}	[s^{-1}]	Rate for absorption at the signal wavelength
W_{21}	[s^{-1}]	Rate for stimulated emission at the signal wavelength
W_p	[s^{-1}]	Pump rate
α	[m^{-1}]	Loss factor
α_{bend}	[m^{-1}]	Loss factor for bend losses
β	[m^{-1}]	Mode-propagation constant

Symbol	Unit	Description
β_2	[s m^{-1}]	Group velocity dispersion
β_m	[s$^m m^{-1}$]	m^{th} derivative of the mode-propagation constant
γ	[(W m)$^{-1}$]	Nonlinear coefficient
Γ		Ratio of power propagating in the fiber core to the total one of the mode
Δ		Relative refractive index difference
$\Delta\nu$	[s^{-1}]	Bandwidth of a laser material
$\Delta\nu_{BS}$	[s^{-1}]	Bandwidth of the Brillouin scattering
$\Delta\nu_{FSR}$	[s^{-1}]	Free spectral range of the laser resonator
$\Delta\nu_{FSR,AOM}$	[s^{-1}]	Free spectral range of the acoustic wave in an acousto-optic modulator
$\Delta\nu_{ML}$	[s^{-1}]	Repetition rate of mode-locking
$\Delta\nu_{Osc}$	[s^{-1}]	Electrical bandwidth of the oscilloscope
$\Delta\nu_{PD\#2}$	[s^{-1}]	Electrical bandwidth of the photo diode#2
$\Delta\nu_{QS}$	[s^{-1}]	Repetition rate of Q-switching
$\Delta\nu_s$	[s^{-1}]	Optical bandwidth of the signal
η_{abs}		Absorption efficiency
η_{CR}		Cross-relaxation efficiency
$\eta_{D,ML}$		Diffraction efficiency of the mode-locker
$\eta_{D,ML,max}$		Maximum achievable diffraction efficiency of the mode-locker
η_e		Extraction efficiency
θ	[rad]	Acceptance angle of a fiber for total internal reflection
λ	[m]	Wavelength
λ_{co}	[m]	Cut-off wavelength of an optical fiber
λ_p	[m]	Pump wavelength
λ_s	[m]	Wavelength of the signal
Λ	[m]	Distance of the air holes in a photonic crystal fiber
ν_p	[s^{-1}]	Frequency of a pump photon
ν_s	[s^{-1}]	Frequency of a signal photon
ρ_e	[C]	Electric charge density
σ_a	[m^2]	Absorption cross-section
σ_e	[m^2]	Emission cross-section
τ	[s]	Lifetime of the upper laser level
τ_c	[s]	Cavity lifetime
τ_{out}	[s]	Out-coupling lifetime
τ_{RT}	[s]	Round-trip time
ϕ_n	[rad]	Phase of an electrical wave
ϕ_{SPM}	[rad]	Phase induced by self-phase modulation
ϕ_{XPM}	[rad]	Phase induced by cross-phase modulation
Φ_0	[m^{-3}]	Vacuum photon flux
Φ_{CW}	[m^{-3}]	Photon flux in continuous wave operation
Φ_i	[m^{-3}]	Intracavity photon flux
Φ_{out}	[m^{-3}]	Output photon flux
χ		Material's magnetic susceptibility

Symbol	Unit	Description
Ψ		Transverse modal profile in an optical fiber
ω	[s^{-1}]	Angular frequency
ω_0	[s^{-1}]	Angular frequency at the center of the bandwidth
ω_n	[s^{-1}]	Angular frequency of the nth electronic field

Physical constants

Symbol	Value	Description
c	2.998×10^{8} ms^{-1}	Speed of light
h	6.626×10^{-34} Js	Planck constant
μ_0	1.256×10^{-6} Hm^{-1}	Vacuum permeability
ε_0	8.854×10^{-12} Fm^{-1}	Vacuum permittivity

Abbreviations

Abbreviation	Description
ACF	Autocorrelation function
Al	Aluminum
AlGaAs	Aluminum gallium arsenide
AOM	Acousto-optic modulator
ASE	Amplified spontaneous emission
AsS	Arsenic sulfide
AsSe	Arsenic selenide
BS	Brillouin scattering
CaF_2	Calcium fluoride
CO	Carbon monoxide
CO_2	Carbon dioxide
Cr	Chromium
CR	Cross-relaxation
CW	Continuous wave
EOM	Electro-optic modulator
Er	Erbium
ESA	Excited state absorption
ESM	Endlessly single-mode
et al.	And others
ETU	Energy transfer upconversion
Fe	Iron
FEL	Free electron laser
FL	Focal length

Abbreviation	**Description**
FOM	Figure of merit
FWHM	Full-width at half-maximum
FWM	Four wave mixing
GVD	Group velocity dispersion
HG	Hermite-Gaussian
Ho	Holmium
HR	High reflective
HWP	Half wave plate
InGaAs	Indium gallium arsenide
InSb	Indium antimonide
IR	Infrared
KLM	Kerr lens mode-locking
LG	Laguerre-Gaussian
LWE	Long-wavelength edge
LWP	Long wave pass
MF	Microstructured fiber
MFA	Mode field area
MFD	Mode field diameter
MI	Modulation instabilities
ML	Mode-locking
Nd	Neodymium
NPR	Nonlinear polarization rotation
OH	Hydrogen monoxide
OPA	Optical parametric amplifier
OPG	Optical parametric generation
OPO	Optical parametric oscillator
PBF	Photonic bandgap fiber
PCF	Photonic crystal fiber
PD	Photodiode
QCL	Quantum cascade laser
QML	Q-switched mode-locking
QS	Q-switching
RF	Radio frequency
RS	Raman scattering
SA	Saturable absorber
SC	Supercontinuum
SCG	Supercontinuum generation
SeH	Hydrogen selenide
SESAM	Semiconductor saturable absorber mirror
SH	Hydrogen sulfide
SiO_2	Silicon dioxide
SPM	Self-phase modulation

Abbreviation	**Description**
SRS	Stimulated Raman scattering
SSFS	Soliton self-frequency shift
SWCNT	Single-wall carbon nanotube
SWE	Short-wavelength edge
TeO_2	Tellerium dioxide
TFP	Thin-film polarizer
THz	Terahertz
Ti:Sa	Titanium sapphire
TIR	Total internal reflection
Tm	Thulium
XPM	Cross-phase modulation
YAG	Yttrium aluminum garnet
Yb	Ytterbium
ZBLAN	ZrF_4-BaF_2-LaF_3-AlF_3-NaF
ZDW	Zero dispersion wavelength
ZnSe	Zinc selenide

Introduction en français

Cette thèse est dédiée à l'étude de la génération de supercontinuum (SCG) de forte puissance moyenne dans le domaine spectral de l'infrarouge moyen (mid-IR) entre 2 μm et 5,5 μm. Un supercontinuum (SC) résulte de plusieurs effets non linéaires et de la dispersion qui contribuent ensemble à l'élargissement du spectre émis au cours de la propagation dans un milieu non linéaire. Un laser à fibre dopée thulium (Tm^{3+}) opérant dans un régime simultanément déclenché et à modes verrouillage de modes (QML) et émettant vers 2 μm a été développé. Il permet de générer les niveaux de puissance crête nécessaires à une conversion de fréquence efficace. La conversion non linéaire a été étudiée dans différentes fibres en verre fluoré et en chalcogénure. Le choix du laser à fibre dopé Tm^{3+} émettant vers 2 μm pour la source laser de pompe est cohérent avec l'objectif de couverture spectrale de 2 μm à 5,5 μm. En effet, plus la longueur d'onde de pompe est proche du spectre visé, meilleure est l'efficacité de conversion pour générer le supercontinuum. Plusieurs ions dopants permettent de générer une émission laser vers 2 μm. L'un des intérêts de l'ion thulium est de pouvoir être pompé par des diodes laser commerciales financièrement abordables. La géométrie d'une fibre optique comme milieu hôte bénéficie des avantages liés à une excellente gestion de la thermique du milieu actif et offre la possibilité de générer des faisceaux présentant une excellente qualité de faisceaux à forte puissance.

Résumé

L'efficacité de la conversion durant le processus de la génération de supercontinuum (SCG) dépend de la puissance crête de la radiation de pompe ce qui explique l'utilisation majoritaire de systèmes impulsionnels pour générer des SC. Des lasers travaillant en régime purement déclenché (QS) ou purement à verrouillage de modes (ML) ne délivrent pas les niveaux de puissance crête requis. Une solution largement choisie est un laser d'injection associé à une chaine amplificatrice. À cette fin, des diodes laser à rétroaction répartie délivrant des durées d'impulsion voisine de la nanoseconde, ou des lasers à fibre à modes bloqués passifs avec des largeurs d'impulsion dans la gamme des picosecondes ont été rapportées. Pour la première option, au moins trois amplificateurs sont nécessaires pour générer des SC dans l'infrarouge moyen à forte puissance et pour la seconde, il s'agit d'un minimum de deux. Le nombre de modules de diodes de pompe, de fibres actives, d'isolateurs et de composants de mise en forme de faisceau est par conséquence accru, rendant ces systèmes relativement complexes et onéreux. Pour générer les fortes puissances crêtes nécessaires, un oscillateur unique opérant en régime QML a été optimisé. Ce laser à fibre original permet de s'affranchir des multiples amplificateurs en cascade. Un régime simultanément déclenché et à modes bloqués est établi par deux modulateurs acousto-optiques massifs implémentés en espace libre dans la cavité laser. Cette cavité originale permet d'atteindre des niveaux de puissance crête et d'énergie par impulsion très élevés sans amplification externe.

Nous avons aussi opté pour une fibre optique pour le milieu non linéaire permettant la SCG. Les propriétés de guidage des fibres donnent accès à de fortes intensités optiques dans le cœur des fibres. De plus, la longueur d'interaction peut être choisie de manière flexible. La silice est un matériau hôte mature pour les fibres optiques mais ses fortes pertes intrinsèques dans le mid-IR la rendent inappropriée pour la SCG dans le mid-IR. Les fibres en fluorure ou en chalcogénure sont par contre transparentes dans ce domaine spectral et des résultats probants de mid-IR SCG ont déjà été démontrés avec ces deux types de fibres. Les caractéristiques des SC générés dans ces deux types de fibres diffèrent en termes de puissance moyenne accessible et de couverture spectrale atteignable. Les fibres fluorures, en particulier celles basées sur la composition ZrF_4-BaF_2-LaF_3-AlF_3-NaF (ZBLAN) permettent la génération de SC de forte puissance moyenne mais l'absorption intrinsèque du matériau limite le spectre d'émission. Avec une fibre ZBLAN, une puissance moyenne d'une vingtaine de watts a été démontrée avec une conversion au-delà des 4 μm. Pour la SCG dans le mid-IR avec des fibres en fluorure, des fibres relativement longues sont généralement nécessaires compte tenu de leur faible coefficient non-linéaire. Des supercontinuum spectralement très larges peuvent être générés dans des fibres en chalcogénure car elles présentent une transmission étendue et une très forte non linéarité. Par contre, les puissances accessibles sont moindres compte tenu de leur faible

seuil d'endommagement.

La génération de supercontinuum couvrant la plage spectrale de 2 μm à 5,5 μm a été réalisée en implémentant différentes fibres en cascade. Des supercontinuums jusqu'à environ 4 μm ont été générés dans des fibres en fluorure puis pour la plage spectrale complémentaire entre 4 μm et 5,5 μm, des fibres en chalcogénure ont été utilisées. Pour éviter de les endommager, les fibres en chalcogénure ont été pompées avec la partie supérieure à 3,5 μm du premier supercontinuum généré dans les fibres ZBLAN. Pour générer de fortes puissances moyennes et reculer les limites dues au seuil de dommage des fibres chalcogénure et fluorure, de gros diamètres de cœurs ont été privilégiés.

Un laser à fibre dopé Tm^{3+} a été spécifiquement développé pour optimiser la génération de supercontiunuum. De nombreuses expériences se sont notamment focalisées sur l'étude du régime QML mais les régimes de fonctionnement continu, purement déclenché et purement à modes bloqués ont également été étudiés. En régime continu le laser à fibre Tm^{3+} a délivré 70 W de puissance moyenne avec une fibre de 8,8 m de long et le rendement différentiel a atteint 41%. Pour ces expériences les diodes de pompe émettaient une longueur d'onde centrée vers 800 nm, correspondant à 40% de la valeur maximale de la section efficace d'absorption vers 790 nm. Avec des diodes de pompe émettant à 790 nm et une fibre plus courte de 2,2 m de long, une puissance de l'ordre de 30 W a été démontrée correspondant à un rendement différentiel de 38%. Des limitations thermiques ont empêché la montée en puissance. La différence entre les niveaux de puissance atteints peut s'expliquer par une densité de chaleur moindre dans la fibre la plus longue présentant un coefficient d'absorption inférieur à la longueur d'onde de pompe de 800 nm. L'utilisation d'un réseau de diffraction pour fermer la cavité laser a permis d'accorder les longueurs d'onde générées entre 1,9 μm et 2,1 μm selon les longueurs de fibres. Une puissance moyenne de 26 W a été atteinte avec la fibre la plus courte de 2,2 m en régime de fonctionnement déclenché; la durée d'impulsion valait 40 ns, l'énergie par impulsion maximale atteinte 750 μJ et la puissance crête 19 kW. L'émission spontanée sans émission (ASE) est un facteur limitant. En fonctionnement purement à modes bloqués avec la fibre dopée Tm^{3+} de 8,8 m de long, une puissance moyenne de 50 W a été démontrée avec des durées d'impulsion de 200 ps et des énergies par impulsion de 0,8 μJ; la puissance crête atteint 4 kW. En régime QML, 26 W moyens ont été obtenus avec un rendement différentiel de 37% pour des taux de répétition en QS de 180 kHz ou plus. L'énergie la plus élevée contenue dans une enveloppe QS a été évaluée à 166 μJ avec 40% de cette énergie, soit 66 μJ, contenue dans la sous-impulsion à verrouillage de mode la plus énergétique. Les impulsions correspondant au régime de modes bloquées sous l'enveloppe QS ont un profil temporel correspondant à un piédestal Gaussien qui contient la plus grande partie de l'énergie. Au sommet de ces piédestaux, des pics temporels très courts ont été observés.

Les largeurs temporelles des piédestaux varient entre 2 ns et 3 ns suivant l'énergie QS du laser à fibre. La plus forte puissance crête générée dans un piédestal atteint 25 kW. L'impulsion ML présente une largeur temporelle entre 10 ps et 20 ps dépendante aussi de l'énergie QS en sortie du laser à fibre. En régime QML, la largeur spectrale maximale atteignait environ 1,5 nm. La qualité de faisceau du laser à fibre a été mesurée en régime continu, déclenché, à modes bloqués et en régime simultanément déclenché et à modes bloqués pour plusieurs puissances moyennes générées. L'émission du laser à fibre correspondait toujours à un facteur de qualité M^2 excellent, entre 1,1 et 1,2.

Pour la SCG dans des fibres en fluorure on dispose des matériaux ZBLAN et InF_3. Le ZBLAN présente une transmission plus limitée dans l'infrarouge comparé à l'InF_3 mais il supporte des niveaux de puissance supérieurs. L'InF_3 offre une fenêtre de transmission plus large mais une absorption plus importante que le ZBLAN. Trois fibres ZBLAN avec des ouvertures numériques (NA) identiques mais des diamètres de cœur différents ainsi qu'une fibre InF_3 ont été testées. Les performances du SC ont été évaluées en termes d'efficacité de conversion en longueurs d'onde, de puissance totale générée et de longueur d'onde maximale atteinte pour le spectre du continuum en fonction des différents paramètres d'opération du laser à fibre. Pour déterminer l'efficacité de conversion, différents filtres passe-haut avec une longueur d'onde de coupure à 3 dB à 2,15 μm/2,65 μm/3,1 μm et 3,5 μm ont été utilisés pour mesurer la puissance moyenne générée au-delà de ces longueurs d'onde.

La puissance moyenne maximale de 7,8 W démontrée pour un supercontinuum dans une fibre en ZBLAN a été limitée par la destruction d'une extrémité de la fibre. La fibre utilisée dans cette expérience présente un diamètre de cœur de 12 μm et une ouverture numérique de 0,23 et elle avait été spécialement conçue pour générer des fortes puissances et pour optimiser l'efficacité de conversion. Le spectre s'étend jusqu'à 4,2 μm. Au total, 69%/43%/30%/16,5% de la puissance totale ont été mesurés au-delà de 2,15 μm/2,65 μm/3,1 μm/3,5 μm respectivement. La qualité de faisceau du supercontinuum infrarouge généré a été évaluée pour deux longueurs d'onde centrale, 2,45 μm et 3,3 μm. En prenant en compte la longueur d'onde centrale dans le calcul, le facteur de qualité valait 1,2 dans les deux directions orthogonales. La fibre en InF_3 a permis d'atteindre une puissance moyenne de 0,8 W pour une puissance injectée de 3 W et le supercontinuum s'étend jusqu'à 2,95 μm. Les performances relativement modestes avec cette fibre sont probablement à imputer à une forte absorption pour les longueurs d'onde entre 2 μm et 4 μm et à son faible seuil de dommage.

Pour les essais d'élargissement spectral complémentaire au-delà des longueurs d'onde limitatives du ZBLAN, trois fibres en chalcogénure ont été utilisées. Il s'agit de fibre en As_2Se_3, GeAsSe et As_2S_3. Les deux premières sont des fibres microstructurées et la troisième est une fibre à saut d'indice. La pertinence de la fibre InF_3 a aussi été évaluée pour l'élargissement spectral du premier supercontinuum généré dans les fibres en ZBLAN.

L'élargissement spectral a été démontré avec succès pour toutes les fibres en chalcogénure. Jusqu'à 20 mW de puissance pour une puissance de pompe de 120 mW ont été obtenus avec la fibre As_2Se_3. Cette fibre a aussi montré le meilleur potentiel en termes d'élargissement spectral. Les expériences ont permis de valider le concept de l'élargissement spectral d'un premier supercontiunuum issu d'une fibre ZBLAN dans une deuxième fibre non linéaire. Les expériences menées n'ayant pas été limitées par l'endommagement des fibres, des puissances moyennes supérieures à celles générées devraient être accessibles. Le spectre a été étendu jusqu'à 4,9 μm (-20 dB). La fibre en InF_3 n'a pas permis de démontrer un élargissement spectral.

Abstract

This thesis is devoted to the investigation of high average power mid-infrared (mid-IR) supercontinuum generation (SCG) between 2 μm and 5.5 μm. Supercontinuum (SC) is a collection of different nonlinear effects and dispersion that altogether broaden the spectrum of radiation during its propagation inside a nonlinear medium. A thulium (Tm^{3+})-doped fiber laser, emitting around 2 μm, has been developed as pump laser system in Q-switched mode-locked (QML) operation to reach the necessary peak power levels for efficient wavelength conversion. For the nonlinear medium, different fluoride and chalcogenide fibers have been investigated.

The choice of the Tm^{3+}-doped fiber laser as pump laser source was based on the vicinity of the emitting wavelength at 2 μm to the desired output wavelength range. The closer the pump wavelength to the targeted mid-IR spectral range is, the higher is the SC efficiency. From all the active laser ions that emit at a wavelength of around 2 μm, thulium offers the advantage that affordable and commercially available pump diodes can be used. The geometry of an optical fiber as host medium exhibits the well-known advantages of very efficient heat removal from the active material and a good beam quality at high output power levels.

The wavelength conversion efficiency during SCG depends on the peak power of the pump radiation. Therefore, mostly pulsed laser systems are used for SCG. Purely Q-switched or purely mode-locked systems do not deliver sufficient peak power levels. Seed lasers with amplifier chains are very often the preferred choice. For this purpose, distributed feedback laser diodes with pulse durations around 1 ns or passively mode-locked fiber lasers with pulse widths in the range of picoseconds have been reported. In case of the first alternative, at least three amplifiers are necessary as pump source for high power mid-IR SCG, and for the latter one at least two, which has in consequence the need of more pump diode modules, active fibers, isolators and beam shaping accessories, making such setups relatively expensive and complex. The pump fiber laser in this research study has been operated in QML regime to bypass the need of multiple cascaded amplifiers and to realize the high peak power operation with a single-oscillator design. To induce QML, two free-space acousto-optic modulators have been implemented in the free-space part of the laser resonator to actively Q-switch and actively mode-lock the system simultaneously. With this cavity design, very high peak power and pulse energy levels have been achieved without the need of further external amplification.

For the geometry of the nonlinear medium for SCG, also the form of an optical fiber has been chosen, which is very popular for this application owing to their guiding properties, enabling high optical intensities in the fiber core over a flexibly chosen interaction length. For the selection of the proper material for mid-IR SCG, silica, as the most mature fiber host material, could not be considered because of its high intrinsic losses in the mid-IR. Fluoride or chalcogenide fibers exhibit transmission and mid-IR SCG in these fiber materials have already

been demonstrated. The expected SC performance from both mentioned materials is although very different in terms of output power and spectrum. Fluoride fibers, in particular based on the most commonly used material composition ZrF_4-BaF_2-LaF_3-AlF_3-NaF (ZBLAN), enable high output power levels, but with limited output spectra owing to its material absorption. Tens of watts have already been demonstrated with wavelength conversion exceeding 4 μm in ZBLAN fibers. For mid-IR SC experiments with fluoride materials, usually long fibers are necessary by reason of their low nonlinear-index coefficient. With chalcogenide fibers, very broadband SC output radiation is feasible because of their wide transmission bandwidth and their high nonlinearity. The output power out of these fibers are orders of magnitude lower compared to fluoride fibers as a result of their low damage threshold.

To cover the wavelength range from 2 μm up to 5.5 μm, different fluoride fibers have been investigated to generate SC output radiation up to around 4 μm. For the wavelength range between 4 μm and 5.5 μm, chalcogenide fibers have been tested to further convert the SC output radiation from the fluoride fibers. The chalcogenide fibers have been pumped with the SC output radiation beyond 3.5 μm to prevent them from damage. Generally, for high power operation, the investigated fluoride and chalcogenide fibers had relatively big core diameters to push their damage threshold in terms of average power operation.

The Tm^{3+}-doped fiber laser has been developed with the goal to enable highly efficient SCG. Therefore, most experiments have been focused on QML operation. But also the regimes of continuous wave, pure Q-switching and pure mode-locking have been investigated. The Tm^{3+}-doped fiber laser provided in continuous wave operation an output power level of 70 W with an active fiber length of 8.8 m. The slope efficiency during this experiment was approximately 41%. The pump diode modules during this investigation emitted at a wavelength of around 800 nm, which relates to an absorption cross-section of the active fiber of around 40 % compared to its peak value at the pump wavelength of approximately 790 nm. With a shorter fiber length of 2.2 m and pump diode modules emitting at 790 nm, the maximum obtained output power level has been around 30 W with a slope efficiency of 38%. The limit in terms of power scaling has been set by thermal issues. The reason for the different output power performance might be the lower heat density of the longer fiber owing to the lower absorption coefficient at the pump wavelength used. Tunability of the lasing wavelength has been realized with a diffraction grating used as cavity end mirror of the laser resonator. The fiber laser was tunable between approximately 1.9 μm and 2.1 μm, dependent on the used fiber length. In Q-switched operation, the shorter fiber (2.2 m) provided an output power of 26 W with pulse energies up to 750 μJ, limited by the onset of amplified spontaneous emission. The pulse width at this output energy was around 40 ns, which resulted in a peak power level of 19 kW. In purely mode-locked operation, 50 W have been achieved with a pulse energy of 0.8 μJ and a pulse duration of 200 ps with the long Tm^{3+}-doped fiber (8.8 m), yielding a peak power level of 4 kW. In QML, 26 W have been obtained with a slope efficiency of 37% at Q-switch repetition rates of 180 kHz or higher. The highest energy of the QS envelopes has been around 166 μJ, where as much as 40%, and hence 66 μJ, have been within the most-energetic ML subpulse. The ML pulses below the QS envelope have been surrounded by a Gaussian-like pedestal that contained most of the pulse energy. On top of these pedestals, very short temporal peaks appeared.

The temporal widths of the pedestals have been in the range of 2 ns to 3 ns, dependent on the QS output energy of the fiber laser. The highest achieved peak power level of a pedestal has been 25 kW. The ML pulses had a width between 10 ps and 20 ps, also dependent on the QS output energy of the fiber laser. In QML operation, the broadest linewidth was approximately 1.5 nm. The beam quality of the fiber laser has been measured in continuous wave, Q-switched, mode-locked and QML operation at different output levels of the fiber laser. The fiber laser provided always an excellent M^2 beam parameter product, M^2, between 1.1 and 1.2.

For SCG in fluoride fibers, the material ZBLAN and InF_3 have been available. ZBLAN exhibits narrower transmission bandwidth but it has proven to support higher output power levels. InF_3 offers a broader transmission window but with overall higher material absorption. In total, three ZBLAN fiber designs with different core diameters but constant NA, and one InF_3 fiber have been tested. The SC output performance has been evaluated in terms of wavelength conversion efficiency, total output power level and the long-wavelength edge of the SC output spectra for different operational parameters of the pump fiber laser. For the determination of the conversion efficiency, different optical long wave pass filters with 3 dB cut-off wavelength at 2.15 μm/2.65 μm/3.1 μm/3.5 μm have been implemented to measure the average output power beyond these filters.

The highest achieved SC output power level from a ZBLAN fiber has been 7.8 W in all spectral bands, limited by the destruction of the fiber end facet. The used ZBLAN fiber in this experiment with a core diameter of 12 μm and a numerical aperture of 0.23 has been especially designed for high output power and conversion efficiency. In total, 69%/43%/30%/16.5% of the transmitted SC output radiation in all spectral bands could be converted beyond the wavelength of 2.15μm/2.65μm/3.1μm/3.5μm, respectively, with the broadest output spectrum from the ZBLAN fiber exceeding 4.2 μm. The beam quality of the mid-IR SC output radiation has been measured two times with very broad SC output spectra and central wavelengths of 2.45 μm and 3.3 μm. The beam quality factors have been around 1.2 in both directions considering the central wavelength of the output spectrum for the calculation of the beam parameter product. The InF_3 fiber provided a total output power of 0.8 W at a launched pump power of 3 W with an output spectrum up to 2.95 μm. The reason for the relatively poor output performance with this fluoride material was probably caused by the rather high absorption values in the wavelength range between 2 μm and 4 μm and its low damage threshold.

For the experiments for further spectral broadening of the wavelength-limited SC output from the ZBLAN fibers, three chalcogenide fibers of the material arsenic selenide, germanium arsenide selenide and arsenic sulfide have been characterized. The first two mentioned chalcogenide fibers exhibited a photonic-crystal and the other one a step-index fiber design. Also the suitability of the InF_3 fluoride fiber has been investigated for further wavelength conversion of the ZBLAN SC output radiation.

With all the chalcogenide fibers, successful broadening has been achieved with as much as 20 mW of output power at the highest pump power level of 120 mW with the arsenic selenide fiber, which has also shown the best potential regarding wavelength broadening. The demonstrated results have been proof-of-principle studies whether the SC output radiation from the ZBLAN fiber can be further broadened. There has been no limitation by fiber damage and therefore higher output power levels are feasible. The output spectrum exceeded a wavelength of 4.9 μm at the -20 dB intensity level. By using the InF_3 fiber, no wavelength broadening has been achieved.

1 Introduction

Many applications nowadays require radiation in the mid-infrared (mid-IR) wavelength region with preferably broad optical spectrum and perfectly high spatial brightness. One example is the telecommunication sector, which is interested in that wavelength range for free-space communication systems [1], using several transmission windows of the atmosphere (see Figure 1.1) and slicing up the optical spectrum into different channels [2]. Other applications for mid-IR sources are directed countermeasures [3], or remote chemical sensing, where spectral fingerprints are recorded based on the numerous absorption lines of different chemicals in this wavelength range, e.g. explosives [4]. Also for military range finding applications, mid-IR sources are highly demanded [5]. But not only the atmospheric transmission window offers plenty of possibilities, also the strong water absorption enables medical applications like tissue ablation [6] or optical coherence tomography [7], making use of the relatively long wavelengths for higher penetration depth.

Up to now, there are many laser systems covering mid-IR wavelengths, e.g. direct laser systems in the form of gas, semiconductor, solid-state, or free-electron lasers (FEL). Many of the named systems are commercially available, for example carbon monoxide (CO) lasers, delivering tens of watts at a wavelength around 5 μm [8], or quantum cascade lasers (QCLs) with minimal footprint and hundreds of milliwatts output power [9]. Chromium (Cr^{2+}) - doped solid-state lasers offer high tunability and watt-level output power [10] and iron (Fe^{2+}) - doped laser media emit even further in the IR wavelength range but offer only very low output power

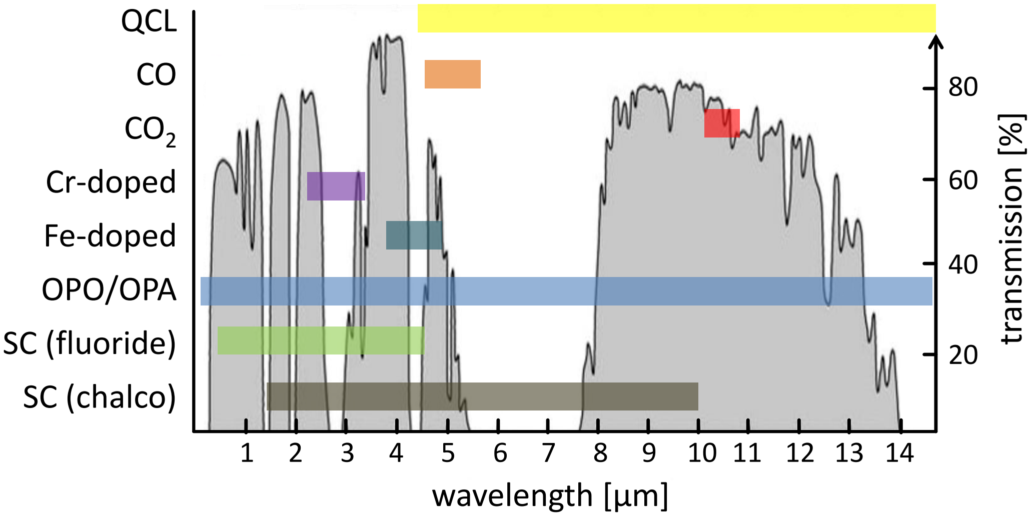

Figure 1.1: Atmospheric transmission measured over a distance of 6000 feets (∼ 1.8 km) with the coverable spectral ranges of mid-IR sources [11].

levels. There are also solid-state upconversion lasers, delivering remarkable output power levels with high beam quality [12, 13]. Free electron laser setups exhibit very high output power levels [14], but require enormous dimensions. The possible spectrum, which can be covered from some of the named technologies, is shown in Figure 1.1. It has to be considered that the rectangles indicate the realizable output spectrum with the different technologies. It is in almost all cases, except for the supercontinuum (SC) sources, not possible to have one source delivering such broad output spectrum at once.

At the moment, for applications demanding very broad optical spectrum, there are only incandescent lamps commercially available, which can cover thousands of nanometers in the mid-IR. But these sources offer spatially very poor brightness levels. All of the named direct sources suffer either in spectral broadness or spatial brightness and it is therefore a trade-off between both parameters for the right choice of a light source for some of the applications named above. For the last decades, there has been an ongoing research effort to bridge this gap between spectral broadness and spatial brightness where it turned out that wavelength conversion processes show high potential to solve this challenge.

One popular technology are optical parametric oscillators (OPOs) and amplifiers (OPAs), where one pump photon is converted into two photons with higher wavelengths via optical parametric generation (OPG). This technology is well-developed and provides efficient high average output power levels. The output spectrum of an OPO is tunable and can be much broader compared to direct laser sources. However, their spectral broadness is limited and for some of the mentioned applications therefore not suitable. For this reason, many research groups have focused on so-called supercontinuum generation (SCG), which enables output spectra covering thousands of nanometers.

Supercontinuum (SC) is a collective term for different effects, which altogether broaden the optical spectrum of radiation during interaction with a nonlinear medium. Dispersion, self- and cross-phase modulation (SPM/XPM), stimulated Raman scattering (SRS), parametric four-wave mixing (FWM), or soliton-related dynamics are only some of the effects included in SC [15]. It is possible to transfer the radiation of a narrow-band pump laser source into a broadband SC source with insignificant degradation in beam quality and thus spatial brightness. SC was first discovered by Alfano *et al.* in 1970, generating an output spectrum from 400 nm to 700 nm by using a frequency doubled mode-locked (ML) neodymium (Nd^{3+})-doped glass laser to pump a borosilicate glass [16]. Since that time, many research studies have been conducted to develop and investigate this technology with various nonlinear media, pump laser configurations and wavelength regions of the SC output radiation. SCG has been demonstrated in solid-state bulk material [16], liquids [17, 18] or gases [19, 20] with very different pump laser systems. The conversion efficiency hereby is dependent on the intensity of the pump laser system, therefore, mainly pulsed pump lasers have been used.

With the advent of optical fibers, SCG gained additional attention because of many advantages offered by this specific solid-state geometry as nonlinear medium, which was first tested by Stolen *et al.* in 1976 for that purpose [21]. Before that proof-of-principle experiment, SCG has been realized by tightly focusing the pump radiation into the nonlinear medium to reach the necessary intensity, which is self-evidently connected to a strong divergence and hence a limited interaction length. Owing to the guiding properties in optical fibers, meaning the spatial confinement of the radiation in the fiber core, high optical intensities are feasible over

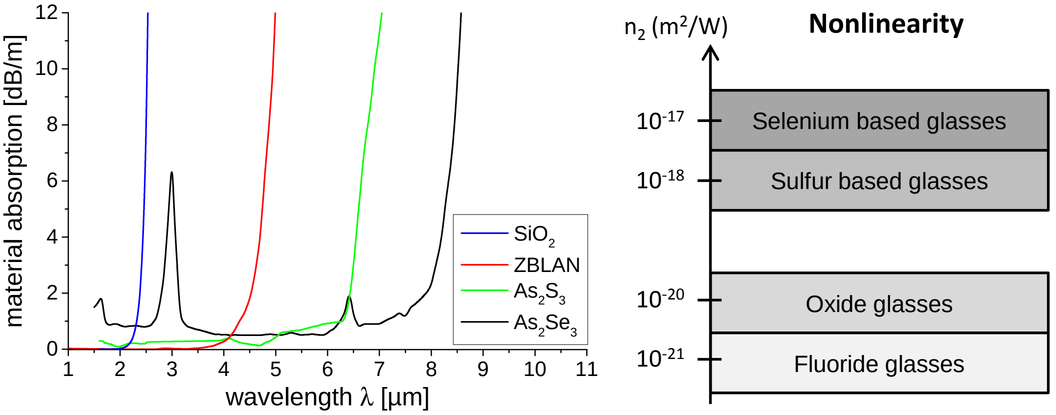

Figure 1.2: *Left*: Material absorption of silicon dioxide (SiO_2) [22], ZrF_4-BaF_2-LaF_3-AlF_3-NaF (ZBLAN) [23], arsenic sulfide (As_2S_3) [24], and arsenic selenide (As_2Se_3) [25]; *right*: Nonlinear-index coefficient, n_2, for different fiber materials.

a flexibly selectable interaction length [2, 26]. Furthermore, SCG in fibers can provide single-mode propagation determined by the fiber design and alignment-free all-fiberized SC systems [27]. Nowadays, the majority of SC experiments reported in literature are based on silica fibers, owing to the well-known parameters of this material, the maturity of the fiber drawing process and the possibility of high power operation. There are commercial SC systems based on silica fibers offering watt-level output power with an output spectrum from 400 nm to 2400 nm [28].

Unfortunately, silica fibers cannot be used for mid-IR SCG due to their high multi-phonon absorption in this wavelength range [23]. Soft-glass fibers are mandatory, in particular chalcogenide or fluoride materials that offer transmission in the mid-IR. The left side of Figure 1.2 displays the material absorption of silica, the fluoride material ZrF_4-BaF_2-LaF_3-AlF_3-NaF (ZBLAN) and two chalcogenide materials, arsenic sulfide (AsS) and arsenic selenide (AsSe). The absorption data indicate the applicability of the shown soft-glass materials for mid-IR SCG, the SC output performance from chalcogenide and fluoride fibers differs significantly. Figure 1.2, right, presents the nonlinear-index coefficient, n_2, of the different fiber materials. They exhibit a nonlinearity, which can be a factor of around 1000 times higher than the one for fluoride fibers and thus, very short interaction lengths are sufficient. Chalcogenide fibers are based on the chalcogen elements sulfur, selenium or tellurium, typically combined with elements from the 13^{th}, 14^{th}, or 15^{th} group of the periodic table. Their transmission bandwidth is much broader compared to fluoride fibers and wavelength conversion far into the IR is feasible. However, as a result of the weak covalent bonds of their atoms and the correspondingly low melting temperatures (600°C to 900°C) [29], these fibers are very fragile and exhibit low optical damage thresholds. Therefore, they are mostly used for low power applications in the range of tens of milliwatts with broad SC output spectra. For high power operation, fluoride fibers, in particular ZBLAN fibers, offer great potential due to relatively high maturity of fluoride fiber fabrication and mechanical resistivity. Output power levels of tens of watts have already been achieved with optical output spectra exceeding 4 μm [3, 30, 31]. The typical emission spectral range from both types of fibers are shown in Figure 1.1.

The wavelength conversion during SCG is much more efficient if the nonlinear material is pumped in the anomalous dispersion region, meaning when the pump radiation experiences a negative group velocity dispersion (GVD), which is reached by pumping the nonlinear medium with a pump wavelength that is longer than its zero dispersion wavelength (ZDW). The reason for this are different nonlinear effects responsible for the broadening whose influence will be discussed in detail in chapter 2. The ZDW of fluoride fibers lies between 1.6 μm and 2 μm, dependent on the fiber design. Therefore, 2 μm laser sources can be directly used without wavelength shifting elements, necessary for pump laser systems at wavelengths around 1 μm or 1.5 μm. It has been proven that 2 μm pump sources provide the largest spectral power density in the mid-IR for SCG in fluoride fibers [32]. Furthermore, pumping at longer wavelength inherently offers higher output power levels thanks to a higher damage threshold of the material [33].

For 2 μm laser system, the lanthanide elements thulium (Tm^{3+}) and holmium (Ho^{3+}) in their trivalent form and the transition metal chromium (Cr^{2+}) in its divalent form are the most commonly used dopants. The most important requirement for the pump laser system is to enable efficient high power mid-IR SC with high compactness. Thus, the fiber design is chosen as geometry for the host material. Furthermore, it offers numerous advantages over the commonly used bulk geometry, e.g. well-defined spatial mode, high robustness, broader gain bandwidth, alignment-free laser setups, high single-pass gain, or excellent thermal management [34]. Silica provides high mechanical strength and stability owing to the strong electronic bond between the silicon and the oxygen. For the choice of a suitable pump laser system, it has to be considered that an output pulse width in the range of pico- or nanoseconds are sufficient for mid-IR SCG.

Tm^{3+}-doped fiber lasers offer a strong absorption band around 790 nm, which can be covered directly by efficient and affordable, commercially available aluminum gallium arsenide (AlGaAs) diodes. That pump wavelength furthermore enables a cross-relaxation of adjacent thulium ions in the host material, allowing a so-called "two-for-one" pumping mechanism increasing the quantum efficiency to theoretically 200%. The broad tunability of Tm^{3+}-doped fiber lasers, ranging from 1.7 μm to 2.1 μm, allows flexible choice of the pump wavelength for SCG and the generation of short pulses via ML. Additionally, the relatively long upper state lifetime provides good energy storage to enable high pulse energy operation with Q-switching (QS) [35]. In terms of average power in continuous wave (CW) operation, 415 W has been achieved with a such fiber laser providing good beam quality [36].

Ho^{3+}-doped silica fibers offer a long upper state lifetime, which is multiple times higher compared to Tm^{3+}-doped silica [37, 38], enabling high energy storage capabilities, e.g. in QS operation. High average output power operation is feasible owing to the small quantum defect, if the system is pumped in-band. So far, 400 W have been demonstrated with a Ho^{3+}-doped silica fiber laser pumped by a high power Tm^{3+}-doped fiber laser [39]. Such pump sources are usually used for that purpose because of the relatively weak and narrow absorption bands of Ho^{3+}-doped materials at 890 nm and 1.15 μm [40], the absence of a comparable "two-for-one" process and the non-availability of efficient laser diodes around 2 μm. But Tm^{3+}-doped fiber lasers as pump source increase the dimensions of the whole laser system.

Cr^{2+}-doped lasers offer high tunability and therefore the possibility for ultra-short pulse generation via ML [41]. In general for SCG, if the nonlinear material is pumped above its ZDW, the wavelength broadening occurs mainly towards longer wavelengths as it will be explained in more detail in a further chapter. Cr^{2+}-doped lasers emit at wavelengths above 2 μm, which means that the first part of the atmospheric transmission window cannot be covered, see Figure 1.1. Another disadvantage of Cr^{2+}-doped lasers for this application is their limited output power levels, which is partially caused by the very high thermal lensing in its most common host material zinc selenide (ZnSe). The fiber geometry for the host material cannot be realized for Cr^{2+}-doped laser systems.

Out of the descriptions above, a Tm^{3+}-doped silica fiber laser has been chosen as a pump source for mid-IR SCG in fluoride materials. Silica fiber lasers are currently replacing crystal-based solid-state lasers in many applications, causing the fast increase of the fiber laser market, also in the wavelength range around 2 μm [42].

Mid-IR SCG in fluoride and chalcogenide fibers has been demonstrated with many different kinds of pump sources, e.g. OPOs [43], gain-switched lasers [44], short pulse amplification systems seeded by semiconductor [23], or direct ML [45, 46]. As pulse generating technique for the pump fiber laser in this thesis, QML is applied. This operational regime is induced by two actively triggered acousto-optic modulators (AOMs). QML provides sufficient peak power levels for the realization of a single-oscillator pump source without the need of amplifier chains, which is very beneficial regarding the compactness of the system. The active modulators exhibit very high damage thresholds, indispensable for this application.

The goal of the investigations in this thesis is the design of a QML Tm^{3+}-doped silica fiber laser to pump appropriate nonlinear fibers to generate high power mid-IR SC radiation. The atmospheric transmission windows between 2 μm and 5.5 μm should be covered with the focus on high average power and compactness. The first task of the thesis concerns the pump laser system. It has to be designed to deliver output pulses enabling efficient mid-IR SCG with high average power. Hereby, the cavity design (cavity elements, Tm^{3+}-doped silica fiber, pump design, ...) has to be chosen and the output performance characterized. The second task comprises the layout of an appropriate beam shaping between pump source and nonlinear fibers to obtain high coupling efficiencies into the nonlinear fiber, including mode field adaption. The investigation and optimization of SCG represents the third part of the thesis. Different nonlinear fibers have to be tested to evaluate their applicability to fulfill the mentioned requirements. The focus is put on ZBLAN fluoride fibers, but also other fluoride and chalcogenide fibers have to be investigated. It has also to be tested, if cascading different nonlinear fibers is reasonable.

This thesis contains six chapters including this introduction. The second chapter treats the theoretical background to derive the basics of fiber optics, including different fiber geometries with the related performance parameters. Furthermore, short-pulse propagation in an optical fiber has to be explained with dispersion, nonlinear effects and losses. These effects play an important role for ML and also for SCG. Furthermore, the fundamental theory of laser physics is deduced based on a Tm^{3+}-doped silica fiber as active material. All the necessary operational regimes of a laser system are derived, CW, QS, ML and QML operation. In the last part of the theory, a qualitative description, based on the already derived effects for short-pulse propagation, is given for SCG with a figure of merit (FOM) to describe quantitatively the suitability of the available fibers for mid-IR SCG.

The third chapter deals with the results obtained from the pump fiber laser. The setup is described with all the implemented optical elements, the available fibers and characterization tools used for the investigations. The results are separated into the different operational regimes. They are compared with calculations for the expected output performance, based on the theory described in chapter 2. Possible reasons for the differences between theory and experiment are explained and the simulations are adapted. A summary in last part of the chapter gives an overview of the state-of-the-art results of Tm^{3+}-doped silica fiber lasers with a comparison to the achieved performance.

The fourth chapter handles about the SCG in fluoride fibers, pumped by the Tm^{3+}-doped fiber laser. The material ZBLAN as nonlinear fiber is hereby investigated mostly. First, an introduction gives an overview about mid-IR SCG in fluoride fibers. Second, the optical setup with all available materials and characterization tools is described. As in the previous chapter, a summary in the end compares the achievements with the state-of-the-art results reported in literature.

The fifth chapter deals about wavelength broadening effects in second nonlinear fibers, which are pumped by the SC output radiation from the first SC stage. Mostly chalcogenide fibers have been implemented as nonlinear material for these experiments. An introductory part gives an overview of mid-IR SCG in chalcogenide fibers and the second part describes the available fibers and the measurement equipment. A summary gives an overview of similar results from the literature and compares them with the results obtained.

By the end of this thesis, the achieved results are summarized in the conclusion and an outlook presents the possibilities to further enhance the performance of the overall system. Hereby, the different parts of the setup, including Tm^{3+}-doped fiber laser, SCG in fluoride fibers and the further wavelength broadening in the chalcogenide fibers, are treated separately.

2 Theory

In this chapter, the necessary theoretical background is derived. It is separated into three parts. The pulse propagation in optical fibers is the first one, which is essential to describe the pulse generation via ML and for SCG in optical fibers, where dispersion and different nonlinear effects are responsible for the wavelength broadening. The second section is devoted to the theory behind the lasing operation of the Tm^{3+}-doped fiber laser in CW, QS, ML and QML operation. In the third section, the SCG is explained qualitatively based on the nonlinear effects explained in the first section of this chapter.

2.1 Pulse propagation in optical fibers

2.1.1 Maxwell equations

For the derivation of pulse generation in optical fibers, the Maxwell equations are introduced, which form the foundation for the propagation of electro-magnetic waves inside a medium:

$$\vec{\nabla} \cdot \mathbf{D} = \rho_e, \tag{2.1}$$

$$\vec{\nabla} \cdot \mathbf{B} = 0, \tag{2.2}$$

$$\vec{\nabla} \times \mathbf{E} = -\frac{\partial \mathbf{B}}{\partial t}, \tag{2.3}$$

$$\vec{\nabla} \times \mathbf{H} = j + \frac{\partial \mathbf{D}}{\partial t}. \tag{2.4}$$

Hereby, $(\vec{\nabla}\cdot)$ is the divergence and $(\vec{\nabla}\times)$ the curl operator. **D** is the electric displacement and ρ_e the electric charge density. **B** and **E** are the magnetic induction and electric fields, respectively, **H** the magnetic field strength and j the electric current density. Hereby, **B** depends on **H**,

$$B(r,t) = \mu_0(H(r,t) + M(r,t)), \tag{2.5}$$

and **D** on **E**,

$$D(r,t) = \varepsilon_0 E(r,t) + P(r,t), \tag{2.6}$$

where μ_0 is the free-space permeability and M the magnetization of the material. ε_0 is the vacuum permittivity and P the material polarization, which consists of a linear part , P_l, and a nonlinear part, P_{nl},

$$\mathbf{P} = \mathbf{P}_l + \mathbf{P}_{nl} = \varepsilon_0 \cdot \chi^{(1)}\mathbf{E} + \varepsilon_0 \sum_{j>1} \chi^{(j)}\mathbf{E}^{(j)}, \tag{2.7}$$

where $\chi^{(j)}$ is the j^{th} order component of the material's magnetic susceptibility tensor, which is defined by the composition and molecular structure of the material. Usually, this tensor is time-dependent, which will be neglected in the further mathematical derivations. If weak electro-magnetic fields are interacting with the material, P_l can be taken as an accurate approximation, but if the field is strong, higher-order susceptibilities have to be taken into account, which cause different nonlinear effects. $\chi^{(2)}$ leads to second harmonic generation, sum or difference frequency generation. $\chi^{(3)}$ is related to the Kerr effect, FWM, or different scattering processes.

To calculate the propagation of the electro-magnetic field in the core of an optical fiber, equation 2.5 will be inserted in the curl of equation 2.3 including the fact that glass is not magnetizable and therefore $\vec{M} = 0$,

$$\vec{\nabla} \times \vec{\nabla} \times \mathbf{E} = -\mu_0(\vec{\nabla} \times \frac{\partial \mathbf{H}}{\partial t}). \tag{2.8}$$

By using equation 2.4, equation 2.8, the simplifications

$$\vec{\nabla} \times \vec{\nabla} \times \mathbf{E} = \vec{\nabla} \cdot (\vec{\nabla} \cdot \mathbf{E}) - \vec{\nabla}^2\mathbf{E} \tag{2.9}$$

and

$$\vec{\nabla} \cdot (\vec{\nabla} \cdot \mathbf{E}) = 0, \tag{2.10}$$

the general wave equation yields a nonlinear differential equation

$$\vec{\nabla}^2\mathbf{E} = \frac{1}{c^2}\frac{\partial^2\mathbf{E}}{\partial t^2} + \mu_0\frac{\partial^2\mathbf{P}}{\partial t^2}, \tag{2.11}$$

with c as the speed of light in vacuum. For solving this equation, numerical tools are necessary. Therefore, the following assumptions are made to find an analytical solution. First, the envelope of the pulse is slowly varying in time, and second, there is only a weak coupling of transverse and longitudinal propagation modes. Taking those assumptions into account, the general propagation equation in an optical fiber results in

$$E(x,y,z,t) = E_0\Psi(x,y)A(z,t)e^{i(\beta z - \omega t)}, \tag{2.12}$$

with β as the mode-propagation constant, which will be further described in a following section. One could also derive these propagation equations with the magnetic field, but in literature, the electrical field is usually preferred. $\Psi(x,y)$ represents the transverse modal distribution and $A(z,t)e^{i(\beta z - \omega t)}$ the longitudinal part of the propagating electro-magnetic wave. The notation x,y,z indicate the position inside the fiber expressed in the Cartesian coordinate system, t the time and ω the angular frequency of the propagating wave, which is

$$\omega = 2\pi\nu, \tag{2.13}$$

with ν as the frequency of the radiation. In the following sections, different effects will be described that influence either $\Psi(x,y)$ or $A(z,t)e^{i(\beta z - \omega t)}$.

2.1.2 Fiber modes

2.1.2.1 Classical fiber geometry

An optical fiber is a special form of a waveguide, where light is guided in a flexible and transparent fiber. The development of optical fibers has been enormously growing since the demonstration of low loss propagation in silica fibers, and therefore their possible application for the telecommunication market. Nowadays, for the transmission of data, optical fibers offer numerous advantages compared to their wired counterparts, e.g. higher bandwidths and data rates, low noise and low loss in propagation. Thanks to this market-driven research, silica fibers are highly developed and fiber processing equipment, like fiber cleavers, splicers, or recoaters, are commercially available.

An optical fiber consists of a core, an inner and optionally an outer cladding. The guidance of light occurs in the fiber core and is enabled by the physical effect of total internal reflection (TIR). The refractive index of the fiber core, n_{core}, is higher than the one of the surrounding inner cladding material, n_{iclad}. Therefore, these fibers are called step-index fibers. The magnitude of this guiding effect is defined by the numerical aperture, NA, which is the Pythagorean subtraction of both refractive indices:

$$NA = \sqrt{n_{core}^2 - n_{iclad}^2}. \tag{2.14}$$

The NA defines the acceptance angle θ of the fiber core, see Figure 2.1:

$$\theta = \arcsin\left(\frac{NA}{n}\right). \tag{2.15}$$

Based on the theory of ray optics, θ is the maximum angle at which the light can still be coupled into the fiber core and will be guided, owing to TIR. The refractive index of the surrounding material of the fiber, n, is 1 in the case of air. In literature, θ is also used as half-angle of the divergence of a laser beam. It has to be considered that the maximum entrance angle for the fiber is defined at the 5% intensity level of the transverse intensity profile [47], whereas the divergence of a free-space laser beam is determined at 13% of it.

The fiber geometry for use as a laser host material was first described in 1961 by Elias Snitzer [48]. The fiber laser offers very promising lasing characteristics, as it has been explained in

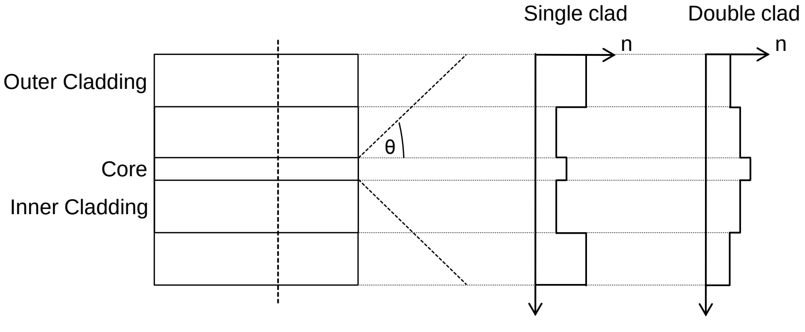

Figure 2.1: Structure of an optical fiber with the acceptance angle θ and the refractive index profile of a single- and double-clad fiber design (*not true to scale*).

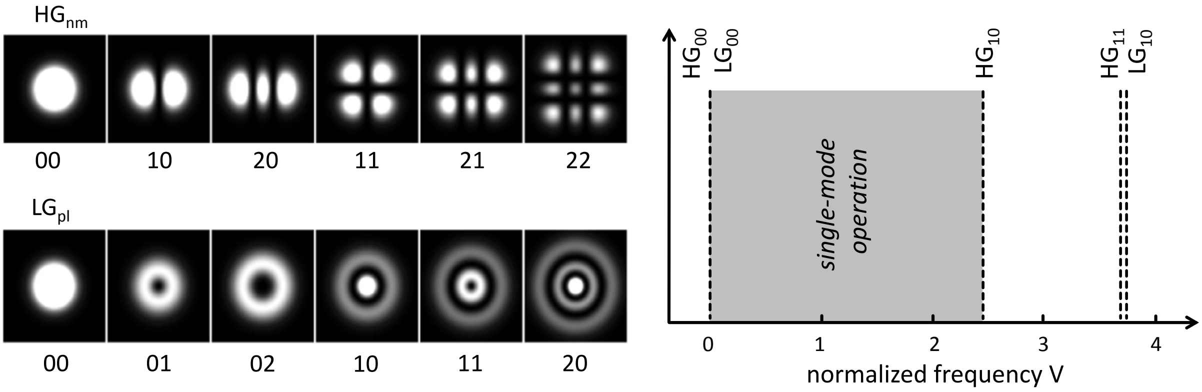

Figure 2.2: *Left*: Intensity profiles of different transverse propagation modes in optical fibers (adopted from [49]); *right*: Thresholds of the first four modes against the normalized frequency.

the introduction. A main drawback at the beginning of fiber laser research was the challenge to couple the pump radiation in the fiber core, which was overcome by the invention of the double-clad fiber design in 1988 [50]. For telecommunication systems, single-clad fibers guide the light only in the core of the fiber and the light in the inner cladding leaks into the outer polymer cladding. In double-clad fibers, the light can also propagate in the inner cladding of the fiber, which is enabled by a higher refractive index of the inner compared to the outer cladding, n_{oclad}, see Figure 2.1. Therefore, high power, low-brightness diode modules could be used for pumping active fibers, which has been a breakthrough in high power fiber laser development. The beam propagation inside the inner cladding is highly multi-mode and many modes do not have any intensity in the center of the inner cladding, where the fiber core is located. Thus, the geometry of the inner cladding is often non-round to break the symmetry, which results in a flat-top intensity profile [51], thereby assuring optimum pump absorption during propagation.

Another important parameter regarding the guidance in optical fibers is the relatively refractive index difference Δ of n_{core} and n_{iclad}:

$$\Delta = \frac{n_{core} - n_{iclad}}{n_{iclad}}. \tag{2.16}$$

Regarding the general wave equation 2.11, its solutions for $\Psi(x,y)$ are the so-called transverse propagation modes and can be divided in two classes. If there is a symmetry to the cartesian/cylindrical coordinate system, the solutions are called Hermite-Gaussian (HG)/Laguerre-Gaussian (LG) modes, respectively. The different intensity profiles of these modes are shown in Figure 2.2, left. To determine, which of these modes can propagate in a fiber core, the normalized frequency V,

$$V = \frac{2\pi a NA}{\lambda}, \tag{2.17}$$

is introduced, where a is the core radius of the fiber and λ the wavelength of the propagating electro-magnetic radiation. If the fiber is highly multi-mode, the total number of modes, M, can be approximated by

$$M \approx \frac{4V^2}{\pi^2} + 2. \tag{2.18}$$

For single-mode operation (HG_{00}/LG_{00}), V has to be below 2.405, see Figure 2.2, right. Its transverse modal profile is a Bessel function of first kind and 0^{th} order inside the fiber core, and the modified Bessel function of second kind and 0^{th} order in the inner cladding. This mode is included in both classes of solutions and is very close to a Gaussian intensity distribution,

$$I_{Gauss}(r) = \frac{2P_0}{\pi(\frac{MFD}{2})^2} e^{-\frac{2r^2}{(\frac{MFD}{2})^2}}, \tag{2.19}$$

where P_0 is the total power of the mode, MFD its mode field diameter and r the radial position in the cylindrical coordinate system. In telecommunication systems, single-mode fibers are most commonly required for long distances and high data rates. The MFD of the fundamental mode has been empirically determined [52]:

$$MFD = 2a(0.65 + 1.619V^{-1.5} + 2.879V^{-6}). \tag{2.20}$$

The MFD is a very important parameter for the pulse propagation in optical fibers, especially for broadband sources, as it is dependent on the wavelength of the radiation.

2.1.2.2 Photonic crystal fibers

In 1970, the flexibility of designing the properties of optical fibers was tremendously increased by the invention of so-called photonic crystal fibers (PCFs) [53]. Their cross-sections consists of the fiber material and hollow air channels in longitudinal direction. Nonlinear, dispersive and modal fiber characteristics could be tailored more flexibly compared to the standard fiber designs. For example, very small core diameters are feasible for enhancing the efficiency of nonlinear processes [24]. On the other hand, very large cores for high power pulsed laser or amplifier systems have been realized to scale the peak power of the output radiation, which is limited by nonlinearities [54]. It is possible to design very low net dispersion with a flat contribution for telecommunication systems, but also high values for dispersion compensation applications. The fiber dispersion can also be tailored to enable phase matching for tunable fiber sources based on OPG [55].

PCFs can be separated into photonic bandgap fibers (PBFs) and microstructured fibers (MFs). The basic difference between both is the guidance mechanism. PBFs are hollow-core fibers with air channels around the core. The effective refractive index of the inner cladding is higher than the one of the core, therefore, TIR is not possible. A two-dimensional photonic bandgap effect in the cladding based on interference phenomena enables the guiding. The radiation is trapped in the hollow core in the radial direction. Only a certain wavelength range fulfills the guidance condition, which results in rather narrow transmission bandwidths of such fibers. It can be broadened using a novel PBF design, whose fiber cross-section has a Kagomé lattice design [56]. In such fibers, the guidance does not rely on the photonic bandgap effect but on a so-called inhibited-coupling guidance, based on a strong phase mismatch of the cladding and the core modes, that prevents leakage of the core modes into the inner cladding. PBFs with gas-filled cores are very attractive for light-gas interaction [57], e.g. with xenon for nonlinear pulse compression [58], or generally for sensing applications [59].

MFs have a solid-state core with air-filled capillaries around it. The fiber properties are defined

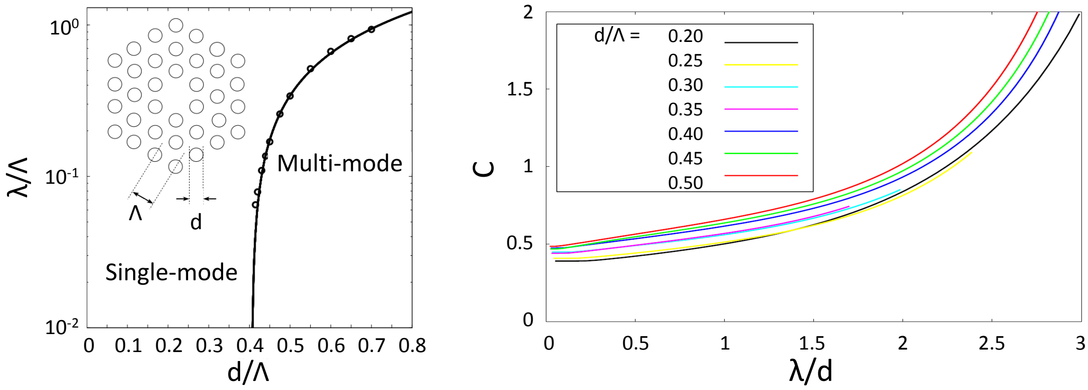

Figure 2.3: *Left*: Limit between single- and multi-mode propagation of a MF shown as wavelength λ over Λ versus the filling factor $\frac{d}{\Lambda}$, *inset*: Typical MF with a hexagonal shape, fiber core and air channels (adopted from [60]); *right*: Numerically determined constant C versus the inverse filling factor $\frac{\lambda}{d}$ [60, 61].

by the diameter of the air channels, d, and their distance to each other, Λ, whose fraction is called filling factor, $\frac{d}{\Lambda}$. Usually, there is one "missing" air channel in the cross-section, which is used as fiber core. The light is guided comparable to step-index fibers through TIR, where the effective refractive index of the inner cladding depends on the filling factor and λ, offering the mentioned flexibility in design. The inset of Figure 2.3, left, shows a picture of a very common MF design with a hexagonal shape.

To derive the modal propagation characteristics of MFs, Mortensen *et al*. found out that the effective area of the propagating mode, which is called mode field area (MFA), can be expressed approximately with the inverse of the filling factor, Λ^2 and a constant C [61]:

$$MFA = C\frac{\Lambda}{d}\Lambda^2. \tag{2.21}$$

The MFA can be calculated via:

$$MFA = \frac{\left(\int\limits_{-\infty}^{\infty}\int\limits_{-\infty}^{\infty}|\Psi(x,y)|^2 dxdy\right)^2}{\int\limits_{-\infty}^{\infty}\int\limits_{-\infty}^{\infty}|\Psi(x,y)|^4 dxdy} = \pi\cdot\frac{MFD^2}{4}. \tag{2.22}$$

The constant C has been determined numerically solving the Maxwell equations for different filling factors and is displayed on the right side of Figure 2.3. The NA of MFs is strongly wavelength-dependent, therefore, an effective refractive index of the inner cladding, $n_{iclad,eff}$, results. The NA can be approximated by:

$$NA = \sqrt{n_{core}^2 - n_{iclad,eff}^2} \approx \sqrt{1+\frac{\pi MFA}{\lambda^2}}. \tag{2.23}$$

This feature enables an almost constant normalized frequency V versus wavelength, allowing single-mode propagation over a broad spectral bandwidth. Such fibers are therefore called endlessly single-mode (ESM) fibers. Technically speaking, they are not "endlessly" single-

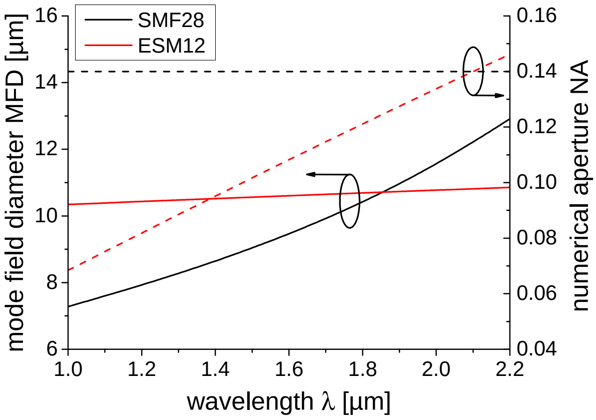

Figure 2.4: Mode field diameter and numerical aperture versus wavelength for a SMF28 fiber and an ESM-12B PCF.

mode, because once the propagating wavelength is in the range of the fiber parameters, the mode leaks into the cladding. The ESM regime is indicated in Figure 2.3, left.

Taking a commercially available "ESM-12B PCF" from Thorlabs [62], it is possible to have a roughly constant MFD with an increasing NA. This fiber has been developed to be as close as possible to a standard step-index SMF28 fiber for telecommunication. The ESM-12B has a pitch of 8 μm with a filling factor of 0.46 [63]. Figure 2.4 shows the comparison of the MFD and NA versus wavelength for the SMF28 and the ESM-12B fiber. The graph displays a much more constant MFD for the ESM-12B PCF, which is very beneficial for SCG and the reason why PCFs have been numerously used for that purpose [64, 65].

PCFs produced in silica are very promising for SCG in the visible wavelength range, because the ZDW of the fiber can be lowered to enable pumping with commercially available ultra-fast titanium-doped sapphire (Ti:Sa) lasers in the anomalous dispersion region of silica at 800 nm [66].

2.1.2.3 Beam quality in optical fibers

The beam quality of a free-space laser beam is defined via the beam propagation factor M^2 and can be formulated as

$$\theta \frac{MFD}{2} = M^2 \frac{\lambda}{\pi}, \tag{2.24}$$

where θ is the half-angle of the divergence of the laser beam. The MFD in this equation is defined by the MFD in the focal plane of the beam caustic. The beam quality of the transverse modes, which were introduced in subsection 2.1.2, can be very simply calculated dependent on their order n, m, l and p: [67]:

$$M_x^2 = 2n+1,\ M_y^2 = 2m+1, \tag{2.25}$$

$$M_{x/y}^2 = 2p+l+1. \tag{2.26}$$

The beam quality of the radiation emitted from an optical fiber can be expressed with the superposition of the different transverse propagation modes. For active fiber lasers, the design of the fiber core and the *NA* can be tailored to obtain the desired beam quality. But the M^2 value of a laser beam generated in an optical fiber is always slightly above 1, because the intensity profile of the propagating fundamental mode is, as mentioned, a Bessel function and the definition of the free-space laser beam quality factor is based on a Gaussian profile.

2.1.3 Dispersion

Dispersion refers to a wavelength-dependent phase velocity of propagating electro-magnetic waves inside a material. In optical fibers, this phenomenon can be separated into waveguide, chromatic, intermodal and polarization mode dispersion. Waveguide dispersion is in particular very important for optical fibers and will therefore be derived in detail. Dependent on the fiber design and wavelength, a non-negligible part of the guided modes propagates in the inner cladding of the fiber. This evanescent electro-magnetic field experiences a lower refractive index, which causes a difference in phase velocity compared to the field propagating in the fiber core. Chromatic dispersion is caused by the wavelength-dependency of the refractive index, which will also be further described. Intermodal dispersion stands for varying propagation characteristics for different transverse modal profiles. This type of dispersion will not be discussed in this thesis due to nearly exclusively used single-mode fibers. Polarization mode dispersion is based on different polarization states of the propagating modes and will also not be further derived owing to the investigation on centrosymmetric fibers in this thesis, which should theoretically not exhibit polarization-dependent propagation behavior.

The waveguide dispersion is deduced for the fundamental transverse mode HG_{00}. The normalized propagation constant b is introduced,

$$b = \frac{n_{eff}^2 - n_{iclad}^2}{n_{core}^2 - n_{iclad}^2} \approx 1 - \left[\frac{1+\sqrt{2}}{1+(4+V^4)^{\frac{1}{4}}} \right]^2 , \tag{2.27}$$

which determines how much of the radiation propagates in the core of the fiber, assuming a rapid decay of the electro-magnetic field in the cladding with respect to its thickness [68]. It is plotted in Figure 2.5 versus the normalized frequency V. With this factor, it is possible to

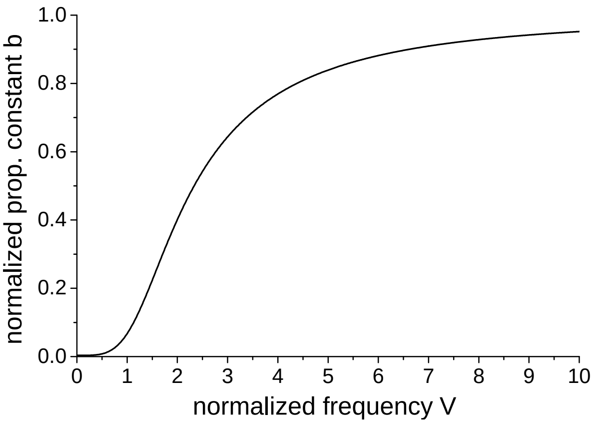

Figure 2.5: Normalized propagation constant versus normalized frequency.

define an effective refractive index, n_{eff}, of the propagating mode:

$$n_{eff}(\lambda) = n_{iclad} + b(n_{core} - n_{iclad}) = \sqrt{n_{core}^2 - NA^2} + b(n_{core} - \sqrt{n_{core}^2 - NA^2}). \tag{2.28}$$

The waveguide dispersion is often quantified via a dispersion parameter D_w, which is the time delay per nanometer wavelength and kilometer propagation distance inside a medium caused by this type of dispersion [68]:

$$D_w \approx -\frac{\lambda}{c} n_{core} \Delta \frac{d^2 b}{d\lambda^2}. \tag{2.29}$$

The chromatic dispersion, also called material dispersion, can be derived with the wavelength-dependent refractive index profile of the material, n_{mat}, which is defined by the Sellmeier coefficients A_j and B_j:

$$n_{mat}(\lambda) = \sqrt{1 + \sum_{j=1}^{m} \frac{B_j \cdot \lambda^2}{\lambda^2 - A_j}}. \tag{2.30}$$

Dependent on the definition, sometimes in literature the "1" in the square root is replaced by an A_0. Taking n_{mat} and the influence of the waveguide dispersion from equation 2.28, the effective refractive index of the propagation mode, including material and waveguide dispersion, yields

$$n_{eff}(\lambda) = \sqrt{n_{mat}^2 - NA^2} + b(n_{mat} - \sqrt{n_{mat}^2 - NA^2}). \tag{2.31}$$

For the mathematical description of the dispersion, the mode-propagation constant β is introduced and described by a Taylor series around the angular frequency ω_0 [69]:

$$\beta(\omega) = n_{eff}(\omega)\frac{\omega}{c} = \beta_0 + \beta_1(\omega - \omega_0) + \frac{1}{2}\beta_2(\omega - \omega_0)^2 + ... + \frac{1}{m!}\beta_m(\omega - \omega_0)^m. \tag{2.32}$$

β_m is the m^{th} derivative of the mode-propagation constant around the frequency ω_0,

$$\beta_m = \left(\frac{d^m \beta}{d\omega^m}\right)\Bigg|_{\omega=\omega_0}. \tag{2.33}$$

The first derivative of β is the reciprocal of the so-called group velocity v_g, which is technically speaking the velocity of the envelope of a propagating pulse inside the fiber:

$$\beta_1 = \frac{1}{v_g} = \frac{n_g}{c} = \frac{1}{c}\left(n_{eff} + \omega\frac{dn_{eff}}{d\omega}\right). \tag{2.34}$$

A group refractive index n_g is used, which relates to the group velocity with $v_g = \frac{c}{n_g}$. The second derivative of β, β_2, is called the group velocity dispersion (GVD) of the pulse,

$$\beta_2 = \frac{1}{c}\left(2\frac{dn_{eff}}{d\omega} + \omega\frac{d^2 n_{eff}}{d\omega^2}\right), \tag{2.35}$$

and stands for the wavelength-dependent phase velocity within the envelope of the pulse. β_2 is a very important parameter, especially in optical fiber communications, because it describes the chirp of the optical pulse and thus the temporal broadening or shortening during its propa-

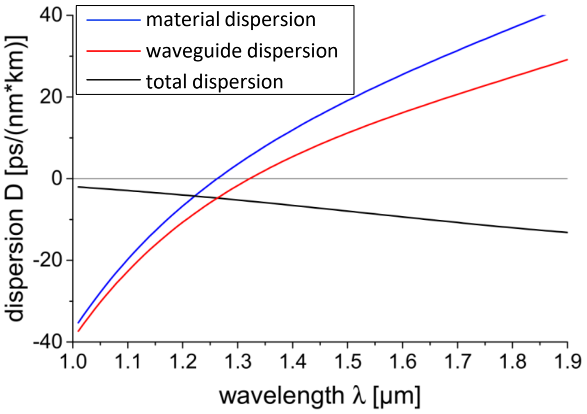

Figure 2.6: Dispersion parameter versus wavelength of a standard SMF fiber including material and waveguide dispersion.

gation. If the propagating light experiences a positive/negative GVD, it is defined as the normal/anomalous dispersion region, respectively. As for the waveguide dispersion, a dispersion parameter D_m can be used to illustrate the influence of the material dispersion:

$$D_m = \frac{\delta\beta_1}{\delta\lambda} = -\frac{2\pi c}{\lambda^2}\beta_2 \approx \frac{\lambda}{c}\frac{\delta^2 n_{mat}}{\delta\lambda^2}. \tag{2.36}$$

The GVD is mostly used in physics and optics, whereas D_m is preferred by the engineering community [70]. If in later chapters the dispersion D of optical fibers is mentioned, the sum of the material and waveguide dispersion, $D = D_m + D_w$, is meant. Dispersion causes a linear frequency chirp, redistributing the frequency components of the signal inside the pulse envelope, which does not generate new frequency components.

The total dispersion of a SMF28 fiber is shown as an example in Figure 2.6. In this case, the influence of the waveguide dispersion is negative and decreases the material dispersion, which also lowers the ZDW. For telecommunication fibers, the ZDW is around 1.5 μm, corresponding to the standard telecommunication band.

2.1.4 Nonlinear effects

As explained in chapter 2.1.1, for high electro-magnetic fields, the polarization of the material cannot be assumed as linear anymore and higher-order susceptibilities have to be taken into account. In this thesis, only amorphous centrosymmetric materials are investigated for nonlinear interactions, therefore, $\chi^{(2)}$ is zero [69]. $\chi^{(3)}$ is responsible for the occurring nonlinear effects, which is a 4^{th}-rank wavelength-dependent tensor with 3^4 elements including the possible combination of three Cartesian components of the polarization and three different material orientations. The most influential nonlinear effects contributing to SCG will be derived in the following.

2.1.4.1 Kerr effect

The Kerr effect describes a change of the refractive index caused by a high optical intensity, I. The refractive index of an optical material contains generally a wavelength-dependent linear part, $n(\lambda)$, and a nonlinear one, $n_2 I$:

$$n(\lambda, I) = n(\lambda) + n_2 I. \tag{2.37}$$

The nonlinear-index coefficient n_2 is directly linked to the real part of χ^3. Assuming a linearly polarized optical field and a cubic material, χ^3 contains only one component in its tensor, which can be used for calculating n_2:

$$n_2(\lambda) = \frac{3}{8n(\lambda)} Re(\chi^{(3)}). \tag{2.38}$$

In literature, a nonlinear coefficient γ is also frequently used for quantifying the nonlinearity of a material,

$$\gamma = \frac{n_2 \omega}{cMFA}. \tag{2.39}$$

If an optical pulse propagates in a fiber, the transverse modal distribution $\Psi(x, y, \omega)$ with local intensity maxima, and its temporal peak causes the Kerr effect. If the fundamental transverse mode HG_{00} is propagating, it causes a so-called Kerr lens due to a refractive index profile in the radial direction comparable to that of a graded-index lens. For high peak power fiber lasers, Kerr lensing can cause fiber damage owing to the connected self-focusing effect. A Kerr lens does not generate a significant chirp of the spectral phase and has therefore only a negligible influence on the spectrum of the pulse.

The Kerr effect, caused by the temporal peak of the pulse envelope, influences the group velocities within the pulse, which has a broadening effect on its spectrum and is thus often used for that purpose, e.g. before pulse compression. The connected refractive index change can be generally caused either by the pulse itself, which is then called self-phase modulation (SPM), or by another pulse, which has been named cross-phase modulation (XPM).

In **SPM**, the nonlinear phase shift can be so strong, especially for high peak power fiber laser systems, that operation under stable conditions is not possible anymore. The phase shift induced by SPM, which occurs if a pulse propagates in a fiber, is wavelength-dependent and can be expressed via n_2:

$$\phi_{SPM} = \frac{2\pi l_{eff}}{\lambda} n_2 I = \gamma \hat{P} l_{eff}. \tag{2.40}$$

$\hat{P}$ is the peak power of the pulse. The effective interaction length, l_{eff}, considers the losses α and the gain coefficient g of a fiber [71], which will be introduced in subsection 2.2.2:

$$l_{eff} = \frac{1 - e^{-\alpha l}}{\alpha}, \tag{2.41}$$

$$l_{eff} = \frac{e^{gl} - 1}{g}. \tag{2.42}$$

The effective fiber length approaches the fiber length l if there are no losses or gain (α=0, g=0):

$$\lim_{\alpha, g \to 0} l_{eff} = l. \tag{2.43}$$

The phase of the pulse is impacted by SPM, but not its temporal pulse shape. The chirp of

SPM is comparable to positive GVD, where shorter wavelength components of the spectrum are shifted towards the trailing edge of the pulse. SPM causes a nonlinear frequency chirp producing a symmetric spectral broadening [70].

XPM has a similar effect on the pulse spectrum compared to SPM. There is no energy transfer between the two electro-magnetic waves during interaction. For calculating the XPM-induced phase shift, the intensity of the signal, I_s, and the one from the co-propagating wave, I_c, have to be considered:

$$\phi_{XPM} = \frac{2\pi l_{eff}}{\lambda} n_2 [I_s + 2I_c]. \tag{2.44}$$

The phase shift shows that the influence of XPM is about a factor of two higher than that from SPM owing to the interference effects between the pulses, assuming the same polarization state. Especially in telecommunication systems, this effect can be very problematic because independent communication channels can cross-talk and influence each other.

2.1.4.2 Four wave mixing

FWM is a nonlinear parametric effect transforming two pump photons ("1" and "2") into two photons at different wavelengths ("3" and "4") by their annihilation. The medium has hereby a passive role, because no energy is transferred to the material. The newly generated photons are separated into a Stokes and an Anti-Stokes wave. The requirements for the FWM process are the match of the photon energies, expressed by ω, and their phase momenta, related to β:

$$\omega_1 + \omega_2 = \omega_3 + \omega_4, \tag{2.45}$$

$$\beta_1 + \beta_2 = \beta_3 + \beta_4. \tag{2.46}$$

FWM is more efficient if ω_1=ω_2, meaning an intense pump pulse produces two new photons, ω_3 and ω_4, leading to spectrally symmetric sidebands, which plays an important role during SCG. This special case is called degenerate FWM and the requirements regarding phase matching are less critical compared to non-degenerate FWM. It can be pictured as an instability of the CW pump radiation caused by background noise. In the time domain, this process leads to a temporal modulation of the CW radiation resulting in modulation instabilities (MI), as it will be explained in one of the next subsections. FWM can be used for parametric amplification systems [69]. Especially since the advent of the PCFs that enable the flexible design of the fiber dispersion and therefore the phase matching condition for FWM, the development of fibered OPAs has been boosted.

2.1.4.3 Scattering Processes

Scattering processes caused by $\chi^{(3)}$ are the inelastic effects of Raman- and Brillouin scattering, where an optical wave interacts with a phonon of the material. Simply stated, the material absorbs a photon and creates an excitation to a virtual level. During the relaxation, a new phase matched photon is generated with an energy that is increased or decreased by the energy of the phonon and whose spectrum is therefore blue- or red-shifted. The probability of the latter one is much higher owing to more relaxed phase matching requirements between photon and phonon, which results in an overall asymmetric gain profile. Both processes exhibit a threshold-like behavior and can be separated regarding the type of interacting phonon, optical phonons for Raman and acoustic ones for Brillouin scattering.

Raman scattering (RS) plays an important role for SCG. The spectra of optical phonons are relatively broad, in the order of 10 THz to 15 THz for silica, enabling a high wavelength shift. RS can be stimulated and used as parametric amplification, where two co-propagating waves transfer energy. The gain spectrum of RS is not dependent on the pump wavelength and offers thus a flexible possibility for power amplification. RS is one of the main limitations in terms of power scalability for high power fiber lasers, especially for pulsed systems. The threshold power for RS, $P_{RS,th}$, is based on the Raman gain coefficient, g_{RS}, of the material:

$$P_{RS,th} \approx 16 \frac{MFA}{g_{RS} l_{eff}}. \tag{2.47}$$

RS is related to the imaginary part of $\chi^{(3)}$. The Raman gain factor is inversely proportional to the pump wavelength, therefore, high power 2 μm fiber laser sources have inherently a higher threshold power for RS compared to 1 μm sources.

The **Brillouin scattering (BS)** is also related to the imaginary part of $\chi^{(3)}$ and has usually a much narrower gain bandwidth compared to RS. The maximum frequency shift for BS in silica is in the range of GHz. The photons are usually scattered, other than for RS, along the opposite direction of the propagating signal. The threshold for BS, $P_{BS,th}$, can be calculated, similar to RS, via a gain factor, g_{BS} [72]:

$$P_{BS,th} \approx 21K \frac{MFA}{g_{BS} l_{eff}} (1 + \frac{\Delta\nu_s}{\Delta\nu_{BS}}). \tag{2.48}$$

K is a polarization factor and has a value between 1 and 2, dependent if the polarization of the Stoke's wave is parallel or perpendicular to the one of the signal, respectively [73]. $\Delta\nu_{BS}$ is the full-width at half-maximum (FWHM) of the Brillouin gain bandwidth and $\Delta\nu_s$ the one of the signal. If the signal is broadband, which is usually the case for ML fiber lasers, the threshold for BS is very high. BS has a more important impact in the telecommunication sector, where narrow band signals with very long interaction lengths are used.

2.1.4.4 Modulation instabilities and solitons

MI describe a process, where a CW or quasi-CW signal is not stable against perturbations of background noise, which then breaks up into a pulse train of much shorter subpulses. This phenomenon has first been determined in other physical systems than optics and has often be named self-pulsing instabilities [69]. In optical fibers, MI was first observed in 1986 by Tai *et al.* [74], where it usually occurs in the anomalous dispersion region. In this regime, the GVD causes a frequency-upshift of the leading and a frequency-downshift of the trailing edge of the pulse. Exactly the opposite is induced by SPM. Therefore, these two effects can balance each other for certain pulse energies and temporal pulse shapes of these subpulses, which are called solitons or solitary waves. They can be separated into fundamental and higher-order solitons. For fundamental solitons, the temporal and spectral pulse shapes are not affected during propagation. The shorter the soliton, the broader its spectrum. For higher-order solitons, the SPM and the dispersion do not match perfectly, therefore, these pulses "breath" and change their spatial and spectral shapes periodically within the so-called soliton period. Solitons play an enormous role in telecommunication systems owing to the non-disturbed propagation [75]. The envelope of the fundamental soliton has a hyperbolic secant pulse shape [76]:

$$A(t,z) = A_0 sech(\frac{t}{t_{p,sol}}). \tag{2.49}$$

A_0 is hereby the peak of the electro-magnetic field and $t_{p,sol}$ its pulse duration at the FWHM. The product of the solitonic pulse energy, $E_{p,sol}$, and its pulse width is determined by the nonlinearity and the dispersion of the fiber [76]:

$$E_{p,sol} t_{p,sol} \approx 3.5 \frac{|\beta_2|}{|\gamma|}. \tag{2.50}$$

MI can generally be described as a degenerate FWM process with an induced phase matching condition via the Kerr nonlinearity, exhibiting two symmetric broad side lobes around the center frequency of the signal. During MI, the surplus energy of the radiation, which does not "fit" to the quantized soliton energies is transferred to so-called dispersive waves that can be pictured as background waves in the normal dispersion region of the nonlinear medium with low amplitude non-solitonic propagation [77]. The wavelength of the dispersive waves is hereby defined via phase matching conditions and is therefore intrinsically narrow-band. Each fundamental soliton generates a dispersive wave. The process of MI destroys any temporal coherence of the input radiation.

If there are disturbances during propagation, e.g. RS, higher-order dispersion, or two-photon absorption, the fundamental solitons automatically adjust themselves to a valid form and are therefore very robust against such perturbations [77]. For very short pulses with broad spectral bandwidth, these disturbances originate from dispersion and for longer pulses, from Raman effects. The residual energy during this adaption is transferred to the co-propagating dispersive wave. Higher-order solitons break up in pulse trains of fundamental solitons during such perturbations. This process is called soliton fission [78]. Regarding its pulse energy, a higher-order soliton stands for a certain number of fundamental solitons, N_{sol}, which is dependent on the dispersion and the nonlinear properties of the fiber:

$$N_{sol} = \sqrt{\frac{\gamma \hat{P} t_{p,sol}^2}{|\beta_2|}}. \tag{2.51}$$

For SCG, this effect has an enormous influence. First, the dispersive wave contributes to the wavelength broadening, and second, the solitons resulting from MI have higher peak power levels than the input signal itself before MI. It is therefore not necessary to use ML lasers for SCG, nanosecond pulses affected by MI, enabling the propagation of a large number of ultra-short solitons with high peak power levels, provide efficient SCG [79].

During soliton propagation, RS can occur within one spectrum of a soliton, which is then continuously red-shifted. This effect is called soliton self-frequency shift (SSFS) and was discovered in 1986 [80]. The shorter the soliton, the faster and stronger the SSFS. This process is although relatively slow, usually several meters of nonlinear fiber are required [81].

2.1.5 Losses

Losses and gain influence the amplitude of an electrical field, $A(z,t)e^{i(\beta z-\omega t)}$ from the equation 2.12, during the propagation through an optical fiber. Gain can only be apparent if the optical fiber is doped with laser active ions, which will be introduced in the next section. Losses can have very different reasons and can be separated into intrinsic and extrinsic losses. Intrinsic losses are caused by the material itself, meaning the wavelength-dependent absorption of light. Extrinsic losses are induced by external influences, e.g. material defects during fiber fabrication or inappropriate usage. During fiber production, microscopic variations of the density or inhomogeneities of the material cannot be avoided completely and cause scattering. Impurities, e.g. transition metals or hydrogen monoxide (OH), can cause additional absorption. OH impurities are especially very detrimental for silica fiber lasers emitting at wavelengths around 2 μm, where their absorption is relatively high. The OH related losses are usually measured at the preform before fiber drawing. For the calculations in this thesis, the material absorption from the literature or the manufacturer is used. The data of the other loss factors caused by the described scattering or inhomogeneities are not available and will therefore not be considered.
Another important extrensic loss factor are **bend losses**, which can be separated into macro- and microbending losses. Macrobending occurs if the fiber is bent too tightly and the guided modes leak into the cladding of the fiber. Microbending is caused by non-perfect fiber production, in the means of variations in either core diameter, roundness or other geometrical parameters. Microbending is very difficult to measure and to quantize, therefore, only macrobending is taken into account, which is an influencing parameter for mid-IR SCG because of its strong wavelength-dependency. But not only SCG, also high power fiber lasers, whose design is trending towards big *MFDs* and low *NA*, are very sensitive to macrobending losses. This loss factor can be studied analytically based on Maxwell equations [52, 82] and calculated by including the design parameters of the optical fiber [33]:

$$2\alpha_{bend} = \frac{\sqrt{\pi}}{2s}\frac{\frac{u}{V}}{(\frac{a^2}{2})K_{l-1}(w)K_{l+1}(w)}\frac{ae^{(\frac{-4w^3\Delta}{3aV^2})R}}{w\sqrt{(\frac{wR}{a})+(\frac{V^2}{2w\Delta})}}. \tag{2.52}$$

α_{bend} represents the losses caused by macrobending, including a degeneracy factor s, which can be approximated as 2 for the fundamental mode [33]. R is the bend radius of the fiber, w and u are parameters related to the waveguide dispersion, which can be calculated with the mode-propagation constant β:

$$w = a\sqrt{\beta^2 - n_{iclad}^2 k_0^2}, \tag{2.53}$$

$$u = a\sqrt{n_{core}^2 k_0^2 - \beta^2}. \tag{2.54}$$

The wavenumber k_0 is defined as

$$k_0 = \frac{2\pi}{\lambda}, \tag{2.55}$$

with K_l as the second kind modified Bessel function of l^{th} order:

$$K_l(x) = \frac{\pi}{2}\frac{I_{-l}(x) - I_l(x)}{\sin(\alpha\pi)}. \tag{2.56}$$

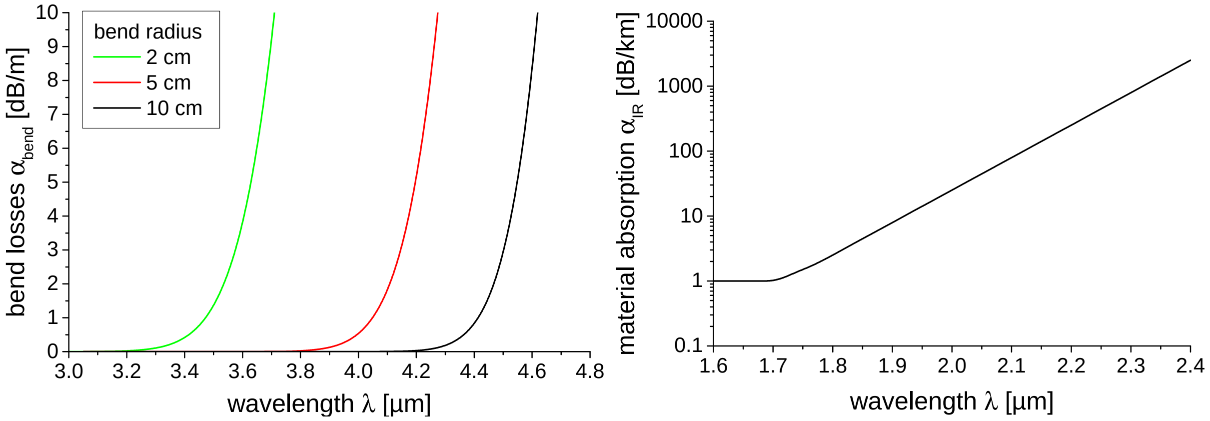

Figure 2.7: *Left*: Bend losses for a standard ZBLAN fiber with a core diameter of 9 μm and a *NA* of 0.2 for different bend radii versus wavelength [83]; *right*: Multi-phonon material absorption in the mid-IR wavelength region of silica (adopted from [22]).

$I_l(x)$ is the modified Bessel function of first kind. For the fundamental mode, K_{l-1} and K_{l+1} are K_1. The macrobending losses of a standard ZBLAN fiber with a core diameter of the 9 μm and a *NA* of 0.2 from the company "Fiberlabs" [83] are shown in Figure 2.7 for different bending radii. It indicates the strong wavelength-dependency of the bend losses.

Figure 2.7, right, shows the IR multi-phonon absorption of silica, α_{IR} [22]. For the wavelength of 2 μm, the losses are around 30 $\frac{dB}{km}$, which can be neglected in the case of fiber lasers because of fiber lengths in the range of meters.

2.2 Laser operation

2.2.1 Thulium-doped fiber lasers

After the first reported Tm^{3+}-doped laser with yttrium aluminium garnet (YAG) as host material in 1965 [84], laser systems emitting in the near-IR region around 2 μm gained tremendous attention owing to the growing scientific and industrial market needs. Laser radiation at wavelengths longer than 1.4 μm is considered to be eye-safe, because its radiation is absorbed in the vitreous body of the human eye and can therefore not reach the retina [85]. This characteristic has been one of the most important key requirements for many applications in free-space communication [86] or sensing systems [87], for which the atmospheric transmission window around 2 μm is utilized. Another important feature for radiation at that wavelength is the strong water absorption combined with weak absorption of human tissue making those sources ideal for biological and medical applications [88, 89, 90]. Minimal penetration depth into human tissue by water absorption in the range of sub-microns is possible resulting in less damage around the exposed area. Furthermore, the deposited heat caused by the absorption of the radiation makes the blood coagulate, which stops bleeding. Material processing is a growing market for 2 μm lasers, in particular for plastics, which are mostly transparent at wavelengths in the near IR around 1 μm but opaque in the mid-IR and the UV. There are reports on plastic welding at 1 μm, which requires however certain additives to the plastic, making them

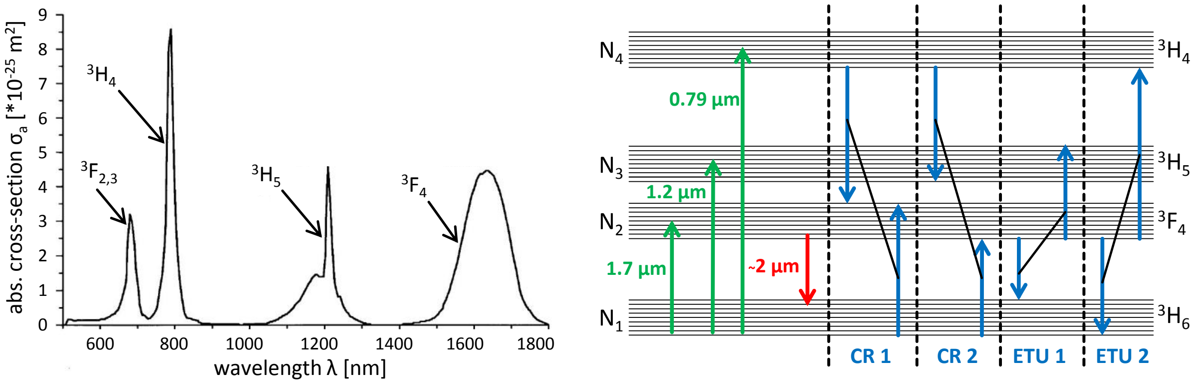

Figure 2.8: *Left*: Absorption cross-section of Tm^{3+}-doped silica [91]; *right*: Energy levels of Tm^{3+}-doped silica and possible energy transfer processes (*not true to scale*) [92].

absorbing. This process complicates the manufacturing process and is in certain cases forbidden, e.g. for plastics used in medicine [93]. Another considerable field of applications is as pump sources for wavelength conversion systems towards the mid-IR or the terahertz (THz) region. The longer pump wavelength, compared to 1 μm or 1.5 μm, increases the conversion efficiency [3, 94, 95].

As it is the trend at other wavelengths, the commonly used bulk laser systems are being replaced by fiber laser systems for many applications. The investigation on Tm^{3+}-doped silica fiber lasers started around 1988, when Hanna *et al.* reported the first Tm^{3+}-doped CW silica fiber laser [96]. Since then, the interest on Tm^{3+}-doped fiber lasers increased rapidly owing to the advantages of the fiber geometry compared to the bulky counterparts, e.g. high compactness, alignment-free systems, high power operation, high tunability and therefore ultra-short pulse generation, easy maintenance, etc. The advent of PCF further boosted this fiber laser research [97].

Figure 2.8, left, shows the absorption cross-section versus wavelength of a Tm^{3+}-doped silica fiber [91]. These lasers can be either pumped around 0.79 μm, 1.2 μm, or in-band at around 1.65 μm. The absorption bands are very broad, enabling pumping with ytterbium (Yb^{3+}), or neodymium (Nd^{3+})-doped laser systems around 1.05 μm and erbium (Er^{3+})-doped systems around 1.57 μm [36]. The most common lasing wavelength is around 2 μm, but also upconversion lasing in the blue emission range is possible, where fluoride fibers are usually used owing to their higher fluorescence lifetimes compared to silica hosts [98]. No matter at which wavelength the fiber is pumped at, the 2 μm laser emission ends in the upper Stark level of the ground state and has therefore to be considered as quasi-three-level laser system with a thermally populated ground state [99].

From all the possible pump wavelengths, 792 nm is the most attractive owing to commercially available and affordable AlGaAs pump diodes. Furthermore, the effect of photodarkening has not been reported at that pump wavelength, which is apparent at a pump wavelength of 1.06 μm [100]. However, pumping at 792 nm has in consequence a very high quantum defect. But regarding the generalized energy diagram of Tm^{3+}-doped silica on the right side of Figure 2.8, there are certain cross-relaxation (CR) processes possible, which transfer energy between two adjacent thulium ions. Especially for Tm^{3+}-doped silica fibers, these processes

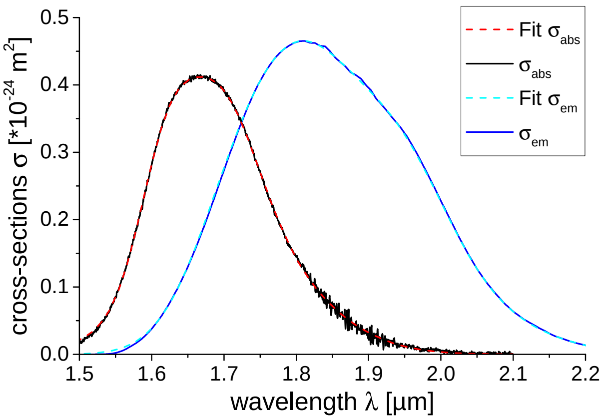

Figure 2.9: Emission and absorption cross-sections of Tm^{3+}-doped silica [91] and their fits, realized by the superposition of multiple Gaussian functions [101].

can be very efficient owing to the relatively high phonon energy of silica and the strong broadening of the manifolds leading to a spectral overlap of the transfer processes. The energy transfer CR1, $^3H_4$,$^3H_6$→$^3F_4$,$^3F_4$, is possible without interaction of a phonon, making it highly probable. With CR1, quantum efficiencies higher than 100% are theoretically possible. In literature, this CR process is called the "two-for-one" pumping scheme, meaning that one pump photon transfers two ions in the upper laser level. For the other cross-relaxation process, CR2 and both energy transfer upconversion processes (ETU), the interaction of at least one phonon is necessary, which decreases their probability. Therefore, they will not be further considered. Generally, the efficiency of energy transfer processes depend, among others, on the distance between the ions in the gain material and can therefore be increased by higher doping levels [102]. Although, if the doping exceeds a certain limit, quenching will occur because of ETU processes. To bypass that limitation, aluminum (Al^{3+}) can be added into the fiber core composition. Experimentally, the ratio of Al^{3+}:Tm^{3+} has to be higher than 9:1 for efficient lasing operation [92, 102]. The highest reported slope efficiency of a Tm^{3+}-doped fiber laser system pumped at 792 nm has been 74%, which yields a quantum efficiency of around 180% [92]. With Tm^{3+}-doped planar waveguides, a slope efficiency of even 80% has been reached [103].

If a Tm^{3+}-doped silica fiber laser is pumped at 792 nm, it can be assumed that every absorbed photon transfers at least one ion directly in the upper laser level $^3F_4$ owing to the low lifetimes of the $^3H_4$ and $^3H_5$ levels of around 20 μs [104] and 7 μs [91], respectively. For the lasing transition $^3F_4 \rightarrow {}^3H_6$, the radiative and non-radiative rates are in the same order of magnitude, because of the relatively high phonon energy [105]. The fluorescence lifetime of this manifold is in the range of 0.34 ms [91], which will be used for all further simulations regarding the performance of the fiber laser. The lifetime of the upper laser level mainly influences the lasing threshold, but not significantly the slope efficiency, because stimulated emission will deplete the conversion once the lasing threshold is reached. Although, in small signal amplifiers, the lifetime influences their noise level. Figure 2.9 shows the cross-sections of the emission and absorption at the wavelength around 2 μm, which are fitted by the superposition of multiple Gaussian functions [101]. These values will be used for further calculations.

The operational regime of a laser can be distinguished dependent on the temporal output of the laser radiation. The most important regimes are CW, QS, ML and QML [106], whose basic laser output parameters are theoretically derived in the further subsections based on a Tm^{3+}-doped silica fiber laser.

2.2.2 Continuous wave operation

According to the energy levels shown in Figure 2.8, the manifold $^3H_4$ has the population density N_4, $^3H_5$ the population density N_3, and $^3F_4/^3H_6$ are defined as the upper/lower laser level with the population densities N_2/N_1, respectively. All population densities N are average densities over the fiber length:

$$N = \frac{1}{l}\int_0^l N(z)dz. \tag{2.57}$$

Owing to the small lifetimes of $^3H_4$ and $^3H_5$, it is assumed that the total number of active ions is $N_{tot} \approx N_1 + N_2$. The feedback condition of an optical resonator is taken as starting point to derive lasing in CW operation, see Figure 2.10. If one round-trip of one photon is observed, the condition

$$GR_{HR}(1-L)GR_{OC} = G^2 R_{HR}(1-L)R_{OC} \overset{!}{=} 1 \tag{2.58}$$

must be valid at the lasing threshold and above. G is the gain factor of one pass though the laser material, R_{HR} is the reflectivity of the cavity end mirror and R_{OC} the one from the output coupler. The loss factor L includes diffraction of the fiber material or coupling losses of the intracavity radiation back into the fiber core and is defined as losses per round-trip in the laser resonator. The gain factor G of an active material based on a quasi-three-level laser system can be calculated with

$$G = e^{\Gamma(N_2\sigma_e(\lambda_s) - N_1\sigma_a(\lambda_s))l} = e^{\Gamma(N_2\sigma_e(\lambda_s) - (N_{tot}-N_2)\sigma_a(\lambda_s)l)} \overset{!}{=} \frac{1}{\sqrt{R_{HR}(1-L)R_{OC}}}, \tag{2.59}$$

where $N_2\sigma_e(\lambda_s)l$ and $N_1\sigma_a(\lambda_s)l$ are the signal gain and absorption at the signal wavelength λ_s under lasing conditions. $\sigma_e(\lambda_s)$ is the emission and $\sigma_a(\lambda_s)$ the absorption cross-section at

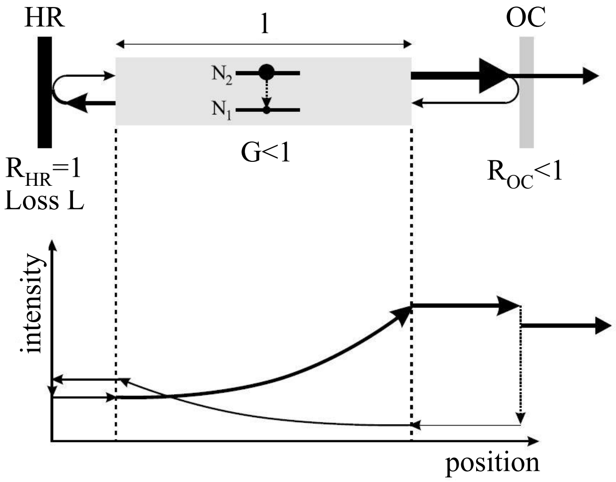

Figure 2.10: Basic scheme of a round-trip in an optical resonator with gain material and the relating intracavity intensity dependent on the position (adopted from [67]).

the signal wavelength. In solid-state lasers, the energy manifolds are split by the Stark effect, which is the result of the crystal field acting onto the active laser ions. σ_e and σ_a represent therefore the cross-sections of an inter manifold transition. The factor Γ from equation 2.59 represents the ratio of the power propagating in the fiber core to the total power included in the propagating mode. This factor has to be considered, since a part of the field of the modes propagates in the non-doped inner cladding of the fiber and does not experience any gain or absorption. It is defined via

$$\Gamma = \frac{\int_0^{2\pi}\int_0^{a} \Psi(r) r \, dr \, d\phi}{\int_0^{2\pi}\int_0^{\infty} \Psi(r) r \, dr \, d\phi} \approx 1 - e^{\frac{-2a^2}{(\frac{MFD}{2})^2}}. \tag{2.60}$$

This relation is valid for the fundamental mode, whose Bessel function is here approximated by a Gaussian intensity profile.
For further calculations, the rate equations of the population densities of the upper and lower laser levels are derived. It is assumed, that all absorbed pump photons produce excited ions in N_2, so there is no excited state absorption (ESA) and all ions are distributed homogeneously over the volume of the active medium. Only CR1 from subsection 2.2.1 is considered as energy transfer process. N_2 in a quasi-three-level laser system can be calculated considering the absorption of the pump radiation and the signal, and the stimulated and spontaneous emission from the upper laser level N_2 [67]:

$$\frac{N_2}{dt} = -\frac{N_1}{dt} = W_p N_1 + W_{12} N_1 - W_{21} N_2 - A_{21} N_2. \tag{2.61}$$

Generally, the index ”12” indicates the transfer rates from N_1 to N_2 and ”21” for the reverse rate. W_p is the pump rate, W_{12} and W_{21} are the rates for the absorption of the signal and stimulated emission, respectively, and A_{21} is the rate corresponding to spontaneous emission. A factor D is introduced, which expresses the ratio of the core area to that of the inner cladding assuming a flat-top pump profile:

$$D = \frac{\int_0^{2\pi}\int_0^{a} \Psi_{pump}(r) r \, dr \, d\phi}{\int_0^{2\pi}\int_0^{\infty} \Psi_{pump}(r) r \, dr \, d\phi} = \frac{A_{core}}{A_{iclad}}. \tag{2.62}$$

It takes into account the effective overlap of the doped core with the the pump radiation. With this factor, the different rates can be formulated as:

$$W_p N_1 = D \frac{I_p}{h\nu_p l} \eta_{abs} \eta_{CR}, \tag{2.63}$$

$$W_{12} = \Gamma \frac{I_i}{h\nu_s} \sigma_a(\lambda_s), \tag{2.64}$$

$$W_{21} = \Gamma \frac{I_i}{h\nu_s} \sigma_e(\lambda_s), \tag{2.65}$$

$$A_{21} = \frac{1}{\tau}. \tag{2.66}$$

$h\nu_p$ and $h\nu_s$ are the energies of a pump and lasing photon, respectively, h is the Planck's constant, ν_p and ν_s are the frequencies of the pump and the lasing photons, respectively. η_{abs} and η_{CR} are the absorption and CR efficiencies. I_i is the intensity of the electro-magnetic field inside the cavity and τ the fluorescence lifetime of the energy level N_2, meaning the average of the lifetimes from all the Stark levels in this manifold. In equation 2.63, the pump radiation is assumed to be flat-top across the fiber. I_p is the pump intensity,

$$I_p = \frac{P_p}{A_{iclad}}, \tag{2.67}$$

with P_p as the pump power. Also the rate equation of the intracavity photon flux,

$$\Phi_i = \frac{I_i}{h\nu_s c}, \tag{2.68}$$

has to be introduced:

$$\frac{d\Phi_i}{dt} = W_{21}N_2 - W_{12}N_1 - \frac{\Phi_i}{\tau_c} = \Gamma\Phi_i c\sigma_e(\lambda_s)N_2 - \Gamma\Phi_i c\sigma_a(\lambda_s)N_1 - \frac{\Phi_i}{\tau_c}. \tag{2.69}$$

The cavity lifetime, τ_c, states how long one photon stays in average inside the laser resonator before it is lost or coupled out:

$$\tau_c = -\frac{\tau_{RT}}{\ln\left[R_{HR}(1-L)R_{OC}\right]} = -\frac{2l_{cav}}{c}\frac{1}{\ln\left[R_{HR}(1-L)R_{OC}\right]}. \tag{2.70}$$

l_{cav} is hereby the optical length of the laser resonator and τ_{RT} the corresponding cavity round-trip time. For the calculation of the threshold pump intensity, η_{abs} has to be defined:

$$\eta_{abs} = 1 - e^{D(-N_1\sigma_a(\lambda_p)+N_4\sigma_e(\lambda_p))l} \approx 1 - e^{-DN_{tot}\sigma_a(\lambda_p)l}. \tag{2.71}$$

It has been assumed that there is no stimulated emission from the manifold $^3H_4$ at the pump wavelength because of the very short lifetime of this manifold. Furthermore, there are no bleaching effects of the lower laser level, which results in a constant N_1, which is approximately N_{tot}, $N_1 \approx N_{tot}$. This assumption is valid because in laser operation of a fiber laser, in most cases only a few percent of the total number of ions are in the upper laser level. D has to be considered owing to the non-absorbed guided pump light in the inner cladding. If the laser is operated below threshold, there is no photon flux in the cavity, $\Phi_i = 0$, and therefore no reabsorption and stimulated emission, which results in

$$\frac{N_2}{dt} = W_pN_1 - A_{21}N_2 \tag{2.72}$$

for the rate equation of the upper laser level. By using equations 2.66, the solution of this differential equation describes the trend of N_2 before reaching the lasing threshold:

$$N_2(t) = W_pN_1\tau(1-e^{-\frac{t}{\tau}}). \tag{2.73}$$

For a very long pumping time t, N_2 can be expressed as

$$\lim_{t\to\infty} N_2 = W_p N_1 \tau. \tag{2.74}$$

Using this relation for N_2 together with equation 2.63 and equation 2.59, the threshold pump intensity $I_{p,th}$ can be defined as

$$I_{p,th} = \frac{I_{p,sat}}{\eta_{abs}} \left(\sigma_a(\lambda_s) N_{tot} l - \frac{1}{2\Gamma} \ln\left[R_{HR}(1-L)R_{OC}\right] \right). \tag{2.75}$$

$I_{p,sat}$ is introduced as the pump intensity causing saturation at the lasing wavelength λ_s, which is connected to the saturation intensity of the lasing material, $I_{s,sat}$, with [67]:

$$I_{p,sat} = \frac{h\nu_p}{\eta_{CR}\tau\sigma_e(\lambda_s) + \sigma_a(\lambda_s)} = \frac{\nu_p}{\nu_s \eta_{CR}} I_{s,sat}. \tag{2.76}$$

After reaching the threshold, N_2 is clamped at the population density of the lasing threshold, $N_{2,th}$:

$$N_{2,th} = \frac{\sigma_a(\lambda_s) N_{tot} l - \frac{1}{2\Gamma} \ln\left[R_{HR}(1-L)R_{OC}\right]}{l(\sigma_e(\lambda_s) + \sigma_a(\lambda_s))}. \tag{2.77}$$

The output photon flux of the laser system, Φ_{out}, can be specified with the derived $I_{p,th}$, yielding

$$\Phi_{out} = \frac{1}{h\nu_p c} \frac{\ln R_{OC}}{\ln\left[R_{HR}(1-L)R_{OC}\right]} \eta_{abs}\eta_{CR}(I_p - I_{p,th}) = \eta_s \frac{I_p - I_{p,th}}{h\nu_p c}. \tag{2.78}$$

The slope efficiency of the fiber laser, η_s, can also defined via the different lifetimes, wavelengths and efficiencies introduced before:

$$\eta_s = \frac{\lambda_p}{\lambda_s} \frac{\tau_c}{\tau_{out}} \eta_{abs}\eta_{CR}. \tag{2.79}$$

τ_{out} is the photon out-coupling lifetime, defined as:

$$\tau_{out} = -\frac{\tau_{RT}}{\ln R_{OC}}. \tag{2.80}$$

The CW performance of a Tm^{3+}-doped fiber laser is simulated and the results for some of the output parameters are shown in Figure 2.11. The left side shows the pump power at the threshold, $P_{p,th}$, and the slope efficiency η_s versus wavelength for a Tm^{3+}-doped fiber using the absorption and emission cross-sections shown in Figure 2.9 and an estimated CR efficiency of 1.5. The right side of the figure also displays $P_{p,th}$ and η_s versus the loss factor L of the resonator. Furthermore, the following data has been used for the simulation: l = 3 m, τ = 0.34 ms, R_{HR} = 1, R_{OC} = 0.04, η_{CR} = 1.5, η_{abs} = 0.9, L = 0.2 (left figure), λ_s = 2 μm (right figure) and a doping level of 2.8%wt.. The horizontal line indicates the limit in terms of tunability. It is restricted by amplified spontaneous emission (ASE), which generally starts at a gain factor G, equation 2.59, of around 20 dB [67]. For the used parameters of the simulation, this gain factor corresponds to a pump power level of 7.5 W, introduced as the ASE threshold power P_{ASE}. According to the result of the simulation, the fiber laser can be tuned from 1.93 μm up

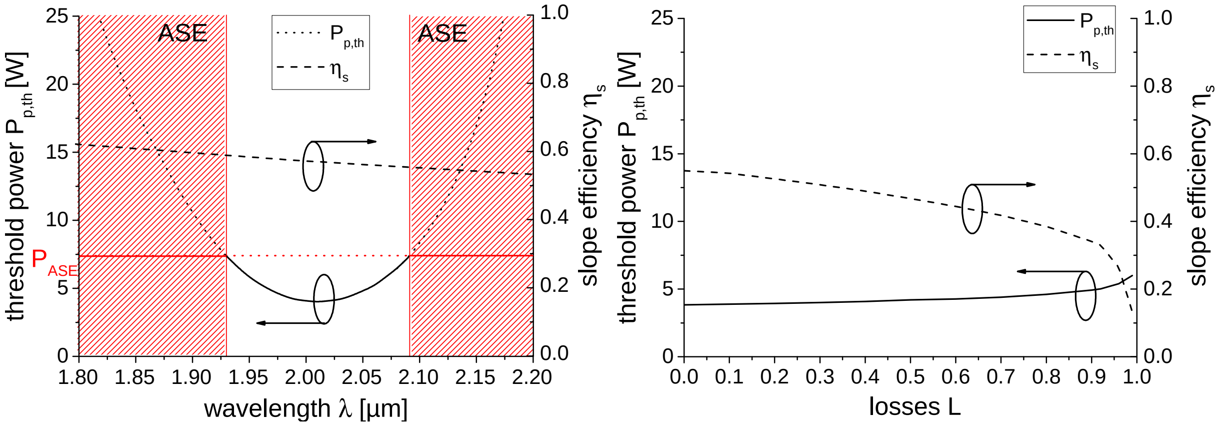

Figure 2.11: Simulation of the pump power at the lasing threshold and the slope efficiency versus wavelength (*left*) and cavity loss factor (*right*).

to 2.08 μm. The slope efficiency η_s decreases in the simulated wavelength range from 57% to approximately 48%, partly caused by the higher quantum defect for longer lasing wavelengths. The right side of the figure displays the threshold power and the slope efficiency versus the cavity losses L, which highlights the insensitive nature of fiber lasers against cavity losses. $P_{p,th}$ increases only slightly whereas η_s decreases from 50% to 30% at a loss factor of 90%.

2.2.3 Q-switching

QS is one of the most common methods to generate short laser pulses. The name originates from the Q-factor of an optical resonator, which depends on the cavity losses and is changed during this process. Figure 2.12 shows on the left side a basic block diagram of a laser cavity with an active QS modulator in both switching statuses. The right part of the figure displays important resonator parameters during QS operation. In the blue phase, the resonator loss fac-

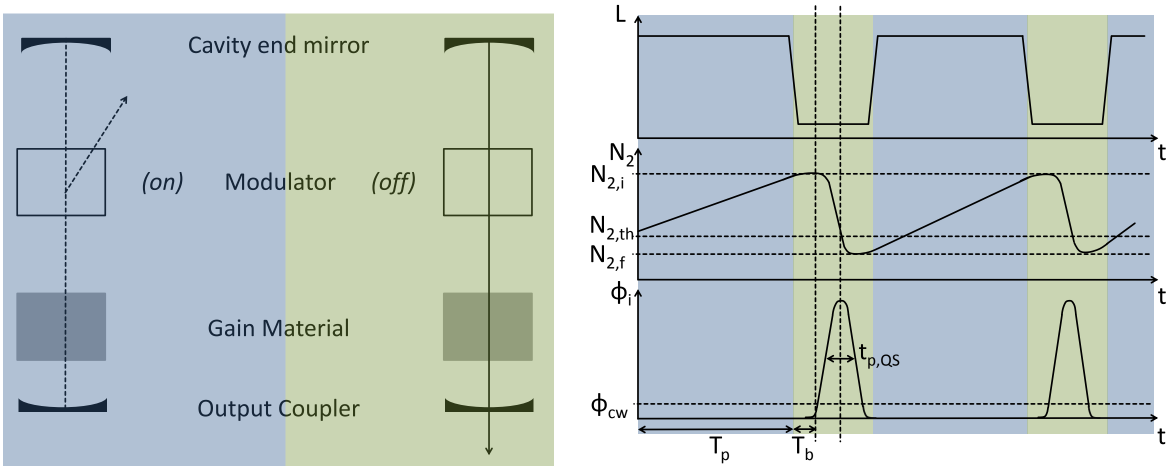

Figure 2.12: *Left*: Laser resonator with an active modulator in both swithcing statuses (*on* and *off*); *right*: Evolution of the loss factor L, the population density of the upper laser level N_2 and the intracavity photon flux Φ_i versus time (*not true to scale*).

tor L (top diagram in Figure 2.12, right), and therefore $P_{p,th}$, is very high for a certain pumping period T_p, because the active modulator partly couples out the intracavity beam and produces therefore losses. During this pumping period, N_2 is not depleted by stimulated emission, which results in a very high initial inversion, $N_{2,i}$, and therefore a high initial gain factor, G_i. The intracavity photon flux contains only the spontaneously emitted photons and is negligible during this phase. At a certain point, the cavity losses are decreased and the energy stored in the active material is extracted within a short period of time, which lowers N_2 and allows the QS pulse to grow (Figure 2.12, green background). The initiation of this process are vacuum fluctuations. On the right side of Figure 2.12, there are two vertical dashed lines indicating two different thresholds. The first one illustrates the situation, when the intracavity photon flux reaches the level for CW lasing, if the cavity would not be in QS operation, and N_2 reaches its peak $N_{2,i}$. The related time constant is called build-up time of the pulse, T_b. The second vertical line displays the situation when N_2 crosses the level at the lasing threshold, $N_{2,th}$. From that moment, Φ_i is decreasing. After the build-up of the pulse, there is a certain residual non-depleted population density, $N_{2,f}$, when the new pumping period starts again.

For the calculation of the most important QS parameters, $N_{2,i}$ has to be calculated including $N_{2,f}$ and the pumping rate from equation 2.73 yielding

$$N_{2,i}(T_p) = N_{2,f}e^{-\frac{T_p}{\tau}} + (W_p N_{1,f}\tau)(1 - e^{-\frac{T_p}{\tau}})\eta_{CR} \tag{2.81}$$

with $N_{1,f}$=N_{tot}–$N_{2,f}$. The first term includes the spontaneous decay from $N_{2,f}$ during the pump phase and the second term is the pump rate. Owing to the losses due to spontaneous emission, T_p should not exceed half of the upper state lifetime τ to reach 80% efficiency [67]. With $N_{2,i}$, the *QS* parameter r can be calculated with the logarithmic ratio of the gain factors G_i and G_{th}:

$$r = \frac{\ln G_i}{\ln G_{th}} = \frac{N_{2,i}\sigma_e(\lambda_s) - N_{1,i}\sigma_a(\lambda_s)}{N_{2,th}\sigma_e(\lambda_s) - N_{1,th}\sigma_a(\lambda_s)}. \tag{2.82}$$

Also here, the population densities in the lower lasing levels in both cases can be expressed as $N_{1,i}$=N_{tot}–$N_{2,i}$ and $N_{1,th}$=N_{tot}–$N_{2,th}$. According to equation 2.73, for high repetition rate systems, where $T_P \ll \tau$, r is dependent on the pump power P_p and the QS repetition rate $\Delta\nu_{QS}$:

$$r \propto W_p N_1 \tau(1 - e^{(\frac{-T_p}{\tau})}) \approx\ W_p N_1 T_p \approx W_p N_1 \frac{1}{\Delta\nu_{QS}}. \tag{2.83}$$

However, for low repetition rate systems, where T_P is in the range of τ, r is only dependent on the pump power P_p:

$$r \propto W_p N_1 \tau(1 - e^{(\frac{-T_p}{\tau})}) \approx\ W_p N_1 \tau. \tag{2.84}$$

With the definition of r, the most important *QS* output parameters can be calculated [67]:

$$\hat{P} = \frac{h\nu_s A_{core} l}{\tau_c}(r - 1 - \ln r)\left[\frac{N_{2,th}\sigma_e(\lambda_s) - N_{1,th}\sigma_a(\lambda_s)}{\sigma_e(\lambda_s) + \sigma_a(\lambda_s)}\right], \tag{2.85}$$

$$E_{QS} = h\nu_s A_{core} l (N_{2,i} - N_{2,f}), \tag{2.86}$$

$$t_{p,QS} = \frac{r}{r - 1 - \ln r}\eta_e \tau_c, \tag{2.87}$$

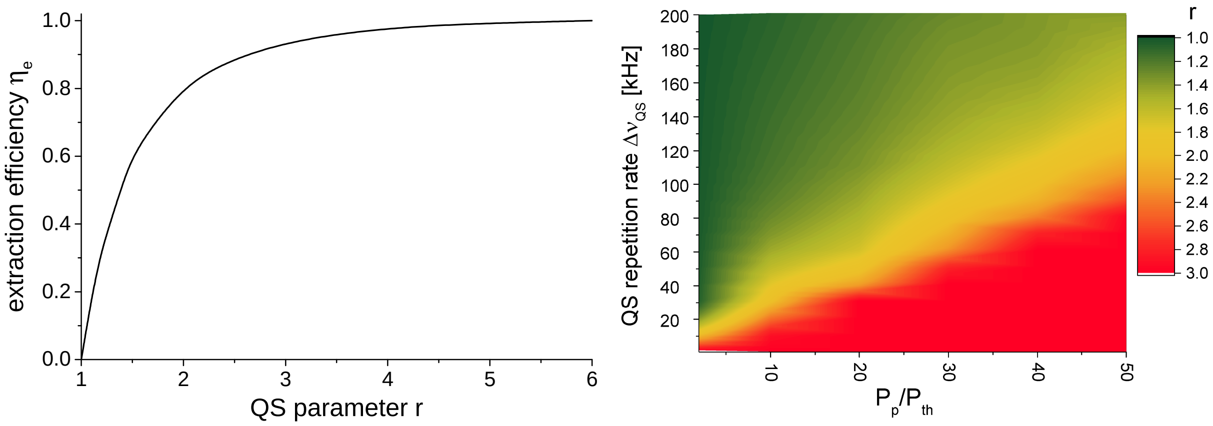

Figure 2.13: *Left*: Extraction efficiency versus the QS parameter [67]; *right*: QS parameter dependent on the QS repetition rate and the ratio of pump power to the pump power at the lasing threshold.

$$T_b = \frac{\tau_c}{r-1}\ln\frac{\Phi_{CW}}{\Phi_0} \approx (22.5 \pm 5)\frac{\tau_c}{r-1}. \tag{2.88}$$

$\hat{P}$ is the peak power of the QS output pulse, E_{QS} its pulse energy, $t_{p,QS}$ its pulse width at the FWHM, T_b the build-up time, Φ_0 the vacuum fluctuation photon density and Φ_{CW} the one if the laser would be operated in CW operation. Usually, the ratio of the two mentioned photon fluxes in equation 2.88 is in the order of 10^8 to 10^{12} [67]. The extraction efficiency, η_e, can be expressed with

$$\eta_e = 1 - \frac{N_{2,f}\sigma_e(\lambda_s) - N_{1,f}\sigma_a(\lambda_s)}{N_{2,i}\sigma_e(\lambda_s) - N_{1,i}\sigma_a(\lambda_s)}, \tag{2.89}$$

which is the basis for another definition of r:

$$r = -\frac{\ln\left[1-\eta_e(r)\right]}{\eta_e(r)}. \tag{2.90}$$

To simulate the QS output performance, equation 2.81, equation 2.82, equation 2.89 and equation 2.90 are solved numerically using the Newton's method. Figure 2.13, left, shows the extraction efficiency η_e versus the QS parameter r. For r = 2, η_e is around 80%. The right side displays r as a function of the QS repetition rate $\Delta\nu_{QS}$ and the ratio of $\frac{P_p}{P_{p,th}}$ for the cavity parameters used for the simulation of the CW lasing operation at a wavelength of 2 μm, see Figure 2.11, left. The limitation of r is hereby around 3, which corresponds to the mentioned ASE-related threshold leading to G = 20 dB.

The techniques to implement QS can be divided regarding the mechanism how the resonator losses are induced. There are passive and active devices. With passive modulators, realized by saturable absorber materials, the QS repetition rate is adjusted by the cavity parameters and not stable with pump power. Once a certain intracavity photon flux is built up, the absorber gets transmissive and the gain will be depleted. A benefit of such passive techniques is their compactness, e.g. in monolithic systems. Because of disadvantages as low damage thresholds and flexibility restrictions regarding the mentioned QS repetition rate, such modulators are not investigated in this thesis.

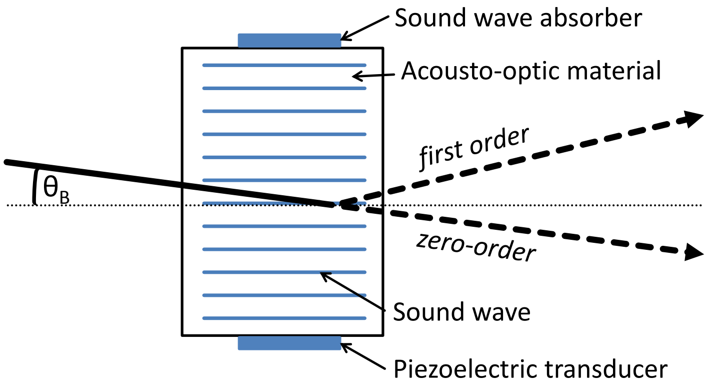

Figure 2.14: Structure of a switched-on AOM for QS operation including sound wave and incident laser beam.

Active devices are either AOMs, electro-optic modulators (EOMs), or mechanical shutters, which all modulate the intracavity intensity. An AOM is based on the acousto-optic effect caused by a sound wave interacting with the modulator material to diffract the intracavity photon flux partially out of the cavity. AOMs are robust against damages but have relatively long build-up times owing to the low propagation speed of the sound wave inside the crystal. EOMs change the polarization state of the intracavity beam by the electro-optic effect, that provides out-coupling of the radiation via polarization-selective elements, e.g. thin-film polarizers (TFPs). EOMs offer very fast circuit times and the possibility to realize very high repetition rates. The most out-dated QS technique are mechanical shutters, where the light path towards the cavity end mirror is completely blocked. Owing to the very low achievable repetition rates and switching times, they are only used rarely nowadays. In this thesis, only AOMs are investigated.

Figure 2.14 shows the setup of a typical AOM used in this thesis. It includes a piezoelectric transducer, which transforms an electrical signal into a sound wave. At the end of the acousto-optic material, a sound wave absorber is implemented. The material of such an AOM can be e.g. SiO_2 or tellerium dioxide (TeO_2). An orientation of the transmitted radiation under the Bragg angle θ_B is required for reaching highest diffraction efficiencies, which can be in the order of 90%. There is also another type of AOM based on the Raman-Nath configuration, which will not be further described here as it is not used within this thesis.

2.2.4 Mode-locking

The pulse generating technique of ML enables the shortest achievable pulse durations from laser systems. In an optical resonator with gain material, there are only a certain number of longitudinal modes that can oscillate, defined by the free spectral range of the resonator,

$$\Delta\nu_{FSR} = \frac{c}{2l_{cav}} = \frac{1}{\tau_{RT}}, \tag{2.91}$$

and the gain bandwidth $\Delta\nu$ of the laser material. The left side of Figure 2.15 displays a typical laser gain bandwidth with the possible longitudinal modes below it, which are above the gain threshold, G_{th}. The total number of oscillating modes can vary from just a few in a

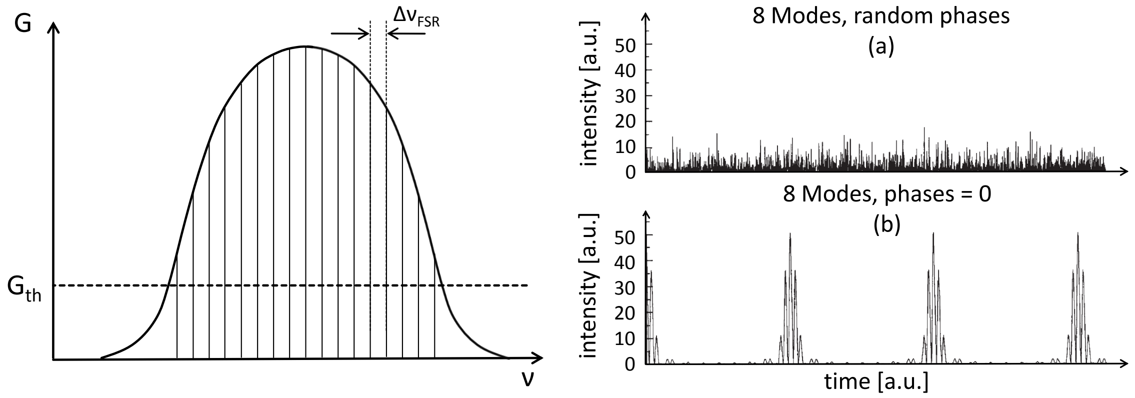

Figure 2.15: *Left*: Gain profile of a laser resonator with the longitudinal modes; *right*: Temporal output of a ML laser with eight oscillating modes with random (a) and fixed (b) phase relation (adopted from [107]).

gas laser, e.g. a helium-neon laser, up to thousands in a transition metal doped laser material, e.g. a Ti:Sa laser [107]. If these modes oscillate in an optical resonator with two partially or highly reflective mirrors, each mode builds up a standing wave inside the cavity with a certain phase. During ML, the phases of these longitudinal modes are forced to be coherent, which results in a circulating pulse inside the cavity with the group velocity of the center frequency of its spectral bandwidth $\Delta\nu$. The right side of Figure 2.15 shows the output intensity of a laser based on eight longitudinal modes with random (a) and fixed (b) phase relation to each other. Hereby, the more modes that are phase-locked, the shorter the output pulses get. If the modes have exactly the same phase, an unchirped pulse results. If they have different but fixed phase relations, the output pulses are chirped and therefore temporarily broader. The reason of such a chirp can be nonlinear effects or dispersion. The electrical field strength, E, inside an optical resonator can be expressed as the superposition of all oscillating longitudinal modes [108]:

$$E(t) = \sum_{n=0}^{N-1} E_n e^{i(\omega_n t + \phi_n)}. \tag{2.92}$$

N is the total number of modes, each with an amplitude of E_n, an angular frequency ω_n and an individual phase ϕ_n. If it is assumed that every mode has the same amplitude E_0 and there is a large number of modes with a non-related phase to each other, the intracavity intensity obtains as:

$$\begin{aligned} I(t) \propto |E(t)|^2 &= E_0^2 \left[\sum_{n=0}^{N-1} e^{i(\omega_n t + \phi_n)} e^{-i(\omega_n t + \phi_n)} + \sum_{n=0}^{N-1} \sum_{m \neq n}^{N-1} e^{i(\omega_n t + \phi_n)} e^{i(\omega_m t + \phi_m)} \right] \\ &\approx E_0^2 \left[\sum_{n=0}^{N-1} e^{i(\omega_n t + \phi_n)} e^{-i(\omega_n t + \phi_n)} \right] = N E_0^2. \end{aligned} \tag{2.93}$$

The last summand in the first line of the equation displays the oscillations on top of the constant value NE_0^2, which are balanced out for a high number of modes. If the phases are locked, the intracavity electrical field can be expressed as [108]:

$$E(t) = E_0 \sum_{n=0}^{N-1} e^{i(\omega_n t+\phi_0)} = E_0 e^{i\phi_0} \sum_{n=0}^{N-1} e^{i\omega_n t} = E_0 e^{i\phi_0} \sum_{n=0}^{N-1} e^{i(\omega_{N-1}-n2\pi\Delta\nu_{FSR})t}$$

$$= E_0 e^{i(\phi_0+\omega_{N-1}t)} \sum_{n=0}^{N-1} e^{-in2\pi\Delta\nu_{FSR}t} = E_0 e^{i(\phi_0+\omega_{N-1}t)} \left[\frac{1-e^{iN\Delta\omega t}}{e^{i\Delta\omega t}}\right]. \tag{2.94}$$

The ML modes are spectrally separated by the angular free spectral range of $2\pi\Delta\nu_{FSR}$. The dependency of the intracavity intensity can then be defined as:

$$I(t) \propto E_0^2 \left[\frac{1-e^{iN\Delta\omega t}}{e^{i\Delta\omega t}}\right]^2 = E_0^2 \frac{\sin^2(\frac{N\Delta\omega t}{2})}{\sin^2(\frac{\Delta\omega t}{2})}, \tag{2.95}$$

whose trend is shown in Figure 2.15, bottem right. The peak intensity, $\hat{I}$, inside the cavity is related to the electrical field via:

$$\hat{I} \propto N^2 E_0^2. \tag{2.96}$$

The peak intensity is thus N times higher compared to the operation with random phase relations between the modes.

The shortest achievable ML pulse duration depends on a factor K and inversely on the product of the total number of modes, N, and $\Delta\nu_{FSR}$, which is the gain bandwidth $\Delta\nu$:

$$t_{p,ML,min} = \frac{K}{\Delta\nu_{FSR}N} = \frac{K}{\Delta\nu}. \tag{2.97}$$

The factor K corresponds to the temporal shape of the ML pulses. For a Gaussian shape, K is around 0.44 [109]. The lowest K value of 0.31 is enabled by a squared hyperbolic secant pulse form [109].

This derivation for the calculation of the ML output performance is simplified, because of unconsidered effects like dispersion, nonlinearities or modulation characteristics. A more accurate description will be given later in this subsection in the explanatory part of the specifically used ML modulation technique implemented in this thesis.

If the modulator is operated at $\Delta\nu_{FSR}$, there is one pulse oscillating inside the laser cavity, which is called fundamental ML. It is also possible to operate the laser system at a multiple of its fundamental repetition rate, $M \times \Delta\nu_{FSR}$, which is called harmonic ML and can be pictured as multiple circulating pulses inside the cavity. Hereby, only every Mth longitudinal mode is phase-coupled. The pulse duration in this regime can be calculated as in fundamental ML.

There are several ways to generate the required phase-locking. The basic idea is to force the laser system to operate "automatically" in ML operation by inducing cavity losses for other lasing regimes. This process can be imagined as a shutter inside the laser cavity, which opens only for a certain time to let the intracavity ML pulse through. The possible modulation techniques can be, as it is in QS, distinguished between passive and active methods. Figure 2.16 displays a laser cavity with the circulating pulse and the basic modulation schemes of both techniques. Active ML has a sinusoidal modulation of the cavity losses, whereas for passive ML, the losses are triggered by the intracavity intensity and the duration of the opening gate

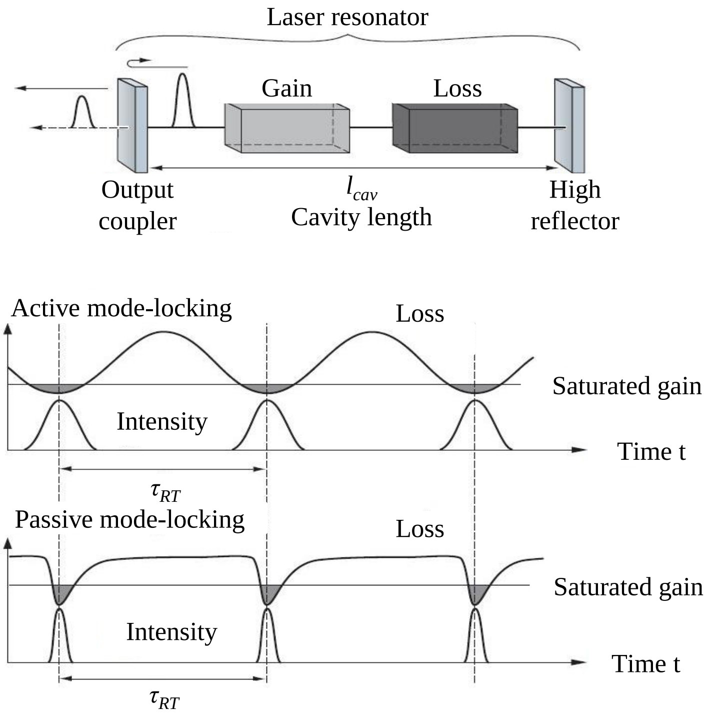

Figure 2.16: Typical laser resonator for ML and comparison of the loss modulation for active and passive techniques (adopted from [76]).

depends on the parameters of the modulator.

Passive ML provides generally the shortest achievable laser pulses [110], therefore, most of the research activities on ML laser systems have been focused on such methods. Passive modulators are based on nonlinear effects, which cause intensity-dependent losses of the cavity. One approach are saturable absorbers (SAs). If the laser is run in CW operation, there are arbitrary peaks in the temporal intensity profile of the laser, which become more amplified, compared to the CW background owing to the saturability of the modulator. Once the saturation intensity of the absorber is reached by the highest intracavity peak, it gets further amplified and passes the modulator each round-trip. ML regime is then initiated [106]. Semiconductor saturable absorber mirrors (SESAMs) are very attractive for this kind of application, because they are very compact and commercially available [111]. Such SESAMs consist of a Bragg mirror and a semiconductor material on top of it and are used as cavity end mirrors [112]. Since their advent, much progress has been done, in particular regarding compact fiber laser systems providing ultra-short pulse durations. The ML initialization process for SESAMs takes, dependent on the SESAM design, usually thousands of round-trips until the first ML pulse is built-up from CW-noise [113]. Also other materials have been successfully implemented as saturable absorbers, e.g. topological insulators [114], carbon nanotubes [115] or graphene [116].

Not only saturable absorption can be used for passive ML, also the Kerr effect. If a laser resonator is built outside of its stability region and it is necessary to have a Kerr lens for stability, the laser starts automatically in ML operation. This specific method using the transverse Kerr effect is called soft aperture Kerr lens ML (KLM). It can also be realized by inserting a hard aperture in the free-space part of the cavity. KLM enables the generation of the shortest achievable pulses among all ML techniques and was therefore a breakthrough after its first demonstration in 1991 [117]. Commercially available laser systems providing the shortest laser pulses are based on KLM. It has become a state-of-the-art as ML mechanism, but only for bulk laser systems. This technique cannot be applied in fiber laser systems as a result of their weak Kerr lensing.

The Kerr effect can also be applied in the longitudinal direction of the gain material. If the laser material is birefringent, the Kerr effect causes an intensity-dependent rotation of the polarization. Combined with a polarization-selective element, intensity-dependent losses can be induced. This nonlinear polarization rotation (NPR) can be implemented in silica fibers owing to their inherent birefringence from manufacturing failures.

Very important parameters of passive modulation techniques are the recovery time of the modulator, which describes how "fast" the shutter can switch, the saturation intensity, which triggers the initiation of the ML, the damage threshold and the insertion losses, which include unsaturable losses in the case of saturable absorbers. Regarding pulse width, the recovery time has the highest influence. KLM and NPR have hereby the advantage of an almost instant recovery time. There is an ongoing research in terms of saturable absorber materials, e.g. single-wall carbon nanotubes (SWCNTs) or graphene [118], for further decreasing the recovery time, saturation intensity, cost and complexity during the fabrication [119].

The modulators for active ML are triggered by an external signal. EOMs and AOMs are the most commonly used modulators for that purpose. Different to the working principle for QS, ML operation with an EOM is not based on intensity modulation but on phase modulation of the passing intracavity radiation. The electric field in this case is directed in the longitudinal direction of the electro-optic material inducing a phase shift. If the phase varies with $\Delta\nu_{FSR}$, the intracavity radiation is frequency-shifted by this value creating two sidebands located around the center frequency which are automatically phase-coherent. After a certain number of round-trips, all longitudinal modes are excited and ML regime is initiated.

AOMs with a sound wave absorber behind the acousto-optic material, as shown in Figure 2.13, have rather slow switching times because of the inertance of the propagating sound wave. For their usage in ML laser systems with fast repetition rates in the range of MHz, the sound wave absorber is replaced by a reflective element, which induces a standing wave pattern of the acoustic wave inside the acousto-optic material. The AOM has therefore an acoustic free spectral range, $\Delta\nu_{FSR,AOM}$. At every zero-crossing of the acoustic field amplitude, the intracavity pulse can pass the modulator with lower diffraction losses.

Therefore, during active ML, the external radio frequency (RF) drive signal for the AOM has to coincide simultaneously with the resonance described by $\Delta\nu_{FSR,AOM}$ and the free spectral range of the laser, $\Delta\nu_{FSR}$, which can be enabled by changing either the cooling temperature of the AOM, and therefore the length of the acousto-optic material, or the optical length of the cavity. The propagation mode gets thus frequency-shifted sidebands, which are exactly spaced by $\Delta\nu_{FSR}$ from its wavelength. After certain round-trips, more and more phase-locked longitudinal modes build-up [67]. This procedure is shown in the gain profile of a laser in Figure 2.17 for the first four round-trips.

To compare active and passive modulation techniques, it can be generally claimed that passively ML systems offer shorter pulses and higher compactness. However, the output power and pulse energy are limited up to a certain level in terms of stability or by the damage thresh-

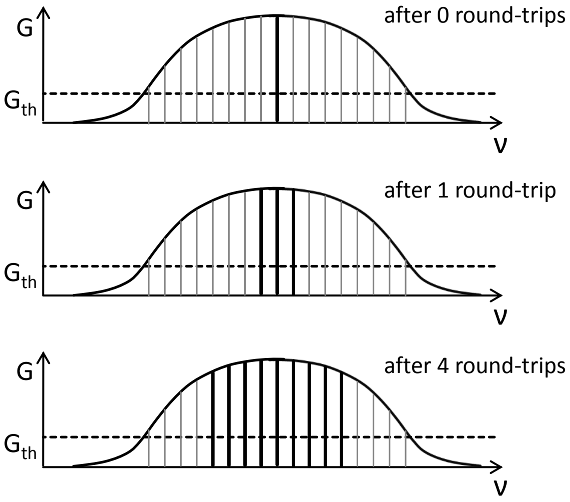

Figure 2.17: The evolution of the oscillation build-up of several longitudinal modes after a certain number of round-trips in active ML.

old of the available passive modulators [120]. Especially SESAMs for ML fiber lasers require a high modulation depth, which increases their thickness of saturable absorbers and decreases their thermal damage threshold. It is often necessary to further amplify the ML output pulses. Furthermore, passive ML is more sensitive to instabilities, e.g. fluctuations in pulse amplitude or timing jitter. In contrary, active modulation techniques provide high optical damage thresholds, enabling the realization of more compact systems without amplifier chains. Therefore, active modulation has been selected for the pump source.

There are certain differences comparing the modulation techniques of AOMs and EOMs as active devices. EOMs offer higher modulation depth, but require a high voltage to be operated with and polarized radiation. Owing to the available non-polarization maintaining active fiber laser in this thesis, only AOMs have been used.

For the calculation of the pulse duration from an actively ML laser systems, the gain dispersion D_g,

$$D_g = \frac{2gl}{(\pi \Delta \nu)^2}, \tag{2.98}$$

and the modulation strength M_s,

$$M_s = \frac{M(2\pi \Delta \nu_{ML})^2}{2}, \tag{2.99}$$

are introduced [121]. $\Delta \nu_{ML}$ is the ML repetition rate and M the modulation depth of the active modulator. For a fiber laser, the gain is usually saturated during ML, hence, the gain factor G within one round-trip must be 25 owing to the 4% Fresnel reflections at the output coupler. Thus, it is valid to define the saturated round-trip gain as $2gl$=ln(25) for fiber lasers. The duration of a Gaussian pulse generated by active ML can be calculated with

$$t_{p,ML} = 1.66 \sqrt[4]{\frac{D_g}{M_s}}. \tag{2.100}$$

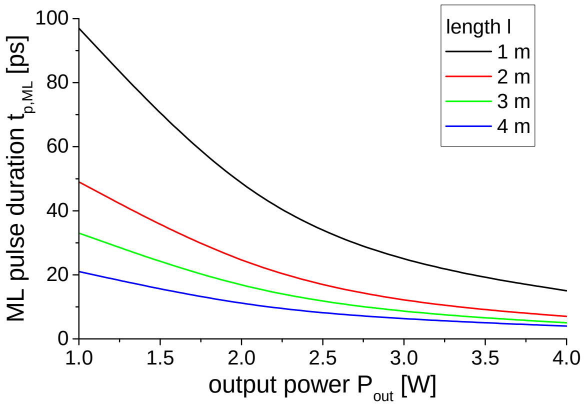

Figure 2.18: ML pulse duration versus output power as example for an actively ML fiber laser system with different fiber lengths.

This equation neglects the influence of SPM, which has to be considered for high peak power pulses [76]:

$$t_{p,ML} = 1.66 \sqrt[4]{\frac{D_g}{M_s + \frac{\phi_{SPM}^2}{4D_g}}}. \tag{2.101}$$

ϕ_{SPM} can be calculated using equation 2.40. Figure 2.18 shows a general evolution of the ML pulse width, $t_{p,ML}$, versus the output power of an actively ML fiber laser at 2 μm with a spectral bandwidth of 1 nm, a core diameter of 25 μm and a modulation depth of 10% for different fiber lengths. The nonlinear-index coefficient of $2.7\times10^{-20}\frac{W}{m^2}$ has been used for silica [122]. The trends of the curves show clearly that the higher the nonlinear phase shift, which is dependent on the length and the output power of the fiber laser, the shorter the output pulses get.

For fiber lasers emitting in the anomalous dispersion region of the host material, there is also the so-called soliton ML possible, where the output pulses are optical solitons. This regime can be induced independent of the modulation type. In soliton ML, the recovery time of the modulator can be a factor of ten longer than the ML pulse width, which makes this ML technique very attractive for ultra-short pulse generation [76]. The ZDW of silica is around 1.3 μm, therefore, Tm^{3+}-doped silica fiber lasers can be operated in soliton ML.

2.2.5 Q-switched mode-locking

A non-amplified ML fiber laser system generally suffers in terms of pulse energy owing to the high repetition rate. For enhancing the output energy, there are reports about the prolongation of the laser cavity to lower the fundamental repetition rate of the laser and thus to increase the pulse energy to some extend. But if very high peak power and energy levels are needed, the only options are further power amplification of the output pulses in fibers or bulk amplifiers, or the simultaneous induction of ML and QS. QML is a special kind of ML, where the temporal ML output pulse train is additionally modulated by a QS repetition rate in the range of kHz. A typical QML output pulse is shown in Figure 2.19. The presented pulse train indicates a modulation depth of the ML subpulses of around 100%. The peak power and pulse energy levels of the ML subpulses below the QS envelope are orders of magnitude higher compared to

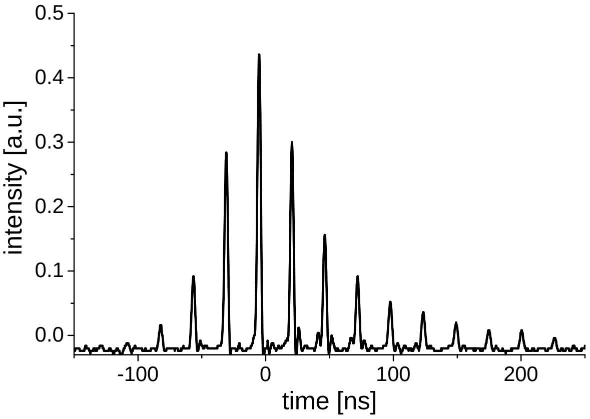

Figure 2.19: Example of a QML pulse train, measured with a photodiode and an oscilloscope.

purely ML systems, but have all different pulse energies and durations. There are several techniques to generate QML. Table 2.1 summarizes the most common approaches from literature and an evaluation for their use in fiber laser systems. The characteristics for this assessment are flexible selectable QS repetition rate, modulation depth of the ML pulses, output stability, high output power operation, compactness of the system and the simplicity of use.

If a laser system is purely ML by one SA as the passive modulator, so-called QS instabilities can occur for certain cavity and modulator parameters. The laser system is then automatically QML with a QS repetition rate that is approximately the same as the relaxation oscillation of the laser system [123]. Usually, these instabilities are rather undesired and there are many investigations for their suppression [124]. But if the laser is operated within certain conditions, QML can be achieved with only one modulator inside the cavity, which offers high compactness. The disadvantages of this technology are instabilities in terms of timing and pulse energy jitter [125, 126], fluctuation in the non-flexibly selectable QS repetition rate [126] and not completely modulated ML subpulses below the QS envelope. Another drawback, especially for fiber lasers, is the high frequency of the relaxation oscillations in the range of multiple

	Flexible QS repetition rate	ML modulation	Stability
Pas. ML	-	-	-
Pas. ML/Act. QS	+	-	0
Act. QS	+	0	0
Act. ML/Pas. QS	-	+	-
Act. ML/Act. QS	+	+	+

	High output power	Compactness	Simplicity
Pas. ML	-	+	+
Pas. ML/Act. QS	-	0	0
Act. QS	+	+	-
Act. ML/Pas. QS	-	0	0
Act. ML/Act. QS	+	-	-

Table 2.1: Different techniques to generate QML regime and their output properties in the case of fiber laser systems.

hundreds of kHz, which leads to relatively low peak power levels of the QML pulse train. The inherent low damage threshold of passive modulators limits the power scalability.

Some of the mentioned disadvantages of a single SA can be circumvented by the additional implementation of an active device for QS [126]. The QS repetition rate can be flexibly chosen and the active modulator does not limit the output power performance owing to its high damage threshold. The output stability is increased by the external trigger of the modulator, which results in reduced jitter. But passive ML needs, as already mentioned, a certain build-up time from noise, therefore, the QS repetition rate is limited dependent on the used passive modulator. Furthermore the complexity of the system is increased.

A simple and compact possibility for QML is the use of a single AOM for QS that is also ML the laser. The necessary ML modulation is induced by operating the AOM with a RF that is exactly the free spectral range of the laser, $\Delta\nu_{FSR}$, which generates a slight frequency shift of the intracavity radiation [127]. This option is not practically convenient for fiber lasers, because the cavity length has always to be adapted and continuously optimized. Additionally, AOMs for QS have usually a fixed RF to be operated with and are thus not tunable.

There are also reports about passive QS and active ML laser systems. This very rarely used technology provides high modulation of the ML pulses owing to the active ML [128, 129]. The QS repetition rate can although not be adjusted and the setup suffers from the low damage threshold and instabilities connected with passive modulators.

For the QML generation with the Tm^{3+}-doped fiber laser in this thesis, two AOMs are chosen, one for each pulse generation technique. High average power and high energy output pulses are feasible owing to the high damage thresholds of the modulators. With this technology, the pulse duration of the QML subpulses might be longer than with passive technologies, but as explained in the preceding subsection, temporarily longer pulses are sufficient for SCG. In actively QS and actively ML systems, the build-up time of the QS envelope is not significantly different compared to purely QS lasers. Stable QML is achieved, if the initial inversion N_{2i} is not much higher than the population density at the threshold N_{2th}, which is the case for high-repetitive QS lasers [130]. In that case, the pulse width for ML and QML operation should be roughly the same [126]. Compared to systems with amplification chains and purely ML systems, this QML laser is more compact because of its realization as single-oscillator and therefore the less need of optical elements or pump diode modules, for example.

2.3 Supercontinuum

2.3.1 Introduction

The generation of new wavelength components as a result of nonlinear effects is investigated since the 1960's. The specific term SC stands, as already mentioned, for the interplay of dispersion and nonlinear effects, which broadens the spectrum of an input radiation during the interaction with an optical material. Alfano *et al.* reported the first time of SCG in 1970, when they observed white light generation in a silica bulk [131]. The broadband SC radiation can be used for many applications, e.g. in metrology systems [132] or in microscopes, where the broad spectrum enables enhanced measurement resolution compared to formerly used lamps.

	Nonlinear effects	output spectra	temp. coh./stab.
norm. disp. / short pulse	SPM, XPM, RS	– / symm.	++
norm. disp. / long pulse	SPM, XPM, RS	– – / symm.	+
anom. disp. / short pulse	SSFS, FWM, XPM , RS	+ / asymm.	0
anom. disp. / long pulse	MI, SSFS, FWM, XPM, RS	++ / asymm.	-

Table 2.2: Evaluation of SCG with the different possible pumping regimes regarding the responsible nonlinear effects for the wavelength conversion, the broadness, temporal coherence and stability of the SC output radiation.

For military systems, it can be used for directed countermeasures, spectroscopy or remote detection of explosives and chemicals.

As nonlinear medium, liquids, dyes, gases or solids can be used for SCG, which can be pumped by numerous types of pump laser systems. In this thesis, only optical fibers are used as nonlinear medium. Therefore, the description in this section is only accounted for this specific geometric form of the nonlinear solid-state medium. The advent of optical fibers has boosted the SCG research activities owing to flexible interaction length and the tight confinement of the radiation inside the fiber core, which enabled superior SC output performance. The invention of the PCF in the 1990's further revolutionized the possibilities thanks to the flexibility in fiber design, which allowed fundamental research for the basic understanding behind certain nonlinearities [66].

In this thesis, it is not foreseen to simulate SCG. Therefore, a qualitative overview is given for the different physical effects behind SCG, which depend sensitively on the fiber and pump source parameters. For the fiber, nonlinearity and dispersion are of primary interest and for the pump source, its wavelength and the output pulse parameters. In general, it is difficult to isolate the influence of the different nonlinear effects during SCG.

For deriving the effects behind SCG, it must be considered if the nonlinear material is pumped in its normal or anomalous dispersion region. Furthermore it has to be distinguished if short pump pulses in the range of femtoseconds, or long pulses in the range of pico- and nanoseconds are used for pumping. Table 2.2 summarizes those cases and lists the nonlinear effects responsible for the wavelength broadening. Additionally, the SC output spectrum is assessed in terms of its broadness, temporal coherence and stability, which refers to low shot to shot fluctuations of the SC output radiation.

In the **normal dispersion** region, the frequency broadening is mainly caused by SPM, XPM and RS, independent of the input pulse duration. The efficiency of the SCG scales with the peak intensity of the pump radiation. The pump pulse duration in this dispersion regime increases during propagation, which lowers the intensity and therefore the conversion efficiency. The output spectrum is typically to some extent symmetric and its broadness is about a magnitude lower compared to SCG in the anomalous pumping region. Pumping with short pulses in the normal dispersion region results in spatially and temporarily high coherence and shot to shot stability, which is necessary for applications like frequency metrology [77].

If the nonlinear material is pumped close to its ZDW but still in the normal dispersion region, the spectral content shifting into the anomalous dispersion regime experiences different nonlinear effects, as it will be explained later in this subsection. Therefore, there is a wavelength-dependence of the SC conversion efficiency within the normal dispersion region. Owing to the mentioned relatively narrow SC output spectrum, it is in most cases tried to pump the nonlinear medium in its anomalous dispersion region to achieve a broader output spectrum.

In the **anomalous dispersion** region, many different nonlinear effects influence the spectral evolution, where soliton-related dynamics, already explained in subsection 2.1.4.4, have the most important influence. The output spectrum in this dispersion regime is usually asymmetric towards longer wavelengths. The SC output performance depends on the pump pulse duration. For short pulses, SCG can be divided into three phases. In the first one, the short input pulse is transformed into a higher-order soliton and experiences the first broadening and temporal change of its shape in the first few centimeters of the fiber. In the second phase, the soliton fission breaks up the higher-order soliton into fundamental solitons. At this point, the bandwidth of the higher-order soliton has reached its peak value. The reason for the fission depends on the pulse width. For relatively long pulses in the range of hundreds of femtoseconds, it is RS, whereas for ultra-short pulse durations in the range of tens of femtoseconds, it is caused by higher-order dispersion. The propagation of the fundamental solitons and the occurring wavelength broadening is the third phase [77]. The responsible broadening effects are mainly SSFS, FWM, XPM, and RS. The FWM gain is usually bigger than the Raman gain, which blurs the discrete Raman steps in the spectrum. If the material is pumped in the normal dispersion region, these steps can be observed.

As explained in subsection 2.1.4.4, the solitons generate dispersive waves in the normal dispersion region during their adaption against distortions. These waves interact with solitons via FWM [77]. But also solitons interact via FWM and XPM with each other. The soliton fission process is hereby not noise-driven which results in a deterministically same output spectrum and therefore a high shot to shot stability [32]. If short nonlinear fibers are chosen with ultra-short pulses, the temporal coherence of the output radiation is relatively high [16]. The shorter the pulse in the femtosecond regime, the higher the temporal coherence of the SC output. Different to SCG in the normal dispersion, an increase of the pump energy in the anomalous dispersion regime does not automatically increase the wavelength broadening, because it saturates at a certain input pulse energy level [70].

If the nonlinear material in this dispersion region is pumped with long pulses, an additional step has to be added to the three steps described in the segment before, which occurs at the beginning of the process. MI breaks up the long pump pulse into higher-order and fundamental solitons, which then are further influenced by soliton fission and soliton-induced broadening effects. MI degrades the temporal coherence and is seeded by noise, which results in low shot to shot stability. But the output spectrum is the broadest compared to the other pumping regimes. The possibility of pumping the nonlinear medium with long pulses revolutionized the SC research activities, because expensive ML laser systems are not necessary anymore for reaching the required peak power levels. Such SC sources can be used for fluctuation-insensitive applications like in imaging or spectroscopy.

The pump wavelength within the anomalous dispersion regime also affects the SC output performance. If the material is pumped far from the ZDW, the output spectrum is the broadest [77]. Hereby, the long-wavelength edge (LWE) of the output spectrum increases and the short-wavelength edge (SWE) stays nearly constant.

Also the pulse energy and its duration have an influence on the SC output performance in the anomalous dispersion regime. Assuming a constant peak power level, the higher the pulse energy and thus the duration of the pulse is, the broader and less coherent is the SC output radiation [70].

2.3.2 Figure of Merit

A figure of merit (FOM) is introduced to evaluate the available nonlinear fibers regarding their suitability for mid-IR SCG. The FOM allows to estimate the LWE of the SC output spectrum and the threshold behavior for SCG. Regarding the theoretical derivation of the nonlinear effects described in section 2.1, the FOM must be dependent on the effective length of the fiber, l_{eff}, which includes fiber absorption and bend losses, and on the mode field area, MFA, because all nonlinear effects depend on the peak intensity of the radiation and on the interaction length with the nonlinear material. The last considered parameter for the FOM is the nonlinearity of the material, expressed by the nonlinear-index coefficient n_2:

$$FOM(\lambda) = \frac{l_{eff}}{MFA} n_2. \tag{2.102}$$

The FOM is an approach to estimate the SC output performance and has been introduced similarly in [33]. As an example for the assessment of a nonlinear fiber for mid-IR SCG, the FOM has been calculated for a standard SMF28 silica fiber with different fiber lengths and is shown in Figure 2.20. The nonlinear-index coefficient, n_2, for silica glass of $2.7 \times 10^{-20}\ \frac{m^2}{W}$ has been chosen for this calculation [122]. Owing to the fact that the pump pulse parameters are not considered for the definition of the FOM, the LWE of the SC output radiation cannot be directly observed from the FOM. The achievable LWE for certain pump pulse parameters can be pictured by a horizontal line, crossing the curve of the FOM, as indicated in the graph. The point of the intersection is approximately at the LWE of the SC output radiation. The more suitable the pump pulses for SCG are, the lower is this horizontal line and the longer the LWE. The intersection of the FOM with the y-axis indicates the SC threshold. If it has a high value, the SC threshold is relatively low.

In the case of the SMF28 fiber, the results indicate that at a certain point, a further increase of the fiber length does not affect the LWE anymore and only decreases the SC threshold. It has

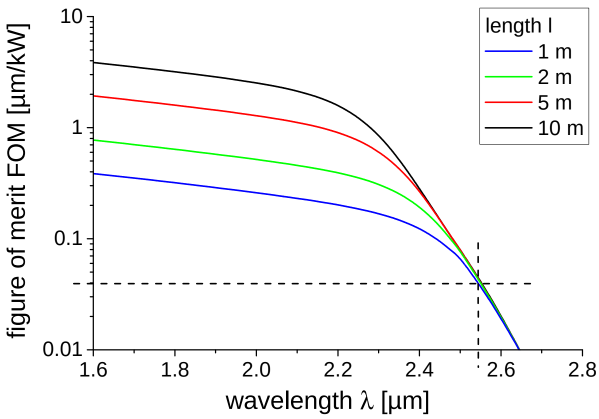

Figure 2.20: FOM of a standard silica fiber SMF28 for telecommunication applications.

been already proven that the wavelength conversion has somewhat of saturation behavior after a certain interaction length, and that a further increase of the fiber length is disadvantageous because of increasing material absorption [77]. SCG in SMF28 fibers, almost independently of the pump pulse characteristics, is limited up to around 2.7 μm, which has been verified by numerous experiments [27, 133, 134].

There are some influences that have been neglected during the definition of the FOM, one of which is the dispersion of the fiber, which has also an effect on SCG. First, during the soliton fission process, where it defines among the nonlinearity the pulse shape of the solitons, and second for the wavelength conversion efficiency, because a low GVD increases the interaction length for two co-propagating waves, which is important for FWM, for example. Another neglected impact is the first derivative of the mode field area versus wavelength, which influences the overlap of co-propagating waves at different wavelengths and therefore the efficiency of the broadening processes based on two waves, e.g. during XPM. The effective length is calculated based on the fiber length, which disregards the fact that many wavelength components of the SC output radiation are generated after some propagation distance.

However, the FOM can be used as a relative fiber evaluation tool with respect to a given pump source. Once the intersection of the horizontal line with the y-axis is found for this specific pump source, the SC performance can be predicted for other fibers. Especially if the same fiber material is used, the FOM can deliver additional information for the design of a new fiber with different *NA*, core diameter or fiber length.

3 Thulium-doped silica fiber laser

3.1 Introduction

This chapter is dedicated to the characterization of the Tm^{3+}-doped pump fiber laser for mid-IR SCG. For the last decades, Yb^{3+}-doped fiber lasers have been the workhorse for high average power, peak power and pulse energy operation among fiber lasers. The increasing attraction nowadays towards Tm^{3+}-doped fiber laser systems emitting at around 2 μm is caused to some extent by the larger modal areas. The thresholds for nonlinearities are therefore inherently larger, e.g. for RS and BS, which are two of the most common limiting factors for high peak power operation [135]. Many challenges regarding the handling and the engineering for high power fiber lasers have already been studied during the power scaling of the Yb^{3+}-doped fibers and the path is therefore paved for high power Tm^{3+}-doped fiber lasers.

This chapter is separated into the description of the experimental setup with the characterization tools, the description of the available Tm^{3+}-doped fibers for lasing experiments, the achieved results and a summary at the end of the chapter, which compares the output performance with similar experiments reported in literature.

The results are distinguished between the different operational regimes of the laser, meaning CW, QS, ML and QML operation. The investigations on the fiber laser have been focused on QML, because this is the only operational regime enabling efficient, high power mid-IR SCG in nonlinear fibers. The other regimes of the fiber laser have been characterized to obtain important material parameters of the Tm^{3+}-doped fibers.

3.2 Experimental setup

A schematic drawing of the fiber laser setup, including pump diode modules, Tm^{3+}-doped fiber, pump beam shaping lenses and cavity elements, is shown in Figure 3.1. All the available diode modules are pigtailed with delivery fibers, whose radiation is collimated by AR-coated achromatic lenses with a focal length (FL) of 25 mm. For the combination of the pump radiation with the laser signal, dichroic mirrors are used, which are transparent for the laser and reflective for the pump wavelength under an incident angle of 45°. Pump injection and laser beam collimation is provided by aspheric coupling lenses, AR-coated for the pump and lasing wavelength, with a FL of 15 mm. The aspect ratio of the collimation and coupling lenses is hence 1.6 for the image of the end facet of the delivery fiber onto the end facet of the silica fiber. The Tm^{3+}-doped fiber is sealed in a steel box, which is floated with water at a temperature of 19°C. The bend radius of the fiber inside that box is around 10 cm, which yields bend

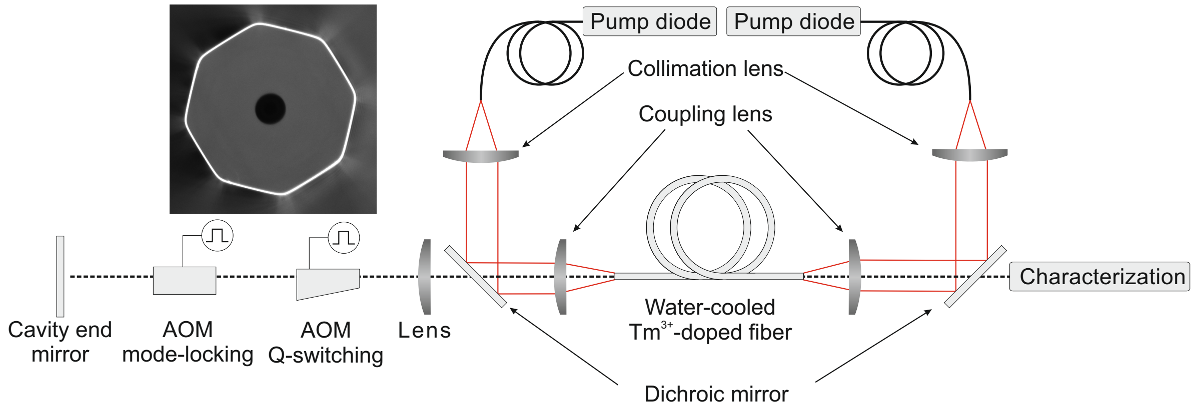

Figure 3.1: Setup of the Tm^{3+}-doped pump fiber laser system; *inset*: Example of a fiber cross-section used for the experiments, recorded with camera system of the fiber splicer.

losses of around 0.006 $\frac{dB}{m}$ at the wavelength of 2 μm (equation 2.52) and will be neglected in further calculations. The fiber is cleaved at one side under an angle of 0°, which is used as output coupler of the laser resonator and provides a feedback of 4% owing to the Fresnel reflections of silica. The fiber end, facing the free-space part of the cavity, is cleaved under an angle of around 8° to protect the active fiber from back-reflections and thus from parasitic lasing. Commercially available cleaving and splicing systems allow the analysis of the cleave angles and fiber end surfaces. An example of a 0° cleave is shown in the inset of Figure 3.1, presenting the octagonal shape of the inner cladding. An intracavity lens with a FL of 500 mm collimates the intracavity laser beam. For active ML and active QS, two AR-coated free-space AOMs are deployed inside the cavity. The data sheet from the manufacturer states a diffraction efficiency of the AOM for QS of more than 90%, operated at a fixed RF of 40 MHz with a build-up time of 500 ns. The AOM for ML provides a diffraction efficiency of at least 10%, dependent on the power of the RF. The frequency generator for ML has a working range from 20-200 MHz. The ML modulator was placed directly in front of the cavity end mirror to let the intracavity pulse pass towards the mirror and back to the fiber, which is a common method for actively ML lasers [108]. At every zero-crossing of the acoustic standing wave inside the acousto-optic material, the cavity loss factor is reduced, which occurs at exactly twice the RF. The ML modulator has to be actively temperature controlled, as it shows a weak but not negligible material absorption at 2 μm, which otherwise would cause an uncontrolled temperature drift. If the temperature of the modulator increases, the acousto-optic crystal will thermally expand, which would drive the acoustic mode out of the resonance with the RF excitation.

There are two cavity end mirrors available, a reflective diffraction grating with 300 groves per millimeter, offering around 70% reflectivity at 2 μm. This cavity end mirror can be implemented for wavelength-tuning, which is enabled by changing its orientation around the vertical axis. Furthermore, a highly reflective (HR) dielectric mirror with a reflectivity of approximately 100% over a broad wavelength range can be used. Both stated reflectivity values of the mirrors will be used for further calculations.

For the characterization of the fiber laser output radiation, a water-cooled power meter is available for measuring its output power. The pulse width is detected, depending on the pulse duration, by either two different photodiodes (PDs) or by an intensity autocorrelator system.

PD#1 is a photo electro-magnetic detector with an electrical bandwidth of 1 GHz. PD#2 is an extended, biased indium gallium arsenide (InGaAs) detector with an electrical bandwidth of 12.5 GHz. For processing the measured signals from the detectors, an oscilloscope with an electrical bandwidth of 3 GHz is available. The transverse intensity beam profile is recorded with a thermographic camera. For measuring the output spectrum, a monochromator with a PD at the output slit is on hand (spectro#1). It is equipped with three diffraction gratings having 300/300/150 grooves per millimeter that are blazed at 1 μm/2 μm/4 μm with a stated dispersion of 9.4 $\frac{nm}{mm}$/9.4 $\frac{nm}{mm}$/18.8 $\frac{nm}{mm}$, respectively. A theoretical resolution of around 0.2 nm/0.2 nm/0.4 nm results with an entrance and exit slit size of 20 μm. These values have been verified by the measurement of the spectrum of a narrowband Nd:YAG laser at different diffraction orders of the gratings. The measured resolution has been 0.5 nm/0.5 nm/1 nm, respectively, which is therefore a factor of 2.5 lower than the stated one. A possible reason for the lower resolution can be a non-optimized collimation of the beam inside the monochromator, resulting from a too low *NA* of the incoupled radiation from the delivery fiber. If the spot size on the grating is decreased, the resulting dispersion value gets higher.

There is also a second spectrometer on hand (spectro#2) with a stated dispersion of 1.3 $\frac{nm}{mm}$, if higher resolution is necessary. With the smallest adjustable slit size, a measured resolution of around 0.15 nm resulted. The detectable wavelength range with this spectrometer is although limited by the sensitivity of the camera at the output of the system. This spectrometer can only be used for the characterization of the pump fiber laser and not for the mid-IR radiation.

There are two different sets of AlGaAs pump diode modules available. Set#1 has a measured wavelength of 804 nm at a cooling temperature of 25°C with a total output power of 300 W per module. Their pump radiation is delivered via cladding-mode-free multi-mode fibers with a core diameter of 400 μm and a *NA* of 0.22, which results in a beam quality factor M^2 of the pump radiation of around 140. For the use of these modules, the cooling water temperature has been chosen to be around 11°C to shift the wavelength towards the absorption peak of Tm^{3+}-doped silica at 790 nm (see Figure 2.8, left). The temperature-induced wavelength change of such diodes is usually around 0.3 $\frac{nm}{K}$ [136], which yielded a measured wavelength of approximately 800 nm at this cooling temperature. The diodes were not cooled to lower temperatures to avoid water condensation. Diode set#2 emits at a wavelength of 792 nm with an average output power of 50 W per module and is cooled by Peltier elements. Their delivery fibers have a diameter of 200 μm with a *NA* of 0.22, which relates to a M^2 value of approximately 70 for the pump radiation out of this delivery fiber. The collimation and coupling lenses, shown in Figure 3.1, have been chosen that the two diode sets can be flexibly changed without modifying the beam shaping for maximum coupling efficiency into the Tm^{3+}-doped fibers. Because of the utilized collimation and coupling lenses, the pump radiation between both lenses is not perfectly collimated, therefore, it was necessary to deploy the additional lens inside the cavity to collimate the intracavity laser beam.

3.3 Materials

The parameters of the available Tm^{3+}-doped fiber, given by its manufacturer, are summarized in Table 3.1. The doping level of the fiber is around 2.8%wt., which should enable a high CR

Parameters	Value
Doping level [%wt.]	2.8
Core diameter [μm]	25
NA core	0.08
Inner cladding diameter [μm]	300
NA inner cladding	0.46
Outer cladding diameter [μm]	460
Absorption at 790 nm [$\frac{dB}{m}$]	4.1
Polarization-maintaining	No

Table 3.1: Parameters of the Tm^{3+}-doped silica fiber used in this thesis from the manufacturer.

efficiency, if the Al^{3+} concentration is optimized [92]. However, there is no data published or available from the manufacturer about the incorporation of Al^{3+} into the fiber core to prevent clustering. The core diameter is 25 μm with a NA of 0.08. The corresponding normalized frequency of this fiber, related to equation 2.17, is 3.14 at the lasing wavelength of 2 μm. Thus, the fundamental and the HG_{10} mode can propagate, which results in a theoretical M^2 value between 1 and 2. The shape of the inner cladding diameter is octagonal with a span of 300 μm, as shown in the inset of Figure 3.1. With this geometric profile, there is less symmetry of the inner cladding, allowing a flat-top intensity profile of the guided pump radiation. The NA of the inner cladding is 0.46, which yields an acceptable pump beam quality M^2 of around 200. Therefore, the coupling of the pump radiation with the mentioned beam quality factors from the diode modules should be very efficient. In the experiments regarding the fiber laser performance in this thesis, it is always assumed that all pump light is injected inside the fiber, besides the 4% Fresnel reflections at the fiber end facets. Therefore, the pump power has been corrected for the Fresnel reflections and the experiments are plotted against launched pump power. The polymer layer, used as outer cladding, is round and has a diameter of 460 μm. The peak absorption at 790 nm is specified as 4.1 $\frac{dB}{m}$ from the manufacturer. According to equation 2.71 and the absorption cross-section in Figure 2.9, the calculated absorption is 4.4 $\frac{dB}{m}$, which shows good agreement regarding the used absorption cross-section of 9×10^{-25} m^2 at 790 nm. The manufacturer also publishes so-called background losses at the wavelength of around 0.86 μm to quantize the loss factor of scattering and additional absorption owing to impurities. This factor is negligible in the range of the fiber lengths used for laser applications and is therefore not included in the table. The active fiber is not polarization-maintaining.

For implementing the Tm^{3+}-doped fiber into the laser cavity, a fiber length must be carefully chosen to absorb sufficient pump light for reaching good lasing efficiencies. Furthermore, the non-absorbed pump radiation is coupled back into the other diode module, which can lead to its destruction. This damage threshold for diode set#2, according to its manufacturer, is around 10% of the maximum output power of the diodes [136]. Therefore, a total pump light absorption of around 10 dB is needed to ensure safe operation for the diode modules over the whole output power range. For diode set#1, the fiber length has to be relatively long because of the weak absorption cross-section at the pump wavelength of around 800 nm. A fiber length of 8.8 m has been selected and is named thulium#1, which should provide a theoretical absorption of 14 dB. The experimental verification, which has been performed by pumping the fiber only from one side and measuring the transmitted power, resulted in a value of 95% (13 dB). For diode set#2, shorter fiber lengths can be used owing to the pump wavelength at the peak of the absorption band. Thulium#2 and thulium#3 had a length of 3.5 m and 2.2 m resulting in a theoretical absorption of 15 dB and 10 dB, respectively. The measured pump light absorption has been around 95% (13 dB) and 89% (9 dB), respectively.

3.4 Results

As it has been mentioned in the introduction of this chapter, this section is separated into the different operational regimes of the fiber laser.

3.4.1 Continuous wave operation

High average power experiments in CW operation have been performed with all the mentioned Tm^{3+}-doped fibers. The simulation for this regime has been conducted based on equation 2.78 from subsection 2.2.2,

$$P_{out} = \frac{\lambda_p}{\lambda_s} \frac{\ln R_{OC}}{\ln[R_{HR}(1-L)R_{OC}]} \eta_{abs} \eta_{CR} (P_p - P_{p,th}), \tag{3.1}$$

where $P_{p,th}$ is the pump power at the lasing threshold, based on equation 2.75 and equation 2.76:

$$P_{p,th} = \frac{hc\Big(\sigma_a(\lambda_s) N_{tot} l - \frac{1}{2\Gamma} \ln[R_{HR}(1-L)R_{OC}]\Big)}{\lambda_p \eta_{abs} \eta_{CR} \tau(\sigma_e(\lambda_s) + \sigma_a(\lambda_s))} A_{iclad}. \tag{3.2}$$

With the available fiber, the efficiency of the CR, which enables the favorable "two-for-one" pumping regime, has not been determined so far. Therefore, the simulation has been performed with different values of η_{CR} and compared with the results achieved with thulium#1 (8.8 m). For the simulation, it has been assumed that the HR mirror, which has been used as cavity end mirror for this experiment, has a reflectivity of 100%. The cavity losses have been 10%, which includes two times the Fresnel reflections of the signal occurring at the angle-cleaved side of the fiber and non-perfect coupling of the intracavity radiation back into the fiber core from the cavity end mirror. Figure 3.2, left, displays the measured and simulated output power versus launched pump power, P_l, for thulium#1 with a CR efficiency of 1.0, 1.1 and 1.2.

A total output power of 70 W has been reached at a launched pump power level of 180 W resulting in a measured slope efficiency of 41%. The threshold power has been around 7.4 W. The lasing wavelength for the experiment was approximately 2.03 μm. The simulated performance exhibited the best fit with the results for a CR efficiency of 1.1. The simulated slope efficiency is almost the same compared to the measurement. The lasing threshold from the simulation is although slightly higher.

The right side of the figure shows the output performance of thulium#2 (3.5 m) and thulium#3 (2.2 m), both pumped with diode set#2 and the diffraction grating implemented as cavity end mirror. The determined CR efficiency of 1.1 has also been used in the simulation for these fiber lengths. Thulium#2 and thulium#3 provided an output power level close to 30 W, a slope efficiency of approximately 38% and a lasing threshold at around 5 W. The CR efficiency of 1.1

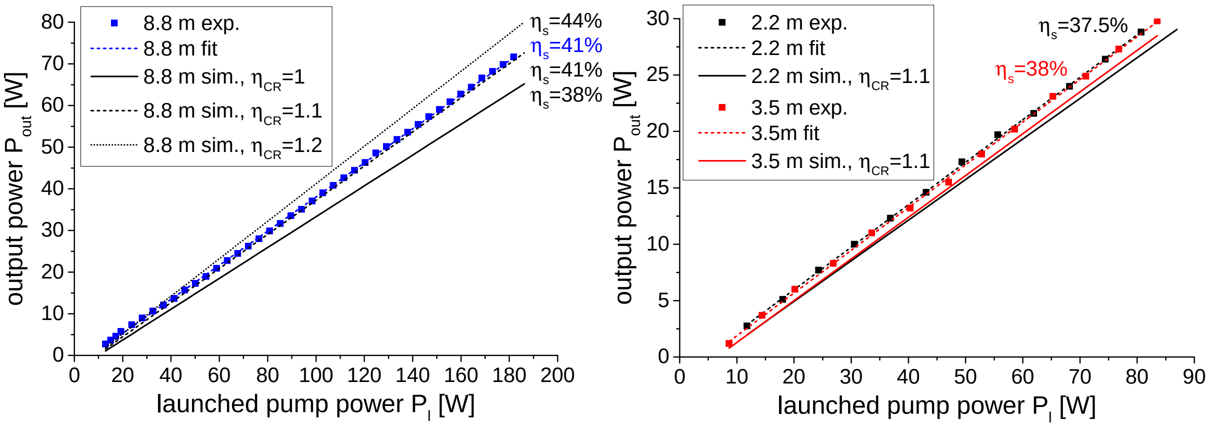

Figure 3.2: *Left*: Output power versus launched pump power for thulium#1 (8.8 m) with diode set#1 and its simulated performance based on three different values of the CR efficiency; *right*: Output power versus launched pump power for thulium#2 (3.5 m) and thulium#3 (2.2 m) with diode set#2 and their simulations conduced with a CR efficiency of 1.1.

also here fits well regarding the slope efficiencies. However, as it is for the longer thulium#1, the threshold of the simulation is higher than the acquired one from the experiment.

The obtained slope efficiency of thulium#1 (8.8 m) is higher than that of thulium#2 and thulium#3 owing to the higher reflectivity of the HR mirror compared to that of the diffraction grating. If the HR mirror is used instead of the grating as cavity end mirror, the slope efficiency increases about 10% and the lasing threshold decreases about approximately 5%. The performance in terms of average output power for all the used fiber lengths is limited by thermal effects. Thulium#1 provides more output power, which is most likely enabled by the lower heat load per fiber length during the experiments. The absorption cross-section of the fiber at the pump wavelength of diode set#1 is only about 40% compared to the one for diode set#2. Thulium#1 has thus a lower heat load per unit length. The achieved output power level from thulium#1 is a factor of around 2.5 higher compared to thulium#2 and thulium#3, which is approximately the same factor between the absorption coefficients, and therefore the heat load.

For all of the shown experimental results in this chapter regarding the pump source, the color code, shown in Figure 3.2 for the different Tm^{3+}-doped fiber lengths, is kept, i.e. blue for thulium#1, red for thulium#2 and black for thulium#3.

The chosen CR efficiency of 1.1 could be in reality higher owing to different loss factors that have been neglected in the simulation, e.g. multi-phonon non-radiative decays from the upper laser level. The phonon energy of silica is around 1100 cm^{-1} [137], which is already greater than a fifth of the photon energy between the two lasing levels, leading to a high probability of such decays. Also upconversion processes, which are caused by clustering, or excited state absorption are not considered in the simulation.

Other material parameters that are influencing the output performance significantly are the emission and absorption cross-sections at the lasing wavelength. The values for the simulation are taken from the literature, see Figure 2.9, and can be considerably different for the used fibers. The real data from the manufacturer is confidential and therefore not available.

The measurement of the beam propagation factor M^2 has been performed with thulium#1

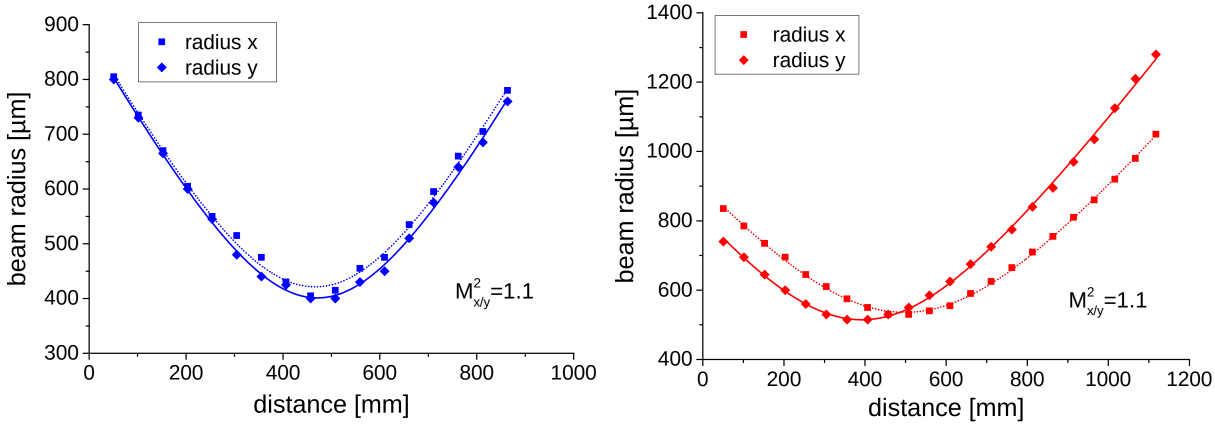

Figure 3.3: M^2 measurement in both directions with thulium#1 (8.8 m) at an output power level of 30 W (*left*) and with thulium#2 (3.5 m) at 15 W (*right*).

(8.8 m) and thulium#2 (3.5 m) in CW operation at an output power level of 30 W and 15 W, respectively. The graphs are shown in Figure 3.3. The M^2 values have been around 1.1 in both directions, which indicates an excellent beam quality very close to the diffraction limit. As this fiber laser is used as pump system for mid-IR SCG and the output radiation has to be coupled into a nonlinear fiber, its beam quality plays an important role, especially if the nonlinear fiber is single-mode at the pump wavelength.

The broad emission cross-section of Tm^{3+}-doped silica fibers enables broad wavelength-tuning of the fiber laser with the diffraction grating as cavity end mirror. The tuning curves of all fiber lengths are shown in Figure 3.4, left, with their simulated performance. In the simulation it has been considered that if the lasing threshold is higher than the ASE-related threshold, there is no lasing operation possible, as already indicated in Figure 2.11. The calculated ASE thresholds regarding launched pump power have been around 15 W/10.7 W/10.5 W for thulium#1 (8.8 m)/thulium#2 (3.5 m)/thulium#3 (2.2 m), respectively, using the determined CR efficiency of 1.1. The ASE thresholds have been verified by placing the power meter in

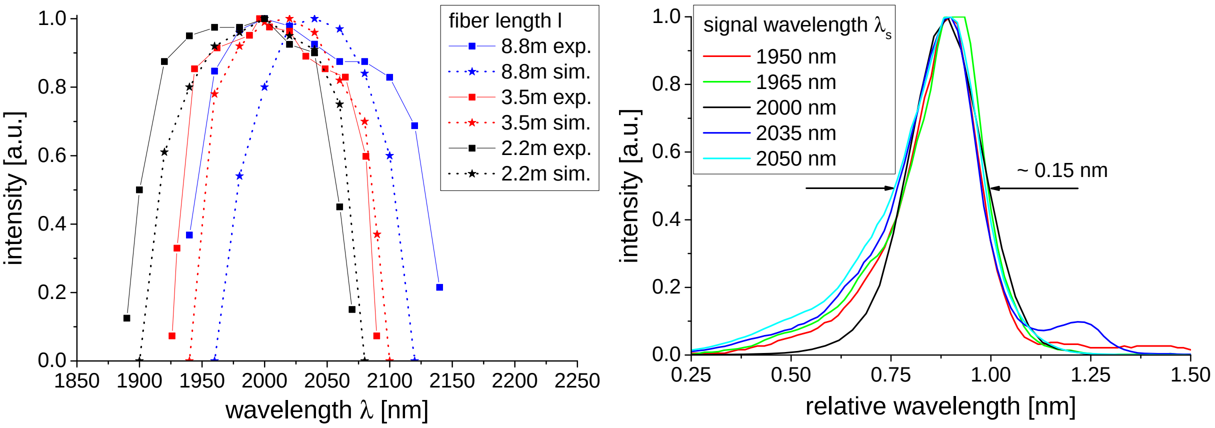

Figure 3.4: *Left*: Tunability of all fiber lasers with their simulated performances; *right*: Output spectra at different operational points of the tunability curve from thulium#3 (2.2 m), measured with spectro#2.

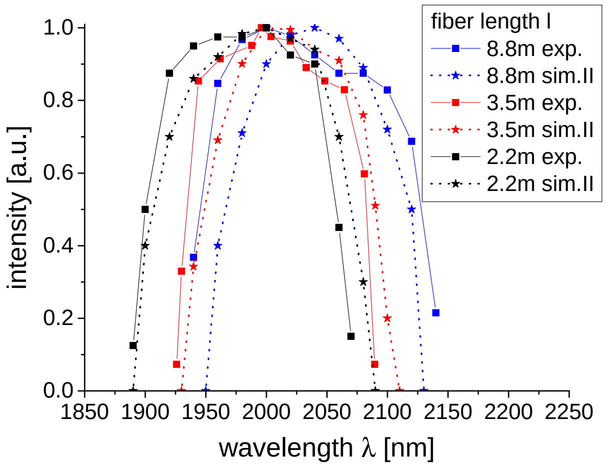

Figure 3.5: Measured tunability of all fiber lasers with their simulations based on a 15% higher emission and a 15% lower absorption cross-section.

front of the cavity end mirror and measuring the onset of ASE in terms of launched pump power. The measured and simulated values fitted roughly.

The fiber lasers provided a tunability span of around 170 nm, independent on the fiber length. The overall tunability curve of thulium#1 (8.8 m) is red-shifted compared to the other fibers, which is inherently connected to longer fibers in quasi-three-level laser gain media [40]. The lasing linewidth of different operational points within the tunability curve of thulium#3 have been recorded with spectro#2 and are shown on the right side of Figure 3.4. The linewidth has been around 0.15 nm, which is at the measurement limit of the spectrometer in terms of resolution. The real lasing linewidth is very likely narrower.

The experimental and simulated results regarding tunability fit approximately for thulium#2 (3.5 m) and thulium#3 (2.2 m), but for thulium#1 (8.8 m), the calculated tunability is much narrower compared to the achieved results. The tunability of a laser system is, especially for long fibers, highly dependent on the emission and absorption cross-sections at the lasing wavelengths of the fiber material. If an adaption of these cross-sections is conducted with a 15% higher emission and a 15% lower absorption cross-section, the tunability curves fit much better for every fiber, which is shown in Figure 3.5. Hence, the cross-sections are adapted by this amount for further calculations. This adaption does not significantly affect the slope efficiency for CW operation, but its lasing threshold. They decrease which yields a smaller deviation between the simulation and the measurement for the high power experiments, see Figure 3.2.

3.4.2 Q-Switching

The QS output characteristics, including the lasing threshold, slope efficiency, tunability and beam quality, are usually very similar to the CW performance, assuming a high QS repetition rate, $\Delta\nu_{QS}$, which yields a relatively short pumping period compared to the upper state lifetime, $T_p \approx \frac{1}{\nu_{QS}} \ll \tau$. Therefore, the spontaneous emission during the pumping period can be neglected. For the QS operational regime, the fiber laser is first characterized in terms of output power versus launched pump power, which is shown in Figure 3.6, left, for thulium#3 (2.2 m)

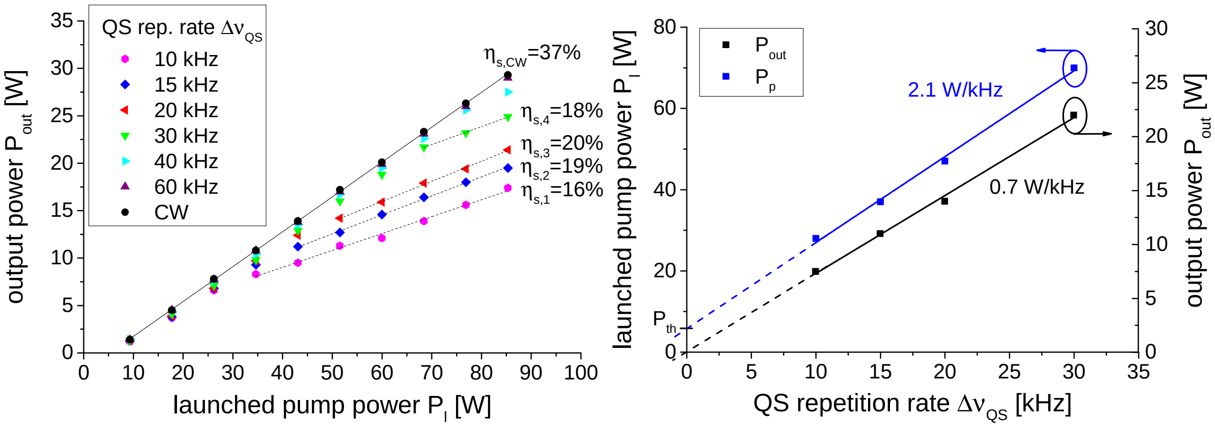

Figure 3.6: *Left*: Output power versus launched pump power in QS operation with thulium#3 (2.2 m) for different QS repetition rates; *right*: Thresholds for the ASE during QS operation in terms of launched pump power and output power versus QS repetition rate with linear fits.

at different QS repetition rates. The slope efficiencies and the lasing thresholds are almost the same compared to CW operation, which is also inserted in the graph. Although, at certain launched pump power levels for the different QS repetition rates, the output power curves indicate a bend. The reason for this phenomenon is ASE. Owing to the diffraction efficiency of the AOM for QS of less than 100%, the active fiber still gets feedback from the cavity end mirror when the AOM is turned on. According to equation 2.58, during the pumping period, the loss factor L is increased by the diffraction losses of the AOM. But once the population density in the upper laser level exceeds a certain value, the lasing process starts even though the AOM is still switched on. In this case, the slope efficiency of the overall output power curve decreases about a factor of two [35, 138]. The threshold for this effect depends on the diffraction efficiency of the AOM. Once it is reached, the initial gain factor G_i and therefore the QS output pulse energy are clamped and a further increase in pump power and inversion is extracted by ASE.

If these thresholds are observed, which are at a launched pump power level of around 68 W/ 44 W/35 W/28 W relating to an output power level of approximately 25 W/14 W/11 W/7.5 W at a QS repetition rate of 30 kHz/20 kHz/15 kHz/10 kHz, respectively, the maximum achievable QS output pulse energy is approximately 750 μJ for thulium#3 (2.2 m) before ASE builds up. Hereby, it has been assumed that the output pulse energy, E_{QS}, can be defined as

$$E_{QS} = \frac{P_{out}}{\Delta\nu_{QS}}, \tag{3.3}$$

which is valid when ASE can be neglected. At that QS output pulse energy, the QS pulse width, which will be later characterized in more detail, has been around 40 ns that results in a peak power level of 19 kW. The extractable QS output pulse energy for thulium#1 (8.8 m) and thulium#2 (3.5 m) is 1.28 mJ and 880 μJ, respectively. The difference in extractable energy for the different fiber lengths comes from a higher threshold power for CW lasing operation. The longer the active fiber is, the higher is the re-absorption of the intracavity radiation and the lasing threshold. Therefore, more energy can be stored in the fiber.

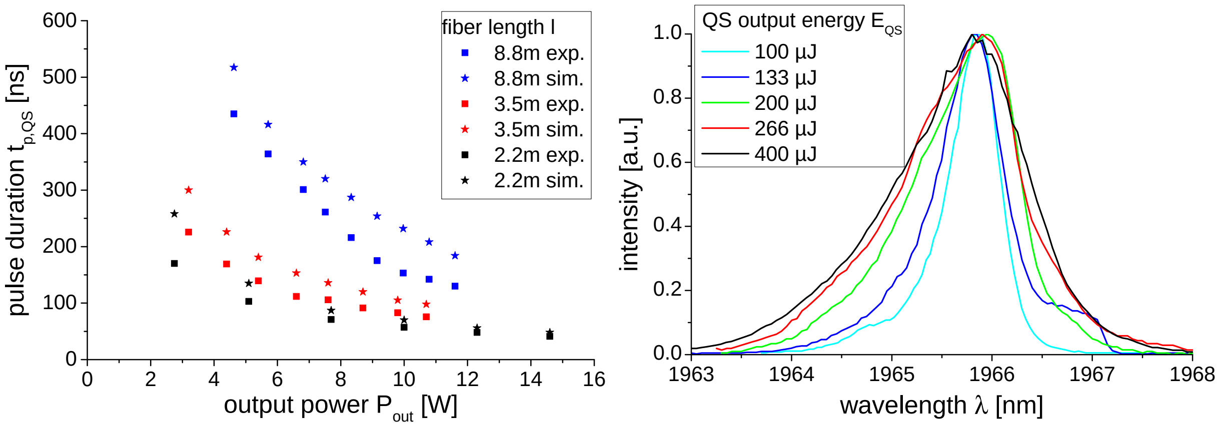

Figure 3.7: *Left*: Measured and simulated pulse duration versus average output power during QS operation for different fiber lengths at a QS repetition rate of 40 kHz; *right*: Measured output spectra for different QS output energy levels for thulium#3 (2.2 m).

The specified thresholds, before ASE decreases the slope efficiency, can be expressed via the launched pump power and the output power level for thulium#3, which is demonstrated in Figure 3.6, right, versus the QS repetition rate of the fiber laser, as it has already been introduced in [35, 138]. For the curve related to the output power, its intersection with the y-axis denotes the launched pump power at the lasing threshold, $P_{p,th}$. The slopes of the linear fits resulted in values of 2.1 $\frac{W}{kHz}$ and 0.7 $\frac{W}{kHz}$ concerning the pump and output power levels, respectively, being around three times higher than in previously reported experiments [35]. The reason for this enhancement might come from the different fiber parameters used. The multi-mode fiber investigated in the mentioned report exhibited a higher fluorescence capture and more relaxed requirements for coupling the intracavity radiation from the end mirror of the laser cavity back into the fiber core, thus enhancing ASE feedback and lowering the ASE threshold.

The QS output pulse duration at the FWHM, $t_{p,QS}$, has been measured with the PD#1 and the oscilloscope for all the fibers at different output power levels at a QS repetition rate of 40 kHz. These experiments have been performed at a lasing wavelength of around 2 μm with the grating as cavity end mirror. The emission wavelength of the fiber laser during QS operation influences the pulse width significantly. The reason is the different ratio of the corresponding emission to the absorption cross-section. For instance, if thulium#2 (3.5 m) is operated at an output pulse energy level of 200 μJ, the output pulse width changes by a factor of two over the whole tunability of the laser. Therefore, to compare the different QS output performances of the fiber lasers, the lasing wavelength has to be constant. Figure 3.7, left, displays the measured and the simulated pulse durations, based on the derivations from subsection 2.2.3.

The curves indicate the typical decrease of the QS pulse duration versus output power. For thulium#1 (8.8 m)/thulium#2 (3.5 m)/thulium#3 (2.2 m), the shortest QS pulse duration has been around 130 ns/60 ns/45 ns, respectively. The maximum achievable pulse energy from this experiment for thulium#3 is around 370 μJ and results with a pulse duration of 45 ns in a peak power of approximately 8 kW.

The simulation of the QS pulse widths has been performed with the adaptions of the material

Fiber	$P_{RS,th}$	$P_{BS,th}$
thulium#1 (8.8 m)	30 kW	240 kW
thulium#2 (3.5 m)	75 kW	600 kW
thulium#3 (2.2 m)	120 kW	900 kW

Table 3.2: Threshold power levels for RS and BS for the three fiber lengths.

parameters mentioned in the previous subsection. The differences between the simulation and the experiments for all the different fiber lengths are in the range of 30%.

Figure 3.7, right, shows the lasing linewidths of the QS output radiation from thulium#3 (2.2 m) for different QS output pulse energies, E_{QS}. For an increasing energy from 100 μJ to 400 μJ, the output spectrum broadens from 0.3 nm to around 1.4 nm.

The main limitation regarding output peak power from fiber lasers are nonlinearities, namely RS and BS. Their thresholds are listed in Table 3.2 for the three used fiber lengths. The calculation is based on the fiber data shown in Table 3.1, equation 2.47 and equation 2.48 with a Brillouin bandwidth in silica of 35 MHz [139] and a Raman gain coefficient of $0.5\times10^{-13}\frac{m}{W}$ at 2 μm, which origins from a gain coefficient of $1\times10^{-13}\frac{m}{W}$ at 1 μm and its linear inverse dependency on the pump wavelength [69]. The Brillouin gain coefficient is around $0.5\times10^{-11}\frac{m}{W}$ [71] and the lowest measured lasing linewidth in QS operation of 0.3 nm has been utilized. For the calculation of the thresholds, the effective length of fiber has been calculated based on the saturated gain factor G of 25, as already explained.

The threshold power levels for BS in this fiber laser setup are much higher compared to the ones for RS owing to the relatively broad output spectrum of the laser. The values for RS indicate that, especially for long fibers and more extractable QS output energies, the operational conditions can be close to the threshold for RS. But no Raman peak has been detected during purely QS operation.

The fiber laser output performance regarding tunability as well as beam quality are very similar compared to CW operation, which has been experimentally verified. Thus, these results are not shown here.

3.4.3 Mode-Locking

The diffraction efficiency of the AOM for ML, $\eta_{D,ML}$, has been characterized as it influences the pulse duration in active ML laser systems, see equation 2.100. It is dependent on the RF power, P_{RF}, the modulator is operated with [67]:

$$\eta_{D,ML} = \eta_{D,ML,max}\sin^2(\sqrt{SP_{RF}}). \tag{3.4}$$

If the AOM is implemented in the cavity of a laser system, the diffraction efficiency cannot reach 100% because of the non-planar wavefront of the passing electro-magnetic radiation. Therefore, $\eta_{D,ML,max}$ is introduced as the maximum possible diffraction efficiency obtainable with the wavefront of the intracavity laser beam. S is a factor that depends, among others, on the material parameters of the acousto-optic material.

The diffraction efficiency of the available AOM has been verified by the detection of the transmitted radiation through the AOM with PD#1 and the oscilloscope for different RF power

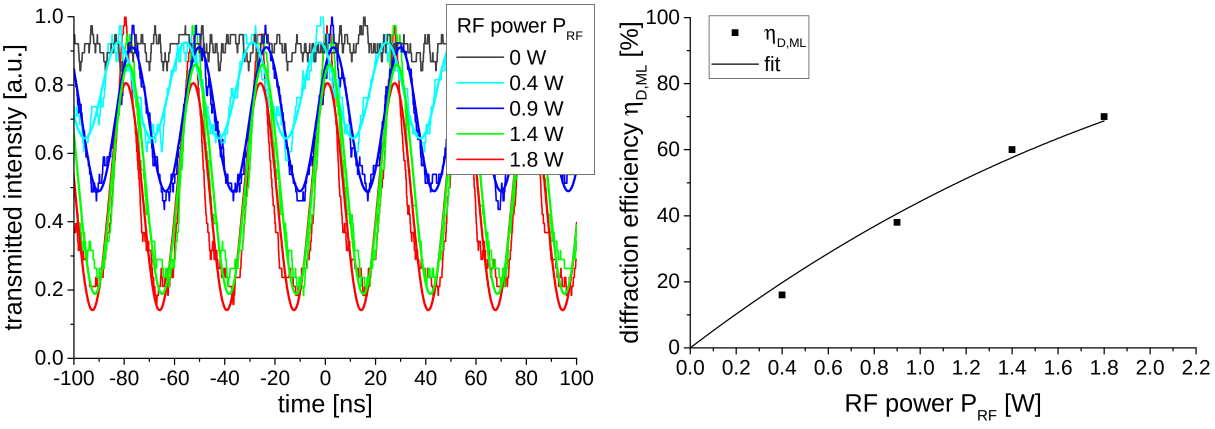

Figure 3.8: *Left*: Measurement of the transmitted radiation of the AOM for different power levels of the external RF signal; *right*: Diffraction efficiency of the AOM versus RF power with proper mathematical fit.

levels. The results are displayed in Figure 3.8, left, with sinusoidal fits for the different curves. The intensity modulation is sinusoidal-like and the related values of the diffraction efficiency against the RF power are plotted on the right side of the figure with a fit based on equation 3.4.

The measured values indicate deviations compared to the fit, but the saturation-like behavior can be recognized. A possible reason for this discrepancy could be losses of the RF power during its transmission to the AOM. The maximum achievable efficiency, $\eta_{D,ML,max}$, from the resulting fit has been almost 100%.

For the measurement of the ML pulse width, PD#2 (12.5 GHz) and the oscilloscope have been used. With this measurement system, the detected pulse width, $t_{p,meas}$, can be very close to the detection limit of the system, $t_{p,sys}$. Therefore, it has to be corrected by mathematical deconvolution to obtain the real ML pulse width, $t_{p,ML}$. For this purpose, the following Pythagorean subtraction has to be executed [140]:

$$t_{p,ML} = \sqrt{t_{p,meas}^2 - t_{p,sys}^2}. \tag{3.5}$$

The pulse durations in this equation are defined at the FWHM. Hereby, the detection limit of the measurement system can be calculated by considering the electrical bandwidth of the oscilloscope, $\Delta\nu_{Osc}$, and that from the PD#2, $\Delta\nu_{PD\#2}$, at the FWHM:

$$t_{p,sys} = \sqrt{\left(\frac{K_{Osc}}{\Delta\nu_{Osc}}\right)^2 + \left(\frac{K_{PD\#2}}{\Delta\nu_{PD\#2}}\right)^2}. \tag{3.6}$$

The influence of the BNC cable, connecting the PD#2 with the oscilloscope, is neglected. The time-bandwidth constants, K_{Osc} and $K_{PD\#2}$, are around 0.40 and 0.31 for the oscilloscope and the PD#2, respectively [140]. With the available measurement equipment, a theoretical detection limit of 150 ps results, which has been verified by measuring the temporal response of the measurement system for an ultra-short input pulse of 20 ps from a commercial 1 μm ML fiber laser. The measured signal and its Gaussian fit are displayed in Figure 3.9, left. The retrieved pulse duration has been approximately 220 ps, which can be used as time constant of

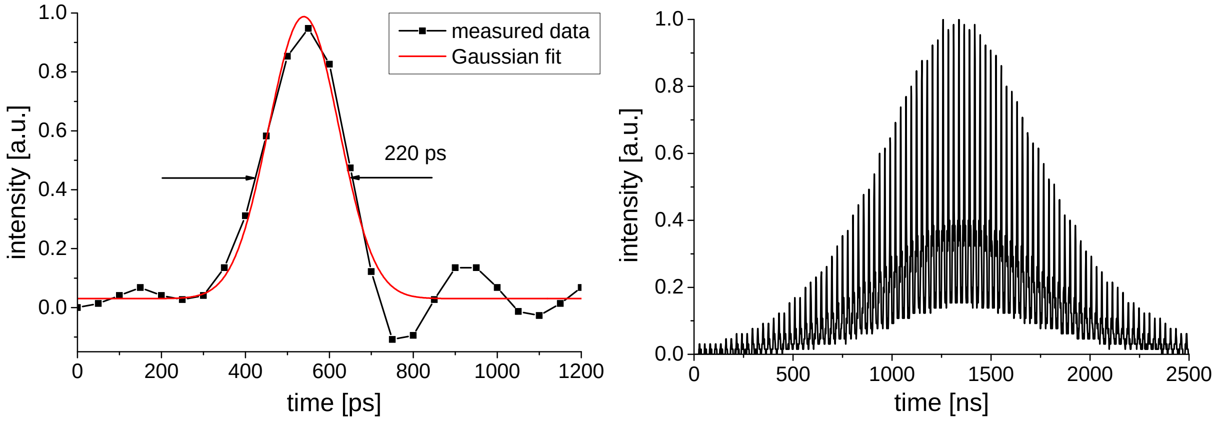

Figure 3.9: *Left*: Detected signal from the photodiode and the oscilloscope for an input pulse width of 20 ps; *right*: Mode beating of the fiber laser in CW operation with an additional modulation caused by relaxation oscillations.

the measurement system, $t_{p,sys}$.

For ML operation, the AOM has to be operated exactly at the fundamental repetition rate of the laser resonator, $\Delta\nu_{FSR}$. By monitoring the mode beating of the laser system in CW operation with PD#1 and the oscilloscope, the round-trip time τ_{RT} can be determined and the fundamental repetition rate calculated. A typical temporal evolution of the mode beating signal is shown in Figure 3.9, right, where the relaxation oscillations of the CW output signal are additionally modulated by this mode beating effect, whose frequency corresponds exactly to the fundamental repetition rate of the laser cavity. With a sinusoidal fit of the data, the fundamental repetition rates have been measured for thulium#1 (8.8 m)/thulium#2 (3.5 m)/ thulium#3 (2.2 m) to be 11.4 MHz/27.1 MHz/40.9 MHz, respectively.

For wavelength-tuning of the shown fiber laser system in ML operation, the change in optical length of the cavity caused by the material dispersion of the fiber has to be considered, especially because of the broad tunability of Tm^{3+}-doped fiber lasers. For each operation point of the tuning curve, the cavity length has to be adapted for proper ML operation. The derivative of the refractive index versus wavelength at around 2 μm for silica is approximately 1.55 nm^{-1} [141], which causes a change of the optical length of the cavity per nanometer wavelength for thulium#1 (8.8 m) of

$$\frac{dl_{thulium\#1}}{d\lambda} = \frac{dn}{d\lambda} l_{thulium\#1} \approx 0.124 \frac{mm}{nm}. \tag{3.7}$$

This value is immense regarding the broad tunability of the laser system of around 170 nm and indicates that it is indispensable to put the diffraction grating on a moveable one dimensional positioning stage, if the fiber laser has to be wavelength-tuned during ML operation. The RF for the AOM cannot be tuned over a broad bandwidth owing to its sensitive standing wave pattern of the acoustic wave.

The temperature of the fiber, which depends on the pump power level, also influences the optical fiber length and can be quantified with 0.07 $\frac{mm}{K}$ for thulium#1 [142]. Thus, the cavity length has also to be adapted for an increasing pump power level.

The performance of high power ML operation has been investigated with thulium#1 (8.8 m).

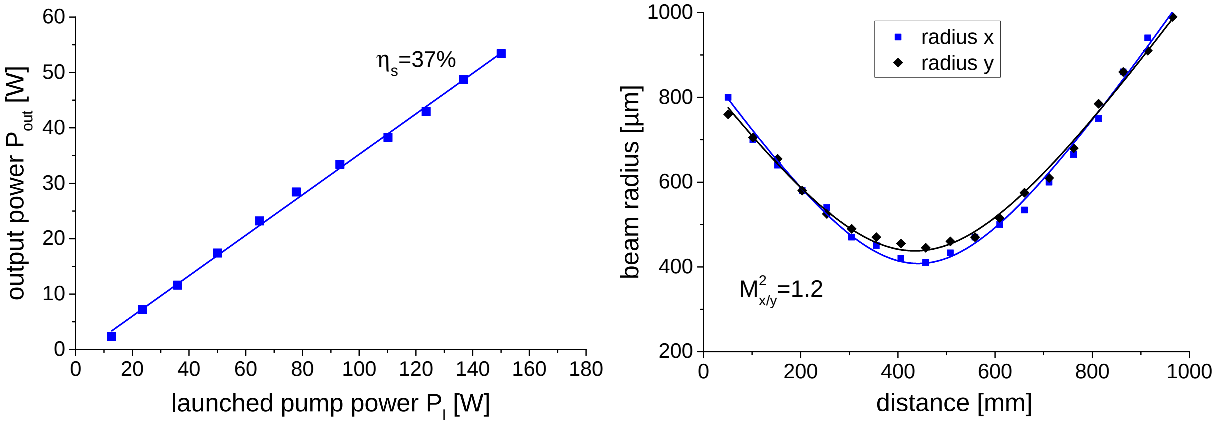

Figure 3.10: *Left*: Output power versus launched pump power for thulium#1 (8.8 m) in ML operation; *right*: M^2 measurement at an output power level of 25 W in ML operation.

The relatively long fiber yields a low fundamental repetition rate of around 11.4 MHz, as mentioned, which has in consequence a RF for the AOM of 5.7 MHz. The area of operation for the frequency generator lies between 20 MHz and 200 MHz and it is therefore necessary to operate the laser system in harmonic ML. The system has been operated in the 6^{th} harmonic order with a ML repetition rate of 68.4 MHz. As cavity end mirror, the grating has been used for this experiment. The output power against launched pump power is displayed in Figure 3.10, left. The laser system provided up to 53 W of output power at a launched pump power level of 158 W resulting in a slope efficiency of 37%. The lasing threshold has been approximately 8 W, similar to the one in CW operation. At the highest output power level, the corresponding pulse energy has been 0.77 μJ.

Figure 3.10, right, shows the measurement of the beam propagation factor M^2 during this experiment at an output power level of 25 W. The fiber laser provided an excellent beam quality with a M^2 value of around 1.2 in both directions, similar to the one achieved in CW operation.

The output lasing linewidth during this experiment at the highest output power, measured with spectro#2, is presented on the left side of Figure 3.11. The output linewidth has been smaller than the resolution limit of the spectrometer and the real value could not be detected.

Figure 3.11, right, shows the measured and simulated ML pulse duration during the high power experiment. The calculation of the pulse width is based on the equation 2.98, equation 2.99 and equation 3.8:

$$t_{p,ML} = 1.66 \sqrt[4]{\frac{2gl}{\pi\Delta\nu\left(\frac{M(2\pi\Delta\nu_{ML})^2}{2} + \frac{(\phi_{SPM}\pi\Delta\nu)^2}{8gl}\right)}}. \tag{3.8}$$

The nonlinear phase shift, as already introduced, can be expressed with:

$$\phi_{SPM} = \frac{2\pi l_{eff}}{\lambda} n_2 I. \tag{3.9}$$

For the calculation of the nonlinear phase shift, the intensity I has been estimated by using 4%

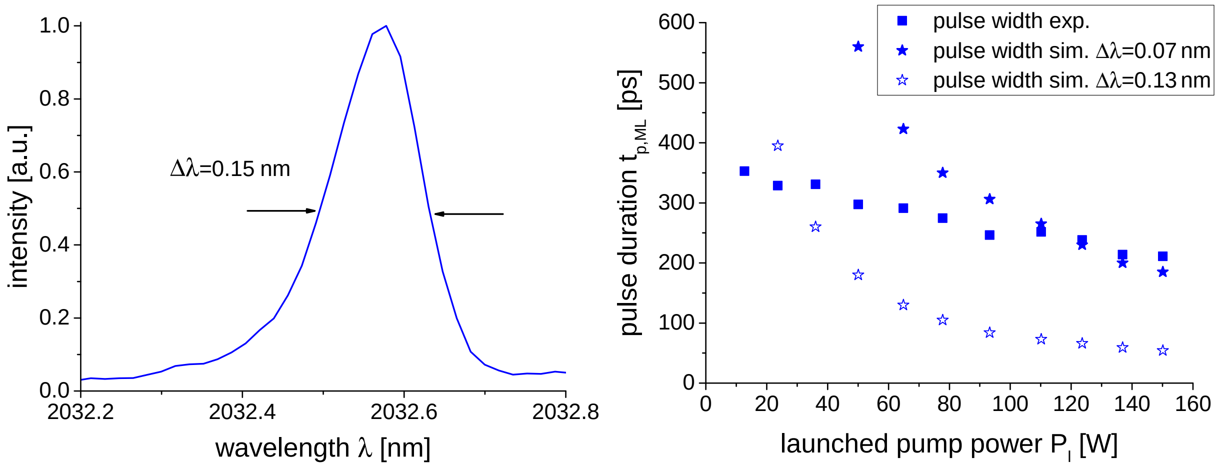

Figure 3.11: *Left*: Output spectrum during ML operation at the highest launched pump power level; *right*: Measured and simulated ML pulse widths versus launched pump power for thulium#1 (8.8 m) with the calculated performance.

of the output intensity of the fiber laser with an effective fiber length of

$$l_{eff} = \frac{e^{gl}-1}{g}. \tag{3.10}$$

The simulations have been performed with a modulation depth of 70%, corresponding to the used value for almost all the ML and QML experiments, a saturated gain factor of $2gl$=ln(25) and a nonlinear-index coefficient for silica of $2.7\times10^{-20}\ \frac{m^2}{W}$ [122]. The output spectra of the ML operation could not be detected owing to the limited resolution of the used spectro#2. Therefore, a lasing bandwidth of $\Delta\lambda$=0.13 nm and $\Delta\lambda$=0.07 nm have been assumed for the calculation to fit the results.

The measured pulse duration is decreasing versus increasing output power, which is theoretically predictable because of the higher nonlinear phase shift. At the highest output power level, the pulse duration was around 200 ps, which results with the highest pulse energy of 0.77 μJ in a pulse peak power of approximately 3.85 kW, assuming a Gaussian pulse shape. This value is far below the RS threshold of 30 kW for this fiber length.

There is a significant difference between the measurement and the simulations. It seems that for an increasing output power level, the number of phase-coupled modes is decreasing. The actual bandwidth of the laser is apparently between the two used values of $\Delta\lambda$=0.13 nm and $\Delta\lambda$=0.07 nm from the simulation. Using a lasing bandwidth of 0.07 nm at the highest output power level, the time-bandwidth limit results in a minimal achievable pulse duration of 88 ps, assuming a Gaussian pulse shape, which is approximately 2.5 times shorter than the measured pulse duration of 200 ps.

Owing to the obtained output energy levels and pulse widths, the ML regime cannot be soliton ML. Based on equation 2.50 for calculating the soliton energy and its pulse duration, a GVD of silica of -100 $\frac{fs}{mm}$ [141], the used nonlinearity of $2.7\times10^{-20}\ \frac{m^2}{W}$ and the measured pulse energy of 0.77 μJ, the resulting soliton pulse width would be far below in the femtosecond region, which is physically not realistic.

Thulium#2 and thulium#3 have not been investigated regarding purely ML operation because this single-oscillator purely ML fiber laser system cannot be used for high power mid-IR SCG in fluoride fibers owing to the insufficient peak power levels. Therefore, it is of higher interest to investigate the QML pulse generating method more profound.

3.4.4 Q-switched mode-locking

If a laser system is operated in QML regime, the output characteristics are much different compared to purely ML or QS lasers. The additional modulation of the ML pulse train with QS repetition rates in the range of kHz causes different pulse energies and peak power levels below the QS envelope, which can be orders of magnitude higher compared to ML or QS systems. The width of the QS envelope and its build-up time in QML operation is approximately the same compared to QS lasers. Figure 3.12, left, shows a typical QML pulse train at an output power level of 10 W, a modulation depth of 70% and a QS repetition rate of 100 kHz for thulium#3 (2.2 m), measured with the PD#1 (1 GHz) and the oscilloscope. The QML pulse train indicates a ML modulation depth of the QS envelope of around 100%. The phase between the ML subpulses in actively ML systems is induced by the RF signal for the AOM and is therefore constant, in contrary to the phase of the QS pulses, which varies owing to their build-up caused by vacuum fluctuations and the connected timing jitter. Hence, the QS envelope and the ML subpulses have not a fixed phase relation to each other and it is not possible to operate the system in a way, that the most-energetic ML subpulse is exactly at the peak of the QS envelope. If there was no QS timing jitter, this operational regime could be realized by operating the system with a ML repetition rate that is exactly a multiple of the one for QS. This experiment has been performed but was not successful because of the mentioned timing jitter in QS fiber lasers.

If the most-energetic ML subpulses (1-5 in Figure 3.12, left) are detected with the fast PD#2 (12.5 GHz) and observed on a more resolved time scale, pedestals below the ML pulses are remarkable, which are presented on the right side of Figure 3.12. In this configuration, the pedestals have a width of approximately 2.5 ns. As a result of the bandwidth-limited mea-

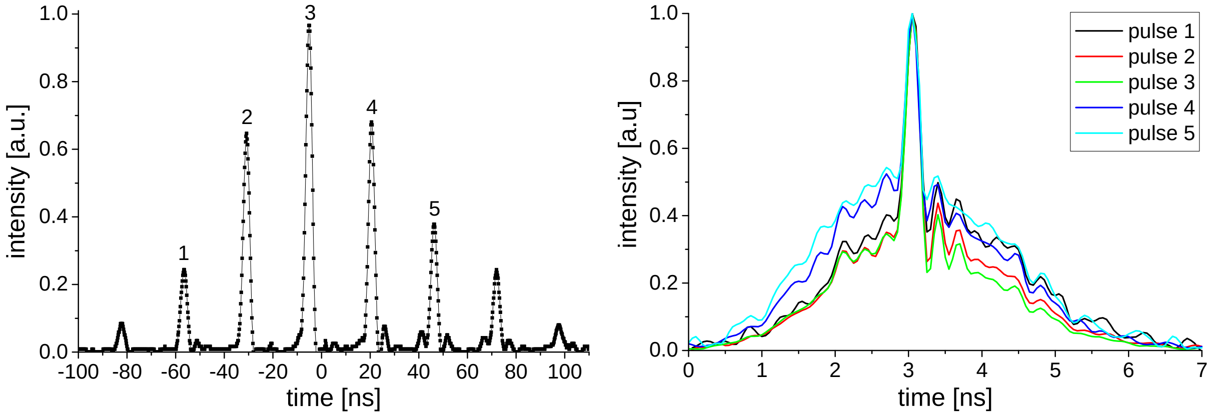

Figure 3.12: *Left*: Typical QML pulse train measured with PD#1 and the oscilloscope with the indication of the five most-energetic ML subpulses; *right*: Temporal profile of these five pulses including their pedestals.

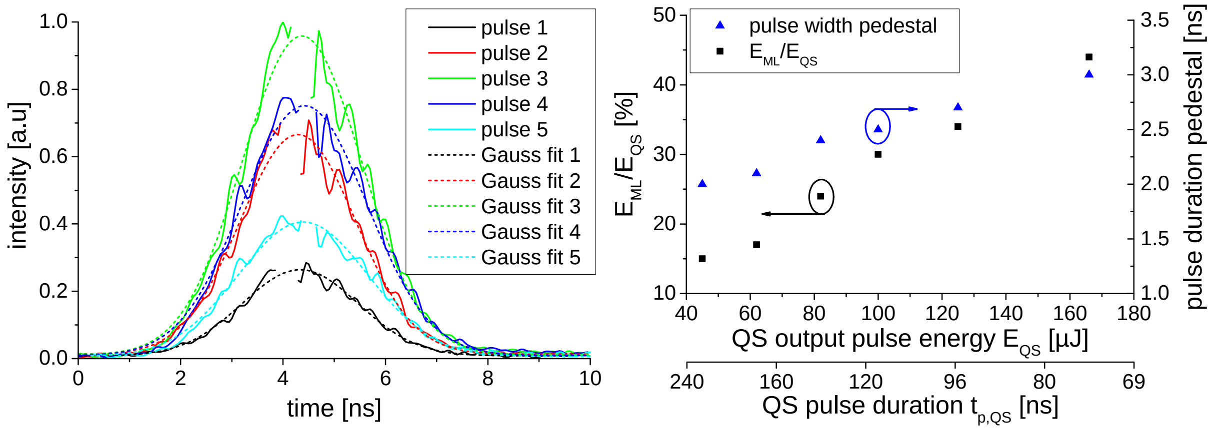

Figure 3.13: *Left*: Comparison of the pedestals by cutting out their short peaks and fitting Gaussian functions; *right*: Percentage of the pulse energy of the highest ML subpulse, E_{ML}, related to the total QS energy, E_{QS}, and the pulse width of the pedestals versus the QS output energy and the pulse duration of the fiber laser.

surement system, the displayed electronic peak power levels of the short peaks on top of the pedestals are distorted. In order to estimate the ratio of energy between the short peaks and their pedestals, their integrals are compared with each other. For that purpose, the peaks are cut out manually to observe only the pedestals, which are fitted with Gaussian functions and are shown in Figure 3.13, left. The integrals of the Gaussian fits are compared to the ones from the short peaks. This calculation resulted in an energy level between 3% and 5% of the total energy of the ML subpulse, E_{ML}, included in the short peaks. For verifying this value, the measurement system, including PD#2 and the oscilloscope, has been calibrated in terms of peak power. A QS pulse of the fiber laser with a known peak power level has been detected to measure the corresponding electrical voltage displayed on the oscilloscope. With that calibration factor, the peak power levels of the pedestals can be determined and its energy content evaluated with the integral of the measured electrical signal, which fitted approximately with the calculated energy content mentioned above. It can be claimed that the peaks contain 3% to 5% of the ML energy within the measured pulse duration of 220 ps, which is the limit in terms of temporal resolution of the measurement system, but its exact temporal evolution cannot be detected.

Figure 3.13, left, indicates a constant width of all pedestals below the QS envelope, which is the case for a perfect match between the external RF drive signal for the AOM and the fundamental repetition rate of the laser resonator. The energy and the peak power levels of the pedestals depend on the QS output pulse parameters from the fiber laser. If the pulses are short, the number of ML subpulses decreases and their pulses contain thus more energy in relation to the QS output pulse energy, E_{QS}. The QS pulse width of a fiber laser is directly related to its pulse energy, assuming a constant fiber length and lasing wavelength. For the characterization of the QML output performance, only thulium#3 (2.2 m) has been used and was always operated close to 2 μm at the peak of its tunability curve (see Figure 3.4, left). To determine the pulse width of the pedestal and the energy content of the most-energetic ML subpulse in relation to the QS energy, the QML pulse trains have been analyzed when the fiber laser was operated at a constant output power level of 10 W with a decreasing QS repetition

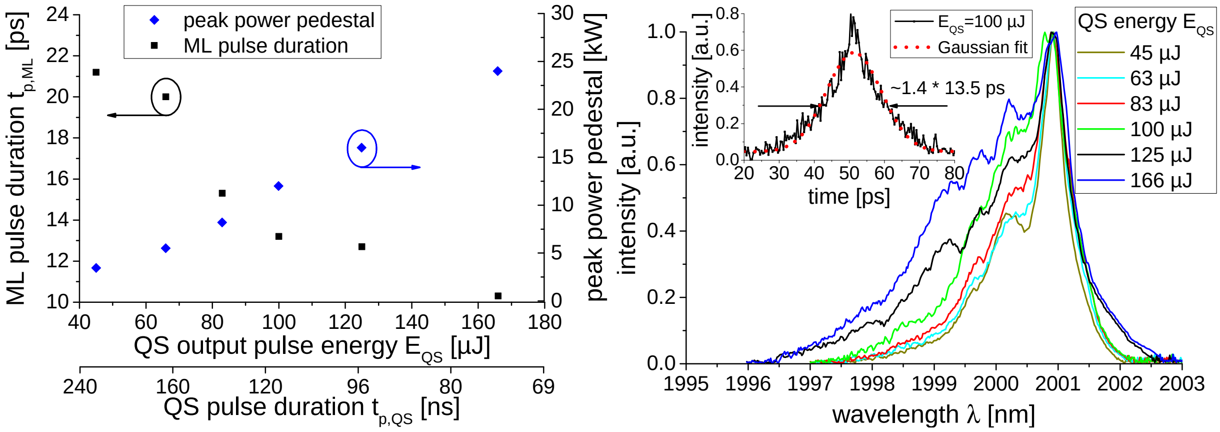

Figure 3.14: *Left*: ML pulse duration and the peak power level of the most-energetic pedestal versus QS pulse energy and duration of the fiber laser; *right*: Output spectrum during QML operation for different QS pulse energies; *inset*: Autocorrelation function with Gaussian fit for a ML pulse duration of 13.5 ps.

rate leading to a QS output energy rising from 42 μJ to 166 μJ. The energy content of the most-energetic ML subpulse relative to the total QS output pulse energy and the width of the pedestals are displayed in Figure 3.13, right, versus the energy and the width of the QS pulse. The relative energy content of the most-energetic ML pulse has grown from around 15% to 43% and the pedestal's width increases from 2 ns to 3 ns. The reason for this prolongation of the pedestal might be connected to the sinusoidal loss modulation of active ML, see Figure 2.16. There is, as already mentioned, a temporal gate in which the ML pulse can pass the modulator to the cavity end mirror and back to the fiber each round-trip. The duration of this gate is probably dependent on the time, the gain of the fiber can balance the losses of the cavity, which are partly induced by the AOM. Therefore, if the gain of the fiber is higher, the temporal duration of this gate, and also of the pedestal, gets probably longer.

The short peaks on top of the pedestals contain, as mentioned, a relatively low energy, but their pulse duration can be measured with the autocorrelator. Figure 3.14, left, displays their pulse width versus the QS energy and pulse duration. It decreased from around 21 ps to the minimum achieved value of 10 ps at a QS output pulse energy of 166 μJ. If it is assumed that a higher QS output energy of the fiber laser yields a higher energy content within the short peak, a shorter pulse width can be explained with a stronger SPM-induced phase shift.

The inset of Figure 3.14, right, shows a typical autocorrelation function (ACF) with Gaussian fit for the ML pulse duration of around 13.5 ps. In the case of a Gaussian pulse shape, the width of an ACF at the FWHM has to be divided by 1.4 to obtain the pulse duration. The retrieved ACFs for a QML system is an average of all ML subpulses below the QS envelope. If the ML pulses have different widths, the ACF might indicate derivations to a Gaussian function. The characterization of each single ML subpulse with an autocorrelator from a QML laser is very challenging [123]. A pulse picker would be necessary to perform this experiment.

In Figure 3.14, left, also the peak power level of the most-energetic pedestal is plotted against the QS output pulse energy and duration. The peak power indicates a nonlinear growth, which is caused by the linear augmentation of the QS pulse energy plus a higher ratio of this energy within the most-energetic pedestal. Even though the pedestals get temporarily longer versus

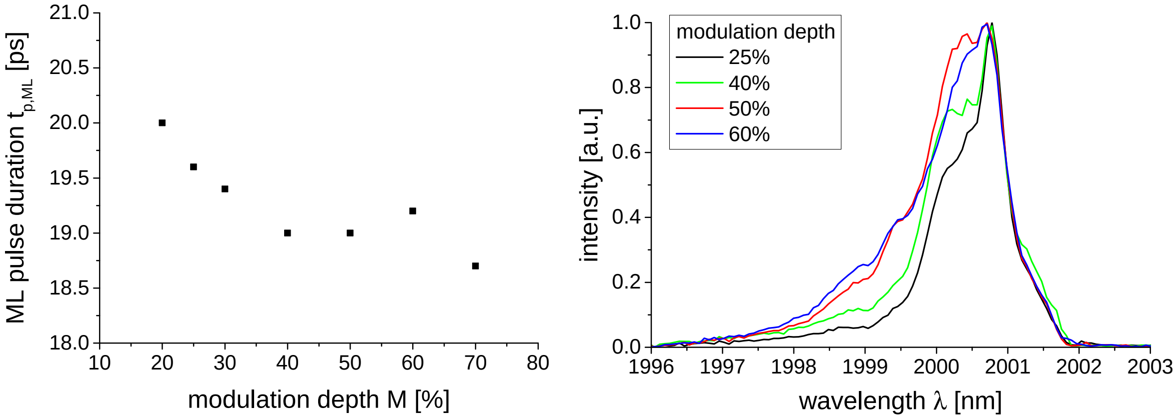

Figure 3.15: *Left*: ML pulse duration versus modulation depth of the AOM; *right*: Output spectra for different modulation depths.

QS output pulse energy, the peak power level still increases nonlinearly.

The right side of Figure 3.14 presents the different lasing bandwidths related to the measurement shown on the left side. The higher the QS output pulse energy of the fiber laser is, the shorter are the ML pulses and the broader is the optical output spectrum. For the highest QS energy level of 166 μJ, the spectral laser linewidth was approximately 2 nm. Although, the energy content of the short peaks has been relatively low, the bandwidth broadened significantly compared to the results achieved in CW, QS or ML operation. Assuming a Gaussian pulse shape, the time-bandwidth product for this emission linewidth at a wavelength of 2 μm results in a minimal achievable pulse duration of approximately 3 ps. The retrieved pulse duration has been around 10.5 ps, which is a factor of 3.5 longer. If other measurement points with different pulse widths and lasing linewidths are observed, the ratios between the theoretical minimal to the achieved values are approximately constant. The reason might be inherently connected to the active ML technique or the dispersion of the silica fiber laser, which is not compensated for.

Another influence on the ML pulse duration is the modulation depth of the AOM for ML. For measuring this dependency, thulium#3 has been operated at an output power level of 10 W and a QS repetition rate of 150 kHz while the modulation depth has been tuned from 15% up to 70%. The ML pulse duration versus modulation depth is shown in Figure 3.15, left. It decreased from around 20 ps to 18.5 ps. Generally, if the nonlinear phase shift is very strong, as it is during QML operation, the modulation depth influences the pulse width not significantly, as confirmed by this measurement.

The right side of the Figure 3.15 displays the related output spectra during this experiment for different modulation depths. The higher it is, the shorter is the ML pulse and the broader is the output spectrum, which increased from around 0.7 nm up to 1.2 nm.

The dependency of the modulation depth on the duration of the pedestals is shown in Figure 3.16, which has been determined during the measurement shown in Figure 3.15. The pedestal's duration declined from 3.5 ns to 2.2 ns. If the modulation depth is changed, the distribution of the QS energy among the ML subpulses below the QS envelope is constant. Therefore, by changing this parameter, the peak power level of the pedestals can be changed

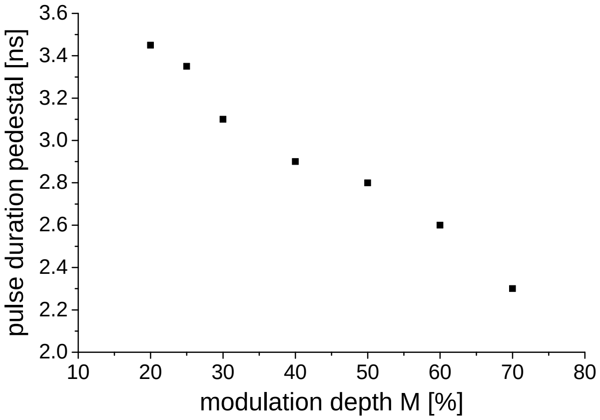

Figure 3.16: Pulse duration of the pedestals versus modulation depth of the ML modulator.

without changing their energy.

If the wavelength of the fiber laser system is tuned during QML operation, many parameters of the laser system are affected. First, the mentioned material dispersion requires readjustment of the laser cavity length, as it has been derived in subsection 3.4.3. Furthermore, the Bragg angle of the AOM, and hence its modulation depth, are wavelength-dependent [67]. If the fiber laser is operated at a QS output energy of around 100 μJ with a modulation depth of 70% and is wavelength-tuned without readjusting these operational parameters, the results shown in Figure 3.17 outcome. The left side presents the duration of the ML pulses and their pedestals. The measurements have been performed for some lasing wavelengths within the tuning range of the laser. The measured ML pulse width varies between 28 ps and 15 ps. The duration of the pedestal changed between 3.4 ns and 2.6 ns. The perfect operation point is obviously around 1980 nm in this case. The right side of the figure displays the related emission spectra during this experiment. It varied between 0.6 nm and 1.6 nm for the different lasing wavelengths.

For high power QML operation, thulium#3 (2.2 m) has been used with the diffraction grating as cavity end mirror. The output power against launched pump power for different QS repetition

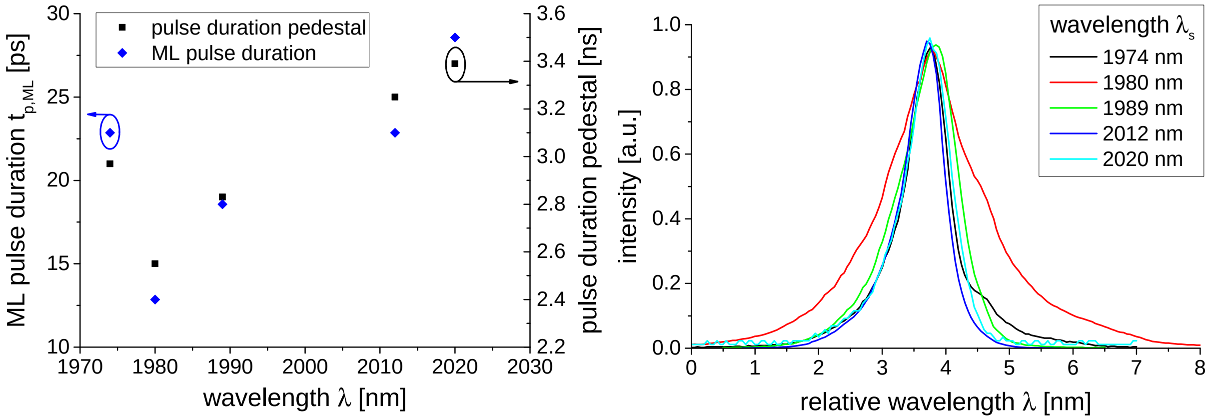

Figure 3.17: *Left*: Pulse duration of the ML pulse and its pedestal during wavelength-tuning without adjusting other cavity parameters; *right*: Related output spectra for some lasing wavelengths within the tuning range of the laser.

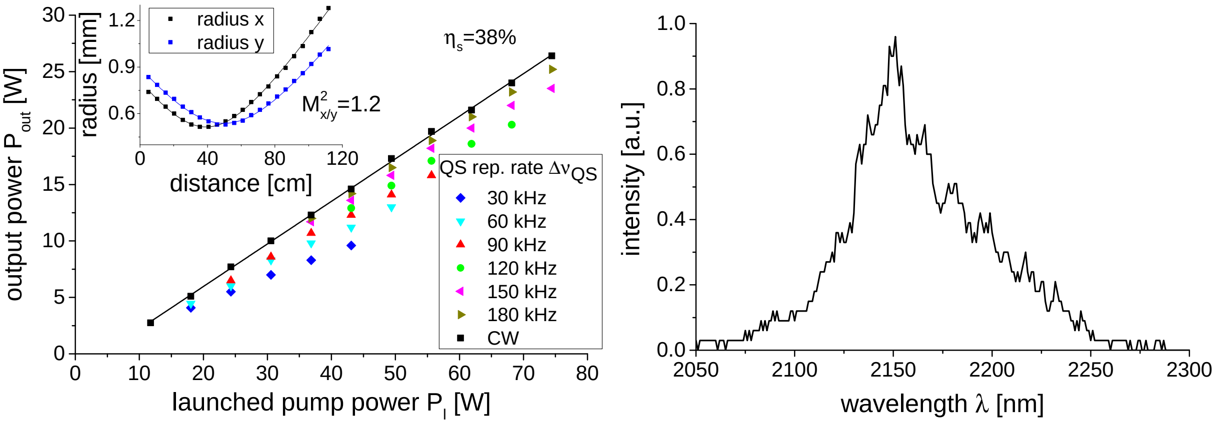

Figure 3.18: *Left*: Output power versus launched pump power in QML operation for different QS repetition rates with thulium#3 (2.2 m); *inset*: M^2 measurement in QML operation at an output power level of 15 W and a QS repetition rate of 90 kHz with thulium#3; *right*: Spectrum of the Raman-shifted output radiation.

rates is displayed together with the CW performance for comparison in Figure 3.18, left. The highest output power level has been 25 W for QS repetition rates of 180 kHz or higher. The lasing threshold has been approximately 5 W, independent on the QS repetition rate, and close to the one for CW operation. The fiber laser has not been operated up to its limit in terms of average output power, because the one achieved has been sufficient for high power mid-IR SC experiments. At the highest output power level and a QS repetition rate of 180 kHz, the laser provided a QS output energy of approximately 140 μJ with a peak power and energy level of the most-energetic pedestal of around 20 kW and 50 μJ, respectively.

The inset of Figure 3.18, left, shows the result of the M^2 measurement, which has been performed at an average output power level of 15 W and a QS repetition rate of 90 kHz. The beam quality factor has been around 1.2 in both directions, close to the values achieved in CW and ML operation.

The curves in QML operation have a lower slope efficiency compared to the CW performance and they exhibit a rollover behavior at a certain launched pump power level dependent on their QS repetition rate. This effects looks similar to the ASE-related losses during purely QS operation, although, the thresholds for the effect in QML are much lower. The reason for this rollover in QML could be nonlinear effects of the silica stimulated by the high peak intensities of the QML pulses. The peak power levels of the pedestals are not sufficient for RS. But the higher peak power of the short ML pulses probably induces RS. At high QS output pulse energies, a Raman peak has been detected with spectro#1, which is shown on the right side of Figure 3.18. This Raman-shifted radiation has only a small average output power level.

Another possible reason for this rollover effect could be spectral cutting at the diffraction grating. The active ML regime builds up the oscillation of many longitudinal modes after some round-trips, which broadens the lasing linewidth in QML operation dependent on the QS output pulse energy level, as shown in Figure 3.14, right. The diffraction grating is only highly reflective within a certain wavelength range. If it does not provide feedback of the coupled longitudinal modes at the wings of the lasing linewidth, their power is coupled out after each round-trip, which causes losses.

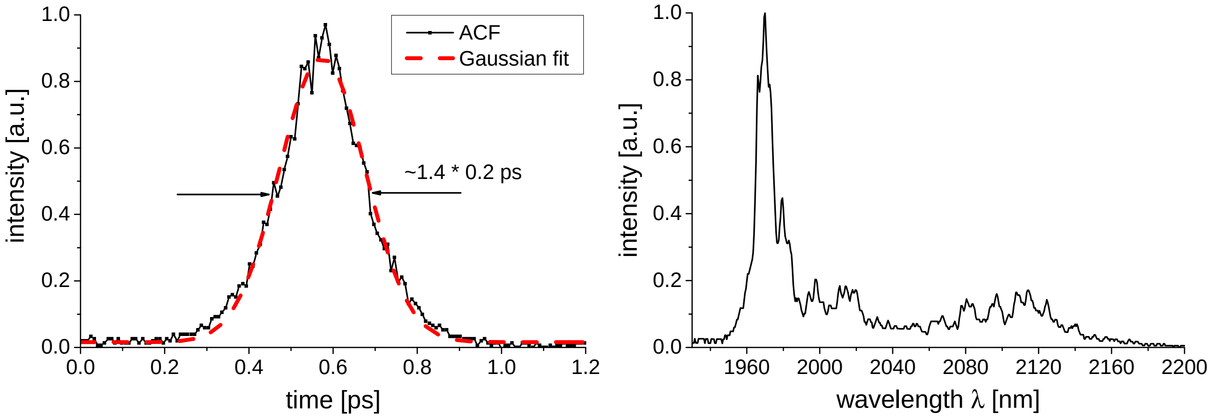

Figure 3.19: *Left*: Autocorrelation function of the ML output pulse during with the HR mirror as cavity end mirror; *right*: Related output spectrum of this experiment.

All experiments in this subsection to characterize the QML lasing regime have been performed with the diffraction grating as cavity end mirror. When the HR mirror has been used, the output characteristics of the pedestals have been similar to the ones described with the diffraction grating, although, the pulse duration of the short peak changed significantly. Figure 3.19, left, displays an ACF measurement with this cavity end mirror yielding a pulse duration of around 200 fs. This value is close to the measurement limit of the autocorrelator system, thus, the real pulse width can be even shorter. The right side of the figure displays the corresponding optical output spectrum, measured with spectro#1, which indicates a lasing bandwidth from around 1.96 μm up to 2.15 μm. The local peaks around 2.1 μm might be caused by stimulated RS, which is enabled by the very broadband HR mirror and therefore the feedback of Raman-shifted radiation back to the fiber laser. If the QML output power versus launched pump power was recorded with the HR mirror, the resulting curves did not exhibit the described rollover effect, which confirms that its reason is probably spectral cutting at the grating. The performance with the HR mirror has not been investigated any further, because it exhibited less conversion efficiency during SCG, which will be explained in the next chapter in further details.

3.5 Summary

In this subsection the achieved output performance of the Tm^{3+}-doped fiber laser is compared to already published results from single-oscillator Tm^{3+}-doped fiber lasers in literature.

In **CW** operation, the highest achieved output power level has been 70 W with thulium#1 (8.8 m) and almost 30 W with thulium#2 (3.5 m) and thulium#3 (2.2 m). The slope efficiency in all experiments have been around 40%. The higher output power level from thulium#1 has been probably enabled by its reduced heat load caused by the lower absorption coefficient at the used pump wavelength. The measured beam quality, even at high output power levels, has been close to the diffraction limit.

The highest reported output power from a Tm^{3+}-doped single-oscillator has been 885 W [143]. The used multi-mode fiber in this experiment had a core diameter of 35 μm and a *NA* of 0.2.

The slope efficiency has been in the order of 50% and the fiber had a length of 7 m. From a single-mode fiber laser, as much as 415 W have been demonstrated with a slope efficiency of 60% with respect to the absorbed pump power at a wavelength of 1.6 μm [36]. During this experiment, an 8 m-long, low-doped active fiber has been selected to decrease the heat load of the fiber.

The reason for the lower achieved output power levels in this thesis is probably connected to the thermal management of the fiber. All of the reported high power experiments included end caps in the form of passive silica fibers, which are spliced onto the active fiber ends to enable more efficient cooling. In the described setup without end caps, there is a certain part of the fiber that is not actively water-cooled, which is the bottleneck of the system regarding power scaling. The implementation of end caps is planned for future experiments and thus, further power scaling should be soon feasible.

The difference in achieved and reported slope efficiencies must be related to the material itself, meaning a lower CR efficiency, or losses caused by upconversion or clustering. The used doping concentration or the composition of the fiber material probably offer potential for improvement. Another reason for the lower values could be the uncooled parts of the fiber, which get very hot and increase therefore the absorption of the intracavity beam.

In **QS** operation, the highest obtained output pulse energy with thulium#3 (2.2 m) has been 750 μJ with a pulse duration of approximately 40 ns and a peak power level of around 19 kW. To the best of my knowledge, this is the highest achieved peak power level from a QS Tm^{3+}-doped fiber laser. The output power level during QS operation has been scaled to almost 30 W. Further power scaling should be enabled by better thermal management and diode modules offering higher pump power, which will soon be available at ISL. For a higher QS pulse energy, the diffraction efficiency of the AOM has to be increased because of the ASE-related limitation.

Tm^{3+}-doped fiber lasers in QS operation have been investigated with passive and active modulation technologies. Passively QS fiber lasers provide generally longer pulses, lower pulse energies and output power levels, thus, they are not considered for a comparison to the achieved results. El Sharif *et al.* demonstrated with an AOM as modulator a pulse energy of around 900 μJ with a pulse duration of 150 ns yielding a peak power of 4 kW [144]. However, the output power level of this experiment has been below 1 W. The closest reported peak power of 9 kW has been demonstrated with a pulse energy of 435 μJ and a pulse width of 49 ns [97]. This experiment has been performed at an output power level of less than 10 W. The reported experiments in [35], which have also been conduced at ISL, yielded a total output power level of 30 W with a pulse energy of 270 μJ and a peak power level of 5 kW.

In **ML** operation, thulium#1 (8.8 m) has been tested and delivered an output pulse energy of around 800 nJ at 53 W of average output power with a pulse width of 200 ps yielding a peak power level of 4 kW.

So far, there are no reports about actively ML Tm^{3+}-doped fiber lasers with an AOM. But an EOM has once been used to provide flexible pulse width, dependent on the harmonic order of ML, with the lowest pulse duration of around 38 ps for fundamental ML. The fiber laser delivered output power levels in the milliwatt range [145]. The output pulse energy and the peak power levels are therefore orders of magnitude lower compared to the described ML system in this thesis. There are reports about actively AOM-ML fiber lasers at the wavelength of 1 μm, which produced a pulse width in the range of 95 ps at very low output power levels

[146]. Most of the research activities for ML Tm^{3+}-doped fiber lasers have been focused on passive modulation techniques, where it is possible to produce temporarily much shorter pulses, even in the range of tens of femtoseconds. Owing to the emitting wavelength around 2 μm and the connected negative GVD in silica, there are two different schemes for generating ultra-fast ML pulses, as mentioned in subsection 2.2.4. First, soliton ML can be realized by carefully matching the nonlinearity and the dispersion of the silica fiber. Or second, the so-called noisy pulse regime, where the propagating pulses are not solitons. With soliton ML, a pulse width of 65 fs has been demonstrated with a saturable absorber as modulator [147]. The pulse energy has been 3 nJ resulting in a peak power level of approximately 50 kW and 0.3 W of average output power. With graphene as ML element in the cavity, 58 fs have been obtained with 1 nJ yielding 20 kW of peak power at an output power level of 0.5 W [148]. The highest ML output pulse energy demonstrated with soliton ML has been 10 nJ [149]. It is very challenging to power and energy scale soliton ML lasers, because of their sensitive match of nonlinearity and dispersion. In the case of the noisy pulse regime, as much as 250 nJ has been achieved with a pulse duration of 350 fs and 0.4 W of output power [150].

In terms of output pulse energy and average output power, the ML system shown in this thesis delivered the highest values. But owing to the long pulses, the peak power levels have been lower compared to ultra-short pulse generation with passive ML techniques.

In **QML** operation, there has been no report with Tm^{3+}-doped fiber lasers. The demonstrated results have in many aspects outstanding performance parameters. The ML pulse energy levels in the range of 66 μJ with pulse durations of the pedestals in the nanosecond regime and peak power levels of 25 kW cannot be compared to QS lasers in terms of pulse widths and not to ML systems regarding pulse energy. Typically, for obtaining such pulses, distributed feedback diodes with at least three amplification stages have to be used to reach the same output performance of the described QML fiber laser system [3, 33]. Unfortunately, the peak power levels of the short peaks on top of the pedestals cannot be determined, which are definitely much higher compared to their surrounding pedestals.

4 2 μm pumped supercontinuum generation in fluoride fibers

4.1 Introduction

SCG in fluoride fibers is a very attractive option for generating mid-IR radiation up to approximately 4 μm, especially if very broad output radiation is required. Fluoride fibers have the lowest losses in the mid-IR [29] and their drawing technology is the second most mature behind silica [151], especially for the material composition ZBLAN, which has a mixture of around 55 mol% ZrF_4, 15 mol% BaF_2, 6 mol% LaF_3, 3 mol% AlF_3 and 15 mol% NaF [152]. ZBLAN fibers are manufactured with the most developed fabrication technology among all IR fibers, resulting in the lowest quantity of impurities [153]. Therefore, for high power mid-IR SCG, these fibers have almost been exclusively used, which have enabled tens of watts of output power. The output spectrum, which can be obtained with this material composition, is limited to a wavelength at around 4 μm owing to its material absorption. The nonlinear-index coefficient of fluoride fibers is smaller than the one for silica fibers, thus, relatively long fibers in the range of meters are necessary for efficient wavelength broadening. Their material parameters, e.g. the tensile elastic modulus and the shear modulus, are only around 70% compared to silica and they exhibit hence much lower tensile and yield strength [154], which makes their handling more difficult. Some fluoride glasses, including ZBLAN, are chemically not resistant against water and must be surrounded by a polymer coating and stored and operated under dry environment. The water diffuses into the outer surface layers of the fiber, which worsens their mechanical parameters dramatically [155].

The material zirconium fluoride, on which the material ZBLAN is mostly based on, was first discovered from Poulain *et al.* in 1975 [156]. The first ZBLAN fiber was drawn in 1984 [152] and the first mid-IR SCG was demonstrated in 2006 [45]. These relatively late inventions prove that the research activity on mid-IR SCG in such fibers is still in its infancy with high potential in performance increase in the future.

Other fluoride materials, such as indium fluoride (InF_3), are also auspicious for SCG because of their broader transmission bandwidth, which could shift the LWE of the SC output radiation further into the IR. Their fiber manufacturing is not yet as mature as it is for ZBLAN fibers, thus, the SC output power levels are much lower. InF_3 fibers are at the advent of their development and the use for applications like SCG. Their glass parameters exhibit a higher fragility compared to ZBLAN and handling is more demanding. InF_3 fibers are already commercially available, but mainly for passive transmission fibers [9].

In the last chapter, the Tm^{3+}-doped pump fiber laser has been characterized in all different lasing regimes. In this chapter, the wavelength broadening via SCG in fluoride fibers is investigated while using the described Tm^{3+}-doped pump fiber laser in QML operation. The experimental setup used for the SC experiments is described with its characterization tools. The available fluoride fibers with their most important material parameters are specified in the third part of this chapter. The achieved results are separated dependent on the material of the nonlinear fiber. A summary in the end of this chapter presents a comparison of the achieved results with the reported experiments from the literature.

4.2 Experimental setup

The experimental setup for SC experiments is shown in Figure 4.1. The beam emitted by the Tm^{3+}-doped pump fiber laser is shaped for its characterization and preparation for coupling into the nonlinear fluoride fibers. Because of the usage of non-polarization maintaining active Tm^{3+}-doped fibers, a polarization stage, which consists of a half wave plate (HWP) and a thin-film polarizer (TFP), reflects one polarization of the beam for the characterization of the fiber laser and lets the other one transmit for pumping the nonlinear fiber. For optical isolation, a Faraday rotator (FR) is implemented to prevent the fiber laser from back-reflections of the system, which can damage the intracavity elements. The attenuation stage, which comprises a HWP and TFP, allows the adjustment of the pump power level for the fluoride fiber to operate the Tm^{3+}-doped fiber laser with constant parameters for stable operation. A zoom optic, realized by three AR-coated spherical silica lenses (L1-L3), changes the beam diameter of the pump beam for mode field adaption to the fluoride fiber. The pump radiation is coupled into the nonlinear fiber using an AR-coated aspheric silica lens with a FL of 15 mm (L4). For reaching highest coupling efficiencies, a six dimensional hexapod stage positions the end facet of the fluoride fiber with a linear/angular accuracy of 0.1 μm/2 μrad, respectively. An uncoated calcium fluoride (CaF_2) lens with a FL of 20 mm (L5) collimates the SC output radiation before the characterization stage. Different optical long wave pass (LWP) filters with 3 dB cut-off wavelengths around 2.15 μm, 2.65 μm, 3.1 μm and 3.5 μm can be implemented to analyze the SC radiation in certain wavelength regions. The average power of the SC output radiation is measured with a power meter. Its spectral power distribution is detected with spectro#1. At the output slit of the monochromator, a liquid-nitrogen cooled indium antimonide (InSb) detector is used, which is sensitive in the wavelength range between 1 μm and 5.5 μm. The detailed detectivity curve of this detector is shown in the appendix A. The measured signal

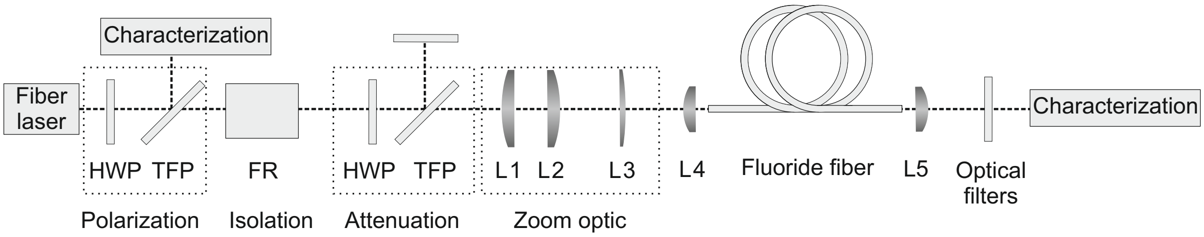

Figure 4.1: Setup for SC experiments with fluoride fibers pumped by the QML Tm^{3+}-doped fiber laser including polarization, isolation, attenuation, zoom optic, fluoride fiber, optical filters, lenses and characterization of the SC output radiation.

from the detector is processed by a preamplifier, a low-pass filter and a lock-in amplifier. For the delivery of the SC radiation to the spectrometer, a hollow-core fiber with an inner silver coating for TIR and a core diameter of 500 μm is available. The complete measurement system, including transport fiber, monochromator and detector, has been calibrated with a black body radiator, emitting at 1000 K. The calibration procedure with the results are described in the appendix A.

4.3 Materials

Three ZBLAN fibers and one InF_3 fiber are available. All of the fibers have a single-clad fiber design and the material composition among the ZBLAN fibers is the same, but the exact ratio from the vendor is confidential and not available. Figure 4.2 presents the specified material absorption for the two different fiber materials from the manufacturer. The material ZBLAN has a phonon energy of 600 cm^{-1} [105] and InF_3 of approximately 500 cm^{-1} [157] offering hence broader transmission bandwidth, but with higher absorption in the wavelength range between 1 μm and 3.8 μm. The high mid-IR absorption at the transmission edge of ZBLAN is mostly caused by the zirconium and aluminum ions in its composition [153]. OH impurities in soft-glass fibers have a significant influence on their mid-IR absorption, owing to the high water absorption in that wavelength range. Both available fibers exhibited an OH-caused absorption band at around 3 μm.

Table 4.1 summarizes the most important design parameters of the fibers. All of them had inner and outer cladding diameters of 125 μm and 250 μm, respectively. The ZBLAN fibers differed mostly regarding their core diameters (core ø) while the *NA* was constant, which has in consequence different cut-off wavelengths (λ_{co}). ZBLAN#1 exhibited single-mode propagation at the pump wavelength of around 2 μm, ZBLAN#2 and the InF_3 fiber offered the propagation of two transverse modes and for ZBLAN#3, four modes could propagate. The higher the number of modes at the pump wavelength are, the lower are the requirements for coupling the pump light into the fiber core. Furthermore, as a result of the different λ_{co}, the influence of waveguide dispersion varies resulting in different ZDWs. Taking the derivation from subsection 2.1.3, the dispersion of the fluoride fibers are shown in Figure 4.3, left, together with the related material

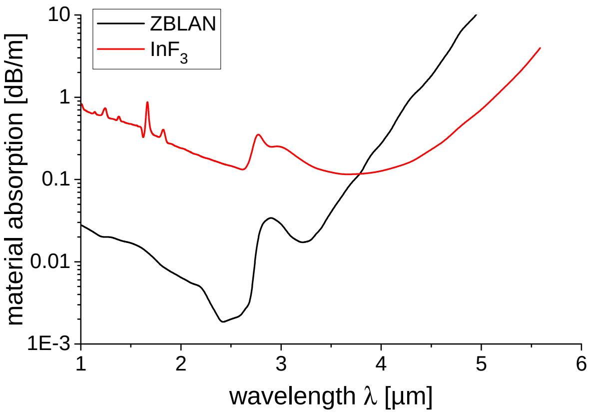

Figure 4.2: Material absorption of the available fluoride fibers.

Parameters	Core ø	*NA*	λ_{co}	ZDW	Clad$_{inn}$ ø	Clad$_{out}$ ø
ZBLAN#1	6.5 μm	0.23	1.95 μm	1.95 μm	125 μm	250 μm
ZBLAN#2	8.5 μm	0.23	2.6 μm	1.7 μm	125 μm	250 μm
ZBLAN#3	12 μm	0.23	3.6 μm	1.65 μm	125 μm	250 μm
InF$_3$	9 μm	0.26	3 μm	1.75 μm	125 μm	250 μm

Table 4.1: Different available fluoride fibers and their most important parameters.

dispersion of ZBLAN, calculated with the Sellmeier coefficients from [158]. The ZDW of the raw material ZBLAN lies around 1.63 μm, as it has also been specified in literature [154]. The dispersion data from the InF$_3$ fiber have been taken from the manufacturer [159]. The strong influence of the waveguide dispersion for ZBLAN#1 shifts its ZDW further towards the IR to 1.95 μm, whereas the other ZBLAN fibers have a ZDW close to that of the bulk material.

The cut-off wavelength of a fiber influences the trend of its *MFA* versus wavelength, as it is shown for all fluoride fibers in Figure 4.3, right. The *MFA* plays an enormous role regarding the efficiency of SCG, as explained in subsection 2.3.2. As mentioned before, also the flatness of the curve affects the wavelength conversion efficiency of the nonlinear effects involving two co-propagating waves. ZBLAN#1 exhibited a very fast increase of the *MFA* beyond a wavelength of around 3.5 μm, which might be the reason of the relatively short LWE of mid-IR SCG in single-mode ZBLAN fibers reported in literature [3, 15, 23, 94]. ZBLAN#3 and the InF$_3$ fiber exhibited the flattest trends of the *MFA* with relatively low values, especially for longer wavelengths, and are thus the most promising fibers in this respect.

The bend losses, introduced in subsection 2.1.5, are plotted in Figure 4.4, left. Hereby, a critical wavelength, λ_{crit}, is introduced at which the bend loss factor is 1 $\frac{dB}{m}$. Bend losses for ZBLAN#2, ZBLAN#3 and the InF$_3$ fiber can be neglected for SCG in the wavelength range between 2 μm and 4.5 μm for bending radii bigger than 0.1 m. However, for the investigation of ZBLAN#1, the bend losses have to be considered.

Based on subsection 2.3.2, the FOMs are calculated for all fluoride fibers with a length of 10 m, a bend radius of 12 cm, which is the radius of the spools the fibers are coiled on, and a nonlinear-index coefficient of 2.1×10^{-20} $\frac{m^2}{W}$ for ZBLAN [160]. The nonlinear-index coef-

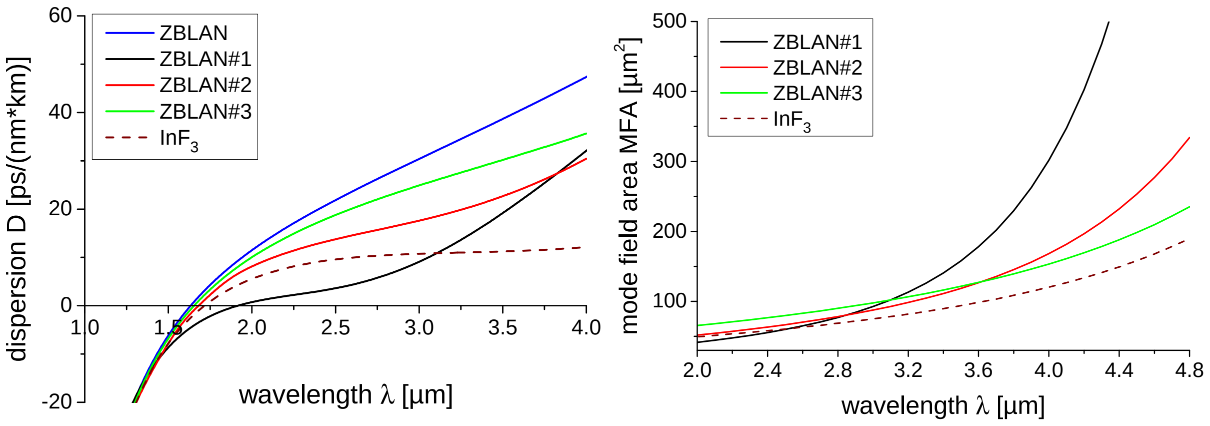

Figure 4.3: *Left*: Dispersion parameter of the fluoride fibers and the material ZBLAN against wavelength; *right*: Mode field area versus wavelength for the fluoride fibers.

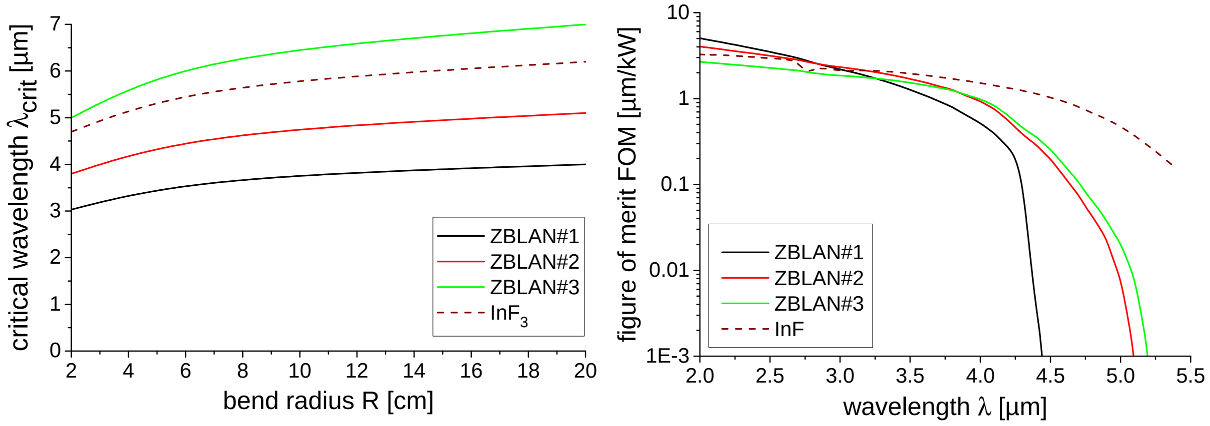

Figure 4.4: *Left*: Macrobending losses versus bend radius based on a critical wavelength exhibiting a bend loss factor of 1 $\frac{dB}{m}$; *right*: Figure of merit versus wavelength for all available fluoride fibers with a length of 10 m.

ficient of InF$_3$ has not been determined experimentally, so far [151]. It is assumed that it has the same nonlinearity as ZBLAN. The different graphs are shown in Figure 4.4, right. In terms of LWE, ZBLAN#2 and ZBLAN#3 offered comparable performance, whereas it has been expected that ZBLAN#1 exhibits a lower LWE of the SC output radiation. The InF$_3$ provided the most promising characteristics for wavelength conversion far into the IR owing to its broader transmission bandwidth and its relatively small MFA. Analyzing the intersections of the FOMs with the y-axis, it can be claimed that with the used fiber length, ZBLAN#1/ZBLAN#3 would have the lowest/highest SC threshold owing to their small/big mode field area at the pump wavelength, respectively.

ZBLAN#3 has been specially designed for enabling high power SCG. The larger mode field areas should enable higher damage thresholds regarding average output power. Furthermore, the flatter trend of the mode field area against wavelength should enhance the SC conversion efficiency. The resulting low bend losses simplifies the fiber handling and more compact systems can be realized owing to lower applicable bend radii.

4.4 Results

This section is separated into the presentation of the SC output performance of the ZBLAN fibers and the results obtained with the InF$_3$ fiber.

4.4.1 ZBLAN fibers

4.4.1.1 Evaluation of the SC output radiation

Figure 4.5 shows a typical result of a mid-IR SC experiment and how it is characterized at ISL. The left side displays the output power versus launched pump power for ZBLAN#3. During this experiment, the pump fiber laser has been operated at an output power level of 5 W with a QS repetition rate of 50 kHz. The different colored curves indicate the output power levels beyond the optical LWP filters, described in subsection 4.2. The output power

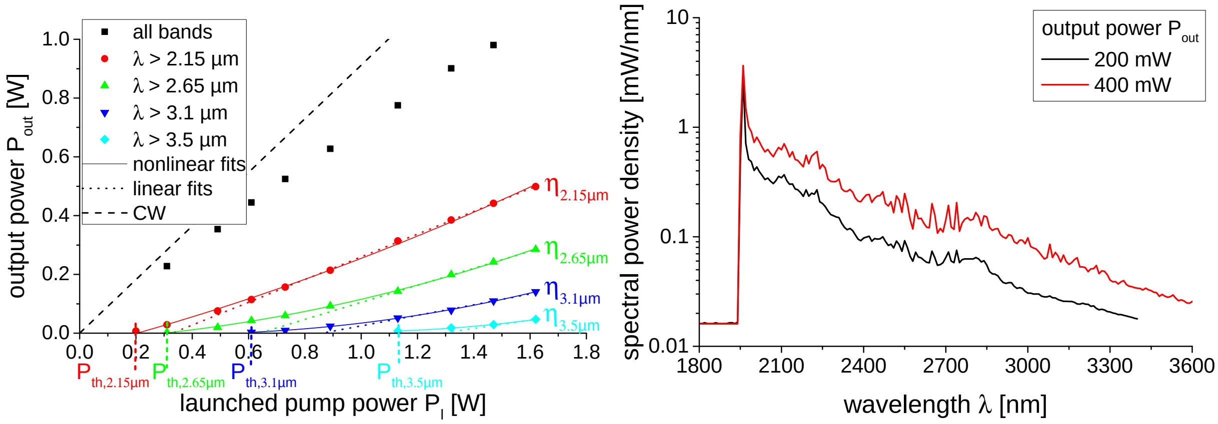

Figure 4.5: *Left*: Output power versus launched pump power beyond the optical LWP filters with the indication of their slope efficiencies and their threshold power levels; *right*: Output spectra for two different output power levels without an optical LWP filter before the spectrometer.

is always plotted against launched pump power, which allows the comparison of different nonlinear fibers with varying coupling efficiencies. The dashed line in the graph presents the expected output radiation, if the fiber would be pumped with a CW signal without wavelength conversion, considering the material absorption at 2 μm and the Fresnel reflections at the end facets of the fiber. If the curve for the output radiation in all spectral bands is observed, it indicates a rollover behavior. The reasons for this effect are higher material absorption of the mid-IR radiation and losses caused by nonlinear effects like RS or SSFS that transfer energy of the pump radiation to the material in the form of phonons. The power curves measured beyond the different optical LWP filters exhibit a nonlinear increase close to their threshold power, P_{th}, whereas for higher launched pump power levels, the curves can be fitted linearly with a corresponding slope efficiency η, which is inserted in the figure. The nonlinear trends of the curves close to their thresholds have already been demonstrated in another report in the literature [23]. The thresholds and the linear slope efficiencies, e.g. $P_{th,2.15\mu m}$ and $\eta_{2.15\mu m}$ beyond the optical LWP filter at 2.15 μm, are used as characterization parameters for the comparison of different SC output performances. In the described setup with a QML pump laser system, the SC output radiation is a superposition of the SC produced from each ML pulse below the QS envelope. Thus, in theory, the output power curves beyond the optical LWP filters should indicate different threshold power levels for the different ML subpulses, which has however not been observed during the experiments.

The right side of Figure 4.5 displays the SC output spectra for two different output power levels of 200 mW and 400 mW from ZBLAN#3 measured during the experiment presented on the left side of the figure. In this case, there has been no optical LWP filter included in the setup before the spectrometer. The spectra indicate broadening only towards the IR, which is typical for the pumping regime deep in the anomalous dispersion region of ZBLAN#3. In the following, all spectral measurements are performed with optical LWP filters in front of spectro#1 to prevent damages of the grating inside the monochromator and the detector at its output slit, because the spectral power density of the residual pump radiation at around 2 μm is much higher compared to the mid-IR SC radiation. Furthermore, the electronic amplification factor of the lock-in amplifier can be adapted to the mid-IR signal and not to the residual pump,

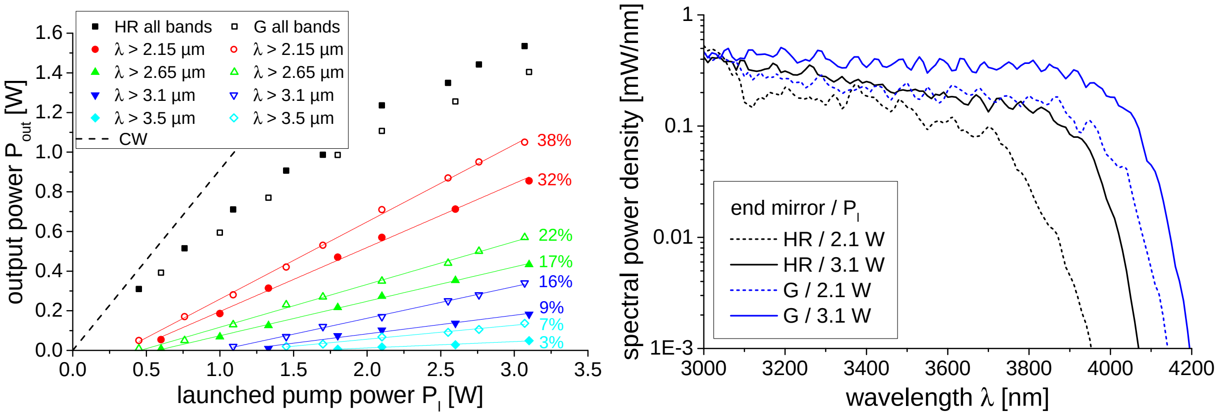

Figure 4.6: *Left*: Comparison of the SC output performance from ZBLAN#3 pumped by the Tm^{3+}-doped fiber laser with the diffraction grating and the HR mirror as cavity end mirror; *right*: Comparison of the SC output spectra for both cavity end mirrors in the pump laser at two different launched pump power levels beyond the optical LWP filter at 3.1 μm.

increasing the signal-to-noise ratio. For the shown experiment, the output power levels have been relatively low, thus, the insertion of an optical LWP filter has not been necessary.

4.4.1.2 Choice of the optimum Tm^{3+}-doped fiber length and cavity end mirror

For high power mid-IR SCG, the most promising Tm^{3+}-doped fiber for the pump laser system has been thulium#3 (2.2 m), because it provided the shortest QS envelopes. Thus, it was used in almost all experiments for pumping the fluorides fibers. SC experiments have also been performed with thulium#1 (8.8 m), but owing to the very long QS pulses, as shown in subsection 3.4.2, the SC conversion efficiency has been very low. To enable wavelength conversion, very high QS pulse energies have been necessary, leading to the damage of the ZBLAN fibers at very low launched pump power levels, because one damage mechanism in ZBLAN fibers is related to the pulse energy of the pump radiation [161]. Hence, mid-IR SCG with thulium#1 as pump laser has not been further investigated.

As mentioned at the end of the last chapter, the SC conversion efficiency has been lower when the HR mirror has been implemented as cavity end mirror compared to the performance achieved with the diffraction grating, which has been discovered by the comparison of the SC output performance while the fiber laser has been operated under similar conditions with both mirrors. The fiber laser with thulium#3 delivered in both cases an output power level of 10 W with a QS repetition rate of 100 kHz at a central wavelength at around 1.97 μm. The ML pulse duration with the HR mirror and the grating has been 200 fs and 20 ps, respectively, with the same width of the QS pulse of around 120 ns and its pedestals of 2.2 ns. The left side of Figure 4.6 shows the SC output power versus launched pump power for both pumping setups with the related slope efficiencies beyond the optical LWP filters. The SC output performance with the grating as cavity end mirror is superior concerning both, the threshold power levels and the slope efficiencies. Also the curve for the SC output radiation in all spectral bands with the diffraction grating as end mirror indicates also a stronger rollover behavior, which is caused by a more efficient wavelength conversion. Obviously, the ML pulse duration of the two experiments can be separated into short and long pulse pumping for SCG, as it has been described in subsection 2.3.1. The short pulses do not exhibit MI, thus, the wavelength broadening is less efficient [77]. But owing to the fact that most of the energy is contained within the pedestals, this explanation might not be the reason for the different SC output performance. The pedestals for both experiments had approximately the same energy, temporal width and peak power level. A possible explanation for this difference is the spectral power density of the input pump radiation, which is in the case of the diffraction grating as cavity end mirror much higher owing to the much narrower spectral linewidth of around 1.5 nm.

The right side of Figure 4.6 presents four SC output spectra beyond the optical LWP filter at 3.1 μm, two for each cavity design with the different end mirrors at a launched pump power level of 2.2 W and 3.1 W. The SC output spectra achieved from pumping the fluoride fiber with the HR mirror are narrower, as expected from the results shown on the left side of the figure. The reason for the different SC performance has to be further investigated more precisely.

4.4.1.3 Characterization of the SC output performance from the different ZBLAN fibers

As shown in Figure 3.14, the output characteristics of the ML subpulses below the QS envelope from the pump fiber laser are varying in terms of peak power and pulse energy level dependent on the operational parameters of the fiber laser. It plays hence an important role for mid-IR SCG how the pump source is operated before the pump power level for the fluoride fiber is adjusted by the optical attenuator. To characterize this dependency of the SC performance, the fiber laser with thulium#3 (2.2 m) has been operated at different output power levels and QS repetition rates at a constant wavelength of around 2 μm, adjusted by the diffraction grating, to pump ZBLAN#3 with a length of 36 m. For the comparison of the SC output performances, the threshold power levels and slope efficiencies beyond the optical LWP filters have been used. Each experiment has been performed at a certain QS output energy level with a corresponding pulse duration of the fiber laser and yielded eight values, four threshold power levels and four slope efficiencies.

The **comparison of the different thresholds** is displayed in Figure 4.7, left. Every dot in the graph stands for one resulting value from an experiment at a corresponding QS output pulse energy and duration of the fiber laser. For the comparison of the threshold behavior, the QS pulse energy at the threshold, E_{th}, is introduced by dividing the pump power level at the SC threshold by the QS repetition rate of the pump fiber laser,

$$E_{th} = \frac{P_{th}}{\Delta\nu_{QS}}, \tag{4.1}$$

which enables the comparison of experiments with different QS repetition rates.

The comparison of the thresholds indicates that independent of the QS output pulse energy and QS pulse width, the threshold QS energies for SCG are constant beyond all the used optical LWP filters. The thresholds for wavelength conversion beyond 2.15 μm/2.65 μm/3.1 μm/ 3.5 μm are in the range of 3 μJ-4.3 μJ/5.2 μJ-7 μJ/8.3 μJ-10.8 μJ/12 μJ-14.8 μJ, respectively. This constant dependency is very remarkable, because, as evidently demonstrated by the second x-axis, the QS pulse duration decreases. A shorter QS pulse contains less ML subpulses

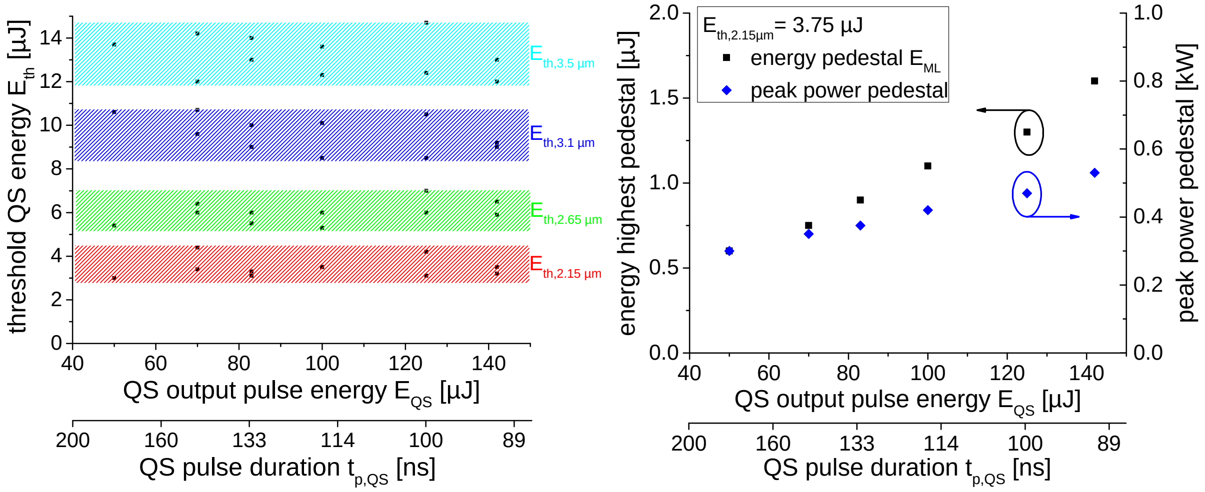

Figure 4.7: *Left*: Comparison of SC performances regarding their threshold behavior for different QS output pulse energies from the pump fiber laser; *right*: Energy and peak power level of the most-energetic pedestal at the QS energy threshold of 3.75 μJ beyond the optical LWP filter at 2.15 μm versus QS output energy and pulse duration of the fiber laser.

below it resulting in a higher pulse energy and peak power level of the most-energetic pedestal. The right side of Figure 4.7 illustrates the peak power and energy of the most-energetic pedestal at the threshold QS energy of 3.75 μJ beyond the optical LWP filter at 2.15 μm dependent on the QS output pulse energy of the pump fiber laser. The peak power and energy levels have not been constant at the SC thresholds for the different performed experiments. Therefore, it seems that the threshold behavior of the SC process is not triggered by the pedestals. The initiation of the SC process is apparently induced by the short peaks on top of the pedestals. The same observations, as shown in Figure 4.7, has been obtained by using the HR mirror as cavity end mirror. The threshold QS energies beyond the optical LWP filters have always been constant versus the QS output pulse energy of the fiber laser. Hence, a possible influence of the cavity end mirror can be excluded.

Another experiment to verify the discovered observations regarding the constant threshold QS energy have been performed by changing the modulation depth of the AOM for ML and comparing the resulting threshold power levels. If the modulation depth of the modulator is decreased, the width of the pedestals increases, as it has been shown in Figure 3.15. At the same time, the energy distribution among the ML subpulses below the QS envelope is constant. Therefore, the peak power level of the pedestal decreases while their pulse energy is constant. Also during this variation, the SC thresholds regarding the QS pulse energy have been constant. Owing to the uncertainty of the peak power levels of the short pulses on top of the pedestals, the reason for the constant threshold QS energy could not yet be derived theoretically. Further investigations on the determination of their exact peak power levels are necessary to further understand this phenomenon.

The **comparison of the slope efficiencies** from the different performed experiments is shown in Figure 4.8. The efficiencies are, different to the thresholds, dependent on the QS output energy of the fiber laser. The higher it is, the more efficient is the wavelength conversion process during SCG. This dependency is reasonable because of the increasing energy and peak

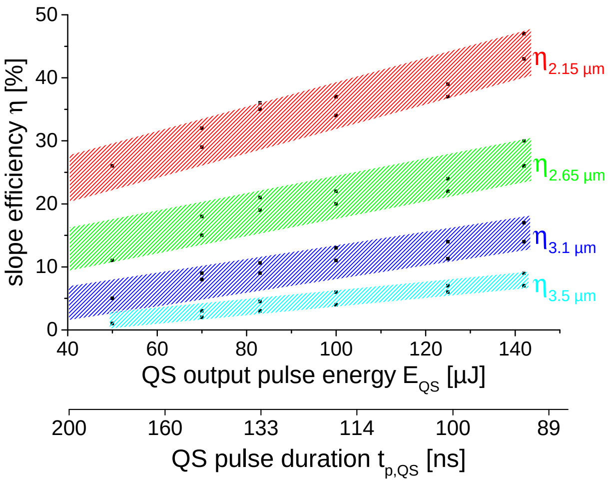

Figure 4.8: Comparison of SC performances regarding their slope efficiencies for different QS output pulse energies and corresponding pulse durations of the pump fiber laser.

power level of the pedestal when the QS output pulse energy grows with a shorter QS envelope as consequence. The pedestal energy and peak power level influence the slope efficiencies but not the thresholds for SCG. Thus it can be stated that the short peak on top of the pedestals initiate the SCG, which once started, converts the energy stored in the pedestals.

During the experiments for the comparison of the SC output performance, shown above, it has been observed that the ratios of the different slope efficiencies, e.g. $\frac{\eta_{2.15\mu m}}{\eta_{3.1\mu m}}$, are always constant for one nonlinear fiber with a constant length, independent at which QS output pulse energy the fiber laser is operated with.

For the investigation of the **influence of the pump wavelength on mid-IR SCG**, the fiber laser has been operated with the same output parameters at different lasing wavelengths for SC experiments. The results demonstrated that the pump wavelength does not play a significant role regarding threshold behavior and slope efficiencies because of the relatively "low" tunability of the fiber laser compared to the difference of the lasing wavelength to the ZDW of ZBLAN#3, which is around 1.65 μm. This behavior has already been demonstrated in other SC experiments in literature [77].

A **comparison of many different performed SC experiments** with all available ZBLAN fibers with different lengths regarding threshold behavior and slope efficiencies is presented in Table 4.2, where the SC thresholds are listed in terms of pump fluence,

$$F_{th} = \frac{E_{th}}{MFA(2\ \mu m)}, \tag{4.2}$$

to compare ZBLAN fibers with different MFA at the pump wavelength of 2 μm. As it has been demonstrated, the slope efficiencies are changing dependent on the QS output pulse energy of the fiber laser, therefore, the experiments in the table have been performed at a fixed QS output pulse energy of approximately 140 μJ to ensure comparable results. ZBLAN#1 had a length of 8 m, ZBLAN#2 of 5 m, 9 m and 16 m, and ZBLAN#3 of 36 m for the presented results.

For ZBLAN#1 with the length of 8 m, the threshold fluences are comparable to the ones for ZBLAN#2 with 9 m owing to the approximately same fiber length and a similar trend

Parameters	$F_{th,2.15\mu m}$	$F_{th,2.65\mu m}$	$F_{th,3.1\mu m}$	$F_{th,3.5\mu m}$	$\eta_{2.1\mu m}$	$\eta_{2.65\mu m}$	$\eta_{3.1\mu m}$	$\eta_{3.5\mu m}$
ZBLAN#1, 8 m	$120\ \frac{nJ}{\mu m^2}$	$180\ \frac{nJ}{\mu m^2}$	$330\ \frac{nJ}{\mu m^2}$	$620\ \frac{nJ}{\mu m^2}$	36%	21%	13%	6%
ZBLAN#2, 5 m	$160\ \frac{nJ}{\mu m^2}$	$250\ \frac{nJ}{\mu m^2}$	$470\ \frac{nJ}{\mu m^2}$	$720\ \frac{nJ}{\mu m^2}$	30%	15%	8%	1.2%
ZBLAN#2, 9 m	$110\ \frac{nJ}{\mu m^2}$	$170\ \frac{nJ}{\mu m^2}$	$320\ \frac{nJ}{\mu m^2}$	$530\ \frac{nJ}{\mu m^2}$	36%	22%	16%	10%
ZBLAN#2, 16 m	$80\ \frac{nJ}{\mu m^2}$	$140\ \frac{nJ}{\mu m^2}$	$290\ \frac{nJ}{\mu m^2}$	$460\ \frac{nJ}{\mu m^2}$	38%	26%	20%	13%
ZBLAN#3, 36 m	$40\ \frac{nJ}{\mu m^2}$	$70\ \frac{nJ}{\mu m^2}$	$110\ \frac{nJ}{\mu m^2}$	$140\ \frac{nJ}{\mu m^2}$	40%	26%	14%	7%

Table 4.2: Summary of the SC output performance of the available ZBLAN fibers with different fiber lengths.

of the MFA, at least beyond the optical LWP filters at 2.15 μm, 2.65 μm and 3.1 μm. The threshold and the slope efficiency regarding the wavelength conversion beyond 3.5 μm are much different, which is probably caused by the fast increase of the MFA in that wavelength range for ZBLAN#1.

The comparison of the results for ZBLAN#2 with different fiber lengths proofs that the threshold behavior is dependent on the length of the ZBLAN fiber with constant core diameter and NA. The slope efficiencies are also increasing against fiber length. However, it is assumed that this relation is limited and the slope efficiencies are decreasing after a certain fiber length, because the influence of the material absorption becomes too high. The wavelength broadening exhibits a saturation-like behavior, as it has already been explained in subsection 2.3.2. This effect can be observed by regarding the results of ZBLAN#3 with a length of 36 m. The threshold fluences are very low, as it has been predicted by the calculation of the FOM. But the slope efficiencies for the wavelength conversion beyond 3.1 μm and 3.5 μm are smaller compared to ZBLAN#2 with 16 m. There is an optimum length of a nonlinear fiber, which is defined by the requirements of the SC output radiation and pump parameters. The empiric determination of this optimal length will not be conducted for the available ZBLAN fibers. This evaluation would only be possible with ZBLAN#2, which has been investigated with three different fiber lengths. More experiments with different fiber lengths would be necessary to determine this optimum length. Furthermore, it depends on the pump pulse parameters, e.g. energy and peak power levels of the pulses, which will be further improved regarding SC conversion efficiency in the near future. From all the three investigated fiber lengths of ZBLAN#2, 16 m offered the best potential for efficient wavelength broadening. During the experiments with the different fiber lengths for ZBLAN#2, a general dependency has been found out that the ratios of the thresholds for the same ZBLAN fiber, e.g. $\frac{F_{th,2.15\mu m}}{F_{th,3.1\mu m}}$, are always constant, independent of the fiber length. These ratios are probably influenced by the fiber design, meaning its core diameter and NA.

ZBLAN#2 and ZBLAN#3 offered multi-mode propagation at the pump wavelength of 2 μm. Thus, it has been analyzed how the **pump power distribution onto the different transverse propagation modes** of the ZBLAN fiber affects the SC conversion efficiency. In the described experiments in this chapter, it has always been tried to couple most of the light into the fundamental transverse mode of the fiber. First, for achieving good beam quality of the SC output radiation and second, for increasing the wavelength conversion efficiency. Beyond the cut-off wavelength of the ZBLAN fibers, the guided radiation is single-mode and the overlap between two guided modes is superior, if they have the same transverse intensity profile. Additionally,

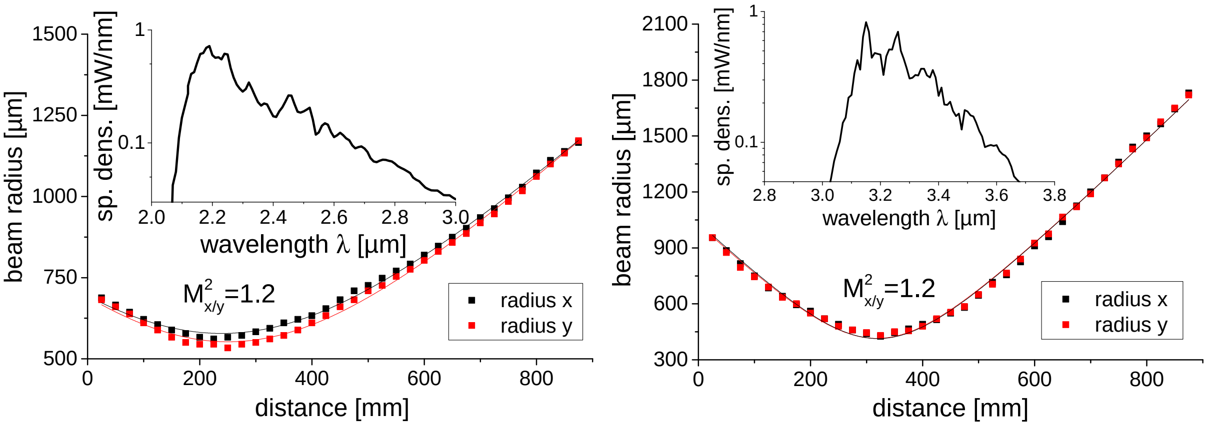

Figure 4.9: M^2 measurements of SC output radiation beyond the optical LPW filters at 2.15 μm (*left*) and 3.1 μm (*right*) in both directions; *insets*: Corresponding SC output spectra for the measurements.

the *MFA* of higher-order modes is bigger, decreasing the optical intensity and hence the conversion efficiency. If ZBLAN#3 is pumped by exciting mostly transverse higher-order modes, which has been forced by the angular rotation of the fiber input facet, the SC efficiency dropped about a factor of two, which has been similarly reported in [16].

Owing to the mentioned high cut-off wavelengths of the used ZBLAN fibers, especially for ZBLAN#3, and therefore multiple number of possible transverse propagation modes that influence the beam quality of the radiation, **M^2 measurements of the SC output radiation** have been performed beyond the optical LWP filter at 2.15 μm (*left*) and 3.1 μm (*right*), see Figure 4.9. The SC output spectra during these experiments are displayed in the insets of the two graphs. The measurement resulted in M^2 values of 1.2 in both directions, if the central wavelength of the spectra is used for the calculation. The good beam quality might result from the mentioned coupling mostly into the fundamental mode of the fiber.

4.4.1.4 High power experiments

With all three ZBLAN fiber designs, high average power experiments have been performed. For the choice of the right output parameters of the fiber laser, it has to be considered that the QS pulse energy cannot be too high to prevent damage of the ZBLAN fiber. On the other hand, the SC efficiency is dependent on the QS output pulse energy of the fiber laser, which is therefore a trade-off.

Figure 4.10 displays the results for high power SCG in **ZBLAN#1** with a fiber length of 8 m. The pump fiber laser has been operated at an output power level of 20 W with a QS repetition rate of 150 kHz, resulting in a QS output pulse energy of 133 μJ. The left side of the figure shows the output power versus launched pump power, which yielded a maximum output power in all spectral bands of 5.1 W at a launched pump power level of 8.3 W. The coupling efficiency during this experiment has been around 65%. A total average output power of 2.9 W/1.6 W/0.9 W/0.28 W has been obtained beyond the optical LWP filters resulting in a slope efficiency of 38%/23%/14%/6%, respectively. Regarding the overall conversion efficiency from the transmitted radiation in all spectral bands towards the

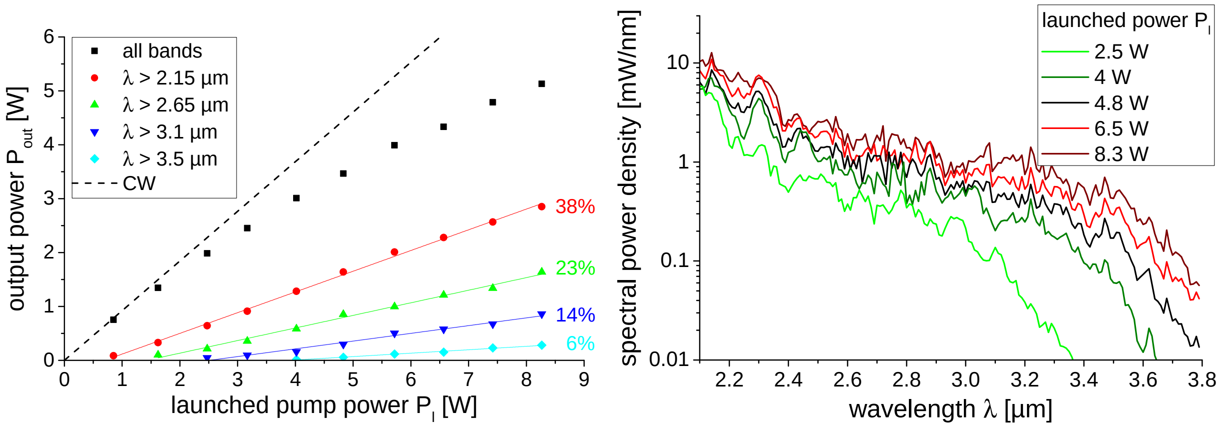

Figure 4.10: *Left*: Output power against launched pump power for SCG in ZBLAN#1 beyond the optical LWP filters with slope efficiencies; *right*: Output spectra for different launched pump power levels from ZBLAN#1 measured beyond the optical LWP filter at 2.15 μm.

mid-IR wavelengths range, 56%/31%/18%/5% have been converted to wavelengths beyond 2.15 μm/2.65 μm/3.1 μm/3.5 μm, respectively. Therefore, at least 56% of the output power has been transferred to higher wavelengths during SCG, neglecting the power content between 2 μm and 2.15 μm, which is cut out by the optical LWP filter. Owing to the fact, that many ML subpulses are involved during the SC process, it is assumed that the most-energetic ML pulse under the QS envelope would enable much higher slope efficiencies.

The right side of Figure 4.10 presents the absolute spectral power distribution of the SC output radiation for different launched pump power levels beyond the optical LWP filter at 2.15 μm. As expected, the higher the launched pump power has been, the broader was the output spectrum and the higher was the LWE of the SC radiation. The wavelength conversion towards the mid-IR has been limited at around 3.8 μm, measured at the -20 dB intensity level of the spectrum. The spectral power distribution at the highest output power declined from around 10 $\frac{mW}{nm}$ at 2.1 μm to 0.4 $\frac{mW}{nm}$ at 3.6 μm. The bend radius of ZBLAN#1 during this experiment has been around 12 cm, which relates to a bend loss factor of 0.9 $\frac{dB}{m}$ at 3.8 μm. The absorption of the fiber at that wavelength is only around 0.2 $\frac{dB}{m}$, which indicates a limitation of conversion caused by bend losses during this SC experiment. The power scaling with ZBLAN#1 has been limited by material impurities, which caused additional local absorption along the fiber. At the highest launched pump power level of 8.3 W, the fiber material melted at the location of these impurities along the fiber. Further power scaling with that fiber design has therefore not been possible.

For **ZBLAN#2**, the high power experiment has been conducted with a fiber length of 16 m. The pump fiber laser has been operated at an output power level of 15 W and a QS repetition rate of 100 kHz resulting in a QS output energy of approximately 150 μJ. The results are displayed in Figure 4.11. The highest output power level in all spectral bands has been 2.3 W with 1.6 W/1 W/0.7 W/0.38 W beyond the optical LWP filters yielding a slope efficiency of 36%/26%/21%/14%, respectively. The coupling efficiency into this fiber has been in the range of 90%, owing to the multi-mode nature at the pump wavelength of around 2 μm.

The right side of the figure shows the SC output spectra for different launched pump power levels. The highest LWE of ZBLAN#2 has been around 4.15 μm at the -20 dB intensity level.

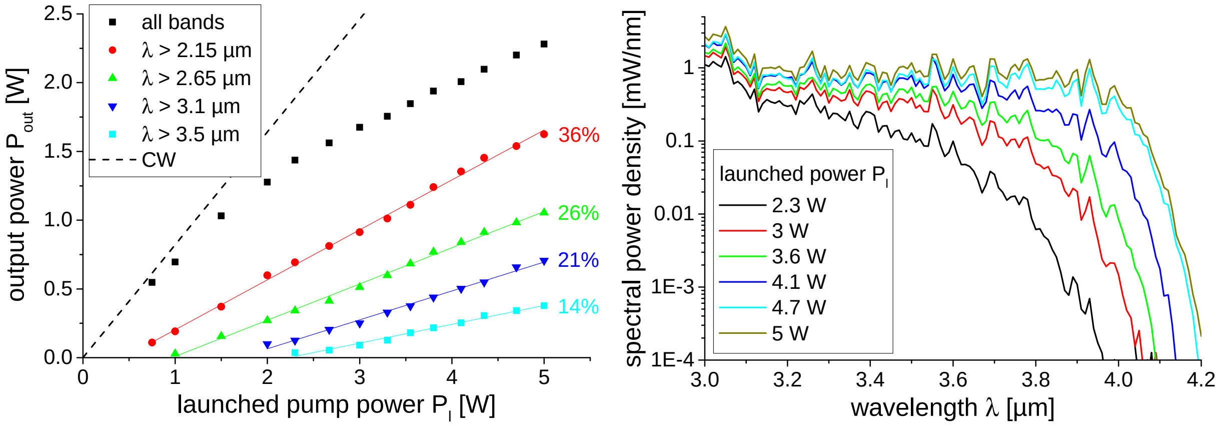

Figure 4.11: *Left*: Output power against launched pump power for SCG in ZBLAN#2 beyond the optical LWP filters with slope efficiencies; *right*: Output spectra for different launched pump power levels from ZBLAN#2 measured beyond the optical LWP filter at 3.1 μm.

The spectral power distribution at the highest output power level is roughly constant at 1 $\frac{mW}{nm}$ in the wavelength range between at 3.1 μm and 4 μm. The bend radius of the fiber during this experiment has also been 12 cm and bend losses can be neglected. The limitation with this fiber in terms of power scaling has also been impurities in the fiber, which caused fiber damage at the highest launched pump power of 5 W.

For **ZBLAN#3**, the length of 36 m has been used for high power SCG, which has been pumped when the fiber laser was operated with a QS output pulse energy of 65 μJ. The results are displayed in Figure 4.12, left. In total, 7.8 W have been reached with 4 W/2.1 W/1.2 W/0.4 W beyond the optical LWP filters leading to slope efficiencies of 29%/17%/9%/4%, respectively. The coupling efficiency has been around 90%, as for ZBLAN#2. A plot of the output spectrum at the highest output power beyond the optical LWP filter at 2.65 μm is displayed in Figure 4.12, right. The spectral power distribution is decreasing from approximately 3 $\frac{mW}{nm}$ at 2.9 μm to around 0.6 $\frac{mW}{nm}$ at 4 μm. In this experiment, the LWE at the -20 dB spectral intensity

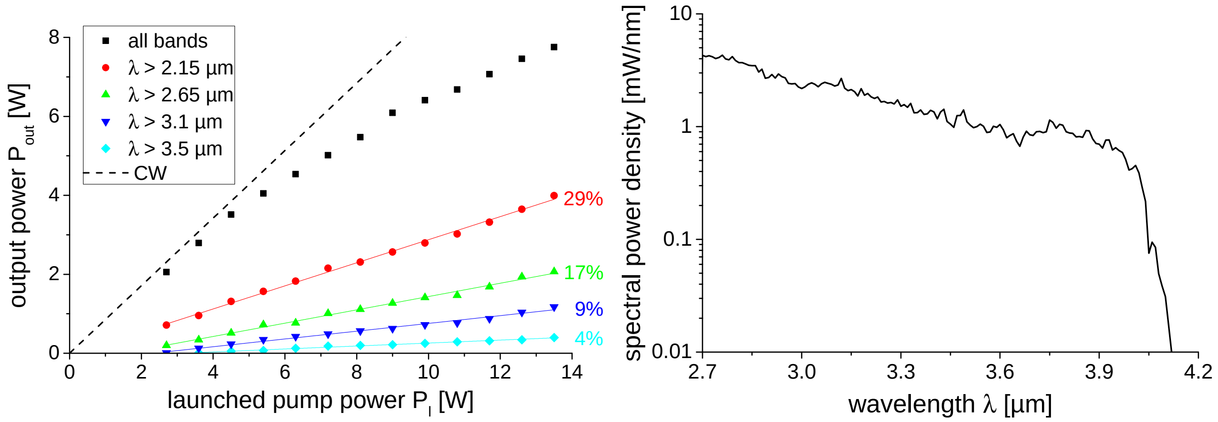

Figure 4.12: *Left*: Output power against launched pump power for ZBLAN#3 pumped by the fiber laser with a QS output pulse energy of around 65 μJ; *right*: Output spectrum at the highest output power level, measured behind the optical LWP filter at 2.65 μm.

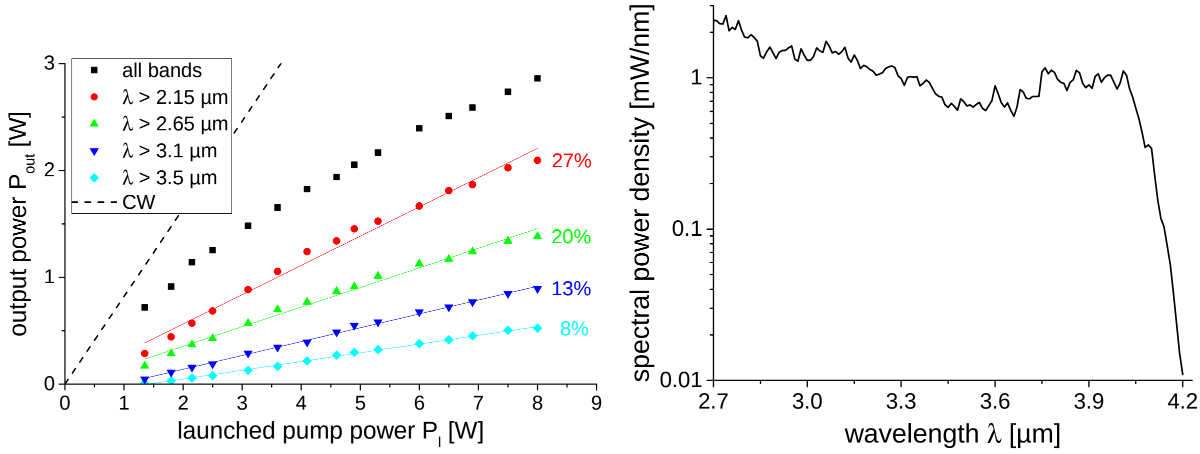

Figure 4.13: *Left*: Output power against launched pump power for ZBLAN#3 pumped by the fiber laser with a QS output pulse energy of around 130 μJ; *right*: Output spectrum at the highest output power level, measured behind the optical LWP filter at 2.65 μm.

level has been around 4.1 μm. The limitation for power scaling with this fiber has not been impurities, but the destruction of the fiber end facet. The reason might be water absorption. Because of the mentioned hygroscopic nature of this type of fluoride glass, the water diffuses through the end facets into the fiber. Once the average output power in the mid-IR wavelength range, where the water absorption is the strongest, becomes too high, the temperature of the fiber increases rapidly and the fiber end facet melts. This effect has already been studied in the scope of Er^{3+}-doped ZBLAN fiber lasers, emitting close to the absorption peak of water around 3 μm [162]. Owing to this limitation, the QS output energy of the pump fiber laser for the high power experiment with ZBLAN#3 has been lower compared to the experiments with ZBLAN#1 and ZBLAN#2. As a result, the efficiency of the SC process and thus the power included in the mid-IR wavelength range is decreased to prevent damaging of the fiber end facet to reach higher output power levels in all spectral bands.

Figure 4.13 displays the results achieved with ZBLAN#3 when the fiber laser has been operated with a QS output energy in the range of 130 μJ. 2.9 W in all spectral bands have been reached with 2.1 W/1.5 W/0.9 W/0.5 W beyond the optical LWP filters with slope efficiencies of 27%/20%/13%/8%, respectively. During this experiment, 69%/43%/30%/16.5% of the transmitted SC output radiation in all spectral bands have been converted beyond the wavelength of 2.15μm/2.65μm/3.1μm/3.5μm, respectively. The slope efficiencies are lower compared to the stated ones in Table 4.2. If the curves beyond the optical LWP filters at 2.15 μm and 2.65 μm are regarded, they exhibit a rollover behavior, probably caused by material absorption. The higher the launched pump power is, the more light is converted into spectral regions with stronger material absorption. If only the first measurement values behind the filters are observed, their slope efficiencies are close to the ones stated in the table. The limiting factor in terms of output power scaling during this experiment has also been the damage of the fiber end facet.

The spectrum at the highest output power level with a LWE of around 4.2 μm is displayed on the right side of Figure 4.13. The spectral power distribution is roughly constant at around 0.9 $\frac{mW}{nm}$ between 3.6 μm and 4 μm. It is expected that the LWE might red-shift slightly if the

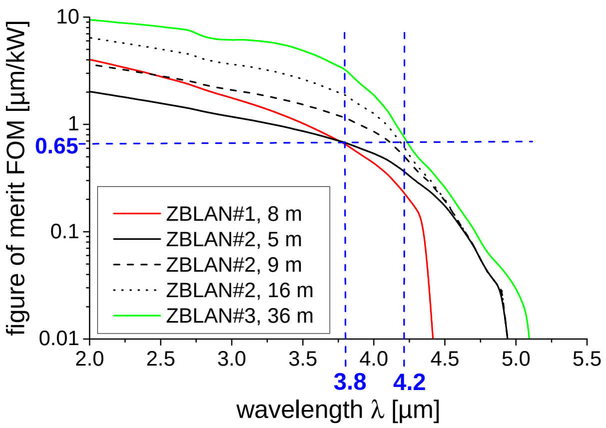

Figure 4.14: Figure of merit for all investigated ZBLAN fibers with corresponding fiber lengths and the indication of their LWE.

optimum fiber length for ZBLAN#3 would be used. But regarding the fast increasing material absorption at wavelengths beyond 4 μm, significant changes of the LWE will probably not be possible.

Figure 4.14 displays the **evaluation of the SC output performances based on their FOMs** for the three different ZBLAN fiber designs, including the results summarized in Table 4.2 and the high power experiments. The intersections of the FOMs with the y-axis exhibited approximately the SC threshold behavior obtained during the experiments. As explained in the subsection 2.3.2, a horizontal line can be used for estimating the LWE of the SC output radiation. For all of the performed experiments, where the LWE has been experimentally determined, it seems that a value on the y-axis of approximately 0.65 $\frac{\mu m}{kW}$ is in good agreement for the used QML source. As already explained in subsection 2.3.2, the absolute values of the FOMs cannot be used for evaluating the SC performance of the fibers. A further increase of the fiber length does not automatically shift the LWE towards the IR and is rather disadvantageous because of the stronger material absorption. An optimization of the pump pulses is necessary for further wavelength-conversion deeper into the IR.

The main goal regarding the SC output performance of the ZBLAN fibers is, as mentioned among others, high average output power. For the output power levels achieved with the ZBLAN fibers in the demonstrated experiments, the temperature of the uncooled ZBLAN fibers has to be considered. For that purpose, a **simulation of the temperature** for an uncooled ZBLAN fiber has been performed with the modeling software COMSOL [163]. A heat load of the fiber of 1 $\frac{W}{m}$ has been used with a thermal conductivity of 0.6 $\frac{W}{mK}$, a heat capacity of 0.15 $\frac{J}{gK}$ and a density of 4.5 $\frac{g}{cm^3}$ for ZBLAN. The data have been taken from a commercial manufacturer of ZBLAN fibers [164]. The heat load has been defined by considering the transferred power in relation to the launched pump power in the case of high conversion efficiency, which is roughly 50%. As an example, this assumption holds valid if a 10 m long fiber is pumped with a launched power of 20 W and a SC output power of 10 W, which is more than demonstrated, so far. For the simulation, the plastic layer had a conductivity of 0.2 $\frac{W}{mK}$, a heat capacity of 0.15 $\frac{J}{gK}$, a density of 1.1 $\frac{g}{cm^3}$ and an emissivity of 0.9. It is not published which plastic the manufacturer is using for the outer coating. The used data are mean values of different plastic materials to roughly evaluate the temperature of the fiber during mid-IR SCG.

For the heat extraction in the simulation, only convection is considered. The output of the simulation yielded a temperature of the fiber core and the surrounding plastic of around 70°C and 67°C, respectively. The melting temperature of ZBLAN is around 265 °C [164], therefore, the plastic will melt first. But owing to the uncertainty of the used plastic for the outer coating of the ZBLAN fiber, a limit regarding heat load cannot be defined. For the experiments shown in this thesis, the temperature has not been a limiting factor. But for further power scaling, a cooling technique must be probably implemented. In literature, it has been stated that a standard uncooled ZBLAN fiber can withstand around 15 W of average power, after that, cooling must be applied [153].

4.4.2 Indium fluoride fibers

For mid-IR SCG experiments with the InF$_3$ fiber, the Tm^{3+}-doped fiber laser has been operated at an output power level of approximately 10 W and a QS repetition rate of 100 kHz with thulium#3 resulting in a QS output energy of 100 μJ. The output power versus launched pump power for this experiment with a fiber length of 16 m is shown in Figure 4.15, left.

In total, a SC output power level in all spectral bands of around 0.8 W has been achieved at a launched pump power of 3 W. The slope efficiency of the output power against launched pump power beyond the optical LWP filters at 2.15 μm and 2.65 μm have been 7% and 3% with an output power level of 0.18 W and 0.08 W, respectively. The coupling efficiency of this experiment is expected to be very efficient owing to the multi-mode nature of the fiber at the pump wavelength. According to the material absorption from the manufacturer, the absorption at the pump wavelength of 2 μm is around 0.2 $\frac{dB}{m}$, see Figure 4.2, which leads to an absorption of 70% of the pump radiation for that fiber length. The transmitted power in CW has been measured to be in the range of 25%, yielding a coupling efficiency of around 90%, as it has been for the mutli-mode ZBLAN fibers. The limitation in terms of power scaling is set by fiber damage owing to impurities incorporated in the fiber. The SC output spectra are shown in Figure 4.15, right, for two launched pump power levels. The LWE edge at the -20 dB intensity level of the broadest output spectrum has been around 2.95 μm.

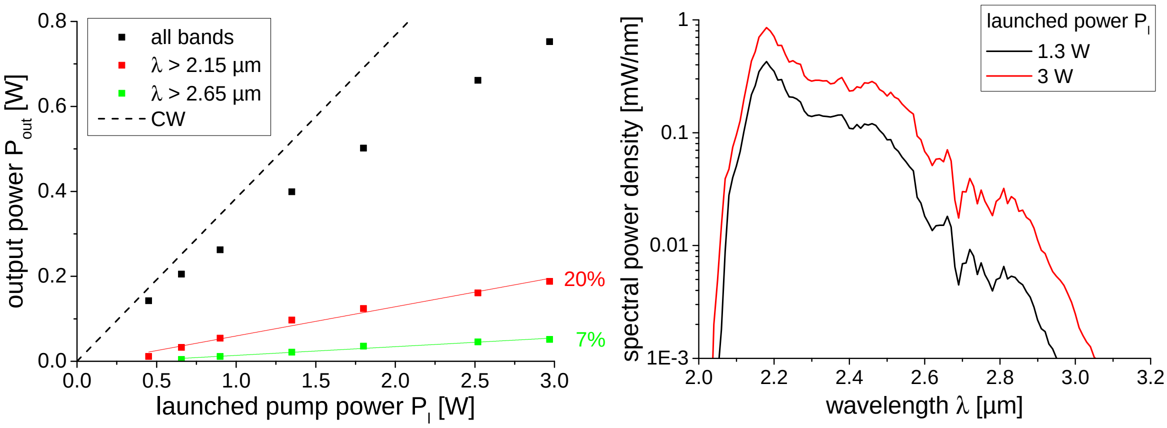

Figure 4.15: *Left*: Output power versus launched pump power beyond different optical LWP filters in the InF$_3$ fiber; *right*: Output spectra for two different launched pump power levels.

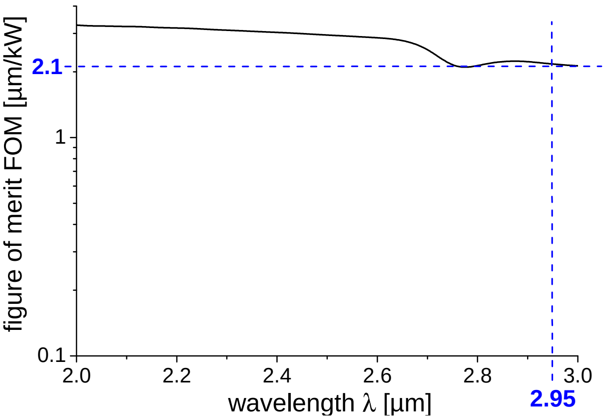

Figure 4.16: Figure of merit of the InF_3 fiber with horizontal line for the indication of its LWE.

Regarding the FOM for the InF_3 fiber, shown in Figure 4.16, the horizontal line crosses the y-axis at a value of approximately 2.1 $\frac{\mu m}{kW}$ for the achieved LWE. Compared to the performance with the ZBLAN fibers, where comparable pump pulses have been used, this value is about a factor of three higher. The reason for this mismatch must be the used parameters for the calculation of the FOM for the InF_3 fiber. The material absorption in the mid-IR wavelength region might be higher than the stated one from the manufacturer. Furthermore, it has been estimated that the nonlinear-index coefficient for InF_3 is the same than for ZBLAN. If the nonlinearity of the fiber is decreased by the same factor of three, the LWE fits with the intersection of the FOMs for ZBLAN fibers at around 0.65 $\frac{\mu m}{kW}$.

4.5 Summary

The highest achieved mid-IR SC output power level in all spectral bands has been 7.8 W after SCG in ZBLAN#3. Further power scaling with this ZBLAN fiber has not been possible because of damage limitation of the fiber end facet, probably caused by water diffusion into the fiber. The highest reported SC output power level in literature from a ZBLAN fiber after mid-IR SCG has been 22 W [31]. In this experiment, the ZBLAN fiber had a cut-off wavelength at 2.4 μm. The efficiency of the SCG from this experiment has not been detected owing to the lack of optical LWP filters. The LWE of the SC output spectrum has been around 3.8 μm. In this report, the limitation regarding the damage of the fiber end facet has not been addressed. There are also no solutions mentioned to bypass this problem, e.g. with end caps out of a different fluoride material that is chemically more stable, or dry-environment conditions around the fiber end facet. There are additionally two reported experiments in literature, which demonstrated higher output power levels. 13 W [165] and 10.5 W [33] have been reached, both with the technique of end caps at the output end facet of the ZBLAN fiber to prevent the described damage mechanism.

In the experiments described in this chapter, the broadest achieved SC output spectrum extended to 4.2 μm, measured at the -20 dB spectral power density level. It is expected that an increase of pump power and the use of an optimized fiber length for ZBLAN#3 shifts the LWE of the output spectrum slightly, as mentioned. The ZBLAN fiber have been pumped with high pulse energies and pump power levels and the output spectra indicated already a saturation in terms of LWE against pump power. Thus, with the increase in pump and peak power, a significant further broadening might be limited.

The broadest reported output spectrum from a ZBLAN fiber, pumped within the long pumping scheme for SCG, extended to a wavelength of 4.5 μm [166]. In [165], a SC output radiation up to 4.3 μm has been stated, but measured at the -20 dB spectral intensity limit, the LWE has been definitely lower than the one from this thesis. The reason for the broader output spectrum in [166] must be the material itself, rather its mid-IR absorption or its nonlinearity. A considerable further broadening of the output spectrum into the IR after SCG can be achieved by pumping it with ultra-short pulses with very high peak power levels and using only very short ZBLAN fibers in the range of centimeters [167]. Of course with this alternative, high average output power operation is very challenging and a trade-off has to be found between average output power and the LWE of the output spectra.

The achieved conversion efficiencies in this thesis have been defined as the slope of the output power beyond the optical LWE filters versus the launched pump power. In literature, usually, the ratio of the output power beyond the filters to the output power level in all spectral bands is used to evaluate the SC efficiency. Using this definition regarding the experiment with ZBLAN#3 at a QS output pulse energy of 130 μJ, which resulted in a total SC output power in all spectra bands of 2.9 W with 2.1 W/1.5 W/0.9 W/0.5 W beyond the optical LWP filter (see Figure 4.13), in total 69%/43%/30%/16.5% of the transmitted SC output radiation in all spectral bands have been converted beyond the wavelength of 2.15μm/2.65μm/3.1μm/3.5μm, respectively.

It is very difficult to compare the achieved efficiency with results reported in the literature because of the different pump laser systems. There are no reports with QML laser systems for the application of pumping a nonlinear medium for mid-IR SCG, which would allow a direct comparison. In literature, Er^{3+}- and Tm^{3+}-doped fiber laser systems have been almost exclusively used for high power mid-IR SCG. The pulse generating method varies from distributed feedback laser diodes with pulse durations around 1 ns [3, 33] to passively ML fiber lasers with pulse widths in the range of picoseconds [31, 165], whose pulses are then further amplified. In all of the reported pump laser systems, the SC is generated by pulse trains with almost identical pulses. In the setup described in this thesis, the SC output radiation is a superposition of the different spectra generated by all ML subpulses. The pulses at the temporal edges of the QS envelope are less energetic and intense than the ones close to the QS peak, making the overall SC efficiency lower. Therefore, if the highest ML pulse would be used solely for pumping the ZBLAN fiber, much higher conversion efficiencies would be feasible. Another reason that makes the comparison of the described results complicated is the non-optimized lengths of ZBLAN fibers.

Generally, a pumping scheme with pulse widths in the range of nanoseconds offers higher SC efficiencies compared to amplified ML pump laser systems. With amplified nanosecond pulses, it has been demonstrated that as much as 27% of the transmitted radiation has been converted beyond the wavelength of 3.8 μm, which is the most efficient SCG towards that wavelength range [166]. In another report with approximately the same pulse width, an efficiency of 60% beyond the wavelength of 3 μm has been obtained [23], which is also an outstanding result. The conversion efficiencies achieved in this thesis with the QML source can definitely compete with amplified ML systems delivering pulses in the picosecond range [31, 165, 168]. The three reported experiments with higher output power levels than the ones presented in this thesis, exhibited lower SC conversion efficiency.

The results retrieved with the InF_3 fiber have been limited by the relatively low damage threshold of the fiber material and lead to an output power level of 0.8 W in all spectral bands. The LWE of the output spectrum at the highest pump power level has been approximately 2.95 μm. Beyond the optical LWP filters at 2.15 μm and 2.65 μm, an output power of 0.18 W and 0.08 W with a slope efficiency of 20% and 7% have been obtained, respectively.

There are much less reports in literature about mid-IR SCG in InF_3 fibers compared to ZBLAN fibers as nonlinear medium. In [169], a similar InF_3 fiber, regarding material absorption, has been used for mid-IR SCG. Also in this paper, the conversion efficiency has been very low and a comparable output spectrum has been achieved with approximately the same LWE. The fiber has been pumped with 1 ns pulses.

As already mentioned in the context of the ZBLAN fibers, the relatively low LWE can be further shifted by using femtosecond pulses. In [170], an InF_3 fiber has been pumped by an OPO delivering pulse durations of 70 fs at 3.4 μm. Wavelength conversion up to 4.7 μm has been achieved. In [171], the same fiber, as in the experiments described here, with a length of centimeters has been pumped by an ultra-fast 2 μm laser, which resulted in a spectrum extending to beyond 4.6 μm. Very recently, relatively long pulses in the range of 400 ps at a wavelength of 2.75 μm demonstrated 1 W of output power with a spectrum exceeding 5.4 μm. The used InF_3 fiber length has been around 15 m with relatively low material absorption [172].

5 Further wavelength broadening of the SC radiation in other soft-glass fibers

5.1 Introduction

In this chapter, further broadening of the SC output radiation from the fluoride fibers is investigated. The main goal is to cover the atmospheric transmission windows up to around 5.5 μm with high average power. The results presented in this chapter are first proof-of-principle investigations, which should demonstrate if the soliton-like SC output radiation from the fluoride fibers is suitable for further wavelength conversion in another soft-glass fiber with a broader transmission bandwidth.

The nonlinear fibers for this broadening stage are mainly chalcogenide materials that offer promising characteristics for this application. In contrary to fluoride materials, chalcogenide glasses consist of very heavy atoms with weak chemical bonds in their lattice, which decrease their vibrational frequencies and result in a low phonon energy. Therefore, their transmission bandwidth is very broad in the mid-IR wavelength range. Another auspicious feature is the high nonlinear-index coefficient that can be a factor of 1000 times bigger compared to silica or fluoride materials [173]. With very short interaction lengths, very broadband SC output radiation is possible. There are many reports in literature exploiting those features in the scope of SCG [43], stimulated Raman [174] or Brillouin scattering [175] in the mid-IR wavelength range.

However, there are also drawbacks connected to the usage of chalcogenide fibers. First, they exhibit relatively poor mechanical properties, which yield a low optical damage threshold and therefore low pump and output power levels. The handling of these fibers is more challenging because of the mentioned fragility and toxic ingredients, which are very often implemented in their composition. Their high ZDWs in the range of 5 μm - 7 μm complicate the realization of compact pump sources for mid-IR SCG in the anomalous dispersion region [24, 176].

There are several attempts to bypass the last mentioned handicap by lowering the ZDW of these fibers. There is the possibility to increase the influence of waveguide dispersion on the total fiber dispersion, which can be realized by decreasing the fiber core diameter. A very promising technology in this regard are PCFs owing to their great flexibility in tailoring their dispersion parameters, as explained in subsection 2.1.2.3. Suspended-core fibers are hereby very popular, because they can be manufactured with core diameters in the range of micrometers surrounded by almost only air, in which the evanescent field of the modes propagates and causes strong waveguide dispersion [24]. A second experimentally-proven alternative to lower the ZDW are tapers in single-clad fibers, which blue-shift the ZDW [177]. The third possibility is multimaterial fibers, where the inner cladding of a single-clad fiber, or the capillaries of a PCF, are made out of another material [178].

As a consequence of the much broader output spectrum if the nonlinear materials are pumped in their anomalous dispersion region, the fiber parameters and the expected SC output performance have been very often simulated based on the different mentioned possibilities to lower the ZDW [178, 179]. But even if the ZDW of a nonlinear fiber is decreased, mid-IR pump sources are still necessary to reach the anomalous dispersion region. Mid-IR ultra-fast OPOs [24], pumped by Ti:Sa lasers [43] or Er^{3+}-doped fiber lasers [180], microchip lasers [181] or SC pump sources [182] have been reported frequently as pump sources for this application, where wavelength broadening up to 10 μm has been demonstrated [183].

However, the small core diameters lower the damage threshold of these fibers in terms of average pump power and pulse energy. Therefore, the used nonlinear fibers in this thesis have relatively big core diameters and are pumped in the normal dispersion region. The expected output spectra are thus narrower, but they contain more average power. Compared to the pumping regime in the anomalous dispersion regime, it is necessary to use longer fibers to reach sufficient nonlinear gain. This work reports the first time on wavelength broadening of SC radiation from a fluoride fiber in chalcogenide fibers in their normal dispersion region. There are reports about pumping chalcogenide fibers in the normal dispersion region, but with different pump sources [174].

This chapter includes the description of the optical setup with the characterization tools for the broadening experiments. Furthermore, the available nonlinear fibers with all important parameters are introduced. The achieved results are presented and compared in the summary with the state-of-the-art reported performance regarding wavelength broadening in such chalcogenide fibers.

5.2 Experimental setup

The setup of the second broadening stage is shown as block diagram in Figure 5.1. The presented experiments in this chapter have been performed with ZBLAN#3 as nonlinear fiber for the first mid-IR SC stage, which is, together with the Tm^{3+}-doped pump fiber laser, summarized with the two left blocks. Between the ZBLAN fiber and the second nonlinear fiber, an optical LWP filter is used to cut out most of the SC radiation from the ZBLAN fiber including

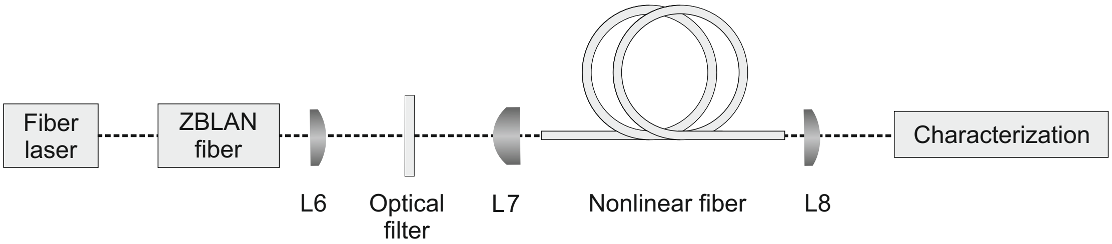

Figure 5.1: Experimemtal setup for further wavelength broadening of the SC output radiation from the ZBLAN fiber including Tm^{3+}-doped fiber laser, ZBLAN#3, optical LWP filter, second nonlinear fiber and characterization.

the residual 2 μm pump radiation to prevent damages of the second nonlinear fiber. The collimation and coupling lenses, L6 and L7, image the output facet of the ZBLAN fiber onto the input facet of the nonlinear fiber. Two antimony germanium selenide (GeSbSe) lenses of the same kind have been chosen because of their high *NA* and to balance out their material dispersion, which is necessary as a result of the broadband SC pump radiation from the ZBLAN fiber. The lenses had a FL of approximately 6 mm and have been AR-coated from 3 μm to 5 μm. The output radiation of the second broadening stage is collimated by the same type of lens, L8, but uncoated. The characterization of the output radiation has been realized, as in the case of the first SC stage, with a power meter and spectro#1.

5.3 Materials

Three chalcogenide fibers and the InF_3 fiber, described in chapter 4, have been available. The InF_3 fiber is tested as second nonlinear fiber to bypass its OH-induced absorption peak around 3 μm, see Figure 4.2, by pumping it with longer wavelengths. Its parameters are listed in Table 4.1. The chalcogenide materials of the other three fibers have been arsenic selenide (As_2Se_3), germanium arsenic selenide (GeAsSe) and arsenic sulfide (As_2S_3). The exact composition of the GeAsSe fiber from the provider is not available.

The most important parameters of the fibers are summarized in Table 5.1. The As_2Se_3 and the GeAsSe fibers were PCFs exhibiting a core diameter of 11.5 μm/13 μm with a distance Λ of 8.5 μm/8.2 μm between the air holes and a filling factor of 0.44/0.47, respectively. Both fibers should be single-mode in the wavelength range between 3 μm and 5 μm, according to Figure 2.3. The ZDWs of the bulk materials are around 7.4 μm for As_2Se_3 and 7 μm for GeAsSe [184]. The ZDWs of the fibers specified in the table are different owing to the waveguide dispersion, whose influence will be shown later in this section. The total lengths of both PCFs have been approximately 2 m. The nonlinear-index coefficient of the bulk material As_2Se_3 is around $2.4\times10^{-17}\ \frac{m^2}{W}$ [185], but varies significantly according to different reports in literature. The material GeAsSe has a nonlinear-index coefficient between $1.2\times10^{-17}\ \frac{m^2}{W}$ and $2.2\times10^{-17}\ \frac{m^2}{W}$, which is among other parameters also dependent on its material composition [186]. In Table 5.1 and for further calculations, a mean value of $1.7\times10^{-17}\ \frac{m^2}{W}$ is used.

The As_2S_3 fiber had a single-clad fiber design with a core diameter of 6.6 μm and a *NA* of 0.28, which results in a cut-off wavelength (λ_{co}) of 2.4 μm. The ZDW of As_2S_3 is close to 4.8 μm [70], but is shifted towards higher wavelengths owing to the waveguide dispersion of the fiber. The fiber length is approximately 1.4 m. This material has a nonlinear-index coefficient of around $5.7\times10^{-18}\ \frac{m^2}{W}$ [185], which is significantly smaller than that of the other

Parameters	Material	core ø	*NA*	λ_{co}	Λ	$\frac{d}{\Lambda}$	ZDW	l	n_2
Chalco#1	As_2Se_3	11.5 μm	-	-	8.5 μm	0.44	6.7 μm	2 m	24
Chalco#2	GeAsSe	13 μm	-	-	8.2 μm	0.47	6.1 μm	2 m	17
Chalco#3	As_2S_3	6.6 μm	0.28	2.4 μm	-	-	5.8 μm	1.4 m	5.7

Table 5.1: Different available chalcogenide fibers and their most important parameters, including the nonlinear-index coefficient, which is specified as $\times10^{-18}\ \frac{m^2}{W}$.

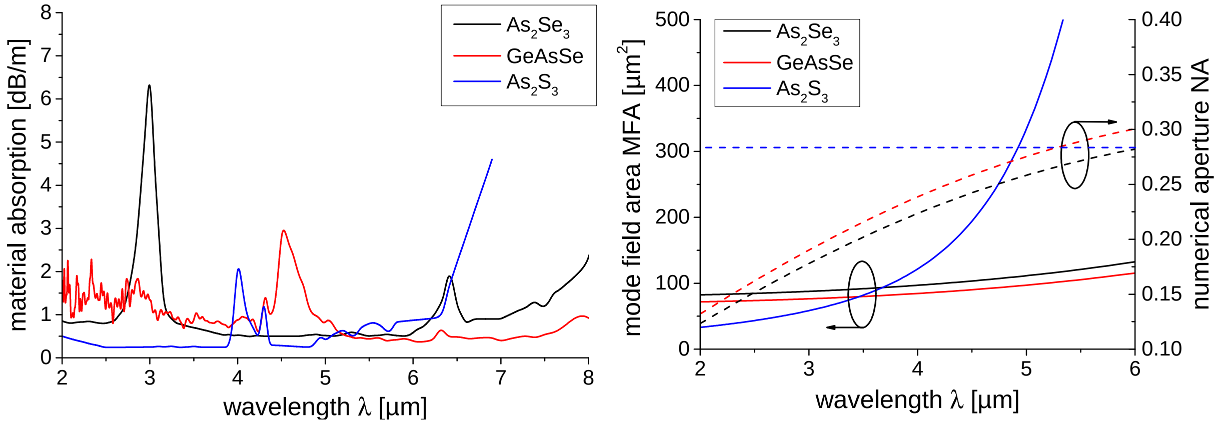

Figure 5.2: *Left*: Material absorption of the As$_2$Se$_3$ [24], GeAsSe [187] and the As$_2$S$_3$ fiber [188]; *right*: Mode field area and numerical aperture versus wavelength for all the available chalcogenide fibers.

two investigated chalcogenide materials.

The absorption of the different materials is displayed in Figure 5.2, left. All available fibers had a stronger absorption for wavelengths below 3 μm compared to the fluoride materials from chapter 4. However, they offered much broader transmission bandwidths. The As$_2$Se$_3$ fiber exhibited a significant OH-caused absorption peak around 3 μm and the GeAsSe fiber suffered from a peak around 4.5 μm, which is caused by hydrogen selenide (SeH). The material GeAsSe had the lowest absorption values for wavelengths beyond 5 μm among all of the used materials. The As$_2$S$_3$ fiber offered the most promising absorption characteristics within the targeted wavelength range between 3 μm and 5 μm, although with an absorption peak around 4 μm caused by hydrogen sulfide (SH).

The refractive indices of the chalcogenide fibers are relatively high (2.8 for As$_2$Se$_3$, 2.6 for GeAsSe and 2.5 for As$_2$S$_3$ [184, 189]), causing Fresnel losses of 20% or more at each fiber end facet. The As$_2$Se$_3$ and the GeAsSe fibers have not been AR-coated. The As$_2$S$_3$ fiber had a so-called moth-eye anti-reflective structure on the input facet, which lowered its Fresnel losses [190]. However, the applied structure has been optimized for a wavelength of around 2 μm and the reflection values at the pump wavelength between 3 μm and 4 μm have not been available.

The right side of Figure 5.2 displays the *NA* and *MFA* versus wavelength of the chalcogenide fibers. In the case of the As$_2$S$_3$ fiber, it has been assumed that the *NA* is constant against wavelength. Owing to its relatively small cut-off wavelength, the *MFA* is increasing very fast beyond the wavelength of around 4 μm, which is very disadvantageous for wavelength conversion, as already discussed. The GeAsSe fiber offered in this respect the most promising features owing to the lowest *MFA* versus wavelength. But the values of the As$_2$Se$_3$ fiber have been only slightly higher.

The bend losses for the nonlinear fibers have been calculated using equation 2.52 and are shown in Figure 5.3, left. As it has been explained in the last chapter, also here the bend losses are plotted based on a critical wavelength, λ_{crit}, at which the fiber exhibits bend losses of 1 $\frac{dB}{m}$. The loss factors for the two PCFs have been negligible. The critical wavelengths for both fibers have been between 13 μm and 15 μm for bending radii bigger than 5 cm and were thus well above the expected output spectrum after wavelength conversion. However, for the As$_2$S$_3$

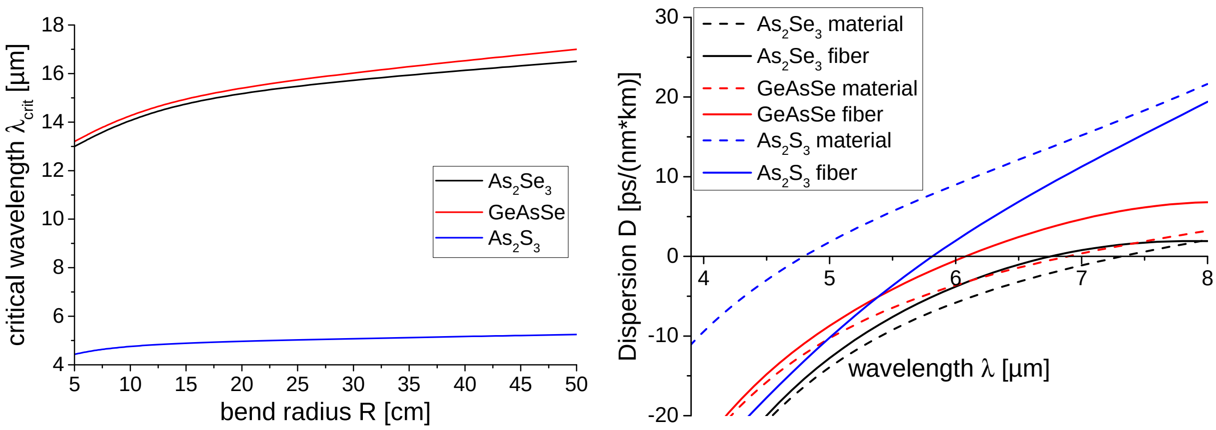

Figure 5.3: *Left*: Macrobending losses versus bend radius based on a critical wavelength exhibiting a bend loss factor of 1 $\frac{dB}{m}$ for the chalcogenide fibers; *right*: Dispersion parameter versus wavelength for the chromatic dispersion of the bulk materials and the related fiber dispersion.

fiber, the critical wavelength has been around 5 μm even for very high bend radii, which had therefore a very strong influence on the total fiber loss.

The chromatic dispersion of the chalcogenide materials together with the total fiber dispersion are displayed in Figure 5.3, right. The Sellmeier coefficients for As_2Se_3 and GeAsSe have been taken from [184] and for As_2S_3 from [191]. The ZDWs of the As_2Se_3 and the GeAsSe PCFs are blue-shifted compared to the ones from the bulk material and are around 6.1 μm and 6.7 μm, respectively. For the As_2S_3 fiber, the influence of the waveguide dispersion red-shifts the ZDW to a wavelength of around 5.9 μm. For all the available fibers, the wavelength conversion process occurred therefore in the normal dispersion region.

The FOMs of all chalcogenide fibers for a fiber length of 2 m are shown in Figure 5.4. In the case of the As_2S_3 fiber, it has been assumed that the fiber orientation is straight, so there are no bend losses. If the absolute values of the FOMs are compared with those calculated for the fluoride fibers from chapter 4, one could expect very good suitability for wavelength conversion with very broad output spectra. But first, the fibers are pumped in the normal

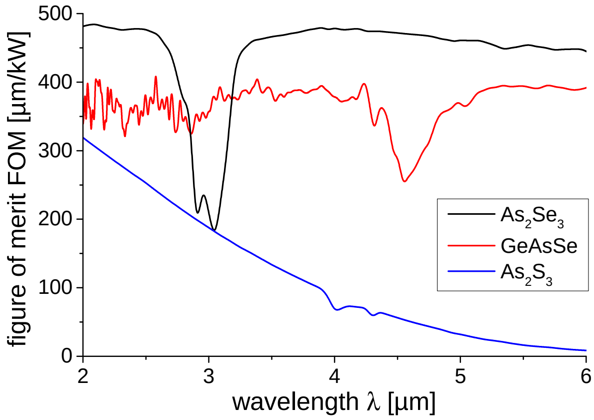

Figure 5.4: Figure of merit for the three available chalcogenide fibers without considering bend losses for a fiber length of 2 m.

dispersion region, which is not considered in the calculation of the FOM. And second, the pump pulse parameters are very different owing to the MI during SCG in the ZBLAN fiber and therefore the soliton-like SC output radiation.

According to the FOMs, the As_2Se_3 fiber exhibits the highest potential for wavelength conversion in the targeted spectral range. The FOM for the As_2S_3 fiber has the lowest values and the trend is decreasing significantly versus wavelength owing to the fast increase of its *MFA* versus wavelength.

5.4 Results

The results in this section are separated into the investigation of the different chalcogenide fibers in the first subsection and the results obtained with the InF_3 fiber in the second subsection.

5.4.1 Chalcogenide fibers

For pumping the chalcogenide fibers with the SC output radiation from the ZBLAN#3 fiber, the optical LWP filter at 3.5 μm has been implemented between the ZBLAN#3 and the chalcogenide fiber. For all the presented experiments, the Tm^{3+}-doped fiber laser with thulium#3 has been operated at an output power level of 20 W with a QS repetition rate of 150 kHz, which has proven to provide good SC efficiencies with ZBLAN#3 and enabled thus the comparison of the different results from the the chalcogenide fibers.

The results of the wavelength broadening experiments using the **As_2Se_3 fiber** are shown in Figure 5.5. The left inset of the left graph displays the cross-section of the fiber end facet with the typical air-filled capillaries around the fiber core, as described in subsection 2.1.2.3. In total, up to 20 mW of average output power has been obtained out of this chalcogenide fiber at the maximum pump power of around 120 mW. The output power scaling has not been limited by any fiber damage. The slope of the output power versus pump power has been

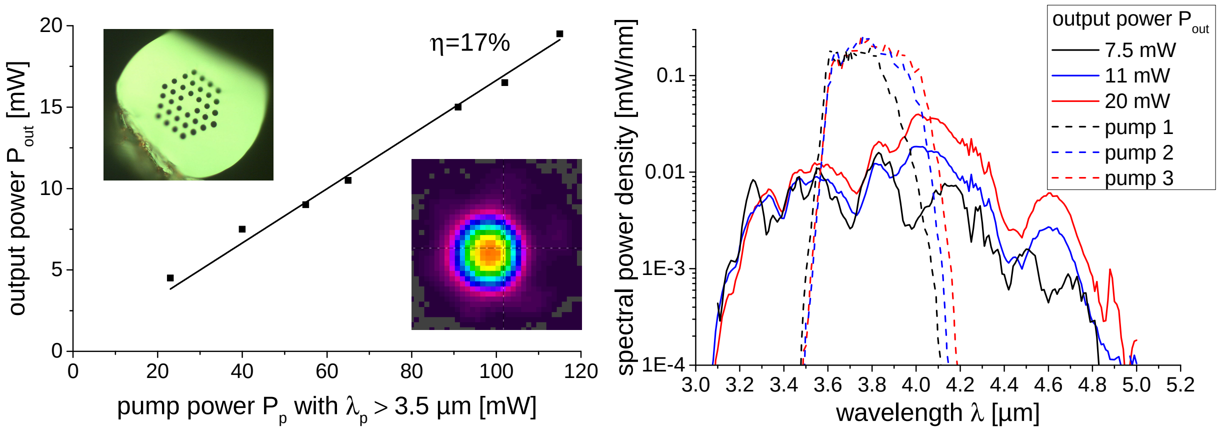

Figure 5.5: *Left*: Output power versus pump power for the As_2Se_3 fiber with the resulting slope efficiency; *left inset*: Cross-section of the end facet of the As_2Se_3 PCF; *right inset*: Intensity profile of the output radiation at the highest output power level; *right*: Pump and output spectra after the wavelength conversion for different output power levels.

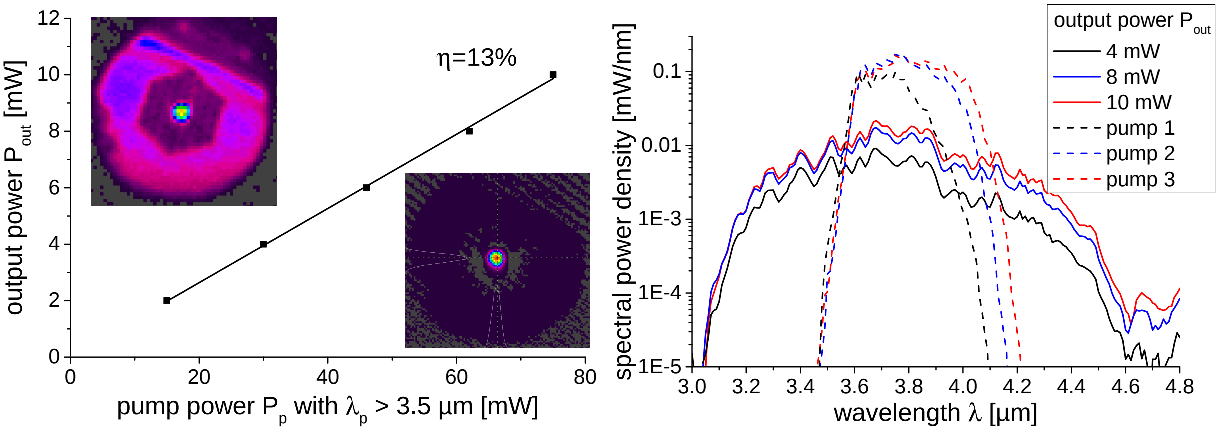

Figure 5.6: *Left*: Output power versus pump power for the GeAsSe fiber with the resulting slope efficiency; *insets*: Intensity profile of the output radiation from the fiber for bad (*left*) and good (*right*) coupling efficiency; *right*: Different pump and output spectra for different output power levels.

17% with a coupling efficiency of around 35%, which has been calculated by considering the average material absorption of the output spectrum and the Fresnel losses of the fiber end facets. The SC pump radiation from ZBLAN#3 should be single-mode beyond 3.6 μm, which is its cut-off wavelength. The achieved relatively low coupling efficiency might be caused by the chromatic dispersion of the collimation and coupling lenses or by additional losses, which can occur by the atmospheric absorption during the propagation of the evanescent field of the modes in the air-filled capillaries of the PCF. The beam quality of the output radiation has not been measured but the right inset of Figure 5.6, left, shows the intensity profile of the output radiation measured at the highest output power level, which seems to be very close to the fundamental mode. The bend radius of this fiber during the experiment has been around 10 cm so the bend losses can be neglected.

The right side of Figure 5.5 displays the output spectra obtained with the As_2Se_3 fiber for different output power levels. The dashed spectra in the graph are the ones from the pump radiation for the corresponding output power levels of the fiber, which had a bandwidth from around 3.5 μm up to 3.9 μm. The pump power for the chalcogenide fibers have been varied by the pump power level of the ZBLAN fiber, which had in consequence different pump spectra at different pump power levels for the chalcogenide fibers. At an output power of 20 mW, the spectrum went from 3.2 μm to 4.9 μm at the -20 dB intensity level. The data from the spectral measurement have been corrected based on the mentioned calibration process of spectro#1 described in the appendix. As it has been for the fluoride fibers in the first SC stage, by increasing the pump power level, the output spectra become broader. However, in this case, blue- and red-shifting of the pump radiation can be observed, which is typical for wavelength broadening in the normal dispersion region.

The output performance of the **GeAsSe fiber** is shown in Figure 5.6. The two insets on the left side of the figure display two different pictures from the output end facet of the GeAsSe fiber during operation. The left one indicates a bad coupling efficiency, because most of the radiation is propagating in the cladding of the fiber. The right inset shows more efficient coupling with much less pump light guided in the cladding, as it has been achieved during the

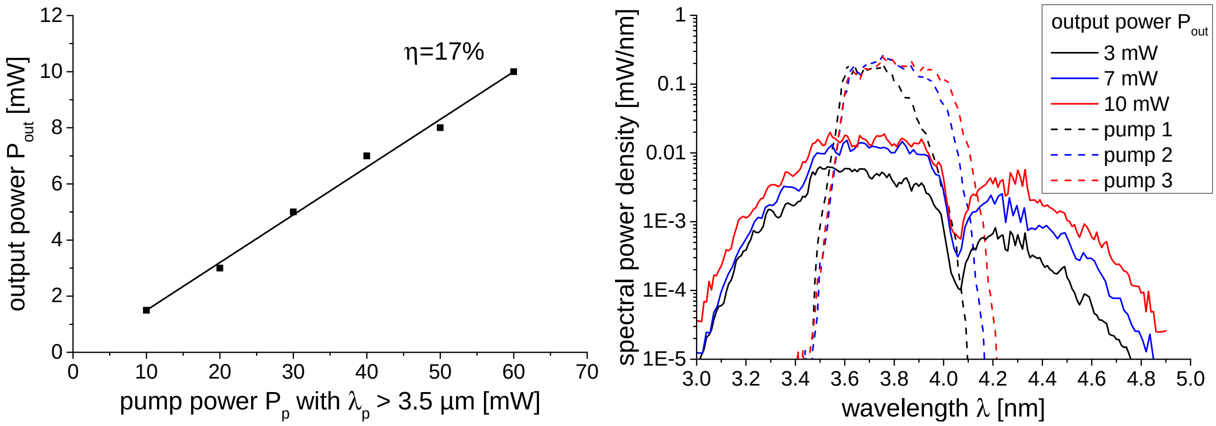

Figure 5.7: *Left*: Output power versus pump power for the As_2S_3 fiber with the resulting slope efficiency; *right*: Different pump and output spectra after the wavelength conversion for different output power levels.

experiments. The radiation in the fiber core has been isolated with a hard aperture before its characterization.

The left graph of Figure 5.6 presents the output power versus pump power. In total, 10 mW have been achieved at a pump power of 75 mW resulting in a slope efficiency of around 13%. The lower slope efficiency with this fiber, compared to the As_2Se_3 fiber, is caused by higher material absorption. Power scaling during this experiment has also not been limited by fiber damage or other restrictions. The coupling efficiency was estimated to be approximately 35%. The beam quality of the output radiation has not been measured but as it is indicated by the right inset in the figure, it seems to be very Gaussian-like. The bend radius of the fiber during this experiment has been approximately 10 cm and the bend losses can be, as mentioned, neglected.

The right side of Figure 5.6 displays the measured output spectra for different output power levels. The broadest spectrum ranged from around 3.2 μm to 4.55 μm, retrieved at the -20 dB level of the spectral intensity.

During the experiments with the **As_2S_3 fiber**, it had to be kept straight because of its high bend losses, see Figure 5.3. Figure 5.7 displays its performance including the output power versus pump power on the left side and the output spectra for different output power levels on the right one. A total average output power of 10 mW has been reached with a slope efficiency of approximately 17%. The output power scaling has also here not been limited by any damage of the fiber. The coupling efficiency during this experiment could not be determined because of the unknown reflectivity of the input facet of the fiber at the pump wavelength.

The spectra on the right side indicate a strong decrease of the spectral power density in the wavelength range of 4 μm, which is caused by the mentioned SH-absorption of the fiber material. The output radiation ranged at the highest output power level from 3.1 μm to approximately 4.7 μm at the -20 dB intensity edge.

For the **comparison of the different chalcogenide fibers** regarding their suitability for wavelength broadening, their spectra are compared at the output power level of around 10 mW, which is shown on the left side of Figure 5.8. The SWEs of the output spectra seemed to be constant for all the fibers at around 3.1 μm. But in terms of LWE, the As_2Se_3 PCF offered

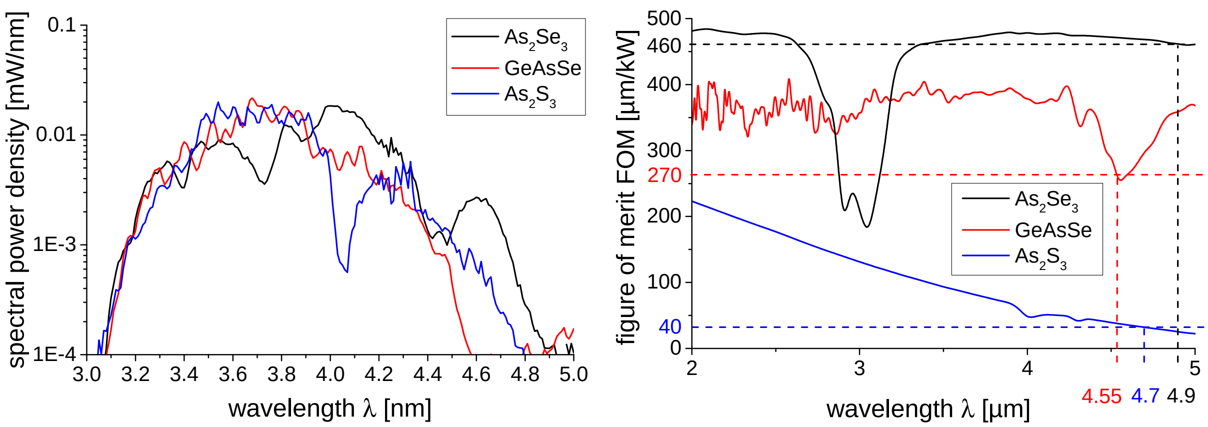

Figure 5.8: *Left*: Comparison of the output spectra of the different investigated chalcogenide fibers at an output power level of around 10 mW; *right*: Comparison of the FOMs with the indication of the LWE of the output spectra for the different fibers.

the highest potential for wavelength conversion with the highest absolute spectral power density levels beyond the wavelength of 4.4 μm. The difference in the trends of the curves is physically related to the mixture of nonlinear effects during the wavelength broadening.

The **evaluation of the output performance based on the FOM** for all the chalcogenide fibers is displayed in Figure 5.8, right. The resulting intersections of the horizontal lines with the y-axis related to the measured LWEs do not match for the different fibers. The intersections with the y-axis for the As_2Se_3/GeAsSe/As_2S_3 fiber are around 460 $\frac{\mu m}{kW}$/270 $\frac{\mu m}{kW}$/40 $\frac{\mu m}{kW}$, respectively. The difference in this estimation for the two PCFs can originate from the large variation of the reported nonlinear-index coefficient in the literature. A 25% higher nonlinear-index coefficient for the GeAsSe fiber and a 25% lower value for the As_2Se_3 fiber would match the intersections with the y-axis. This variation is definitely in the range of the reported values in the literature. Regarding the performance with the As_2S_3 fiber, the calculated FOM is much lower compared to the other two fibers, but it provided good experimental performance, which can have several reasons. First, the nonlinear-index coefficient of the fiber material can vary from the used one for the calculation of the FOM. Second, the reason for the low FOM values for this fiber is the fast increase of the *MFA*, which is dependent on the fiber core and the *NA*. If one of the two stated parameters is different, the absolute values of the FOM can increase significantly. Third, the dispersion of the As_2S_3 fiber is superior compared to the other fibers (see Figure 5.3), which is not considered in the definition of the FOM. And fourth, the already mentioned atmospheric absorption of the guided radiation in the air-filled capillaries of the PCFs is, of course, prevented in the singe-clad design of the As_2S_3 fiber.

5.4.2 Indium fluoride fiber

For the wavelength broadening experiments using the InF_3 fiber as second nonlinear fiber, the Tm^{3+}-doped fiber laser has been operated at an output power level of 20 W with a QS repetition rate of 150 kHz, as it has been the case for pumping the chalcogenide fibers. The optical LWP filter at 3.1 μm has been used between the ZBLAN and the InF_3 fiber, which had a fiber length of around 7 m for this experiment. The output spectrum has been recorded without an optical LWP filter between the InF_3 fiber and the spectrometer. The results are

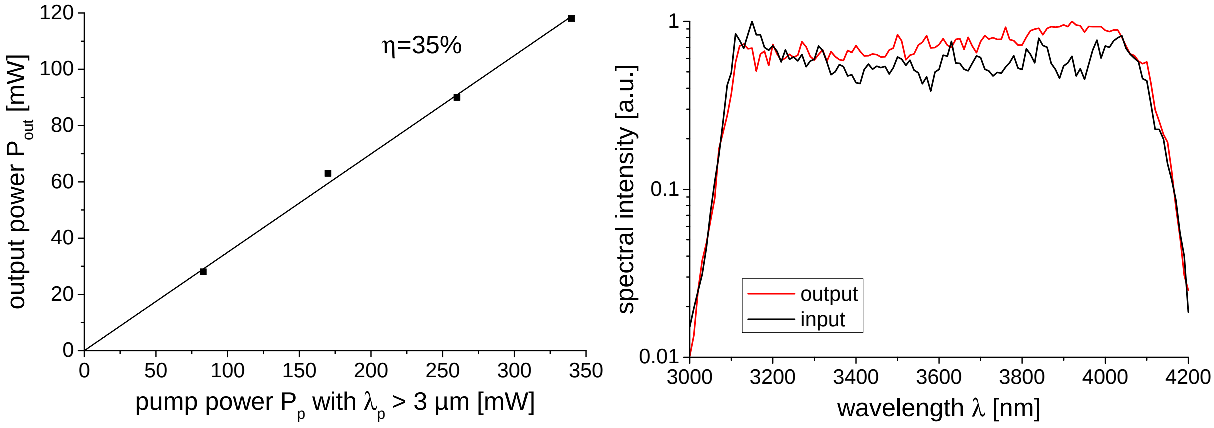

Figure 5.9: *Left*: Output power versus pump power for the InF_3 fiber with the resulting slope efficiency; *right*: Pump and output spectra after the wavelength conversion at the highest output power level.

shown in Figure 5.9.

The left side of the figure shows the output power versus the pump power of the wavelength broadening experiment with this fiber. In total, an output power level of around 120 mW has been reached at a pump power level of approximately 350 mW. The slope efficiency has been in the range of 35%. This relatively low value is caused by the high material absorption and a coupling efficiency of only around 60% because of the single-mode nature of the InF_3 fiber at the used pump wavelengths.

The right side of the figure shows the input and output spectra at the highest output power level. No wavelength broadening has been observed neither in the direction of longer nor smaller wavelengths. The InF_3 fiber has been pumped in the anomalous dispersion region, thus, a blue-shift of the input spectra has not been expected. The output spectrum has been limited at around 4.2 μm, which corresponds to the LWE of the pump spectrum from the ZBLAN fiber. One can observe a change in the spectral power distribution, which indicates a red-shift of the input radiation within the spectral boundaries of the pump radiation, probably caused by SSFS. It could not be discovered why the InF_3 fiber did not provide further wavelength broadening into the mid-IR region in neither the first nor the second broadening stage. The beam quality during the experiment has not been measured, but it is expected to be very good owing to the cut-off wavelength of the InF_3 fiber that is smaller than the wavelength of the pump radiation.

5.5 Summary

As mentioned in the introduction of this chapter, the performed experiments have been first proof-of-principle investigations. The scaling of the average output power has not been pushed up to the limits and the goal was to proof the concept for pumping different nonlinear fibers out of chalcogenide and fluoride materials with the soliton-like output radiation from the ZBLAN fibers. To the best of my knowledge, wavelength broadening with such a mid-IR SC pump source in InF_3 fibers, or in the normal dispersion region of chalcogenide fibers, has not been reported in literature so far.

In total three chalcogenide fibers and one InF_3 have been analyzed for further wavelength broadening experiments. The chalcogenide fiber materials have been made out of As_2Se_3, GeAsSe and As_2S_3. The first two fibers had a PCF and the last one a single-clad fiber design. The As_2Se_3 fiber has been pumped up to a pump power level of 120 mW resulting in an output power of 20 mW with a slope efficiency of 17%. The spectrum of the transmitted radiation at the highest output power level extended to 4.9 μm. With the GeAsSe fiber, in total 10 mW have been obtained with an output spectrum exceeding 4.55 μm. The slope efficiency of the output power versus pump power with this fiber has been around 13%. The single-clad As_2S_3 fiber delivered 10 mW of output power with a slope efficiency of 17% and an output spectrum at the highest output power level up to 4.7 μm. The direct comparison of the output spectra from the three chalcogenide fibers proposed the As_2Se_3 fiber as the best candidate in terms of wavelength broadening suitability. The results achieved with the InF_3 fiber have not exhibited any spectral broadening. The input and output spectra of the experiment have been different, but their spectral boundaries have not been changed.

It is difficult to compare the achieved results with reported experiments in literature. InF_3 fibers have not been investigated for further spectral broadening of mid-IR SC radiation so far. In the case of the chalcogenide fibers, there is only one report with a similar SC pump setup and an As_2Se_3 PCF as nonlinear medium, which has been pumped in the anomalous dispersion region [182]. The output radiation exceeded 6.5 μm with a total average output power of 6.5 mW. In [179], Kubat *et al.* simulated the output performance of almost the same setup, also pumped in the anomalous dispersion region, that has foreseen an output spectrum up to 9 μm .

Mid-IR SCG in chalcogenide fibers have been investigated more often using mid-IR pump sources, which have been commonly realized by ultra-fast mid-IR OPOs. With such high peak power pulses at 4.5 μm, an output spectrum up to 7 μm with an output pulse energy of 11 μJ have been demonstrated in an As_2S_3 fiber with a large core diameter of 100 μm [25]. In [24], an output spectrum up to 7.8 μm has been reached in an As_2Se_3 suspended-core fiber with a core diameter of 4.5 μm and a total output power of 15.6 mW, which is outstanding in terms of average output power for pumping chalcogenide fibers in their anomalous dispersion region. In both reports, the tremendous difference regarding the output spectrum is demonstrated, if the fiber is pumped in the normal or anomalous dispersion region with similar pump pulses. A record concerning LWE of mid-IR SCG in chalcogenide fibers, so far, has been set by Yu *et al.* [183]. A single-clad GeAsSe fiber, composed of different materials in the core and inner cladding, has been pumped by a 4 μm ultra-fast OPO that yielded an output spectrum exceeding 10 μm.

The reported output spectra from experiments with normal-dispersion pumping have been much narrower. In [181], an As_2Se_3 PCF has been pumped by a mid-IR microchip laser at a pump wavelength of around 3.8 μm that resulted in a wavelength broadening up to 4.6 μm. This experiment has been performed to proof the feasibility of wavelength broadening with such a pump setup. In [192], the limits of power scaling of an As_2S_3 fiber with a 10 μm core diameter has been investigated at a pump wavelength of 2 μm. As much as 500 mW of output power have been achieved with an output spectrum up to 4.8 μm, which shows the high potential for power scaling with such fibers. Even wavelength broadening in the normal dispersion region of a chalcogenide fiber with a core diameter of 100 μm has been demonstrated, which yielded a LWE of 4.5 μm at a pump wavelength of 3.9 μm [25].

If the material is pumped in its anomalous dispersion region, the output spectrum is the broadest. The highest reported output power from such experiments is in the range of 15.6 mW. With the results described in this thesis, this output power level has already been outperformed, although, power scaling has not been pushed. If the achieved LWE of around 4.9 μm from the As_2Se_3 fiber is compared with normal-dispersion pumping results from literature, it is already very competitive. In terms of output power level, the demonstrated 500 mW are very promising for further power scaling of the investigated chalcogenide fibers.

6 Conclusion

A Tm^{3+}-doped fiber lasers has been built and characterized in CW, QS, ML and QML operation. In CW operation, as much as 70 W have been reached out of a Tm^{3+}-doped fiber with a length of 8.8 m. QS operation resulted in an output power level of 30 W with variable QS repetition rates. The highest output energy from a 2.2 m-long Tm^{3+}-doped fiber has been 750 μJ with a pulse width of around 40 ns leading to a peak power of 19 kW, which is to the best of my knowledge the highest QS peak power level from a 2 μm fiber laser. In ML operation, an average output power level of 50 W have been demonstrated with a pulse duration of around 200 ps yielding a pulse energy and peak power level of around 800 nJ and 4 kW, respectively. The output power and pulse energy are the highest from a single-oscillator ML fiber laser, but owing to the relatively long pulses, ultra-short pulse generation provides higher peak power levels. For ML experiments, a fiber length of 8.8 m has been used. In QML operation, the output performance is in many different aspects outstanding. First, the additional modulation of the ML pulse train by the QS envelopes enabled very high ML pulse energies of around 50 μJ, which would demand multiple amplifiers if common passively ML fiber lasers are used as seed lasers. The ML pulses had a temporal shape of a short peak on top of a pedestal with pulse durations in the range of 15 ps and 2.5 ns, respectively. The energy of the ML pulse has been contained mostly in the pedestals. The peak power levels of the short peaks could not be identified, the ones from the pedestals have been approximately 20 kW at a ML pulse energy of 50 μJ. The average output power level in QML has been almost 25 W.

The Tm^{3+}-doped fiber laser output in QML operation has been used for pumping different fluoride fibers for mid-IR SCG. The focus has been set on the fluoride material ZBLAN, where three different fiber designs, differed by their core diameters, and one InF_3 have been investigated. The ZBLAN fiber with the biggest core diameter of 12 μm and a NA of 0.23 provided 7.8 W in all spectral bands. The highest SC efficiency during the investigations with this ZBLAN fiber resulted in 69%/43%/30%/16.5% of the transmitted SC output radiation that has been converted beyond the wavelength of 2.15 μm/2.65 μm/3.1 μm/3.5 μm, respectively, with an output spectrum exceeding 4.2 μm. The SCG in the InF_3 fiber resulted in an output spectrum up to around 2.95 μm with an output power level of 0.8 W in all spectral bands.

The SC output radiation from the ZBLAN fiber has been coupled into different nonlinear fibers for further spectral broadening. For these proof-of-principle experiments, three chalcogenide fibers out of As_2Se_3, GeAsSe and As_2S_3 have been pumped in their normal dispersion region. Wavelength broadening has been successfully demonstrated in all chalcogenide fibers with the soliton-like SC radiation from the ZBLAN fiber. The best performance has been provided by the As_2Se_3 fiber, which delivered 20 mW of average power with an output spectrum from 3.1 μm up to 4.9 μm at the -20 dB spectral intensity level.

7 Outlook

There are many different opportunities to further improve the described system including Tm^{3+}-doped fiber laser, first mid-IR SC stage with the fluoride fibers and the second broadening stage with the chalcogenide fibers. The outlook here is separated into the mentioned parts of the setup.

7.1 Tm^{3+}-doped fiber laser

The Tm^{3+}-doped fiber laser has to be further power scaled. With thulium#2 and thulium#3, which were the more promising fiber lengths for mid-IR SCG, the limitation in terms of average power has not been investigated in detail, because an average output power level of almost 30 W has been sufficient for mid-IR SC experiments. The pump power of around 90 W has been close to the maximum output power of the pump diodes. With new available high power diode modules, which have been acquired recently at ISL, power scaling of the Tm^{3+}-doped fiber lasers is feasible and must be performed.
Fiber splicers will soon be available at the institute, which enable the usage of end caps for the active Tm^{3+}-doped fiber. It has been numerously reported in literature that the splice of passive silica fibers to the end facets of the active fiber enables more efficient cooling and therefore higher output power levels and better lasing efficiencies. With the setup used here, the endpieces of the fiber were not actively water-cooled. Additionally in the near future, an all-fiber laser system seems to be feasible, especially owing to the ongoing research activities on fiber-coupled modulators and cavity end mirrors in the form of fiber Bragg gratings (FBG).
The QML operational regime of the fiber laser, induced by the two actively-triggered AOMs, can probably be simplified. As it has been explained in subsection 2.2.5, there are many different ways for generating QML pulses. For instance, one single AOM for QS would be possibly sufficient to induce QML, if the radio frequency of the modulator fits to the fundamental repetition rate of the laser cavity or is a multiple of it. It has to be found out, if AOMs for QS with tunable radio frequency and high diffraction efficiencies are commercially available. Another possibility for a simplification of the current setup could be the replacement of both AOMs by only one SESAM. It has to be identified, if the fiber laser can be operated by using the QML instabilities inherently associated with this passive modulator. However, the QS repetition rates of the QML instabilities are in the range of the relaxation oscillations, which are most likely not suitable for efficient SCG. With a FBG implemented as cavity output coupler, whose reflectivity influences the QS repetition rate of the QML instabilities, this limitation could be bypassed. There is also the possibility of operating the fiber laser cavity with a SESAM and additionally one AOM for QS. A sophisticated laser cavity design is presumably necessary be-

cause of the relatively long build-up time of the ML pulses in fiber lasers based on SESAMs. For the existing setup with the two AOMs, it has to be further investigated how the energy distribution between the ML subpulses and their pedestals can be influenced. The goal is to transfer the energy from the pedestal to its ML pulse to reach higher peak power levels. Furthermore, it has to be characterized if the temporal width of the pedestals can be shortened to reach higher SC conversion efficiencies. A temporarily shorter pedestal would yield a higher peak power level and probably lead to a better SC efficiency. Perhaps the distance of the AOM for ML to the cavity end mirror influences the duration of the pedestal because the opening gate for the intracavity pulse, which is passing the AOM to the cavity end mirror and back to the fiber, is hereby changed.

The output performance of the fiber laser must be analyzed more in detail when the HR mirror is implemented as cavity end mirror. The surprisingly bad performance for SCG with this end mirror has to be further investigated, together with the achieved ultra-short pulse duration of 200 fs.

There is a polarization-maintaining Tm^{3+}-doped silica fiber available, which has been already tested in other fiber laser setups at ISL. This fiber can be implemented in the QML laser setup to investigate its suitability for this application.

7.2 Mid-IR SCG in fluoride fibers

The mid-IR SCG in fluoride fibers can also be improved in regards to many different aspects. For higher output power levels, it might be beneficial to splice the input facet of the ZBLAN fiber onto a passive silica fiber. The damage threshold of silica is much higher compared to ZBLAN and the diffusion of water into the fiber could be prevented, which causes the mentioned degradation of its mechanical properties and decreases its optical damage threshold [193]. There are many reports on mid-IR SCG, which describe the implementation of a single-mode silica fiber before the fluoride fiber to induce a first wavelength broadening and MI in the silica fiber. It has to be found out, if that change would not only increase the damage threshold of the modified nonlinear fiber, but also enhance the efficiency of the SCG. One could also splice the Tm^{3+} fiber directly to the ZBLAN fiber towards an all-fiberized system.

The current limitation of ZBLAN#3 in terms of power scaling is the damage of the fiber end facet caused by the diffusion of water into the fiber. There are several ways to bypass this restriction. A sealed box with dry air could reduce the water diffusion into the fiber. Such a box has already been mechanically designed and will be very soon available for experiments. Furthermore, an end cap of another fluoride material, which is chemically more resistant against water, could be spliced onto the end facet of the ZBLAN fiber. In literature, AlF_3 has been proven to be a promising material for that purpose because it is approximately ten times more stable against the described water diffusion [162]. However, the material absorption of AlF_3 in the mid-IR is higher than the one for ZBLAN, thus, only a very short piece of fiber can be used as end cap.

Another limiting aspect for high average power SCG is the cooling of the fluoride fiber. As mentioned in the thesis, the simulated temperature of the fiber during SCG is already in the range of 70°C for a heat load of 1 $\frac{W}{m}$. For further power scaling, the fiber has to be actively cooled, which can be realized by air-cooling or by gluing it onto a copper heat sink.

Among all ZBLAN fibers, ZBLAN#3 with the relatively big core diameter of 12 μm enabled the highest damage thresholds in terms of average power and pulse energy levels and high SC conversion efficiencies. It has to be investigated, if even a bigger core diameter would further optimize the damage behavior and the SC efficiency of the fibers.

The *NA* of the fiber has also to be considered for a new fiber design. A more suitable evolution of the mode field diameter or better fiber dispersion parameters could further improve the SC output performance.

In literature, it has been discovered that a second ZDW of fluoride fibers, which lies further in the IR, can cause dispersive waves during SCG beyond that wavelength [77]. There are several methods to generate a second ZDW, including the tailoring of the waveguide dispersion of a common single-clad fluoride fiber with [194] or without a taper [182]. A PCF design also enables the realization of a second ZDW [195].

Furthermore, the optimum fiber lengths for the ZBLAN fibers must be determined, which can be empirically done without simulating the SC process by performing SC experiments with ZBLAN#3 and different fiber lengths.

The SC output performance with the InF_3 fiber has been relatively poor concerning output power level and output spectra achieved with it. The reasons for this performance have been fiber impurities and too high material absorption in the mid-IR wavelength range of interest. But generally, the material InF_3 offers a great potential for mid-IR SCG owing to its broader transmission range compared to the commonly used ZBLAN material. The commercial market for InF_3 fibers has to be monitored for fibers with lower absorption losses. In the future, it might be sufficient to splice some meters of InF_3 onto the output end facet of the ZBLAN fiber to further red-shift the LWE edge of the SC output radiation from the ZBLAN fiber.

With the QML pump laser system, a pulse picker can be inserted in the setup in front of the ZBLAN fiber to isolate the most-energetic pulse below the QS envelope. With that optical element, the SC efficiency would most likely increase significantly.

7.3 Second broadening stage with the chalcogenide fibers

Regarding the second broadening stage with the chalcogenide fibers, there are also many opportunities to enhance the output performance. In the experiments performed in this thesis, it has been proven that the SC output radiation from a ZBLAN fiber is suitable for further wavelength conversion in chalcogenide fibers and therefore, the focus has to be put now on the right choice of the fiber material and design. Different materials and compositions must be tested. For example tellurite fibers, which offer a broader transmission range compared to ZBLAN [3] with a much higher nonlinear-index coefficient of $3.8\times10^{-19}\ \frac{m^2}{W}$ [196]. The damage threshold of these fibers lies somewhere between the ones for fluoride and chalcogenide fibers and would offer thus probably higher output power levels compared to the chalcogenide fibers. This material has the lowest phonon energy among all the oxide glasses and its ZDW is close to 2.3 μm. Therefore, these fibers cannot be pumped directly with the Tm^{3+}-doped fiber laser in their anomalous dispersion region. But maybe cascading fluoride and tellurite fibers or splicing a passive silica fiber for first broadening onto the input end facet could be an alternative to bypass this challenge.

The available chalcogenide fibers have to be further power scaled to discover their damage thresholds with the connected fiber designs. As it has already been demonstrated in literature, much bigger core diameters are feasible for wavelength broadening. It has to be researched if that is also possible with the SC pump radiation from the ZBLAN fibers. More chalcogenide fibers with much bigger core diameters have to be acquired and characterized.

The material As_2S_3 offers, as mentioned, a relatively low ZDW, which could maybe enable a fiber design with a ZDW shorter than the LWE of the SC output radiation from the ZBLAN fiber. With such a fiber, much broader output spectra after wavelength conversion are feasible. Furthermore, the necessary design would also most probably offer a flatter trend of the MFD, which would be beneficial for the SC efficiency.

The coupling efficiency of the ZBLAN output radiation to the chalcogenide fibers must be improved, which could be realized by microscope objectives out of chalcogenide glass with a fixed magnification factor. Another possibility to increase the coupling efficiency is to splice them together. This possibility is challenging because of the two different fiber materials. With such a multiple-material spliced fiber design, the pump parameters for the ZBLAN fiber would have to be adapted not to damage the chalcogenide fiber.

A Appendix

Calibration of the optical spectrum analyzer

As mentioned in section 3.3, the mid-IR SC output radiation has been measured in terms of spectral power distribution with a self-built spectrometer, including a monochromator and an InSb detector. The sensitivity of this detector with a field of view (FOV) of 60° is shown in Figure A.1, left. The spectrometer has been calibrated with a black body radiator, operated at an absolute temperature of 1000 K. The right side of the figure displays the Planck spectrum for that temperature, calculated with

$$P(\lambda) = \frac{2\pi hc^2}{\lambda^5 (e^{\frac{hc}{\lambda kT}} - 1)}, \tag{A.1}$$

having its highest intensity at the wavelength of

$$\lambda_p = \frac{2.898 \cdot 10^3}{T} \mu m \cdot K. \tag{A.2}$$

The black curve in the graph presents the measured values from the spectrometer. The measurement of the radiation from the black body radiator has been conducted with an optical LWP filter between the emitter and the spectrometer for preventing the detection of the second diffraction order. The optical LWP filter at 2.1 μm and 2.65 μm have been used for that pur-

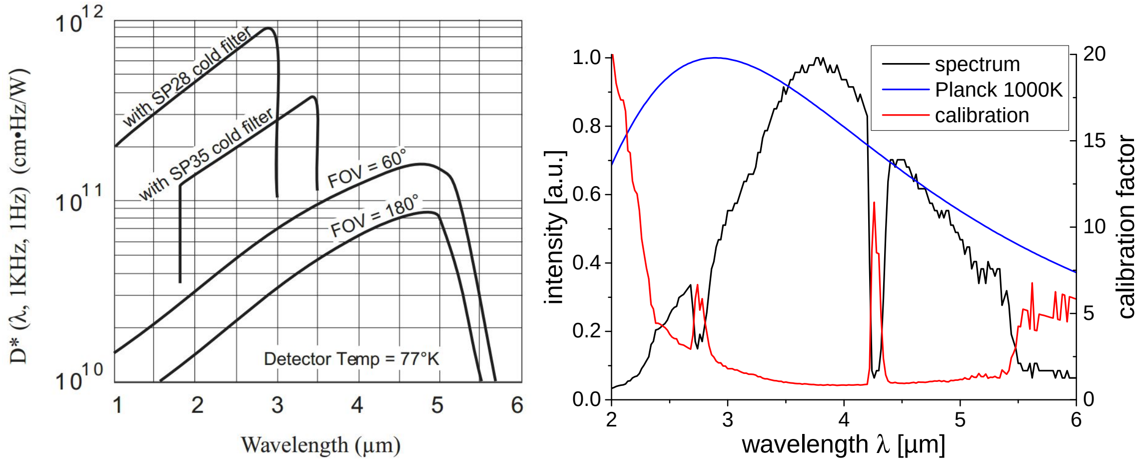

Figure A.1: *Left*: Sensitivity of the used InSb detector with a field of view of 60°; *right*: Measured signal from the monochromator for an input radiation from a black body radiator emitting at 1000 K and the related calibration curve.

pose. Up to 3.5 μm, the spectrum is recorded only with the optical LWP filter at 2.15 μm and corrected with the measured transmission of the filter. Beyond 3.5 μm, the filter at 2.65 μm has been implemented and the measured spectrum has been corrected with the transmission curve of that filter. The wavelength region beyond 5 μm did not play an important role in this thesis. For future measurements with broader output spectra, a mercury cadmium telluride detector is available with a sensitivity up to beyond 10 μm, which can be implemented instead of the InSb in the monochromator.

B List of publications

... in peer reviewed journals

B. Donelan, C. Kneis, G. Scurria, B. Cadier, T. Robin, E. Lallier, A. Grisard, B. Gérard, M. Eichhorn, and C. Kieleck, "Optical parametric generation by a simultaneously Q-switched mode-locked single-oscillator thulium-doped fiber laser in orientation-patterned gallium arsenide," Optics Letters **41**, pp. 5063-5066 (2016).

C. Kneis, B. Donelan, I. Manek-Hönninger, T. Robin, B. Cadier, M. Eichhorn, and C. Kieleck, "High-peak-power single-oscillator actively Q-switched mode-locked Tm^{3+}-doped fiber laser and its application for high-average output power mid-IR supercontinuum generation in a ZBLAN fiber," Optics Letters **41**, pp. 2545-2548 (2016).

C. Kneis, B. Donelan, A. Berrou, I. Manek-Hönninger, T. Robin, B. Cadier, M. Eichhorn, and C. Kieleck, "Actively mode-locked Tm^{3+}-doped silica fiber laser with wavelength-tunable, high average output power," Optics Letters **40**, pp. 1464-1467 (2015).

... as conference contribution

C. Kneis, B. Donelan, I. Manek-Hönninger, T. Robin, B. Cadier, L. Brilland, J. Troles, C. Caillaud, M. Eichhorn, and C. Kieleck, "Mid-Infrared Supercontinuum Generation From Cascaded Soft-Glass," in *High-Brightness Sources and Light-Driven Interactions*, Optical Society of America, paper MM6C.3 (2016).

C. Kneis, T. Robin, B. Cadier, L. Brilland, C. Caillaud, J. Troles, I. Manek-Hönninger, M. Eichhorn, and C. Kieleck, "Generation of broadband mid-infrared supercontinuum radiation in cascaded soft-glass fibers," in *Fiber Lasers XIII: Technology, Systems, and Applications*, Proc. SPIE **9728**, paper 97282A (2016).

C. Kneis, T. Robin, B. Cadier, F. Joulain, M. Poulain, I. Manek-Hönninger, M. Eichhorn, and C. Kieleck, "Mid-IR Supercontinuum Generation in ZBLAN Fibers with High Output Power and High Conversion Efficiency," in *Advanced Solid State Lasers*, Optical Society of America, paper AW4A.10 (2015).

C. Kneis, I. Manek-Hönninger, T. Robin, B. Cadier, F. Joulain, M. Poulain, M. Eichhorn, and C. Kieleck, "5.1 W Mid-Infrared Supercontinuum Generation in a Fluoride Fiber from an Actively Q-switched Mode-Locked Tm^{3+}-doped Silica Fiber Laser," in *IONS Student Conference* (2015).

C. Kneis, B. Donelan, A. Berrou, I. Manek-Hönninger, B. Cadier, T. Robin, M. Poulain, F. Joulain, M. Eichhorn, and C. Kieleck, "4.5 W mid-infrared supercontinuum generation in a ZBLAN fiber pumped by a Q-switched mode-locked Tm^{3+}-doped fiber laser," in *Solid State Lasers XXIV: Technology and Devices*, Proc. SPIE **9342**, paper 93420B (2015).

C. Kieleck, A. Berrou, C. Kneis, B. Donelan, M. Eichhorn, "2 μm and mid-IR fiber-laser-based sources for OCM," in *Technologies for Optical Countermeasures XI; and High-Power Lasers 2014: Technology and Systems*, Proc. SPIE **9251**, paper 92510C (2014).

C. Kneis, A. Berrou, I. Manek-Hönninger, M. Eichhorn, C. Kieleck, "High-power actively mode-locked Tm^{3+}-doped silica fiber laser," in *Solid State, Fibre, and Waveguide Coherent Light Sources*, EPS-QEOD Europhoton, paper WeB-T3-O-04 (2014).

C Conclusion en français

Un laser à fibre dopé Tm^{3+} a été spécifiquement développé pour optimiser la génération de supercontiunuum (SC). En régime continu le laser à fibre Tm^{3+} a délivré 70 W de puissance moyenne avec une fibre de 8,8 m de long. Pour ces expériences les diodes de pompe émettaient une longueur d'onde centrée vers 800 nm, correspondant à 40% de la valeur maximale de la section efficace d'absorption vers 790 nm. Avec des diodes de pompe émettant à 790 nm et une fibre de 2,2 m de long, une puissance de 30 W a été démontrée. Une puissance moyenne de 26 W a été atteinte avec la fibre de 2,2 m en régime de fonctionnement déclenché; la durée d'impulsion valait 40 ns, l'énergie par impulsion maximale atteinte 750 μJ et la puissance crête 19 kW. En fonctionnement purement à modes bloqués avec la fibre de 8,8 m de long, une puissance moyenne de 50 W a été démontrée avec des durées d'impulsion de 200 ps et des énergies par impulsion de 0,8 μJ; la puissance crête atteint 4 kW. En régime QML, 26 W moyens ont été obtenus. L'énergie la plus élevée contenue dans une enveloppe QS a été 166 μJ avec 40% de cette énergie, soit 66 μJ, contenue dans la sous-impulsion à verrouillage de mode la plus énergétique. Les impulsions correspondant au régime de modes bloquées sous l'enveloppe QS ont un profil temporel correspondant à un piédestal Gaussien qui contient la plus grande partie de l'énergie. Au sommet de ces piédestaux, des pics temporels très courts ont été observés. Les largeurs temporelles des piédestaux varient entre 2 ns et 3 ns. La plus forte puissance crête générée dans un piédestal atteint 25 kW. L'impulsion ML présente une largeur temporelle entre 10 ps et 20 ps. La qualité de faisceau du laser à fibre a été mesurée en régime continu, déclenché, à modes bloqués et en régime simultanément déclenché et à modes bloqués. L'émission du laser à fibre correspondait toujours à un facteur de qualité M^2 excellent, entre 1,1 et 1,2.

La puissance moyenne maximale de 7,8 W a été démontrée pour un SC dans une fibre en ZBLAN avec un diamètre de cœur de 12 μm et une ouverture numérique de 0,23. Le spectre s'étend jusqu'à 4,2 μm. Au total, 69%/43%/30%/16,5% de la puissance totale ont été mesurés au-delà de 2,15 μm/2,65 μm/3,1 μm/3,5 μm respectivement. La fibre en InF_3 a permis d'atteindre une puissance moyenne de 0,8 W et le SC s'étend jusqu'à 2,95 μm.

Pour les essais d'élargissement spectral complémentaire au-delà des longueurs d'onde limitatives du ZBLAN, trois fibres en chalcogénure ont été utilisées. Il s'agit de fibre en As_2Se_3, GeAsSe et As_2S_3. L'élargissement spectral a été démontré avec succès pour toutes les fibres. Jusqu'à 20 mW pour une puissance de pompe de 120 mW ont été obtenus avec la fibre As_2Se_3. Cette fibre a aussi montré le meilleur potentiel en termes d'élargissement spectral. Les expériences menées n'ayant pas été limitées par l'endommagement des fibres, des puissances moyennes supérieures à celles générées devraient être accessibles. Le spectre a été étendu jusqu'à 4,9 μm (-20 dB).

Bibliography

[1] C. M. Payne, *Principles of Naval Weapons systems* (Naval Institute Press, 2010).

[2] T. Morioka, K. Mori, S. Kawanishi, and M. Saruwatari, "Multi-WDM-channel, GBit/s pulse generation from a single laser source utilizing LD-pumped supercontinuum in optical fibers," IEEE Photon. Technol. Lett. **6**, 365-368 (1994).

[3] J. Świderski, M. Michalska, C. Kieleck, M. Eichhorn, and G. Mazé, "High Power Supercontinuum Generation in Fluoride Fibers Pumped by 2 μm Pulses," IEEE Photon. Technol. Lett. **26**, pp. 150-153 (2014).

[4] J. Mandon, E. Sorokin, I. T. Sorokina, G. Guelachvili, and N. Picqué, "Supercontinua for high-resolution absorption multiplex infrared spectroscopy," Opt. Lett. **33**, pp. 285-287 (2008).

[5] A. Manninen, T. Kääriäinen, T. Parviainen, S. Buchter, M. Heiliö, and T. Laurila, "Long distance active hyperspectral sensing using high-power near-infrared supercontinuum light source," Opt. Express **22**, pp. 7172-7177 (2014).

[6] R. R. Anderson, W. Farinelli, H. Laubach, D. Manstein, A. N. Yaroslavsky, J. Gubeli, K. Jordan, G. R. Neil, M. Shinn, W. Chandler, G. P. Williams, S. V. Benson, D. R. Douglas, and H. F. Dylla, "Selective photothermolysis of lipid-rich tissues: A free electron laser study," Lasers Surg. Med. **38**, pp. 913-919 (2006).

[7] H. Lim, Y. Jiang, Y. Wang, Y. Huang, Z. Chen, and F. Wise, "Ultrahigh-resolution optical coherence tomography with a fiber laser source at 1 μm," Opt. Lett. **30**, pp. 1171-1173 (2005).

[8] *https://www.laser2000.de/Laser-Sources-Systems/Laser-Lichtquellen/Gaslaser/Durchstimmbare-CO-Laser-2/*

[9] *http://www.thorlabs.com/newgrouppage9.cfm?objectgroup_id=6932*

[10] S. B. Mirov, V. V. Fedorov, D. V. Martyshkin, I. S. Moskalev, M. S. Mirov, and V. P. Gapontsev, "Progress in mid-IR Cr^{2+} and Fe^{2+} doped II-VI materials and lasers," Opt. Mat. Expr. **1**, pp. 898-910 (2011).

[11] P. Loubere, "The Global Climate System," Nature Education Knowledge, *http://www.nature.com/scitable/knowledge/library/the-global-climate-system-74649049* (2012).

[12] D. Faucher, M. Bernier, G. Androz, N. Caron, and R. Vallée, "20 W passively cooled single-mode all-fiber laser at 2.8 μm," Opt. Lett. **36**, pp. 1104-1106 (2011).

[13] S. Y-Suzuki, K. Ishii, and K. Awazu, "Medical application of free electron lasers," *Proceedings of the 2004 FEL Conference*, pp. 692-694 (2004).

[14] Y. Socol, "High-Power Free-Electron Lasers - Technology and Future Applications," Opt. Laser Technol. **46**, pp. 111-126 (2013).

[15] C. Xia, M. Kumar, M.-Y. Cheng, R. S. Hegde, M. N. Islam, A. Galvanauskas, H. G. Winful, and F. L. Terry, Jr.,"Power scalable mid-infrared supercontinuum generation in ZBLAN fluoride fibers with up to 1.3 watts time-averaged power," Opt. Express **15**, pp. 865-871 (2007).

[16] R. R. Alfano, *The supercontinuum laser source: fundamentals with updated references* (Springer, 2006).

[17] W. Werncke, A. Lau, M. Pfeiffer, K. Lenz, H.-J. Weigmann, and C. D. Thuy, "An anomalous frequency broadening in water," Opt. Commun. **4**, pp. 413-415 (1972).

[18] W. L. Smith, P. Liu, and N. Bloembergen, "Superbroadening in H_2O and D_2O by selffocused picosecond pulses from a YAlG:Nd laser," Phys. Rev. A **15**, pp. 2396-2403 (1977).

[19] P. B. Corkum, C. Rolland, and T. Srinivasan-Rao, "Supercontinuum generation in gases," Phys. Rev. Lett. **57**, pp. 2268-2271 (1986).

[20] V. François, F. A. Ilkov, and S. L. Chin, "Experimental study of the supercontinuum spectral width evolution in CO_2 gas," Opt. Commun. **99**, pp. 241-246 (1993).

[21] C. Lin and R. Stolen, "New nanosecond continuum for excited state spectroscopy," Appl. Phys. Lett. **28**, pp. 216-218 (1976).

[22] *http://www.fiberguide.com/wp-content/uploads/2013/03/All_Silica_Fiber_0301131.pdf*

[23] J. Świderski and M. Michalska, "High-power supercontinuum generation in a ZBLAN fiber with very efficient power distribution toward the mid-infrared," Opt. Lett. **39**, pp. 910-913 (2014).

[24] U. Møller, Y. Yu, I. Kubat, C. R. Petersen, X. Gai, L. Brilland, D. Méchin, C. Caillaud, J. Troles, B. Luther-Davies, and O. Bang, "Multi-milliwatt mid-infrared supercontinuum generation in a suspended core chalcogenide fiber," Opt. Express **23**, pp. 3282-3291 (2015).

[25] F. Théberge, N. Thiré, J.-F. Daigle, P. Mathieu, B. E. Schmidt, Y. Messaddeq, R. Vallée, and F. Légaré, "Multioctave infrared supercontinuum generation in large-core As_2S_3 fibers," Opt. Lett. **39**, pp. 6476-6477 (2014).

[26] H. Takara, "Multiple optical carrier generation from a supercontinuum source," Opt. Photon. News **13**, pp. 48-51 (2002).

[27] W. Gao, M. Liao, L. Yang, X,. Yan, T. Suzuki, and Y. Ohishi "All-fiber broadband supercontinuum source with high efficiency in a step-index high nonlinear silica fiber," Appl. Opt. **51**, pp. 1071-1075 (2012).

[28] *http://www.nktphotonics.com/product/superk-extreme-supercontinuum-lasers/*

[29] J. A. Harrington, "Infrared Fibers," in Handbook of Optics Vol. 3, Classical, Vision & X-ray Optics, M. Bass, J. M. Enoch, E. W. Van Striland, and W. L. Wolfe, eds. (Optical Society of America, 2002).

[30] C. Kneis, B. Donelan, A. Berrou, I. Manek-Hönninger, B. Cadier, T. Robin, M. Poulain, F. Joulain, M. Eichhorn and C. Kieleck, "4.5 W mid-infrared supercontinuum generation in a ZBLAN fiber pumped by a Q-switched mode-locked Tm^{3+}- doped fiber laser," Proc. of SPIE **9342**, 93420B (2015).

[31] K. Liu, J. Liu, H. Shi, F. Tan, and P. Wang, "High power mid-infrared supercontinuum generation in a single-mode ZBLAN fiber with up to 21.8 W average output power," Opt. Express **22**, pp. 24384-24391 (2014).

[32] J. M. Dudley and G. Genty, "Supercontinuum light," Physics Today, American Institute of Physics **66**, pp.29-34 (2013).

[33] C. Xia, Z. Xu, M. N. Islam, F. L. Terry, M. J. Freeman, A. Zakel, and J. Mauricio, "10.5 W Time-Averaged Power Mid-IR Supercontinuum Generation Extending Beyond 4 μm With Direct Pulse Pattern Modulation," IEEE J. Sel. Top. Quantum Electron. **15**, pp. 422-434 (2009).

[34] D. J. Richardson, J. Nilsson, and W. A. Clarkson, "High power fiber lasers: current status and future perspectives," J. Opt. Soc. Am. B **27**, pp. B63-B92 (2010).

[35] M. Eichhorn and S. D. Jackson, "High-pulse-energy, actively Q-switched Tm^{3+}-doped silica 2 μm fiber laser pumped at 792 nm," Opt. Lett. **32**, pp. 2780-2782 (2007).

[36] M. Meleshkevich, N. Platonov, D. Gapontsev, A. Drozhzhin, V. Sergeev, and V. Gapontsev, "415 W single-mode CW thulium fiber laser in all-fiber format," in CLEO/Europe and IQEC 2007 Conference Digest, Optical Society of America, paper CP2_3 (2007).

[37] D. C. Hanna, R. M. Percival, R. G. Smart, J. E. Townsend, and A. C. Tropper, "Continuous wave oscillation of a holmium-doped silica fibre laser," Electron. Lett. **25**, pp. 593-594 (1989).

[38] M. Eichhorn and S. D. Jackson, "Comparative study of continuous wave Tm^{3+}-doped silica and fluoride fiber lasers," Appl. Phys. B **90**, pp. 35-41 (2008).

[39] A. Hemming, N. Simakov, A. Davidson, S. Bennetts, M. Hughes, N. Carmody, P. Davies, L. Corena, D. Stepanov, J. Haub, R. Swain, and A. Carter, "A monolithic cladding pumped holmium-doped fibre laser," in *Conference on Lasers and Electro-Optics*, Optical Society of America, paper CW1M.1 (2013).

[40] M. Eichhorn, "Quasi-three-level solid-state lasers in the near and mid infrared based on trivalent rare earth ions," Appl. Phys. B **93**, pp. 269-316 (2008).

[41] N. Tolstik, E. Sorokin, and I. T. Sorokina, "Kerr-lens mode-locked Cr:ZnS laser," Opt. Lett. **38**, pp. 299-301 (2013).

[42] *http://www.industrial-lasers.com/articles/print/volume-30/issue-1/features/fiber-lasers-continue-growth-streak-in-2014-laser-market-revenues-increase-despite-mixed-global-manufacturing-growth.html*

[43] F. Théberge, J.-F. Daigle, D. Vincent, P. Mathieu, J. Fortin, B. E. Schmidt, N. Thiré, and F. Légaré, "Mid-infrared supercontinuum generation in fluoroindate fiber," Opt. Lett. **38**, pp. 4683-4685 (2013).

[44] J. Świderski, M. Michalska, and G. Mazé, "Mid-IR supercontinuum generation in a ZBLAN fiber pumped by a gain-switched mode-locked Tm-doped fiber laser and amplifier system," Opt. Express **21**, pp. 7851-7857 (2013).

[45] C. L. Hagen, J. W. Walewski, and S. T. Sanders, "Generation of a Continuum Extending to the Midinfrared by Pumping ZBLAN Fiber With an Ultrafast 1550-nm Source," IEEE Photon. Technol. Lett. **18**, pp. 91-93 (2006).

[46] I. Kubat, C. S. Agger, P. M. Moselund, and O. Bang, "Mid-infrared supercontinuum generation to 4.5 μm in uniform and tapered ZBLAN step-index fibers by direct pumping at 1064 or 1550 nm," J. Opt. Soc. Am. B **30**, pp. 2743-2757 (2013).

[47] *http://course.ee.ust.hk/elec342/readings/corning%20numerical%20aperture%20measurement.pdf*

[48] E. Snitzer, "Proposed fiber cavities for optical masers," J. Appl. Phys. **32**, pp. 36-39 (1961).

[49] *http://www.phys.keio.ac.jp/guidance/labs/sasada/research/orbangmom-en.html*

[50] E. Snitzer, H. Po, F. Hakimi, R. Tumminelli, and B. C. McCollum, "Double-clad, offset core Nd fiber laser," in *Proc. of Optical Fiber Sensors '88*, paper PD5 (1988).

[51] M. N. Zervas and C. A. Codemard, "High Power Fiber Lasers: A Review," IEEE J. Sel. Top. Quantum Electron. **20**, 0904123 (2014).

[52] D. Marcuse, "Loss analysis of single-mode fiber splices," Bell Syst. Tech. **56**, pp.703-718 (1977).

[53] P. Kaiser, E. A. J. Marcatili, and S. E. Miller, "A new optical fiber," Bell Syst. Tech. J. **52**, pp. 265-269 (1973).

[54] J. Limpert, N. Deguil-Robin, I. Manek-Hönninger, F. Salin, F. Röser, A. Liem, T. Schreiber, S. Nolte, H. Zellmer, A. Tünnermann, J. Broeng, A. Petersson, and C. Jakobsen, "High-power rod-type photonic crystal fiber laser," Opt. Express **13**, pp. 1055-1058 (2005).

[55] G. K. L. Wong, A. Y. H. Chen, S. G. Murdoch, R. Leonhardt, J. D. Harvey, N. Y. Joly, J. C. Knight, W. J. Wadsworth, and P. St. J. Russell, "Continuous-wave tunable optical parametric generation in a photonic-crystal fiber," J. Opt. Soc. Am. B **22**, pp. 2505-2511 (2005).

[56] G. J. Pearce, G. S. Wiederhecker, C. G. Poulton, S. Burger, and P. St. J. Russell, "Models for guidance in kagome-structured hollow-core photonic crystal fibres," Opt. Express **15**, pp. 12680-12685 (2007).

[57] J. C. Travers, W. Chang, J. Nold, N. Y. Joly, and P. St. J. Russell, "Ultrafast nonlinear optics in gas-filled hollow-core photonic crystal fibers [Invited]," J. Opt. Soc. Am. B **28**, pp. A11-A26 (2011).

[58] M. Gebhardt, C. Gaida, S. Hädrich, F. Stutzki, C. Jauregui, J. Limpert, and A. Tünnermann, "Nonlinear compression of an ultrashort-pulse thulium-based fiber laser to sub-70 fs in Kagome photonic crystal fiber," Opt. Lett. **40**, pp. 2770-2773 (2015).

[59] B. Troia, A. Paolicelli, F. De Leonardis, and V. M. N. Passaro, "Photonic Crystals for Optical Sensing: A Review," in Advances in Photonic Crystals, V. Passaro, ed. (InTech, 2013).

[60] N. A. Mortensen, J. R. Folkenberg, M. D. Nielsen, and K. P. Hansen, "Modal cutoff and the V parameter in photonic crystal fibers," Opt. Lett. **28**, pp. 1879-1881 (2003).

[61] N.A. Mortensen, "Effective area of photonic crystal fibers," Opt. Expr. **10**, pp. 341-348 (2002).

[62] *http://www.thorlabs.de/newgrouppage9.cfm?objectgroup_id=1902&pn=ESM-12B#1903*.

[63] R. R. Sangam, *Development of Polychromatic laser beacon fiber coupling system based on photonic crystal fibers*, PhD thesis at the University of Dayton (2013).

[64] A. Husakou and J. Herrmann, "Supercontinuum generation in photonic crystal fibers made from highly nonlinear glasses," Appl. Phys. B **77**, pp. 227-234 (2003).

[65] T. Sylvestre, A. R. Ragueh, M. W. Lee, B. Stiller, G. Fanjoux, B. Barviau, A. Mussot, and A. Kudlinski, "Black-light continuum generation in a silica-core photonic crystal fiber," Opt. Lett. **37**, pp. 130-132 (2012).

[66] J. K. Ranka, R. S. Windeler, and A. J. Stentz, "Visible continuum generation in air-silica microstructure optical fibers with anomalous dispersion at 800 nm," Opt. Lett. **25**, pp. 25-27 (2000)

[67] M. Eichhorn, *Laserphysics* (Springer, 2014).

[68] C. DeCusatis, *Handbook of Fiber Optic Data Communication* (Academic Press, 2002).

[69] G. P. Agrawal, *Nonlinear fiber optics* (Academic press, 2001).

[70] J. M. Dudley, J. R. Taylor, *Supercontinuum Generation in optical fibers* (Cambridge University Press, 2010).

[71] G. Agrawal, *Applications on Nonlinear Fiber Optics* (Academic Press, 2010).

[72] I. Ļašuks, "The Effect of Stimulated Brillouin Scattering on WDM-PON," Electronics and Electrical Engineering **7**, pp. 105-108 (2010).

[73] S. P. Singh, R. Gangwar, and N. Singh, "Nonlinear scattering effects in optical fibers," Progress In Electromagnetics Research, PIER **74**, pp. 379-405 (2007).

[74] K. Tai, A. Hasegawa, and A. Tomita, "Observation of modulational instability in optical fibers," Phys. Rev. Lett. **56**, pp. 135-138 (1986).

[75] M. Suzuki, N. Edagawa, H. Taga, H. Tanaka, S. Yamamoto, and S. Akiba, "10 Gb/s, over 12200 km soliton data transmission with alternating-amplitude solitons," IEEE Photon. Technol. Lett. **6**, pp. 757-759 (1994).

[76] Landolt-Börnstein, *Laser Physics and Applications* (Springer, 2007).

[77] J. M. Dudley, G. Genty, and S. Coen, "Supercontinuum generation on photonic crystal fiber," Rev. Mod. Phys. **78**, pp. 1135-1184 (2006).

[78] E. A. Golovchenko, E. M. Dianov, A. M. Prokhorov, and V. N. Serkin, "Decay of optical solitons," JETP Lett. **42**, pp. 87-91 (1985).

[79] C. Xia, M. Kumar, M.-Y. Cheng, O. P. Kulkarni, M. N. Islam, A. Galvanauskas, F. L. Terry, Jr., M. J. Freeman, D. A. Nolan, and W. A. Wood, "Supercontinuum generation in silica fibers by amplified nanosecond laser diode pulses," IEEE J. Sel. Top. Quantum Electron. **13**, pp. 789-797 (2007).

[80] F. M. Mitschke and L. F. Mollenauer, "Discovery of the soliton self-frequency shift," Opt. Lett. **11**, pp. 659-661 (1986).

[81] P. M. Moselund, C. Petersen, S. Dupont, C. Agger, O. Bang, and S. R. Keiding, "Supercontinuum- broad as a lamp bright as a laser, now in the mid- infrared," Proc. SPIE **8381**, 83811A (2012).

[82] J.-I. Sakai and T. Kimura, "Bending loss of propagation modes in arbitrary index profile optical fibers," Appl. Opt. **17**, pp. 1499-1506 (1978).

[83] *http://www.fiberlabs-inc.com/fiber_smff.htm*.

[84] L. F. Johnson, J. E. Geusic, and L. G. V. Uitert, "Coherent oscillation from Tm^{3+}, Ho^{3+}, Yb^{3+} and Er^{3+} ions in yttrium aluminum garnet," Appl. Phys. Lett. **7**, pp. 127-129 (1965).

[85] American National Standard Z136.6-2005, "Safe use of lasers outdoors".

[86] R. J. DeYoung and N. P. Barnes, "Profiling atmospheric water vapor using a fiber laser lidar system," Appl. Opt. **49**, pp. 562-567 (2010).

[87] N.P. Barnes, B. M. Walsh, D. J. Reichle, and R. J. DeYoung, "Tm:fiber lasers for remote sensing," Optical materials **31**, pp. 1061-1064 (2009).

[88] N. M. Fried, "High-power laser vaporization of the canine prostrate using a 110 W thulium fiber laser at 1.91 μm," Las. Surg. Med. **36**, pp. 52-56 (2005).

[89] N. M. Fried and K. E. Murray, "New Technology in endurology-high power thulium fiber laser ablation of urinary tissues at 1.94 μm," J. Endourol **15**, pp. 25-31 (2005).

[90] J. Kourambas, F. C. Delvecchio, and G. M. Preminger, "Low-power holmium lasers for the management of urinary tract calculi, structures and tumors," J. Endourol **15**, pp. 529-532 (2001).

[91] S. D. Jackson and T. A. King,"Theoretical Modeling of Tm-Doped Silica Fiber Lasers," J. Lightwave Technol. **17**, pp. 948-956 (1999).

[92] S. D. Jackson, "Cross relaxation and energy transfer upconversion processes relevant to the functioning of 2 μm Tm^{3+}-doped silica fibre lasers," Opt. Commun. **230**, pp. 197-203 (2004).

[93] K. Scholle, S. Lamrini, P. Koopmann, and P. Fuhrberg, "2 μm laser sources and their possible applications," in Frontiers in Guided Wave Optics and Optoelectronics, B. Pal, ed. (Intech, 2010).

[94] M. Eckerle, C. Kieleck, J. Świderski, S. D. Jackson, G. Maze, and M. Eichhorn, "Actively Q-switched and mode-locked Tm^{3+}-doped silicate 2 μm fiber laser for supercontinuum generation in fluoride fiber," Opt. Lett. **37**, pp. 512-514 (2012).

[95] D. Creeden, P. A. Ketteridge, P. A. Budni, S. D. Setzler, Y. E. Young, J. C. MaCarthy, K. Zawilski, P. G. Schunemann, T. M. Pollak, E. P. Chicklis, and M. Jiang, "Mid-infrared ZnGeP$_2$ parametric oscillator directly pumped by a pulsed 2 μm Tm-doped fiber laser," Opt. Lett. **33**, pp. 315-317 (2008).

[96] D. C. Hanna, I. M. Jauncey, R. M. Percival, I. R. Perry, R. G. Smart, P. J. Suni, J. E. Townsend, and A. C. Tropper, "Continuous-wave oscillation of a monomode thulium-doped fiber laser," Electron. Lett. **24**, pp. 1222-1223 (1988).

[97] P. Kadwani, N. Modsching, R. A. Sims, L. Leick, J. Broeng, L. Shah, and M. Richardson, "Q-switched thulium-doped photonic crystal fiber laser," Opt. Lett. **37**, pp. 1664-1666 (2012).

[98] R. Paschotta, N. Moore, W. A. Clarkson, A. C. Tropper, D. C. Hanna, and G. Mazé, "230 mW of Blue Light From a Thulium-Doped Upconversion Fiber Laser," IEEE J. Sel. Top. Quantum Electron. **3**, pp. 1100-1102 (1997).

[99] W. Koechner, *Solid-state laser engineering* (Springer, 2006).

[100] M. M. Broer, D. M. Krol, and D. J. DiGiovanni, "Highly nonlinear near-resonant photodarkening in a thulium-doped aluminosilicate glass fiber," Opt. Lett. **18**, pp. 799-801 (1993).

[101] P. Hübner, *Actively mode-locked thulium-doped silica fiber laser*, master thesis at the French-German Research Institute of Saint-Louis and Karlsruhe Institute of Technology (2011).

[102] S. D. Jackson and S. Mossman, "Efficiency dependence on the $Tm^{3+}$and Al^{3+} concentrations for Tm^{3+}-doped silica double-clad fiber lasers," Appl. Opt. **42**, pp. 2702-2707 (2003).

[103] K. van Dalfsen, S. Aravazhi, C. Grivas, S. M. García-Blanco, and M. Pollnau, "Thulium channel waveguide laser with 1.6 W of output power and 80% slope efficiency," Opt. Lett. **39**, pp. 4380-4383 (2014).

[104] M. Eichhorn, *Untersuchung eines diodengepumpten Faserverstärkers mit Emission bei 2 μm*, PhD thesis at the French-German Research Institute of Saint-Louis and Albert-Ludwigs-University Freiburg (2005).

[105] M. J. F. Digonnet, *Rare Earth Doped Fiber Lasers and Amplifiers* (Marcel Dekker, Inc., 1993).

[106] U. Keller, K. J. Weingarten, F. X. Kartner, D. Kopf, B. Braun, I. D. Jung, R. Fluck, C. Hönninger, N. Matuschek, and J. Aus der Au, "Semiconductor saturable absorber mirrors (SESAM's) for femtosecond to nanosecond pulse generation in solid-state lasers," IEEE J. Sel. Top. Quantum Electron. **2**, pp. 435-453 (1996).

[107] C. Rullière, *Femtosecond Laser Pulses, Principles and Experiments* (Springer, 2003).

[108] W. Silvast, *Laser Fundamentals* (Cambridge University Press, 2004).

[109] A. E. Siegman, *Lasers* (University Science Books, 1986).

[110] U. Keller, "Recent developments in compact ultrafast lasers," Nature **424**, pp. 831-838 (2003).

[111] *http://www.batop.de/products/products.html*

[112] R. C. Sharp, D. E. Spock, N. Pan, and J. Elliot, "190-fs passively mode-locked thulium fiber laser with a low threshold," Opt. Lett. **21**, pp. 881-883 (1996).

[113] C. Saraceno, private communication (2014).

[114] M. Jung, J. Lee, J. Koo, J. Park, Y.-W. Song, K. Lee, S. Lee, and J. H. Lee, "A femtosecond pulse fiber laser at 1935 nm using a bulk-structured Bi_2Te_3 topological insulator," Opt. Express **22**, pp. 7865-7874 (2014).

[115] M. A. Solodyankin, E. D. Obraztsova, A. S. Lobach, A. I. Chernov, A. V. Tausenev, V. I. Konov, and E. M. Dianov, "Mode-locked 1.93 μm thulium fiber laser with a carbon nanotube absorber," Opt. Lett. **33**, pp. 1336-1338 (2008).

[116] H.Ahmad, K. Thambiratnam, F. D. Muhammad, M. Z. Zulkifli, A. Z. Zulkifli, M. C. Paul, and S. W. Harun, "Q-Switching and Mode-Locking in Highly Doped Zr_2O_3-Al_2O_3-Er_2O_3-Doped Fiber Lasers Using Graphene as a Saturable Absorber," IEEE J. Sel. Top. Quantum Electron. **20**, 1100108 (2014).

[117] D. E. Spence, P. N. Kean, and W. Sibbett, "60-fsec pulse generation from a self-mode-locked Ti:sapphire laser," Opt. Lett. **16**, pp. 42-44 (1991).

[118] M. Ober, M. Hofer, U. Keller, and T. Chiu, "Self-starting diode-pumped femtosecond Nd fibre laser," Opt. Lett. **18** , pp. 1532-1534 (1993).

[119] Z. Sun, T. Hasan, F. Torrisi, D. Popa, G. Privitera, F. Wang, F. Bonaccorso, D. M. Basko and A. C. Ferrari, "Graphene mode-locked ultrafast laser," ACS Nano **4**, pp. 803-810 (2010).

[120] P. Hübner, C. Kieleck, S. D. Jackson, and M. Eichhorn, "High-power actively mode-locked sub-nanosecond Tm^{3+}-doped silica fiber laser," Opt. Lett. **36**, pp. 2483-2485 (2011).

[121] F. X. Kärtner, "Ultrafast Optical Physics II," lecture notes at the University of Hamburg (2014).

[122] E. M. Vogel, M. J. Weber, and D. M. Krol, "Nonlinear optical phenomena in glass," Physics and Chemistry of Glasses **32**, pp. 231-254 (1991).

[123] Y.-F. Chen, J.-L. Lee, H.-D. Hsieh, and S.-W. Tsai, "Analysis of Passively Q-Switched Lasers With Simultaneous Modelocking," IEEE J. Quantum Electron. **38**, pp. 312-317 (2002).

[124] C. Hönninger, R. Paschotta, F. Morier-Genoud, M. Moser, and U. Keller, "Q-switching stability limits of continuous-wave passive mode locking," J. Opt. Soc. Am. B **16**, pp. 46-56 (1999).

[125] M. Li, S. Zhao, K. Yang, G. Li, D. Li, and J. An,"Diode-pumped actively Q-switching and mode-locking Nd:$GdVO_4$ laser," Laser Phys. Lett. **5**, pp. 722-725 (2008).

[126] P. K. Datta, S. Mukhopadhyay, S. K. Das, L. Tartara, A. Agnesi, and V. Degiorgio, "Enhancement of stability and efficiency of a nonlinear mirror mode-locked Nd:YVO_4 oscillator by an active Q-switch," Opt. Express **12**, pp. 4041-4046 (2004).

[127] H. Huang, J. He, X. Fan, Y. Zhong, H. Chai, and Y. Wang, "The acousto-optic Q-switched mode-locking Nd:YVO_4 laser," Opt. Laser Technol. **40**, pp. 828-831 (2008).

[128] N. Kishi, J. N. Carter, R. Mottahedeh, P. R. Morkel, R. G. Smart, A. J. Seeds, J. S. Roberts, C. C. Button, D. N. Payne, A. C. Tropper, and D. C. Hanna, "Actively mode-locked and passively Q-switched operation of thulium-doped fibre laser using multiquantum well asymetric Fabry - Perot Modulator," Electron. Lett. **28**, pp. 175-177 (1992).

[129] J. Lee, J. Koo, Y. M. Chang, P. Debnath, Y.-W. Song, and J. H. Lee, "Experimental investigation on a Q-switched, mode-locked fiber laser based on the combination of active mode locking and passive Q switching," J. Opt. Soc. Am. B **29**, pp. 1479-1485 (2012).

[130] D. J. Kuizenga, D. W. Phillion, T. Lund, and A. E. Siegman, "Simultaneous Q-Switching and mode-locking in the CW Nd:YAG laser," Opt. Commun. **9**, pp. 221-226 (1973)

[131] R. R. Alfano and S. L. Shapiro, "Emission in the region 4000 to 7000 $^\circ$A via four-photon coupling in glass," Phys. Rev. Lett. **24**, pp. 584-587 (1970).

[132] R. Holzwarth, Th. Udem, T. W. Hänsch, J. C. Knight, W. J. Wadsworth, and P. St. J. Russell, "Optical frequency synthesizer for precision spectroscopy," Phys. Rev. Lett. **85**, pp. 2264-2267 (2000).

[133] V. V. Alexander, Z Shi, M. N. Islam, K. Ke, M. J. Freeman, A. Ifarraguerri, J. Meola, A. Absi, J. Leonard, J. Zadnik, A. S. Szalkowski, and G. J. Boer, "Power scalable >25 W supercontinuum laser from 2 to 2.5 μm with near-diffraction limited beam and low output variability," Opt. Lett. **38**, pp. 2292-2294 (2013).

[134] J. Ren, R. Zhou, S. Lou, W. Hou, Y. Ju, and Y. Wang "Supercontinuum generation in a standard single-mode fiber by a Q-switched Tm, Ho:YVO$_4$ laser," Chin. Opt. Lett. **12**, 090605 (2014).

[135] J. W. Dawson, M. J. Messerly, R. J. Beach, M. Y. Shverdin, E. A. Stappaerts, A. K. Sridharan, P. H. Pax, J. E. Heebner, C. W. Siders, and C. P. J. Barty, "Analysis of the scalability of diffraction-limited fiber lasers and amplifiers to high average power," Opt. Express **16**, pp. 13240-13266 (2008).

[136] Diode company "Dilas", private communication, (2014).

[137] M. Yamane and Y. Asahara, *Glasses for Photonics* (Cambridge University Press, 2004).

[138] M. Eichhorn and S. D. Jackson, "High-pulse-energy, actively Q-switched Tm^{3+},Ho^{3+}-codoped silica 2 μm fiber laser," Opt. Lett. **33**, pp. 1044-1046 (2008).

[139] M. Niklès, L. Thévenaz, and P. A. Rober, "Brillouin Gain Spectrum Characterization in Single-Mode Optical Fibers," J. Lightwave Technol. **15**, pp. 1842-1851 (1997).

[140] M. Jelínek, V. Kubeček, and M. Čech, "Single Shot Diagnostics of Quasi-Continuously Pumped Picosecond Lasers Using Fast Photodiode and Digital Oscilloscope," in Photodiodes-Communications, Bio-Sensings, Measurements and High-Energy Physics, J.-W. Shi, ed., (InTech, 2011).

[141] I. H. Malitson, "Interspecimen Comparison of the Refractive Index of Fused Silica," J. Opt. Soc. Am. **55**, pp. 1205-1209 (1965).

[142] R. M. Waxler and G. W. Cleek, "The effect of Temperature and Pressure on the Refractive Index of Some Oxide Glasses," Journal of Research of the National Bureau of Standards - A. Physics and Chemistry **77A**, pp. 755-763 (1973).

[143] P. F. Moulton, G. A. Rines, E. V. Slobodtchikov, K. F. Wall, G. Frith, B. Samson, and A. L. G. Carter, "Tm-Doped Fiber Lasers: Fundamentals and Power Scaling," IEEE J. Sel. Top. Quantum Electron. **15**, pp. 85-92 (2009).

[144] A. F. El-Sherif and T. A. King, "Analysis and optimization of Q-switched operation of a Tm^{3+}-doped silica fiber laser operating at 2 μm," IEEE J. Quantum Electron. **39**, pp. 759-765, (2003).

[145] K. Yin, B. Zhang, W. Yang, H. Chen, S. Chen, and J. Hou, "Flexible picosecond thulium-doped fiber laser using the active mode-locking technique," Opt. Lett. **39**, pp. 4259-4262 (2014).

[146] M. Bello-Jiménez, C. Cuadrado-Laborde, D. Sáez-Rodríguez, A. Diez, J. L. Cruz, and M. V. Andrés, "Actively mode-locked fiber ring laser by intermodal acousto-optic modulation," Opt. Lett. **35**, pp. 3781-3783 (2010).

[147] J. Bethge, J. Jiang, C. Mohr, M. Fermann, and I. Hartl, "Optically referenced Tm fiber-laser Frequency Comb," in *Lasers, Sources, and Related Photonic Devices*, Optical Society of America, paper AT5A.3 (2012).

[148] J. Jiang, C. Mohr, J. Bethge, A. Mills, W. Mefford, I. Hartl, M. E. Fermann, C.-C. Lee, S. Suzuki, T. R. Schilbli, N. Leindecker, K. L. Vodopyanov, P. G. Schunemann, "500 MHz, 58 fs highly coherent Tm fiber soliton laser," in *Conference on Lasers and Electro-Optics*, Optical Society of America, paper CTh5D.7 (2012).

[149] P. Wan, L.-M. Yang, and J. Liu, "High pulse energy 2 μm femtosecond fiber laser," Opt. Express **21**, pp. 1798-1803 (2013).

[150] J. Li, Z. Zhang, Z. Sun, H. Luo, Y. Liu, Z. Yan, C. Mou, L. Zhang, and S. K. Turitsyn, "All-fiber passively mode-locked Tm-doped NOLM-based oscillator operating at 2-μm in both soliton and noisy-pulse regimes," Opt. Express **22**, pp. 7875-7882 (2014).

[151] J. Świderski, "High-power mid-infrared supercontinuum sources: Current status and future perspectives," Prog. Quantum Electron. **38**, pp. 189-235 (2014).

[152] K. Ohsawa and T. Shibata, "Preparation and characterization of ZrF_4 -BaF_2 -LaF_3 -NaF-AlF_3 glass optical fibers," J. Lightwave Technol. **2**, pp. 602-606 (1984).

[153] C. Xia, *Mid-Infrared Supercontinuum Laser System and its Biomedical Applications*, PhD thesis at the University of Michigan (2009).

[154] P. W. France, M. G. Drexhage, J. M. Parker, M. W. Moore, S. F. Carter und J. V. Wright, *Fluoride glass optical fibres* (Blackie and Son Ltd., 1990).

[155] C. J. and J. H. Simmons, "Chemical durability of fluoride glasses," in Fluoride glass fiber optics, I. D. Aggarwal und G. Lu, eds., (Academic Press, Inc., 1991).

[156] M. Poulain, M. Poulain, J. Lucas, and P. Brun, "Verres fluores au tetrafluorure de zirconium - proprietes optiques d'un verre dope au Nd^{3+}," Mater. Res. Bull. **10**, pp. 243-246 (1975).

[157] A. Akella, E. A. Downing, L. Hesselink, "New fluoroindate glass compositions," J. of Non-Cryst. Solids **213**, pp. 1-5 (1997).

[158] F. Gan, "Optical properties of fluoride glasses: a review," J. of Non-Cryst. Solids **184**, pp. 9-20 (1995).

[159] *https://www.thorlabs.de/newgrouppage9.cfm?objectgroup_id=7999*

[160] C. Xia, M. Kumar, O. P. Kulkarni, M. N. Islam, F. L. Terry, Jr., M. J. Freeman, M. Poulain, and G. Mazé, "Mid-infrared supercontinuum generation to 4.5 μm in ZBLAN fluoride fibers by nanosecond diode pumping," Opt. Lett. **31**, pp. 2553-2555 (2006).

[161] M. Eichhorn, "Numerical modeling of Tm-doped double-clad fluoride fiber amplifiers," IEEE J. Quantum Electron. **41**, pp. 1574-1581 (2005).

[162] N. Caron, M. Bernier, D. Faucher, and R. Vallée, "Understanding the fiber tip thermal runaway present in 3 μm fluoride glass fiber lasers," Opt. Express **20**, pp. 22188-22194 (2012).

[163] K. Diener, private communication (2015).

[164] *http://www.fiberlabs-inc.com/fiber-index.htm.*

[165] W. Yang, B. Zhang, G. Xue, K. Yin, and Jing Hou, "Thirteen watt all-fiber mid-infrared supercontinuum generation in a single mode ZBLAN fiber pumped by a 2 μm MOPA system," Opt. Lett. **39**, pp. 1849-1852 (2014).

[166] O. P. Kulkarni, V. V. Alexander, M. Kumar, M. J. Freeman, . N. Islam, F. L. Terry, Jr., M. Neelakandan, and A. Chan, "Supercontinuum generation from 1.9 to 4.5 μm in ZBLAN fiber with high average power generation beyond 3.8 μm using a thulium-doped fiber amplifier," J. Opt. Soc. Am. B **28**, pp. 2486-2498 (2011).

[167] G. Qin, X. Yan, C. Kito, M. Liao, C. Chaudhari, T. Suzuki, and Y. Ohishi, "Ultrabroadband supercontinuum generation from ultraviolet to 6.28 μm in a fluoride fiber," Appl. Phys. Lett. **95**, 161103 (2009).

[168] W. Yang, B. Zhang, K. Yin, X. Zhou, and J. Hou, "High power all fiber mid-IR supercontinuum generation in a ZBLAN fiber pumped by a 2 μm MOPA system," Opt. Express **21**, pp. 19732-19742 (2013).

[169] J. Świderski, F. Théberge, M. Michalska, P. Mathieu, and D. Vincent, "High average power supercontinuum generation in a fluoroindate fiber," Laser Phys. Lett. **11**, 015106 (2014).

[170] F. Théberge, J.-F. Daigle, D. Vincent, P. Mathieu, J. Fortin, B. E. Schmidt, N. Thiré, and F. Légaré, "Mid-infrared supercontinuum generation in fluoroindate fiber," Opt. Lett. **38**, pp. 4683-4685 (2013).

[171] R. Salem, Z. Jiang, D. Liu, R. Pafchek, D. Gardner, P. Foy, M. Saad, D. Jenkins, A. Cable, and P. Fendel, "Mid-infrared supercontinuum generation spanning 1.8 octaves using step-index indium fluoride fiber pumped by a femtosecond fiber laser near 2 μm," Opt. Express **23**, pp. 30592-30602 (2015).

[172] J.-C. Gauthier, V. Fortin, J.-Y. Carrée, S. Poulain, M. Poulain, R. Vallée, and M. Bernier, "Mid-IR supercontinuum from 2.4 to 5.4 μm in a low-loss fluoroindate fiber," Opt. Lett. **41**, pp. 1756-1759 (2016).

[173] G. Lenz, J. Zimmermann, T. Katsufuji, M. Lines, H. Hwang, S. Spalter, R. Slusher, S. Cheong, J. Sanghera, and I. Aggarwal, "Large Kerr effect in bulk Se-based chalcogenide glasses," Opt. Lett. **25**, pp. 254-256 (2000).

[174] M. Duhant, W. Renard, G. Canat, T. N. Nguyen, F. Smektala, J. Troles, Q. Coulombier, P. Toupin, L. Brilland, P. Bourdon, and G. Renversez, "Fourth-order cascaded Raman shift in AsSe chalcogenide suspended-core fiber pumped at 2 μm," Opt. Lett. **36**, pp. 2859-2861 (2011).

[175] K. H. Tow, Y. Léguillon, P- Besnard, L. Brilland, J. Troles, P. Toupin, D. Méchin, D. Trégoat, and S. Molin, "Relative intensity noise and frequency noise of a compact Brillouin laser made of $As_{38}Se_{62}$ suspended-core chalcogenide fiber," Opt. Lett. **37**, pp. 1157-1159 (2012).

[176] I. Kubat, C. S. Agger, U. Møller, A. B. Seddon, Z. Tang, S. Sujecki, T. M. Benson, D. Furniss, S. Lamrini, K. Scholle, P. Fuhrberg, B. Napier, M. Farries, J. Ward, P. M. Moselund, and O. Bang, "Mid-infrared supercontinuum generation to 12.5 μm in large NA chalcogenide step-index fibres pumped at 4.5 μm," Opt. Express **22**, pp. 19169-19182 (2014).

[177] Y. Sun, S. Dai, P. Zhang, X. Wang, Y. Xu, Z. Liu, F. Chen, Y. Wu, Y. Zhang, R. Wang, and G. Tao, "Fabrication and characterization of multimaterial chalcogenide glass fiber tapers with high numerical apertures," Opt. Express **23**, pp. 23472-23483 (2015).

[178] H. Saghaei, M. Ebnali-Heidari, and M. K. Moravvej-Farshi, "Midinfrared supercontinuum generation via As_2Se_3 chalcogenide photonic crystal fibers," Appl. Opt. **54**, pp. 2072-2079 (2015).

[179] I. Kubat, C. R. Petersen, U. V. Møller, A. Seddon, T. Benson, L. Brilland, D. Méchin, P. M. Moselund, and O. Bang, "Thulium pumped mid-infrared 0.9-9 μm supercontinuum generation in concatenated fluoride and chalcogenide glass fibers," Opt. Express **22**, pp. 3959-3967 (2014).

[180] A. Marandi, C. W. Rudy, N. C. Leindecker, V. G. Plotnichenko, E. Dianov, K. Vodopyanov, and R. L. Byer, "Mid-Infrared Supercontinuum Generation from 2.4 μm to 4.6 μm in Tapered Chalcogenide Fiber," in *Conference on Lasers and Electro-Optics*, Optical Society of America, paper CTh4B.5 (2012).

[181] R. R. Gattass, L. B. Shaw, and J. S. Sanghera, "Microchip laser mid-infrared supercontinuum laser source based on an As_2Se_3 fiber," Opt. Lett. **39**, pp. 3418-3420 (2014).

[182] C. R. Petersen, P. M. Moselund, C. Petersen, U. Møller, and O. Bang, "Spectral-temporal composition matters when cascading supercontinua into the mid-infrared," Opt. Express **24**, pp. 749-758 (2016).

[183] Y. Yu, B. Zhang, X. Gai, C. Zhai, S. Qi, W. Guo, Z. Yang, R. Wang, D.-Y. Choi, S. Madden, and B. Luther-Davies, "1.8-10 μm mid-infrared supercontinuum generated in a step-index chalcogenide fiber using low peak pump power," Opt. Lett. **40**, pp. 1081-1084 (2015).

[184] H. G. Dantanarayana, N. Abdel-Moneim, Z. Tang, L. Sojka, S. Sujecki, D. Furniss, A. B. Seddon, I. Kubat, O. Bang, and T. M. Benson, "Refractive index dispersion of chalcogenide glasses for ultra-high numerical-aperture fiber for mid-infrared supercontinuum generation," Opt. Mat. Expr. **4**, pp. 1444-1455 (2014).

[185] J. Harbold, F. Ilday, F. Wise, J. Sanghera, V. Nguyen, L. Shaw, and I. Aggarwal, "Highly nonlinear As-S-Se glasses for all-optical switching," Opt. Lett. **27**, pp. 119-121 (2002).

[186] F. Smektala, C. Quemard, V. Couderc, and A. Barthelemy, "Non-linear optical properties of chalcogenide glasses measured by Z-scan," Journal of Non-Crystalline Solids **274**, pp. 232-237, (2000).

[187] Perfos, private communication (2015)

[188] Rafael Gattass, private communication (2015).

[189] C. S. Sheela, S. K. Varshney, and S. Mahapatra, "Dispersion engineering and mid-IR Supercontinuum generation in As_2S_3 step-index fiber," in *IEEE Photonics Conference*, pp. 558-559 (2012).

[190] R. J. Weiblen, C. R. Menyuk, L. E. Busse, L. B. Shaw, J. S. Sanghera, and I. D. Aggarwal, "Optimized moth-eye anti-reflective structures for As_2S_3 chalcogenide optical fibers," Opt. Express **24**, pp. 10172-10187 (2016).

[191] C. Chaudhari, T. Suzuki, and Y. Ohishi, "Design of Zero Chromatic Dispersion Chalcogenide As_2S_3 Glass Nanofibers," J. Lightwave Technology **27**, pp. 2095-2099 (2009).

[192] R. R. Gattass, L. B. Shaw, V. Q. Nguyen, P. C. Pureza, I. D. Aggarwal, and J. S. Sanghera, "All-fiber chalcogenide-based mid-infrared supercontinuum source," Opt. Fiber Techn. **18**, pp. 345-348 (2012).

[193] R. H. Doremus, D. Murphy, N. P. Bansal, W. A. Lanford, and C. Burman, "Reaction of zirconium fluoride glass with water: kinetics of dissolution," J. Mater. Sci. **20**, pp. 4445-4453 (1985).

[194] Z. Chen, A. J. Taylor, and A. Efimov, "Coherent mid-infrared broadband continuum generation in non-uniform ZBLAN fiber taper," Opt. Express **17**, pp. 5852-5860 (2009).

[195] K. M. Hilligsøe, T. V. Andersen, H. N. Paulsen, C. K. Nielsen, K. Mølmer, S. Keiding, R. Kristiansen, K. P. Hansen, and J. J. Larsen, "Supercontinuum generation in a photonic crystal fiber with two zero dispersion wavelengths," Opt. Express **12**, pp. 1045-1054 (2004).

[196] M. Liao, C. Chaudhari, G. Qin, X. Yan, T. Suzuki, and Y. Ohishi, "Tellurite microstructure fibers with small hexagonal core for supercontinuum generation," Opt. Express **17**, pp. 12174-12182 (2009).